nanomaterials

MDPI

Review

Advances in Nanomaterials-Based Electrochemical Biosensors for Foodborne Pathogen Detection

Ivan Bobrinetskiy [1], Marko Radovic [1], Francesco Rizzotto [2], Priya Vizzini [3], Stefan Jaric [1], Zoran Pavlovic [1], Vasa Radonic [1], Maria Vesna Nikolic [4,*] and Jasmina Vidic [2,*]

1 BioSense Institute, University of Novi Sad, 21102 Novi Sad, Serbia; bobrinet@biosense.rs (I.B.); marrad@biosense.rs (M.R.); sjaric@biosense.rs (S.J.); zoran.pavlovic@biosense.rs (Z.P.); vasarad@biosense.rs (V.R.)
2 Micalis Institute, INRAE, AgroParisTech, Université Paris-Saclay, 78350 Jouy-en-Josas, France; francesco.rizzotto@inrae.fr
3 Department of Agriculture Food, Environmental and Animal Sciences, University of Udine, 33100 Udine, Italy; vizzini.priya@spes.uniud.it
4 Institute for Multidisciplinary Research, University of Belgrade, 11030 Belgrade, Serbia
* Correspondence: mariavesna@imsi.rs (M.V.N.); jasmina.vidic@inrae.fr (J.V.)

Abstract: Electrochemical biosensors utilizing nanomaterials have received widespread attention in pathogen detection and monitoring. Here, the potential of different nanomaterials and electrochemical technologies is reviewed for the development of novel diagnostic devices for the detection of foodborne pathogens and their biomarkers. The overview covers basic electrochemical methods and means for electrode functionalization, utilization of nanomaterials that include quantum dots, gold, silver and magnetic nanoparticles, carbon nanomaterials (carbon and graphene quantum dots, carbon nanotubes, graphene and reduced graphene oxide, graphene nanoplatelets, laser-induced graphene), metal oxides (nanoparticles, 2D and 3D nanostructures) and other 2D nanomaterials. Moreover, the current and future landscape of synergic effects of nanocomposites combining different nanomaterials is provided to illustrate how the limitations of traditional technologies can be overcome to design rapid, ultrasensitive, specific and affordable biosensors.

Keywords: electrochemical biosensing; nanomaterials; graphene; carbon nanomaterials; gold nanoparticles; metal oxides; quantum dots; 2D nanomaterials; foodborne pathogen

Citation: Bobrinetskiy, I.; Radovic, M.; Rizzotto, F.; Vizzini, P.; Jaric, S.; Pavlovic, Z.; Radonic, V.; Nikolic, M.V.; Vidic, J. Advances in Nanomaterials-Based Electrochemical Biosensors for Foodborne Pathogen Detection. *Nanomaterials* **2021**, *11*, 2700. https://doi.org/10.3390/nano11102700

Academic Editor: Daniela Iannazzo

Received: 29 September 2021
Accepted: 9 October 2021
Published: 13 October 2021

1. Introduction

Pathogen diagnostics are currently critical for applications in healthcare, food safety analysis and environmental monitoring. Foodborne and waterborne pathogens (i.e., bacteria, fungi, viruses and some parasites) cause infections in humans via contaminated food or water. The high incidence of infection caused by foodborne pathogens indicates that the prevention, surveillance and management of foodborne diseases need to be strengthened [1–3].

The traditional technologies to detect pathogens in food and water are constrained by delayed analysis times, expensive and laborious sample preparation steps and the need for highly trained personnel. The major conventional detection methods can be classified as counting methods, immune-assays and polymerase chain reaction (PCR)-based methods. Counting bacterial colonies on microbiological culture plates is inherently a complex, time-consuming and error-prone method. The detection time takes 3 to 9 days while up to 2 weeks are needed for confirmation of positive results. The confirmation includes observation of the bacterial colony color and morphology together with biochemical tests in a specific medium that is performed after pathogen isolation. Alternatively, immunoassays, such as the enzyme-linked immunosorbent assay (ELISA), lateral flow and dot blot immunoassay, enable detection of pathogen antigens [4–8]. They can use

monoclonal or polyclonal antibodies that specifically bind to the targeted pathogen and can be applied for testing large-scale samples and for the on-site detection of pathogens. However, they usually show low sensitivity and thus have to be confirmed by an additional test. In contrast, PCR-based methods allow rapid and highly specific pathogen diagnosis. In spite of these advantages, PCR-based methods have some limitations. For instance, they can produce false negative results due to a DNA polymerase inhibition by food matrix molecules and ions, which may completely block amplification of target DNA, or false positive results due to the cross-amplification of PCR-generated fragments of non-target DNA.

Biosensors provide a promising tool for such applications due to their portability and simplicity of utilization. The most used types of sensors are by construction optical (plasmonic, UV-Vis/Infrared spectroscopy, Raman, attenuated total reflection), electrochemical, electromagnetic, mechanical, airflow and acoustic. The principal issue in all these technologies is to enable sensitive and selective detection of pathogens in complex food samples that contain low analyte concentrations. Nonspecific adsorption of biomolecules presented in the sample (originated from either the matrix or microorganisms that constitute normal sample microflora) at the biosensor surface can drastically obstruct detection performance, diminish the signal intensity and specificity of the biosensor and increase background "noise".

In the last years, innovative and portable biosensors have emerged as they overcome limitations of traditional and molecular detection technologies and even other biosensors concerning the quantitative detection and screening of pathogens in clinical, environmental and food analysis [9,10]. Among different biosensors, electrochemical platforms are the most popular because they are highly specific towards the analyte and can be adapted for multiplex analysis providing high analytical accuracy even in complex food matrices of various composition, densities and pH. Electrochemical detection of a pathogen exploits a working electrode modified with specific recognition elements (such as antibody, aptamer, DNA probe) ensuring the selectivity, sensitivity and specificity of the measurements. Various strategies and concepts have been developed to prevent nonspecific binding to the electrode surface in biosensors. The concept of such strategies primarily relies on the fabrication method, sample composition, electrochemical technique and performance of each detection principle. Recent literature highlights that different nanomaterials are incorporated into electrochemical biosensors as enhancers, labeling factors or immobilizer supports to enable the overall feasibility of the platform for diagnostic/detection applications.

In this review, we present some basic principles of the electrochemical methods used in biosensors and the state-of-the-art nanomaterial-based electrochemical biosensors for foodborne pathogen (virus, bacteria and bacterial toxin) detection.

2. Electrochemical Methods and Electrode Functionalization

Electrochemical biosensors transduce biochemical events into electrical signals (current, potential, impedance or resistance). They can be divided into biocatalytic using enzymes as recognition elements and affinity (biocomplexing) biosensors using selective and strong binding biomolecules. Affinity biosensors can be further divided into immunosensors based on antibodies or nanobodies, aptasensors based on DNA or RNA aptamers and genosensors based on single strand DNA (ssDNA). Besides, some electrochemical biosensors for pathogen detection use peptides, phages, microRNA, antibiotics or molecularly imprinted polymers (MIPs) as recognition elements [10]. Various electrochemical techniques with different signal mechanisms exist, as illustrated in Figure 1. Their applicability and efficiency depend on the target properties and design of the sensor platform. Voltammetry is performed under controlled potentials when the measured current reflects electron transfer between the sample and the electrode surface. It is possible to measure current values during the potential sweeping towards and backwards while cycling (cyclic voltammetry). By holding the potential of the electrode constant (amperometry), or

holding the current constant (potentiometry), the obtained information in the timescale gives the change in current and potential, respectively. Capacitance, as one of the electric properties of (bio)molecular and biological layers at the surface of the electrochemical electrode, represents important information of the layer charging effect while sensing certain molecules/pathogens. Electrochemical impedance spectroscopy (impedance/resistance of the system) is usually employed for measuring the impedance of the catalytic layer that changes upon target binding to the immobilized recognition element. Electrochemical impedance spectroscopy is frequently used in detecting pathogen microorganisms due to its high sensitivity. Increase in the diameter of electrochemical impedance plotted in a Nyquist diagram shows the increase in system impedance. It is directly proportional to the electron transfer resistance of the system and enables quantitative detection. Potentiostatic systems usually work in a three-electrode format (working, auxiliary and reference electrode) while conductometry and electrochemical impedance spectroscopy are mainly performed in a two-electrode format (working and auxiliary).

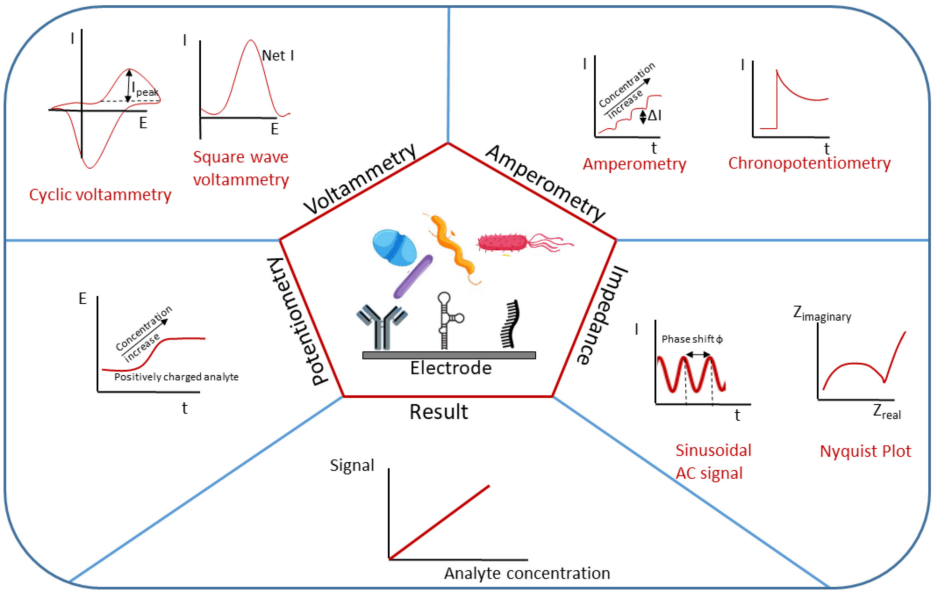

Figure 1. Electrochemical biosensors utilizing different methods (potentiometry, voltammetry, amperometry and electrochemical impedance) for analyte detection and concentration evaluation.

An ideal electrochemical sensor should achieve high sensitivity and specificity, a wide dynamic range of detection, measurement reproducibility, rapid response with real-time analysis and multiple uses. It should also be portable, user-friendly and cost-effective with self-calibration and self-cleaning. To enable simultaneous detection of several targets in the same sample (multiplexing), electrochemical biosensors can be combined with microfluidic systems and integrated with microelectronics. The development of screen-printed electrodes is important in making sensors economical and widely commercially available. Furthermore, data post-processing plays a very important role in obtaining credible and accurate detection results. Many of these properties are an issue in detecting analytes in complex matrices. Affinity biosensors, especially, may have difficulty operating in samples such as food matrices due to nonspecific adsorption on the electrode surfaces that compromises the performance of the device.

The electrode material, its design and fabrication may significantly increase the sensor specificity and selectivity. Surface chemistry is used to immobilize recognition elements onto the working electrode and to prevent a background signal [11]. To eliminate the matrix effect, common strategies involve electrode functionalization using specific surface chemistry and additional electrode covering with poly(ethylene glycol) (PEG) or oligo(ethylene glycol) (OEG) layers that effectively passivate the electrode [12]. Usually,

immobilization of biomolecules is performed via amine-, carboxyl-, aldehyde- and thiol-conjugation, depending on the chemical reactivity of the electrode material and its modifications. Finally, to enable sensitive electrochemical detection, a redox indicator is added to the sample. Ferrocene is the most commonly used redox indicator [10], but others such as protamine [13], tripropylamine [14] or methylene blue [15] also enable estimation of the target concentration by measuring changes in peak intensity. For instance, target binding on the electrode surface may decrease peak intensities of the redox indicator due to the higher electron transfer resistance of the electrode system while increasing the concentration of the captured target. To simplify biosensor utilization and to increase signal intensities, the redox marker can be immobilized onto the electrode surface as shown for influenza A virus detection using conducting copolypyrrole integrating ferrocenyl group electrodes [16,17]. Finally, in cases when the analyte can undergo oxido-reduction on the working electrode itself, no additional redox marker is needed [18].

3. Nanomaterial-Based Electrochemical Biosensors

Many types of sensing electrochemical devices come up, and some of them represent a scaled-down lab to a single chip (lab on a chip). However, despite the intense development of electrochemical biosensors, their high sensitivity and reproducibility remain challenging [19]. Employing various nanomaterials may improve analytical performances of electrochemical sensors by signal enhancement [9,20]. Association of nanomaterials with the electrode increases surface area which can boost loading capacities and mass transport of reactants, resulting in signal amplification. Moreover, nanomaterials can be carriers of redox probes to provide sensitive detection or can improve dynamics of redox exchanges, which significantly amplifies the read-out [21].

Nanomaterials are generally classified as 0D—quantum dots, carbon dots, nanoparticles, 1D—nanotubes, nanowires, nanorods, 2D—nanoplates, nanosheets, nanodisks and 3D—nanoflowers, nanocones, nanoballs [22] (Figure 2). In all 0–3D forms, nanomaterials have been extensively incorporated into electrode construction in electrochemical biosensors applied in the detection of foodborne pathogens [23]. Generally, 0D nanomaterials comprise nanoparticles, usually metal or metal oxide nanoparticles [24–26], carbon and quantum dots [27,28] with nanoscale dimensions. Metal nanoparticles, most commonly gold nanoparticles, are often selected for application in electrochemical biosensors for detection of foodborne pathogens due to their high conductivity and biocompatibility and retention of biomolecule activity over time [29,30]. Quantum dots (QDs) have great potential for application in small size electrochemical biosensing devices due to their small compact size and good and stable performance [31]. In terms of material type, quantum dots can be classified as metal QDs, carbon dots (CDs) and graphene quantum dots (GQDs). One-dimensional (1D) nanomaterials applied in electrochemical biosensing generally include carbon nanotubes [32] and metal oxides synthesized in the form of nanowires, nanotubes or nanorods [33]. Two-dimensional (2D) nanomaterials have come into the limelight starting with the discovery of graphene in 2004 [34]. Besides atomic layer thickness, tunable electronic properties, good mechanical strength and chemical activity, they feature a high surface-to-volume ratio making them good candidates for electrochemical biosensing, gas sensing, energy conversion, storage devices and many other biomedical applications [35–38]. Besides graphene and its derivatives, research has focused on the development of other emerging 2D nanomaterials including boron nitride, graphite carbon nitride, transition metal dichalcogenides, MXenes, black phosphorous, transition metal oxides and also, more recently, heterostructures incorporating at least one 2D nanomaterial [39–41]. Metal oxides, when exfoliated into monolayers, can form a 2D oxide nanostructure [40]. Most common 3D nanomaterial structures applied in electrochemical biosensing of foodborne pathogens are generally various metal oxides, often grown in the form of nanoflowers [42] or other 3D structures, and, more recently, carbon allotropes such as laser-induced graphene [43,44]. Especially, nanomaterials with intrinsic conductivity, such as metal oxide, carbon nanomaterials and metal nanoparticles, significantly

improve the sensing devices that relied on electrical signal. Moreover, synergic effects can be achieved by combining two or more 0–3D nanomaterials, forming a nanocomposite heterostructure on the same electrode [45–48].

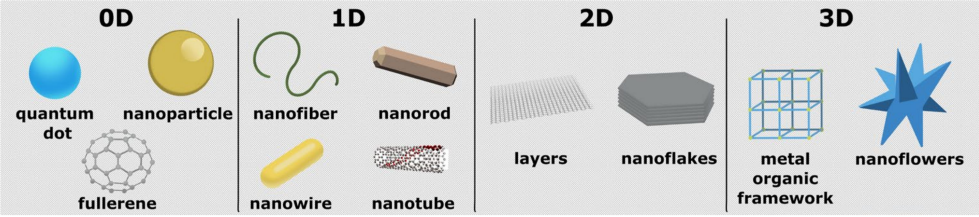

Figure 2. Illustration of some 0–3D nanostructured material morphologies.

Different surface modifications involving thiols, amines and silanes are performed to functionalize electrodes carrying nanomaterials in order to attach biorecognition elements to the electrode in a stable way. Proper functionalization is one of the key elements in biosensor development since maintaining the full biological activity upon immobilization allows optimal analytical properties of the biosensor [49]. For instance, DNA probes thiolated at 5′ or 3′, or peptides modified with a cysteine residue at one end, covalently bind to gold film or gold nanoparticles [14], while an antibody can be immobilized covalently via amino links on a gold electrode surface with a previously attached self-assembled thiol layer that was activated with a mixture of 1-ethyl-3-(3-dimethylaminopropyl)carbodiimide (EDC) and N-hyrdoxysuccinimide (NHS) [50]. In addition, non-covalent binding of recognition elements to the electrode via streptavidin–biotin interaction allows for a highly stable biosensor surface [51,52].

3.1. Metal Oxide Nanomaterials

Metal oxides are semiconductor materials due to their crystalline ordering, electronic band structure, specific surface and quantum related properties. According to the semi-classical theory [53], the conductivity of a semiconductor can be easily modified/enhanced by changing the concentration or the mobility of free charge carriers. Such features represent an ideal starting point for the design of electrochemical biosensors for pathogen detection. Previous studies have shown that the concentration of free charge carriers in metal oxide materials can be modified by oxygen vacancy concentration, doping, particle size, temperature, humidity, electromagnetic radiation and surface adsorbed species [26,33]. Metal oxide nanomaterials can be synthesized in various morphologies ranging from 0 to 3D, providing an interesting playground for the design of electrochemical biosensors [25]. They are low cost, highly biocompatible, show an antimicrobial effect and have a large catalytic area and electrocatalytic activity [45]. The synthesis procedure has a significant influence on metal oxide nanoparticle morphology and resulting properties [26,33]. Some examples of metal oxide nanostructures include nanoparticles [54,55], nanowires [56], nanocubes [57], nanosheets [58], flower-like structures [59], etc.

Recent research has focused on nanocomposite heterostuctures, where different characteristics of each component lead to improved performance and characteristics of electrochemical biosensors for food pathogen detection [46]. Metal oxide 0–3D nanomaterials have great potential to improve the biorecognition performance, where focus is on engineering the microstructure, as shown by Zhai et al., where a 3D networked carbon nanowall/diamond supporting CuO architecture was developed combining microwave plasma chemical vapor deposition of the hybrid carbon nanowall/diamond film on fluorine tin oxide (FTO) glass substrate. It was then used as a template for deposition of Cu nanoparticles by magnetron sputtering followed by growth of CuO nanoparticles by an electrochemical method [45]. Fatema et al. performed a comparative study of two mesoporous nanocomposites, ZrO_2-Ag-G-SiO_2 and In_2O_3-G-SiO_2 (Figure 3), for rapid and highly efficient detection of *Escherichia coli* using cyclic voltammetry, achieving detection in the range from 10^1 CFU/mL to 10^{10} CFU/mL [46].

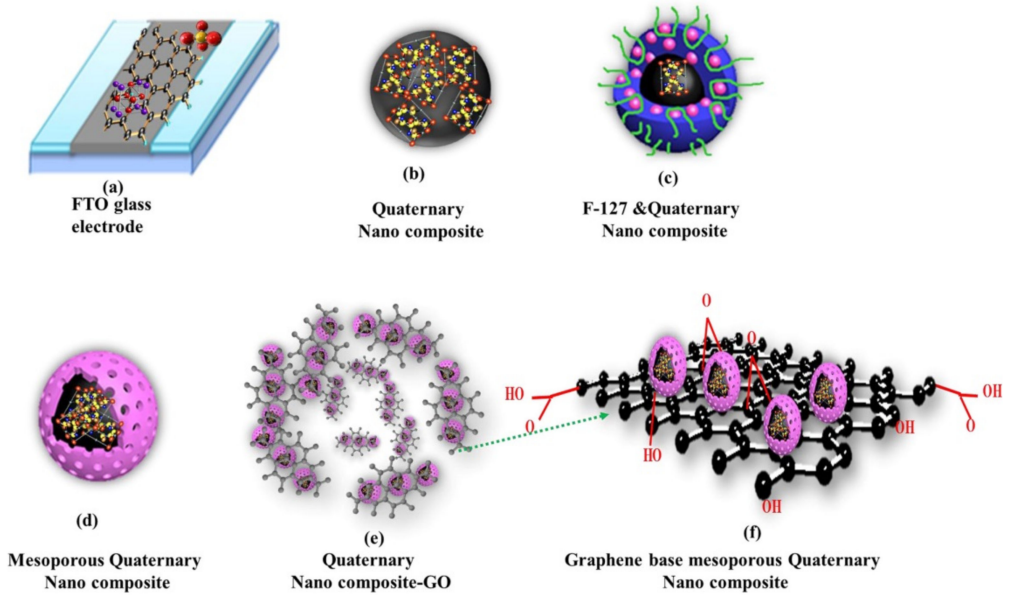

Figure 3. Schematic presentation of the synthesis process of the ZrO_2-Ag-Graphene Oxide -SiO_2 nanocomposite. Adapted with permission from [46] Copyright 2020, American Chemical Society.

Several reports have indicated significant sensing improvements obtained by using metal oxide nanoparticles in electrochemical biosensors. Muniandy et al. [60], developed a reduced graphene oxide–nano TiO_2 composite for an aptasensor used in the detection of *Salmonella enterica* (Figure 4). The bacterial cells captured by the aptamers incorporated on the electrode surface were a physical obstacle for electron transfer, which decreased the voltammetric signal proportionally to the bacterial concentration. Performance of the sensor was evaluated using cyclic voltammetry and electronic impedance spectroscopy. The developed aptasensor exhibited high sensitivity with a wide detection range (1–10^8 CFU/mL), low detection limit of 1 CFU/mL, good selectivity for Salmonella strains and acceptable long-term stability. Nadzirah et al. [61] used pure TiO_2 nanoparticles (NPs) and fabricated interdigitated electrodes for *E. coli* detection. A specific ssDNA probe was immobilized on the electrode surface upon its chemical functionalization with (3-aminopropyl) triethoxysilane (APTES) to provide contact between the organic and inorganic surfaces of a ssDNA probe and TiO_2 NPs. The obtained genosensor showed high sensitivity since it was able to detect as low as 1.0×10^{-13} M of *E. coli* O157:H7 DNA in bacterial lystes, with a high specificity and reproducibility.

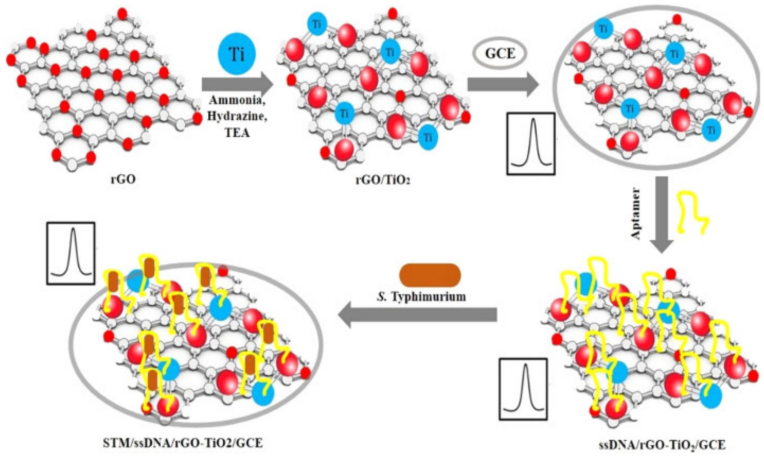

Figure 4. Schematic presentation of the fabrication of rGO-TiO2 electrodes and their employing for electrochemical detection of bacteria. Adapted with permission from [60] Copyright 2019, Elsevier.

Teng et al. [62] showed that ZnO nanorods in an electrochemical immunoassay for detection of *E. coli* led to signal enhancement. They immobilized both the detection antibody (anti-*E. coli* polyclonal antibody) and the redox probe (ferrocene) onto the surface of ZnO nanorods which surfaces were coated with a layer of silica. When coated with silica, the nanorods form core–shell nanorods that can be easily modified with various functional groups. The obtained complex antibody-ZnO-ferrocene was incubated with an *E. coli* contaminated sample and then washed and deposited on to a gold electrode carrying a capturing anti-*E. coli* antibody. The designed immunoassay showed a detection limit of 50 cfu/mL. In another study, Purwidyantri et al. [63] used ZnO nanograss decorated with Au nanospeckles to develop a sensing platform for *Staphylococcus epidermidis*, based on DNA hybridization. Applying the thermal evaporation, Au nanoparticles were deposited on the hydrothermally synthesized ZnO nanograss. The deposition increased by approximately two-fold the effective surface area and diffusion coefficient compared to the non-speckled ZnO nanograss. The fabricated genosensor carrying a DNA probe complementary to the 16S region in the genome of *S. epidermidis* attained a limit of detection (LoD) of 0.506 pM.

Earth abundant transition metal oxides are showing great potential for electrochemical applications, including electrochemical biosensors for foodborne pathogens [64]. Thus, rapid detection of *Salmonella typhimurium* was achieved using an SiO_2@MnO_2 nanocomposite impedance biosensor developed on interdigitated array microelectrodes combined with immunomagnetic separation [65]. Magnetic beads were used to capture monoclonal antibodies and separate *S. typhimirium* cells rapidly from samples, while detection was achieved by release of Mn^{2+} by H_2O_2 monitored as a change in impedance, as shown in Figure 5.

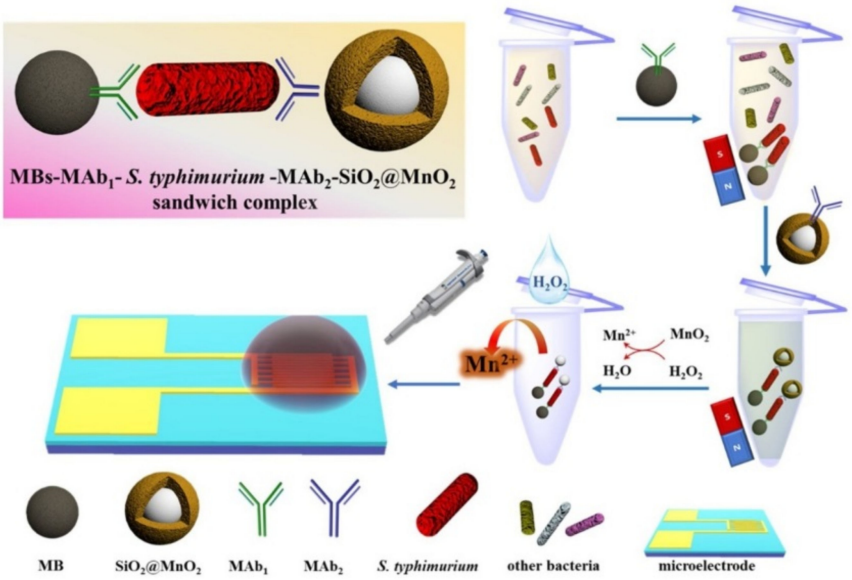

Figure 5. Illustration of the detection of *S. typhimirium* using immunomagnetic separation and impedance monitoring of the release of Mn^{2+} from the SiO_2@MnO_2 nanocomposite. Adapted with permission from [65] Copyright 2020, Elsevier.

An electrochemical genosensor based on SnO_2 nanocrystalline quantum dots was developed by Patel et al. [66] for detection of *Vibrio cholerae* using the DNA hybridization principle. The electrode was obtained by electrophoretic deposition of SnO_2-QDs onto indium-tin oxide coated glass substrate. Subsequently, a DNA probe was attached to SnO_2 NPs via its phosphate groups. The study showed that SnO_2 NPs provided not only an effective surface for DNA probe immobilization, but also enhanced electron transport and improved signal read-out. The fabricated sensor detected *V. choleare* complementary DNA sequences with the limit of detection of 31.5 ng/µL and showed high long-term stability.

Bacteria remain the most commonly detected pathogen with metal oxide based electrochemical biosensors. Moreover, current trends are focused on the use of metal oxide photocatalytic properties in inactivation and elimination of bacteria [67–70]. For instance, a multifunctional electrochemical platform was obtained by combining ZnO, colloidal Ag and vancomycin [71]. AgNPs/3D-ZnO nanorod arrays, functionalized with vancomycin, were immobilized onto the working electrode. The platform detected *S. aureus* with a detection limit of 330 CFU/mL and eliminated bacterial cells with 50% efficiency at low bacterial concentrations of about 10^3 CFU/mL.

3.2. Carbon Nanomaterials

Carbon materials have long been a main companion in electrochemical sensor electrodes, in the form of either glassy carbon or activated carbon due to high chemical inertness and a high specific surface area needed for catalytic material impregnation. The discovery of new carbon allotropes, such as fullerene, carbon nanotubes (CNTs) [72,73] and graphene [74], has triggered active investigation of their application in different types of biosensors. Graphene has a unique two-dimensional honeycomb lattice structure, while the structure of CNTs consists of cylindrical graphene rolled up into a seamless cylinder with a diameter of the order of a nanometer. They provide unprecedentedly high specific surface areas up to 2630 m^2/g [75] and 1315 m^2/g [76], respectively, combined with a high electrical conductivity and charge carrier mobility. A number of reviews have discussed the perspectives of graphene and carbon nanomaterial application as materials for electrodes to improve electrochemical sensors [77–79], including foodborne pathogen detection [80].

Application of carbon nanomaterials, including graphene-related materials, is fostered by a deeper understanding of their physical and chemical properties as well as scalable production, processing and functionalization methods [81]. Examples of electrochemical biosensors utilizing different carbon nanomaterials are summarized in Table 1. The development of stable solutions of graphene and carbon nanotubes makes them prospective for electrodes integrated with conventional technologies for low-cost disposable electrochemical sensors in point-of-need devices. The graphene and carbon nanotube technology combines well with screen printed technologies for portable electrochemical sensors development [82], as well as paper based devices [83]. In foodborne pathogen detection, graphene-based electrochemical sensors also bring advances as they can operate directly in biological and food matrices. Graphene-based composites with functional nanomaterials and bioreceptors (antibodies, aptamers, DNA probes, etc.) provide low LoD down to pico/femto molar concentrations, and reduction of the time of analysis [80].

Electrochemical sensors based on graphene screen-printed disposable electrodes were found to be useful for analysis of meat adulteration [84]. For instance, graphene-based electrochemical biosensors combined with a loop-mediated isothermal amplification (LAMP) assay were used for *V. parahaemolyticus toxR* gene detection in seafood products [85]. The nonspecific interaction of the DNA backbone by π-π stacking on graphene-modified screen-printed carbon electrode was used for analysis of amplicons on the picogram level.

3.2.1. Graphene Nanoplatelets (GNPs)

In spite of the superior properties of graphene, its bare form of a monolayer atomic sheet is rarely used for electrochemical sensing applications. The technology of scalable monolayer graphene production based on chemical vapor deposition (CVD) is still in development to become low cost. Moreover, the defects and active sites in graphene are highly desirable for the binding of molecules and increasing sensitivity and selectivity [86]. Thus, bare graphene does not meet these demands because of its ideal crystalline structure, which would require additional treatment and, subsequently, increase the complexity of electrochemical electrode preparation.

In contrast, graphene nanoplatelets (GNPs) are a robust graphene-derived material with a 3D structure formed by multiple graphene layers, with properties similar to single-layer graphene. They provide a stable solution in organic solvents without the need

for special chemical pre-treatment. GNPs and monolayer graphene were compared in a capacitive sensing platform for foodborne pathogenic *E. coli* O157:H7 detection [87]. The CVD-grown graphene was deposited on a silicon substrate with electrical contacts. Antibodies specific to *E. coli* were immobilized on graphene surface for the selective response during impedance measurements (Figure 6). Higher sensitivity was demonstrated for the monolayer graphene-based sensor, compared to the GNPs, with sensitivities of 10 cells/mL and 100 cells/mL, respectively. Nevertheless, the technology of preparation of less-defective graphene sensing monolayers was more complicated.

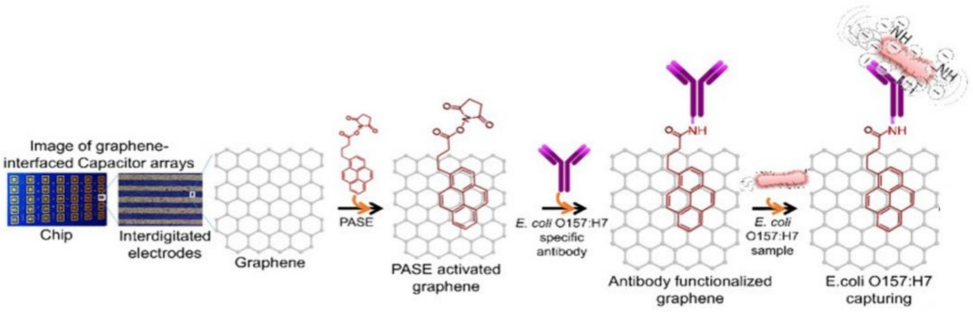

Figure 6. Scheme of a graphene chip and the process of PASE activation and antibody immobilization. Adapted with permission from [87] Copyright 2017, Elsevier.

GNPs have been applied in the first electrochemical paper-based biosensor. Paper was coated by GNPs and Poly(N-isopropyl acrylamide) (PNIPAm) followed by Au deposition [88]. This biosensor can be applied directly with liquid samples without the use of a bioreceptor. Detection of bacterial cells, Gram negative *E. coli* and positive *S. mutans* and *B. subtilis*, was performed by monitoring the electrical resistance. The achieved detection LoD was only 5 cells/mL.

3.2.2. Graphene Oxide

Graphene derivatives, such as graphene oxide (GO) and reduced graphene oxide (rGO), are preferable materials for electrochemical electrode modification due to a low-cost scalable technology of production and processing in integrated devices [86,89]. The difference between GO and rGO is the number of oxygen molecules present, hence the conductivity. GO shows insulating or semi-conducting behavior, while rGO is electrically conductive but its conductivity also depends on the degree of reduction. Full reduction of GO is still difficult to achieve, while partial reduction of GO is rather easy.

Table 1. Detection of pathogens in food with carbon-based integrated electrochemical sensors.

Nanomaterial	Target Pathogen	Working Electrode/Nanomaterial Recognition Complex	EC Technique	Linear Range	LOD	Food Matrix	References
Graphite felt	*E. coli* O157:H7	GF-GCE	OSWV	-	400 cells/mL	Beef	[90]
	Salmonella	GF-GCE	OSWV	-	10^3 cells/mL	-	[91]
Graphene	*E. coli* O157:H7	Cx-Gnfs/ITO	EIS	10^{-6} M–10^{-17} M	1×10^{-17} M	-	[92]
	S. aureus	ssDNA/GNDs-Zeo/PAD	CV/DPV		0.1 nM	Fruit juice	[93]
	Vibrio parahaemolyticus	SPGEs	CV	8×10 to 8×10^6 CFU/mL	2 CFU/25 g	Seafood	[85]
	E. coli *S. mutans* *B. subtilis*	PNIPAm-GR/Au platform	EIS	10^1–10^5 cells/mL	5 cells/mL	Water Milk	[88]
	E. coli O157:H7	SiO2-MG SiO2-GNPs	EIS	10–10^7 cells/mL	10–100 cells/mL	-	[87]
GO	*E. coli* O157:H7	ssDNA/GO/CSGCE	EIS	1×10^{-14} to 1×10^{-8} M	3.584×10^{-15} M	-	[94]
	Salmonella	GCE/GO/AuNPs	EIS	2.4–2.4×10^3 CFU/mL	3 CFU/mL	-	[95]
	S. Typhimurium	SPCE/rG-GO	EIS	-	10 CFU/mL	Orange juice Water	[96]
rGO	*E. coli* O157:H7	SPCE/PANI-AuNPs-Ab_1; rGO-NR-Au@Pt-Ab_2 (measurement of H_2O_2 reduction)	CV	8.9×10^3–8.9×10^9 CFU/mL	2840 CFU/mL	Milk Pork	[97]
	E. coli	rGO/Al_2O_3	FET	1–100 CFU/µL	10^4 CFU/mL	River water	[98]
	E. coli	rGO–CysCu	EIS	10–10^8 CFU/mL	3.8 CFU/mL	Water Fruit Juice Milk	[99]
	E. coli O157:H7	rGO–NR–Au@Pt	CV	4.0×10^3–4.0×10^8 CFU/mL	4.0×10^2 CFU/mL	Pork Milk	[100]
	L. monocytogenes	p-rGO/AuNPs/CILE	DPV	1.0×10^{-13}–1.0×10^{-6} M	3.17×10^{-14} M	-	[101]

Table 1. *Cont.*

Nanomaterial	Target Pathogen	Working Electrode/Nanomaterial Recognition Complex	EC Technique	Linear Range	LOD	Food Matrix	References
	Salmonella	PPy-rGO/GCE/AuNPs	DPV	1.0×10^{-16}–1.0×10^{-10} M 9.6–9.6×10^{4} CFU/mL	4.7×10^{-17} M DNA 8.07 CFU/mL	-	[102]
	Salmonella	rGO-MWCNT	EIS	75 to 7.5×10^{5} CFU/mL	25 CFU/mL	Chicken meat	[103]
	Salmonella	rGO–CHI	DPV	10–10^{6} CFU/mL	10 CFU/mL	Chicken meat	[104]
	S. enterica	rGO-TiO_2	CV & EIS	10^{1}–10^{8} CFU/mL	10 CFU/mL	Chicken meat	[59]
LIG	*S. enterica*	LIG	EIS	25 to 10^{5} CFU/mL	13 ± 7 CFU/mL	Chicken broth	[44]
	E. coli O157:H7	AuNPs-LIG	EIS	10^{2}–10^{8} CFU/mL	10^{2} CFU/mL	-	[105]
SWCNT	*S. aureus*	SWCNT	EIS	-	10^{4} CFU/mL	-	[106]
	S. aureus	SWCNT	DPV	10–10^{6} CFU/mL	13 CFU/mL	Milk	[107]
MWCNT	*Klebsiella pneumoniae* *Enterococcus faecalis* *E. coli*	ClavA-CNTs-Cys	EIS	10^{2}–10^{6} CFU/mL	10^{2} CFU/mL	-	[108]
	E. coli	PPy/AuNP/MWCNT/CHI	amperometry	30–30^{6} CFU/mL	30 CFU/mL	-	[109]
	E. coli O157:H7	ITO/MWCNT/PEI	EIS	1–10^{4} CFU/mL	1 CFU/mL		[110]
	S. enterica	c-MWCNT/AuNP	CV	0.0976–100 ng/µL	0.5 pg/mL	Milk	[111]
	S. enteritidis	MWCNT/ITO	CV	10^{-1}–10^{-8} CFU/mL	5.5×10^{1} CFU/mL 6.7×10 CFU/mL	-	[112]
	S. Typhimurium	SPCE/MWCNT	DPV	10–10^{6} CFU mL^{-1}	7.9 CFU/mL	Milk	[113]
	S. aureus	c-MWCNTs-PEI	DPV	-	5 CFU mL^{-1}	Milk	[114]
	Listeria monocytogenes	MWCNT/fiber electrode	DPV	10^{2}–10^{5} CFU/mL	1.07×10^{2} CFU/mL	Milk	[115]

Ab, antibody; c-MWCNT, carboxylated multi-walled carbon nanotube; CILE, carbon ionic liquid electrode; CSGCE, chitosan (CS) hybrid nanocomposites modified glassy carbon electrode (GCE); CHI, chitosan; ClavA, antimicrobial peptide clavanin A; CNTs, carbon nanotubes; CV, cyclic voltammetry Cx-Gnfs, carboxylated graphene nanoflakes; DPV, differential pulse voltammetry; EIS, electrochemical impedance spectroscopy; FET, Field-Effect Transistor; GCE, glassy carbon electrode; GF, graphite felt; GND, graphene nano dots; GNP, graphene nanoplatelets; GO, graphene oxide; GR, graphene nanoplatelet; ITO, indium tin oxide; LIG, laser induced graphene; MG, monolayered graphene; MWCNT, multi-walled carbon nanotubes; NR, neutral red; OSWV, Osteryoung square wave voltammetry; p-rGO, partially reduced graphene; PAD, paper analytical device; PANI, regenerative leucoemeraldine base polyaniline; PEI, polyethyleneimine; PNIPAm, poly(N-isopropylacrylamide) polymer; PPy, polyrrole; rG-GO, reduced graphene-graphene oxide; rGO, reduced graphene oxide; rGO-CHI, electrochemically-reduced graphene oxide-chitosan; rGO-CysCu, graphene wrapped copper (II) assisted cysteine hierarchical structure; rGO-TiO_2, reduced graphene oxide-titanium dioxide; SPCE, screen-printed carbon electrode; SPGE, screen-printed graphene electrodes; SWCNT, single-walled carbon nanotube; Zeo, zeolite.

GO is soluble in aqueous solutions without the need for surfactant addition that is typically the case for graphene and carbon nanotubes. Moreover, the naturally high concentration of defects in GO [116] allow easy functionalization with specific receptor molecules. GO combined with chitosan has been demonstrated to be an excellent means for electron transfer for the detection of short DNA sequences achieving the detection limit of 3.584×10^{-15} M [94]. Paper-based sensors with screen-printed electrodes modified by a Nafion/PPy/GO composite were proposed for the detection of lipopolysaccharides (LPSs), which are a marker for Gram-negative bacteria [117]. Raw264.7 macrophage cells were used as a recognition element. The cells were grown in a 3D structure in a Nafion/PPy/GO composite scaffold, serving as a NO gas release to be electrochemically oxidized and detected as a differential pulse voltammetry signal change. GO was shown to be both a good electrical conductor and biocompatible material for cell growth. A sensitivity of 3 pg/mL of LPSs was demonstrated in peach and orange juice.

A rGO-based FET sensor passivated with a layer of Al_2O_3 was functionalized with specific antibody immobilized on gold nanoparticles [98]. This sensor was developed to detect *E. coli* in water. Detection was performed by monitoring the change in electrical conductivity of the rGO channel. The LoD was 10^3 cells/mL. The sensitivity can be improved using rGO modified with cysteine (Cys) in the presence of Cu^{2+} -ions. Such electrochemical immunosensor achieved a LoD of 3.8 CFU/mL of *E. coli* O157:H7 through maintaining the antibody bioactivity [99]. In addition, the biosensor was able to distinguish pathogenic *E. coli* O157:H7 from nonpathogenic *E. coli* strains.

A rapid and sensitive electrochemical *inv*A gene biosensor for the detection of *Salmonella* was designed by applying a polypyrrole-rGO nanocomposite on a glassy carbon electrode [102], as shown in Figure 7. Signal amplification was achieved using horseradish peroxidase streptavidin biofunctionalized AuNPs. The LoD was 8.07 CFU/mL with a detection range 9.6–9.6 $\times$ 10^4 CFU/mL.

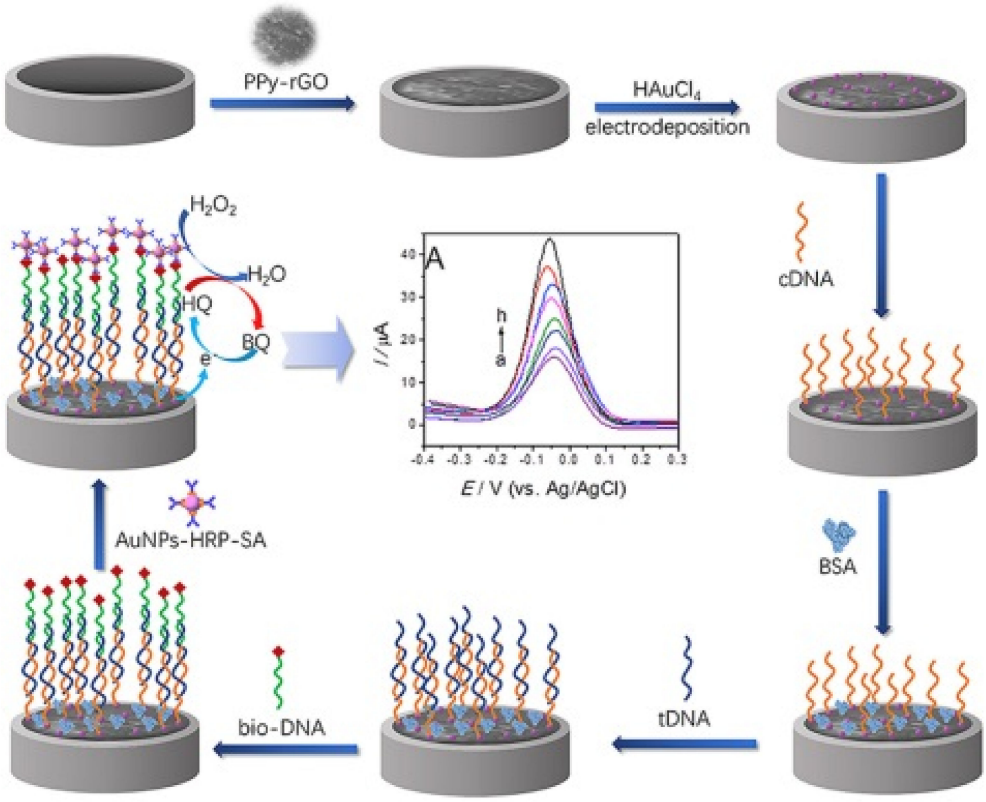

Figure 7. Scheme of the strategy for the electrochemical detection of the *Salmonella inv*A gene. Adapted with permission from [102] Copyright 2019, Elsevier.

3.2.3. Laser-Induced Graphene

Recently, novel methods of direct graphene-based electrode writing were applied for portable sensor development [118]. Laser-induced graphene (LIG) is a very simple and scalable technology of porous graphene material production by a local thermal treatment of polymers like polyimide [119]. The obtained material combines the advantages of graphene like a high surface area, electrical conductivity with numerous active centers for surface modifications with different receptors [120].

A one step method was proposed to create an electrochemical substrate composed of 3D porous graphene and gold nanoparticles [105]. The aim was to improve the detection performance with a more stable sensor due to the synergic effect of the two nanocomponents. The antibodies were immobilized on the NPs-LIG substrate for the detection of the *E. coli* O157:H7. Despite the use of NPs, the limit of detection achieved was 10^2 CFU/mL.

In another study, LIG electrodes modified with polyclonal antibodies were used for the highly selective detection of *Salmonella enterica* serovar Typhimurium [44]. The developed immunoassay demonstrated the linear range of 25×10^5 CFU/mL with a low detection limit of 13 CFU/mL in spiked chicken broth samples and a response time of 22 min. Notably, no special preparation of samples was needed to perform measurements.

3.2.4. Carbon Nanotubes (CNTs)

Carbon nanotubes were used as electrode materials long before the graphene. CNTs are divided into single-walled carbon nanotubes (SWCNTs) and multi-walled carbon nanotubes (MWCNTs) based on the number of graphene sheets [121]. SWCNTs have a diameter range of 0.5 nm to 12 nm but the smallest diameter of SWCNTs is 0.4 nm with different tube lengths starting from several micrometers depending on manufacturing and treatment techniques. MWCNTs consist of multi-rolled layers of graphene inserted one into the other and the number of graphene walls may reach more than 25 walls with a spacing of 0.34 nm. The outside diameter of MWCNTs ranges from 1 nm to 50 nm while the inside diameter is several nanometers. Nevertheless, the problem of good aqueous suspension of carbon nanotubes still prevents their wide usage in integrated electrodes. In addition, proper functionalization of nanotubes is needed which reduces the electrical properties of these nanomaterials.

SWCNT composites were used for highly sensitive detection of bacterial and virus model species *E. coli* O157:H7 and the bacteriophage T7, respectively [122]. The carbon nanotube was used as a transduction element aligned in parallel to bridge two gold electrodes. To provide recognition, SWNTs were functionalized with specific antibodies. The sensor exhibited excellent selectivity, sensitivity and a fast response time of about 5 min in the case of T7 detection, while the response time for the detection of *E. coli* was 60 min.

SWCNTs with immobilized antibodies were integrated into a disposable bio-nano combinatorial junction sensor for detection of *E. coli* K-12 [123]. Measurements were performed on gold tungsten wires coated with polyethyleneimine with aligned functionalized SWCNTs to form a crossbar junction. Changes in electrical current observed after the SWCNT surface interaction with bacterial cells were monitored to evaluate the sensor's performance. The biosensor had a LoD of 10^2 CFU/mL with a detection time of less than 5 min. A low-cost paper-based electrochemical immunosensor was developed utilizing an antibody-SWCNT bioconjugate for rapid detection of *S. aureus* using differential pulse voltammetry (Figure 8), achieving a detection time of 30 min with a detection limit of 13 CFU/mL in spiked milk samples [107].

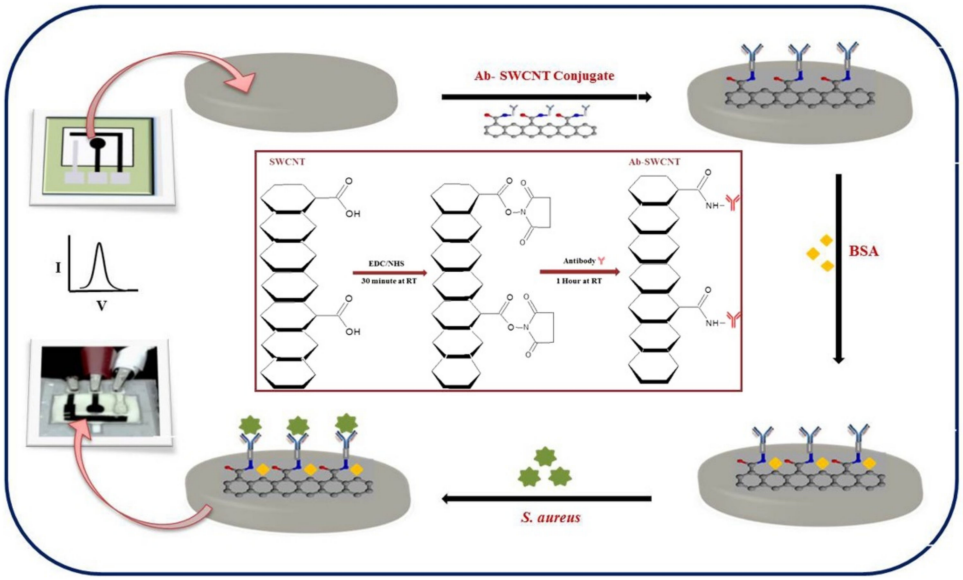

Figure 8. Scheme of the development of an antibody-SWCNT bioconjugate paper-based electrochemical immunosensor. Adapted with permission from [107] Copyright 2017, Elsevier.

As a material modification, MWCNTs is better than SWCNTs as it is stiffer, easier and cheaper to produce on a large scale, and several studies have demonstrated to have better sensitivity. Indeed, MWCNTs deposited on an Indium tin oxide (ITO) electrode and modified with aptamers to detect *S. enteritidis* and *S. thyphimuri* achieved a detection limit of 5.5 $\times$ 10^1 CFU/mL and 6.7 $\times$ 10^1 CFU/mL, respectively [112]. Measurements were performed in food samples using cyclic voltammetry and electrochemical impedance spectroscopy techniques to characterize the electrochemical properties and conductivity of the aptasensor. The impedance measured at the aptamer/MWCNT/ITO electrode surface increased after exposure to target *Salmonella* cells, due to the capturing of Salmonella by the immobilized aptamers. A promising electrode substrate was developed with c-MWCNTs to confer an electrical conductivity at bacterial cellulose fibre (BCF) [114]. The BCF was modified with poly- ethyleneimine cation (PEI) to allow the immobilization of phages used as a bioreceptor for *S. aureus*. The LoD of 5 CFU/mL and 2 CFU/mL was found in milk and phosphate buffer saline, respectively, with effective discrimination between dead and live cells and within only 30 min. Moreover, the produced electrodes were maintained stable for over 6 weeks.

Carbon nanomaterials are often used as one of the components in nanocomposite electrochemical biosensors for foodborne pathogen detection. For example, grapheme oxide as part of mesoporous nanocomposite for detection of *E.coli* [46]. A rapid and sensitive detection in the dynamic range from 10^1 CFU/mL to 10^8 CFU/mL with a detection limit of 10^1 CFU/mL of *S. enterica* was achieved with a nanocomposite of rGO and CNT modified with an amino-modified DNA aptamer [124].

The low-cost carbon materials, including graphene and carbon nanofibers, provide a large specific surface area, high electron transfer rate and good catalytic properties, which is of high importance for development of sensing platforms that can be miniaturized for point-of-need testing.

3.3. Gold Nanoparticles

Gold nanoparticles (AuNPs) have been increasingly used in the design of electrochemical biosensors for their biocompatibility, conductivity, catalytic activity, stability and high surface-to-volume ratio [125]. Deposition of AuNPs onto gold electrodes enables a significant increase in the electrode surface area for target recognition and, consequently, its analytical performance [126,127]. When AuNPs are immobilized on the surface of

electrodes made of other materials (such as carbon, graphene, paper, etc.), they increase the surface biocompatibility, promote electron transfer between electrode and immobilized molecules and enable easy bio-conjugation of recognition elements besides increasing the electrode surface area. Raj et al. [128] developed a label-free electrochemical biosensor for the detection of *E. coli* based on a glassy carbon electrode with immobilized a complex of polyaniline nanocomposites (PANI), gold nanoparticles and MoS_2 (Au@MoS_2–PANI), in order to increase conductivity, stability and electro-activity of the electrode. The surface of AuNPs were treated with mercaptopropionic acid to covalently immobilize antibodies against *E. coli* and to minimize the nonspecific adsorption on the electrode surface. The biosensor was simple, rapid and specific, with a LoD of 10 CFU/mL and a linear detection range of 10–10^7 CFU/mL. A schematic representation of this electrode construction is shown in Figure 9. In another study, AuNPs were immobilized on a carbon screen-printed electrode to increase the stability and efficacy of the electrochemical biosensor for the label-free detection of *E. coli* [29]. The modified electrode was treated with N-(γ-Maleimidobutyryloxy) succinimide (GMBS) to create -NHS groups for cross-linking of *E. coli* O157-specific polyclonal antibodies. The analysis showed rapid and efficient pathogen detection with a dynamic range of 10–10^6 CFU/mL and a LoD of 15 CFU/mL.

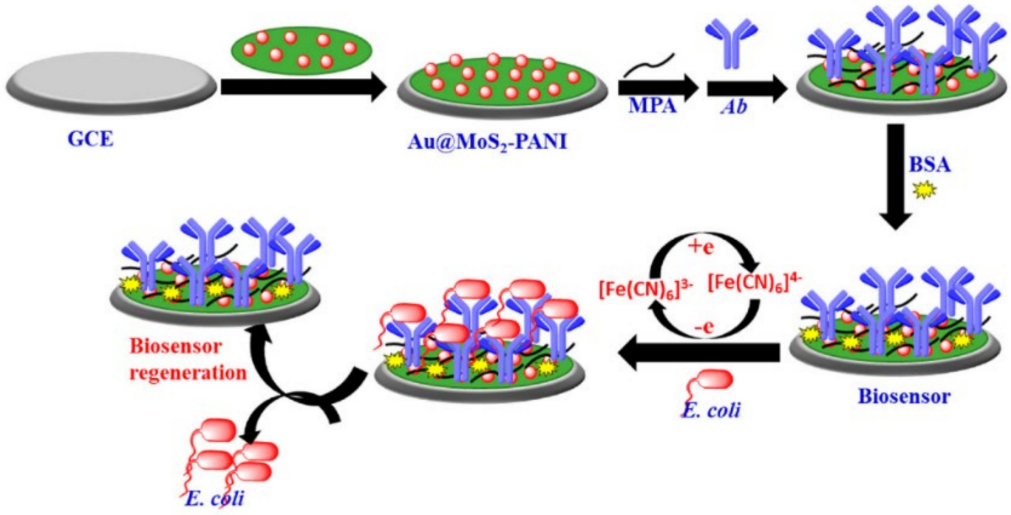

Figure 9. Schematic representation of the label-free electrochemical biosensor based on Au@MoS_2–PANI. Adapted with permission from [128] Copyright 2021, MDPI.

The electrocatalytic properties of AuNPs towards hydrogen evolution reaction was employed for rapid and highly sensitive immunodetection of *E. coli* O157:H7 in minced beef and water [129]. The test was performed in a sandwich format where superparamagnetic microbeads modified with the first antibody were used to perform pre-concentration/purification of the bacterial cells from the sample and AuNPs modified with the second antibody provided the catalytic reaction. The method showed a LoD of 457 CFU/mL in minced beef and 309 CFU/mL in water. When compared with a commercial lateral flow kit in terms of LoD, specificity, reproducibility and detection range, the electrochemical method showed clear advantages. Similarly, the magneto-immunoassay and AuNPs as label for electrochemical detection was developed for the detection of *Salmonella enterica* subsp. enterica serovar Typhimurium LT2 (S) in skimmed milk by Alfonso et al. [130]. A magnet is incorporated under the screen-printed carbon electrode to attach magnetic beads carrying *Salmonella* specific antibodies. Beads were added to milk samples to pre-concentrate bacterial cells and then deposited onto the electrode. A sandwich was created using AuNPs modified with antibodies to provide a redox signal. Applying differential pulse voltammetry, a linear range from 10^3 cells/mL to 10^6 cells/mL and a LoD of 143 cells/mL was found for skimmed milk samples contaminated with *Salmonella*. AuNP modified

screen-printed carbon electrodes were combined with magnetic nanoparticles coupled to specific peptides via a streptavidin interaction to achieve multiplexed electrochemical detection of *Listeria monocytogenes* and *Staphylococcus aureus* with a low detection limit of 9 CFU/mL and 3 CFU/mL, respectively [131].

Magnetic and gold nanoparticles have also been combined in impedance biosensors. For instance, Wang et al. [132] used urease-modified AuNPs to amplify the signal of impedance biosensors implemented with magnetic nanoparticles for the detection of *Listeria monocytogenes.* Bacterial cells captured between magnetic nanoparticles decorated with a monoclonal antibody and AuNPs–urease complex carrying the polyclonal antibody were resuspended in urea to catalyze its hydrolysis into ammonium and carbonate ions. Generated ions were detected by a screen-printed interdigitated electrode. The technique, characterized by low cost and high specificity, gave a linear range from 1.9×10^3 CFU/mL to 1.9×10^6 CFU/mL, and a LoD of 1.6×10^3 CFU/mL, in spiked lettuce samples.

Expensive mono- and poly-clonal antibodies can be replaced with lectins that recognize LPS on the bacterial surface. Oliveira et al. [133] immobilized Cramol L lectin on AuNPs functionalized with l-cysteine. Cramol L is a *Cratylia mollis* lectin used as the recognition interface by making hydrogen bonds with methyl-α-d-mannoside in LPS. To build the biosensor the gold electrode surface was covered by a poly (vinyl chloride-vinyl acetate maleic acid) layer to attach Au-cysteine-Cramol L nanoparticles through the electrostatic interactions. Bovine serum albumin was used to block the remaining non-functionalized electrode surface. The sensor, tested on *E. coli*, *Serratia marcescens*, *Salmonella enterica* and *Klebsiella pneumoniae*, was able to selectively discriminate bacterial species due to their different LPS composition with a high sensitivity.

Although AuNPs based electrochemical biosensors have been extensively employed, their complexity is still an issue limiting the general application, especially in complex food matrices. Usually a multistep procedure, it involves user manual interventions during the test, such as for repetitive washing, loading of samples and reagents. These steps increase the time of analysis and cause imprecise result. Attempts have been made to automatize manual interventions by coupling microfluidic with electrochemical cell. Microfluidic can also enable multiplex detection of different pathogens in the same sample. A disposable microfluidic device for *Salmonella typhimurium* detection in milk was proposed by de Oliveira et al. [134]. The microfluidic device allowed the simultaneous measurement of eight samples by a magneto-immunoassay, as illustrated in Figure 10. The bacteria were captured from the sample by magnetic beads modified with a monoclonal antibody. A sandwich was then completed with AuNPs labeled with a polyclonal antibody. The complex was injected into the device and magnetically placed on the electrode surface. This approach allowed to obtain an easy to use and rapid detection, with a LOD of 7.7 cells/mL.

A sandwich-type electrochemical immunosensor for the detection of *L. monocytogenes* proposed to use 3,4,9,10-perylene tetracarboxylic acid/graphene ribbon nanohybrids as a sensing platform and ferrocene/AuNPs as a signal amplifier [135]. A low detection limit of 6 CFU/mL and linear range of 10–2×10^4 CFU/mL was achieved, showing that incorporation of nanomaterials, such as graphene and AuNPs, enables improved sensing properties.

Electrochemical biosensors based on AuNPs have been successfully applied for virus detection [136]. For instance, the Middle East respiratory syndrome coronavirus (MERS-CoV), which is one of the highly pathogenic viruses, was found to contaminate dairy products [137]. It was detected by the competitive assay carried out on an array of carbon electrodes modified with gold nanoparticles [136]. The electrode array enabled multiplexed detection of different strains of CoVs through the indirect competition between free virus in the sample and immobilized MERS-CoV protein S1 or a fixed concentration of antibody added to the sample. By using ferrocyanide/ferricyanide as a redox probe, voltammetric measurements performed within 20 min showed low detection limit of 1.0 pg/mL for MERS-CoV and high selectivity.

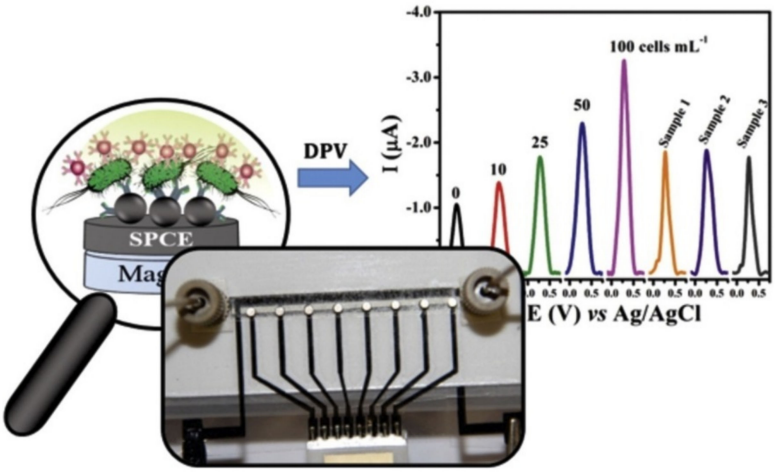

Figure 10. The microfluidic device connectors and the eight magnets externally attached with double-sided tape over each working electrode, together with a schematic representation of detection. Adapted with permission from [134] Copyright 2018, Elsevier.

3.4. Other 0–3D Nanomaterials

Besides AuNPs, silver nanoparticles (AgNPs) have also been applied for electrochemical detection. For instance, chitosan stabilized AgNPs were applied for electrochemical detection of negatively charged LPS, enabling detection of *E. coli* in the range 10–10^7 CFU/mL [138].

The high benefits of graphene as a transducer layer for working electrodes in electrochemical biosensors have resulted in an increased interest in the 2D nanomaterial family for application in electrochemical sensing [33]. Semiconductor 2D materials, such as transition metals dichalcogenides (TMDC) and transition metal carbides and carbonitrides (MXenes), have a high surface area and conductivity and possess an intrinsic energy band providing sensitivity to the weak changes in the charge state on electrodes. They can thus greatly improve the performance of electrochemical sensors [139]. A technological process of defect-free 2D materials production is still based on the CVD method, which is an expensive technological process demanding high-purity precursors. In contrast, the richness of defects and boundary grains in MXene production is very simple and inexpensive and better adapted for applications in portable electrochemical devices [140]. Two-dimensional transition metal materials provide a robust sensing surface due to their structural stability and excellent electrochemical properties such as conductivity, catalytic performance and abundant active sites. Previous reviews have discussed the perspective of the electrochemical sensor development based on molybdenum disulfide (MoS_2) [141] and MXene nanomaterials [142].

Hexagonal MoS_2 is a stratified crystal which has thicknesses equal to the unit cell of the material in a way that each plane of MoS_2 is made of molybdenum atoms sandwiched between sulfur atoms and stabilized by van der Waals bonds. Two-dimensional MoS_2 is obtained when the material is exfoliated into one or a limited number of layers. Two-dimensional MoS_2 shows remarkable electronic, optical, mechanical and chemical characteristics that also make it advantageous for biosensing applications. In addition, when grown into planes with relatively large lateral dimensions, 2D MoS_2 is particularly stable in liquid and oxygen containing gaseous media which facilitate their utilization when incorporated into biosensing structures [143]. An electrochemical lab-on-paper genosensor was developed based on carbon ink screen-printed on cellulose paper with a working electrode modified by drop-casted MoS_2 nanosheets for detecting *Salmonella*-specific DNA [144]. The sensitivity of the MoS_2-modified electrode was increased more than 10 times due to the enhanced transfer rate of charge carries and unique electron transfer kinetics in MoS_2. To provide the selectivity towards *Salmonella*-DNA, the specific

complementary DNA probe was immobilized on MoS_2 for on electrode hybridization. The LoD of 20 nM was obtained. Another method for foodborne pathogen detection was suggested based on antibody immobilized onto a microfluidic chip. Exfoliated MoS_2 nanosheets in the presence of a surfactant were deposited on ITO electrodes integrated with a microfluidic channel to develop an impedimetric biosensor [145], as shown in Figure 11. The specific antibody directed against *Salmonella typhimurium* was immobilized on a MoS_2/ITO electrode treated with glutaraldehyde. Proper functionalization of 2D nanosheets and optimization of the procedure for antibody molecules association with MoS_2 yielded superior electron conduction and resulted in a 1.5 CFU/mL limit of detection.

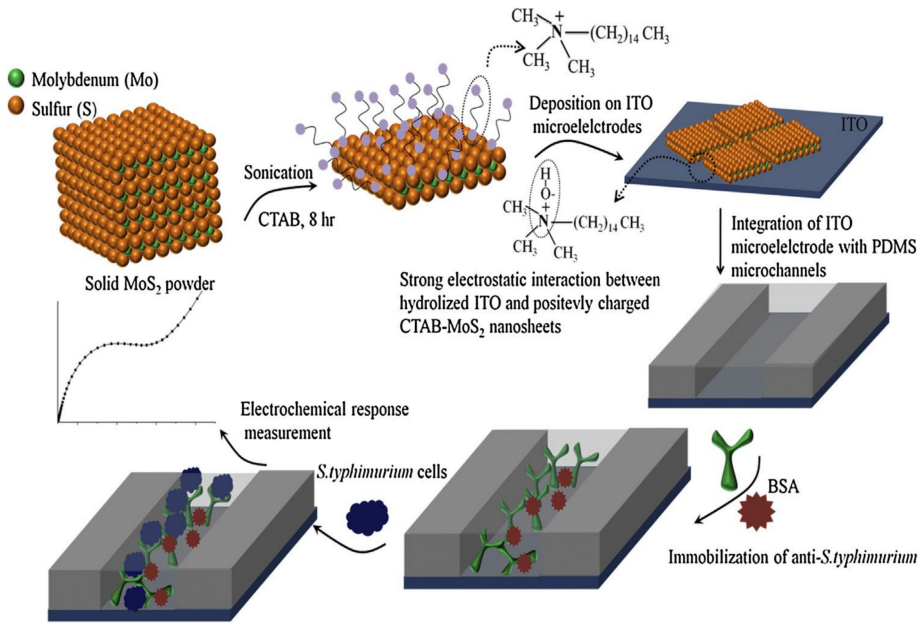

Figure 11. Design of a MoS_2 based biosensor for *S. typhimurium* detection. Adapted with permission from [145] Copyright 2018, Elsevier.

Metal organic frameworks (MOFs) are a rapidly emerging new class of microporous materials with a wide range of promising applications [146,147]. They basically represent 2D or 3D porous materials assembled using metal cation salts or clusters bridged with polydentate organic ligands with coordination type connections, though 0D and 1D nanostructures are being synthesized also [148]. They have a very high surface area, high pore volume, high porosity and surface functionality and an easily tunable structure. Nanoscale MOFs combine the properties of both MOFs and nanostructures. MOFs are often used to design complex nanocomposite materials through a controlled assembly of MOF nanoparticles, such as NP@MOFs. Two-dimensional metal organic frameworks (MOF) have recently come into focus for biosensing applications [149]. The possibility of tuning their properties in a controllable way and the extremely high surface area is expected to outperform traditional electrochemical sensors. Still, their poor conductivity demands a combination with other highly conductive nanomaterials in the form of nanocomposites. Sensitive impedimetric detection of *E. coli* in the range 2.1×10^2–2.1×10^8 CFU/mL with a detection limit of 4 CFU/mL was achieved by combining a (MOF) with a conducting polymer (CP) and PEDOT on modified carbon screen-printed electrodes [150]. Copper (Cu)-MOFs were directly self-assembled and deposited onto a glassy carbon electrode, followed by in situ reduction of AuNPs on the MOF surface and conjugated with a DNA aptamer enabling detection of *S. aureus* in the range 7–7×10^6 CFU/mL [151]. Graphene and a zirconium based MOF (UiO-67) were combined together with an aptamer loaded AuNP-horseradish conjugate to detect *S. typhimurium* in spiked milk samples with a detection limit of 5 CFU/mL [152].

Quantum dots (QDs), carbon dots (CDs) and graphene quantum dots (GQDs) are another category of nanomaterials with great potential for application in electrochemical biosensing of foodborne pathogens [27,31]. QDs have been used to modify the structure of polymeric nanodendrons for direct culture-free electrochemical detection of *Salmonella* in milk with a detection limit of 4 CFU/mL [153]. GQDs combine characteristics both from graphene and carbon dots, offering great versatility for modification with other modifiers and nanomaterials besides low cost, low toxicity, high solubility and good electronic properties. Photoelectrochemical sensing represents an integration of electrochemistry and photochemistry offering high sensitivity, robustness, low cost and simple instrumentation. For instance, GQDs doped with nitrogen were coupled with non-metallic two dimensional hydrated defected tungsten oxide to design a photoelectrochemical aptamer biosensor for *E.coli* detection in the range 0.1–10^4 CFU/mL with a low detection limit of 0.05 CFU/mL [154].

4. Conclusions and Perspectives

The present review summarizes the unique properties of 0–3D nanomaterials and their application in the design of electrochemical biosensors for foodborne pathogen detection. Despite the progress and advances in culture based and molecular methods for foodborne pathogen detection, challenges remain for their practical application because they still do not reach the sensitivity, fast response time and low cost needed. Effective foodborne pathogen monitoring that will enable efficient risk assessment and outbreak prediction has to be rapid, ultrasensitive, specific and affordable to be applied in low-resource settings. Electrochemical biosensors offer an exciting opportunity to realize immediate and continuous pathogen detection for on-site risk evaluation. We have highlighted examples showing that electrochemical methods can release results within several hours or even several minutes. Besides, a wide variety of strategies used to improve sensitivity are presented. Some foodborne pathogens, such as *Campylobacter*, *E. coli* O157 and *L. monocytogenes,* have very low infectious doses of a dozen to several hundred cells. Consequently, it is of high importance that low contaminated food items can be identified. Amplification of the detection signal using nanomaterials as electronic conductors, carriers or catalysts enable electrochemical biosensors to exhibit LoDs as low as a single colony forming unit (CFU/mL) or several femto M or even atto M ranges and linear ranges of several orders of magnitude. Although the presented nanomaterials can be used with other detection techniques, such as plasmonic and fluorescent, electrochemical biosensors have the advantage of simple utilization by persons without previous training, versatile detection schema providing a wide range of applications and easy miniaturization [155–157]. Moreover, the inexpensive and miniaturized electrochemical devices in handheld formats are excellent candidates for on-site application.

Cyclic voltammetry, differential pulse voltammetry, square wave voltammetry and electrochemical impedance spectroscopy are the methods mostly used for detection of pathogens and their toxins in food samples. At the same time, nanomaterials are generally applied with these methods to enhance the detection signal. Planar gold electrodes are the most commonly used working electrodes. However, nanomaterials with their outstanding properties that arise from their small dimensions and surface reactivity are applied to alleviate the limitations of electrochemical biosensors, such as slow recognition time, low biocompatibility or instability. In addition, some nanomaterials, such as gold nanoparticles or graphene, may tune the electrode properties and offer a variety of surface engineering strategies and functionalization to attach biological entities assuring recognition (e.g., antibodies, aptamers, ssDNA, phages). One of the trends in recent electrochemical biosensors for pathogen detection is to combine several nanomaterials as nanocomposites in electrode design to obtain remarkable synergic effects leading to improved sensing performances. Moreover, specific nanomaterials, such as graphene or metal oxide nanoparticles, have inherent antibacterial activity. Biosensors integrating such nanomaterials are multi-functional, providing not only pathogen identification and quantification but also their elimination.

During the past decade, significant progress has been made in the biosensors field to advance electrochemical devices, taking into account food industry demands. Hence, further improvement is needed to facilitate wide practical applicability of biosensors for detecting foodborne pathogens. Biocompatibility is one high concern. The electrode design, surface modification and functionalization integrating nanomaterials are of great promise to improve the stability and compatibility of electrodes in biological environments for an extended period. Besides, due to the diversity of foodborne pathogens and the possibility of food co-contamination by various microorganisms, multi-electrode detection devices that exhibit different biorecognition elements for simultaneous multiplex detection without mutual interference are also needed for improved detection efficiency. In addition, most electrochemical biochips are designed only for single utilization. We expect that future studies will anticipate environmental friendliness and resource conservation and will include reusability of electrodes in sensor design.

Analytical performances of the majority of presented biosensors refer only to LoD and linear range of detection. However, other parameters, notably accuracy, repeatability, precision, and specificity, should be also investigated and improved to enable sensors general accessibility. Furthermore, the synthesis procedure of integrated nanomaterials has to be optimized to obtain rigorous protocols for mass production and strict quality control of the material without chemical impurities that can alter sensing properties or induce environmental pollution.

Finally, pathogen detection in foods requires sample treatment and transport to the electrode surface, which may cause analyte loss. For this reason, advanced electrochemical biosensors based on nanomaterials that detect pathogens and their toxins in complex matrices without important interferences should be designed. Coupling detection with a microfluidic system for sample handling holds great potential.

In the future, additional excellent nanomaterial-based electrochemical biosensors will emerge, and new design and solutions will be proposed. It is evident that the field of nanomaterials is making tremendous progress and significantly affects biosensor development. Active collaboration between material scientists, microbiologists, electrochemists and device developers in the fields of nanotechnology and food science will result in point-of-need diagnostic devices integrating electrochemical biosensors, microfluidics and nanomaterials. Such devices will offer the food industry food safety analyses and foodstuff screening that can be performed during all phases, from production, packaging, storing and distribution to consumption.

Author Contributions: I.B. and M.R., conceptualization, writing—original draft preparation; F.R., P.V., S.J. and Z.P., writing—original draft preparation; V.R., conceptualization; M.V.N., conceptualization, writing—review and editing; J.V., conceptualization, writing—review and editing, supervision. All authors have read and agreed to the published version of the manuscript.

Funding: This research was supported, in part, by the European Union's Horizon 2020 research and innovation program under the Marie Skłodowska-Curie grant agreement IPANEMA No 872662 (I.B., M.R, V.R., F.R., S.J. and J.V) and by the Ministry for Education, Science and Technology Development of the Republic of Serbia, under the contract 451-03-9/2021-14/200053 (M.V.N.).

Institutional Review Board Statement: Not applicable.

Informed Consent Statement: Not applicable.

Data Availability Statement: This study did not report any data.

Conflicts of Interest: The authors declare no conflict of interest.

References

1. Havelaar, A.H.; Kirk, M.D.; Torgerson, P.R.; Gibb, H.J.; Hald, T.; Lake, R.J.; Praet, N.; Bellinger, D.C.; De Silva, N.R.; Gargouri, N. World Health Organization global estimates and regional comparisons of the burden of foodborne disease in 2010. *PLoS Med.* **2015**, *12*, e1001923. [CrossRef]
2. Balbinot, S.; Srivastav, A.M.; Vidic, J.; Abdulhalim, I.; Manzano, M. Plasmonic biosensors for food control. *Trends Food Sci. Technol.* **2021**, *111*, 128–140. [CrossRef]
3. Vidic, J.; Vizzini, P.; Manzano, M.; Kavanaugh, D.; Ramarao, N.; Zivkovic, M.; Radonic, V.; Knezevic, N.; Giouroudi, I.; Gadjanski, I. Point-of-need DNA testing for detection of foodborne pathogenic bacteria. *Sensors* **2019**, *19*, 1100. [CrossRef] [PubMed]
4. Farre, C.; Viezzi, S.; Wright, A.; Robin, P.; Lejal, N.; Manzano, M.; Vidic, J.; Chaix, C. Specific and sensitive detection of Influenza A virus using a biotin-coated nanoparticle enhanced immunomagnetic assay. *Anal. Bioanal. Chem.* **2020**, 1–12. [CrossRef]
5. Vidic, J.; Manzano, M.; Chang, C.-M.; Jaffrezic-Renault, N. Advanced biosensors for detection of pathogens related to livestock and poultry. *Vet. Res.* **2017**, *48*, 1–22. [CrossRef]
6. Vizzini, P.; Manzano, M.; Farre, C.; Meylheuc, T.; Chaix, C.; Ramarao, N.; Vidic, J. Highly sensitive detection of *Campylobacter* spp. In chicken meat using a silica nanoparticle enhanced dot blot DNA biosensor. *Biosens. Bioelectron.* **2020**, *171*, 112689. [CrossRef] [PubMed]
7. Vidic, J.; Chaix, C.; Manzano, M.; Heyndrickx, M. Food Sensing: Detection of Bacillus cereus Spores in Dairy Products. *Biosensors* **2020**, *10*, 15. [CrossRef]
8. Ramarao, N.; Tran, S.-L.; Marin, M.; Vidic, J. Advanced methods for detection of Bacillus cereus and its pathogenic factors. *Sensors* **2020**, *20*, 2667. [CrossRef]
9. Kotsiri, Z.; Vidic, J.; Vantarakis, A. Applications of biosensors for bacteria and virus detection in food and water–A systematic review. *J. Environ. Sci.* **2022**, *111*, 367–379. [CrossRef]
10. Vidic, J.; Manzano, M. Electrochemical biosensors for rapid pathogen detection. *Curr. Opin. Electrochem.* **2021**, *29*, 100750. [CrossRef]
11. Cesewski, E.; Johnson, B.N. Electrochemical biosensors for pathogen detection. *Biosens. Bioelectron.* **2020**, *159*, 112214. [CrossRef]
12. Russo, M.J.; Han, M.; Desroches, P.E.; Manasa, C.S.; Dennaoui, J.; Quigley, A.F.; Kapsa, R.M.; Moulton, S.E.; Guijt, R.M.; Greene, G.W. Antifouling Strategies for Electrochemical Biosensing: Mechanisms and Performance toward Point of Care Based Diagnostic Applications. *ACS Sens.* **2021**, *6*, 1482–1507. [CrossRef] [PubMed]
13. Ding, J.; Lei, J.; Ma, X.; Gong, J.; Qin, W. Potentiometric aptasensing of Listeria monocytogenes using protamine as an indicator. *Anal. Chem.* **2014**, *86*, 9412–9416. [CrossRef]
14. Manzano, M.; Viezzi, S.; Mazerat, S.; Marks, R.S.; Vidic, J. Rapid and label-free electrochemical DNA biosensor for detecting hepatitis A virus. *Biosens. Bioelectron.* **2018**, *100*, 89–95. [CrossRef] [PubMed]
15. Bonnet, R.; Farre, C.; Valera, L.; Vossier, L.; Léon, F.; Dagland, T.; Pouzet, A.; Jaffrézic-Renault, N.; Fareh, J.; Fournier-Wirth, C. Highly labeled methylene blue-ds DNA silica nanoparticles for signal enhancement of immunoassays: Application to the sensitive detection of bacteria in human platelet concentrates. *Analyst* **2018**, *143*, 2293–2303. [CrossRef] [PubMed]
16. Miodek, A.; Sauriat-Dorizon, H.; Chevalier, C.; Delmas, B.; Vidic, J.; Korri-Youssoufi, H. Direct electrochemical detection of PB1-F2 protein of influenza A virus in infected cells. *Biosens. Bioelectron.* **2014**, *59*, 6–13. [CrossRef] [PubMed]
17. Miodek, A.; Vidic, J.; Sauriat-Dorizon, H.; Richard, C.-A.; Le Goffic, R.; Korri-Youssoufi, H.; Chevalier, C. Electrochemical detection of the oligomerization of PB1-F2 influenza A virus protein in infected cells. *Anal. Chem.* **2014**, *86*, 9098–9105. [CrossRef]
18. Kubičárová, T.; Fojta, M.; Vidic, J.; Tomschik, M.; Suznjevic, D.; Paleček, E. Voltammetric and chronopotentiometric measurements with nucleic acid-modified mercury film on a glassy carbon electrode. *Electroanal. Int. J. Devoted Fundam. Pract. Asp. Electroanal.* **2000**, *12*, 1390–1396. [CrossRef]
19. Akimov, V.; Alfinito, E.; Pennetta, C.; Reggiani, L.; Minic, J.; Gorojankina, T.; Pajot-Augy, E.; Salesse, R. An impedance network model for the electrical properties of a single-protein nanodevice. In *Nonequilibrium Carrier Dynamics in Semiconductors*; Springer: Berlin/Heidelberg, Germany, 2006; pp. 229–232.
20. Zhang, R.; Belwal, T.; Li, L.; Lin, X.; Xu, Y.; Luo, Z. Nanomaterial-based biosensors for sensing key foodborne pathogens: Advances from recent decades. *Compr. Rev. Food Sci. Food Saf.* **2020**, *19*, 1465–1487. [CrossRef]
21. Quesada-González, D.; Merkoçi, A. Nanomaterial-based devices for point-of-care diagnostic applications. *Chem. Soc. Rev.* **2018**, *47*, 4697–4709. [CrossRef]
22. Pokropivny, V.; Skorokhod, V. Classification of nanostructures by dimensionality and concept of surface forms engineering in nanomaterial science. *Mater. Sci. Eng. C* **2007**, *27*, 990–993. [CrossRef]
23. Reta, N.; Saint, C.P.; Michelmore, A.; Prieto-Simon, B.; Voelcker, N.H. Nanostructured electrochemical biosensors for label-free detection of water-and food-borne pathogens. *ACS Appl. Mater. Interfaces* **2018**, *10*, 6055–6072. [CrossRef]
24. Zhou, X.; Pu, H.; Sun, D.-W. DNA functionalized metal and metal oxide nanoparticles: Principles and recent advances in food safety detection. *Crit. Rev. Food Sci. Nutr.* **2021**, *61*, 2277–2296. [CrossRef] [PubMed]
25. Nikolova, M.P.; Chavali, M.S. Metal oxide nanoparticles as biomedical materials. *Biomimetics* **2020**, *5*, 27. [CrossRef] [PubMed]
26. Stankic, S.; Suman, S.; Haque, F.; Vidic, J. Pure and multi metal oxide nanoparticles: Synthesis, antibacterial and cytotoxic properties. *J. Nanobiotechnol.* **2016**, *14*, 1–20. [CrossRef] [PubMed]
27. Campuzano, S.; Yáñez-Sedeño, P.; Pingarrón, J.M. Carbon dots and graphene quantum dots in electrochemical biosensing. *Nanomaterials* **2019**, *9*, 634. [CrossRef]

28. Ji, C.; Zhou, Y.; Leblanc, R.M.; Peng, Z. Recent developments of carbon dots in biosensing: A review. *ACS Sens.* **2020**, *5*, 2724–2741. [CrossRef]
29. Vu, Q.K.; Tran, Q.H.; Vu, N.P.; Anh, T.-L.; Le Dang, T.T.; Matteo, T.; Nguyen, T.H.H. A label-free electrochemical biosensor based on screen-printed electrodes modified with gold nanoparticles for quick detection of bacterial pathogens. *Mater. Today Commun.* **2021**, *26*, 101726. [CrossRef]
30. Omerović, N.; Djisalov, M.; Živojević, K.; Mladenović, M.; Vunduk, J.; Milenković, I.; Knežević, N.Ž.; Gadjanski, I.; Vidić, J. Antimicrobial nanoparticles and biodegradable polymer composites for active food packaging applications. *Compr. Rev. Food Sci. Food Saf.* **2021**, *20*, 2428–2454. [CrossRef]
31. Du, H.; Wang, X.; Yang, Q.; Wu, W. Quantum dot: Lightning invisible foodborne pathogens. *Trends Food Sci. Technol.* **2021**, *110*, 1–12. [CrossRef]
32. Muniandy, S.; Teh, S.J.; Thong, K.L.; Thiha, A.; Dinshaw, I.J.; Lai, C.W.; Ibrahim, F.; Leo, B.F. Carbon nanomaterial-based electrochemical biosensors for foodborne bacterial detection. *Crit. Rev. Anal. Chem.* **2019**, *49*, 510–533. [CrossRef] [PubMed]
33. Nikolic, M.V.; Vasiljevic, Z.Z.; Auger, S.; Vidic, J. Metal oxide nanoparticles for safe active and intelligent food packaging. *Trends Food Sci. Technol.* **2021**, *116*, 655–668. [CrossRef]
34. Li, S.; Ma, L.; Zhou, M.; Li, Y.; Xia, Y.; Fan, X.; Cheng, C.; Luo, H. New opportunities for emerging 2D materials in bioelectronics and biosensors. *Curr. Opin. Biomed. Eng.* **2020**, *13*, 32–41. [CrossRef]
35. Nguyen, E.P.; Silva, C.D.C.C.; Merkoçi, A. Recent advancement in biomedical applications on the surface of two-dimensional materials: From biosensing to tissue engineering. *Nanoscale* **2020**, *12*, 19043–19067. [CrossRef] [PubMed]
36. Nikolic, M.V.; Milovanovic, V.; Vasiljevic, Z.Z.; Stamenkovic, Z. Semiconductor gas sensors: Materials, technology, design, and application. *Sensors* **2020**, *20*, 6694. [CrossRef]
37. Mei, J.; Liao, T.; Kou, L.; Sun, Z. Two-dimensional metal oxide nanomaterials for next-generation rechargeable batteries. *Adv. Mater.* **2017**, *29*, 1700176. [CrossRef]
38. Murali, A.; Lokhande, G.; Deo, K.A.; Brokesh, A.; Gaharwar, A.K. Emerging 2D nanomaterials for biomedical applications. *Mater. Today* **2021**, in press, corrected proof. [CrossRef]
39. Jia, Y.; Yi, X.; Li, Z.; Zhang, L.; Yu, B.; Zhang, J.; Wang, X.; Jia, X. Recent advance in biosensing applications based on two-dimensional transition metal oxide nanomaterials. *Talanta* **2020**, *219*, 121308. [CrossRef]
40. Shavanova, K.; Bakakina, Y.; Burkova, I.; Shtepliuk, I.; Viter, R.; Ubelis, A.; Beni, V.; Starodub, N.; Yakimova, R.; Khranovskyy, V. Application of 2D non-graphene materials and 2D oxide nanostructures for biosensing technology. *Sensors* **2016**, *16*, 223. [CrossRef]
41. Bhati, V.S.; Kumar, M.; Banerjee, R. Gas sensing performance of 2D nanomaterials/metal oxide nanocomposites: A review. *J. Mater. Chem. C* **2021**, *9*, 8776–8808. [CrossRef]
42. Xue, L.; Huang, F.; Hao, L.; Cai, G.; Zheng, L.; Li, Y.; Lin, J. A sensitive immunoassay for simultaneous detection of foodborne pathogens using MnO2 nanoflowers-assisted loading and release of quantum dots. *Food Chem.* **2020**, *322*, 126719. [CrossRef]
43. Vivaldi, F.M.; Dallinger, A.; Bonini, A.; Poma, N.; Sembranti, L.; Biagini, D.; Salvo, P.; Greco, F.; Di Francesco, F. Three-Dimensional (3D) Laser-Induced Graphene: Structure, Properties, and Application to Chemical Sensing. *ACS Appl. Mater. Interfaces* **2021**, *13*, 30245–30260. [CrossRef]
44. Soares, R.R.A.; Hjort, R.G.; Pola, C.C.; Parate, K.; Reis, E.L.; Soares, N.F.F.; McLamore, E.S.; Claussen, J.C.; Gomes, C.L. Laser-induced graphene electrochemical immunosensors for rapid and label-free monitoring of Salmonella enterica in chicken broth. *ACS Sens.* **2020**, *5*, 1900–1911. [CrossRef]
45. Zhai, Z.; Leng, B.; Yang, N.; Yang, B.; Liu, L.; Huang, N.; Jiang, X. Rational Construction of 3D-Networked Carbon Nanowalls/Diamond Supporting CuO Architecture for High-Performance Electrochemical Biosensors. *Small* **2019**, *15*, 1901527. [CrossRef]
46. Fatema, K.N.; Liu, Y.; Cho, K.Y.; Oh, W.-C. Comparative Study of Electrochemical Biosensors Based on Highly Efficient Mesoporous ZrO2-Ag-G-SiO2 and In2O3-G-SiO2 for Rapid Recognition of *E. coli* O157: H7. *ACS Omega* **2020**, *5*, 22719–22730. [CrossRef] [PubMed]
47. Moro, L.; Turemis, M.; Marini, B.; Ippodrino, R.; Giardi, M.T. Better together: Strategies based on magnetic particles and quantum dots for improved biosensing. *Biotechnol. Adv.* **2017**, *35*, 51–63. [CrossRef] [PubMed]
48. Kubičárová, T.; Fojta, M.; Vidic, J.; Havran, L.; Paleček, E. Mercury film electrode as a sensor for the detection of DNA damage. *Electroanal. Int. J. Devoted Fundam. Pract. Asp. Electroanal.* **2000**, *12*, 1422–1425. [CrossRef]
49. Kaya, H.O.; Cetin, A.E.; Azimzadeh, M.; Topkaya, S.N. Pathogen detection with electrochemical biosensors: Advantages, challenges and future perspectives. *J. Electroanal. Chem.* **2021**, *882*, 114989. [CrossRef]
50. Vidic, J.; Hou, Y. Immobilization of Olfactory Receptors Carried by Nanosomes onto a Gold Sensor Surface. In *G Protein-Coupled Receptor Screening Assays*; Springer: Berlin/Heidelberg, Germany, 2021; pp. 85–95.
51. Minic, J.; Grosclaude, J.; Aioun, J.; Persuy, M.-A.; Gorojankina, T.; Salesse, R.; Pajot-Augy, E.; Hou, Y.; Helali, S.; Jaffrezic-Renault, N. Immobilization of native membrane-bound rhodopsin on biosensor surfaces. *Biochim. Biophys. Acta Gen. Subj.* **2005**, *1724*, 324–332. [CrossRef]
52. Hou, Y.; Jaffrezic-Renault, N.; Martelet, C.; Zhang, A.; Minic-Vidic, J.; Gorojankina, T.; Persuy, M.-A.; Pajot-Augy, E.; Salesse, R.; Akimov, V. A novel detection strategy for odorant molecules based on controlled bioengineering of rat olfactory receptor I7. *Biosens. Bioelectron.* **2007**, *22*, 1550–1555. [CrossRef] [PubMed]

53. Cardona, M.; Peter, Y.Y. *Fundamentals of Semiconductors*; Springer: Berlin/Heidelberg, Germany, 2005.
54. Zare, M.; Namratha, K.; Byrappa, K.; Surendra, D.; Yallappa, S.; Hungund, B. Surfactant assisted solvothermal synthesis of ZnO nanoparticles and study of their antimicrobial and antioxidant properties. *J. Mater. Sci. Technol.* **2018**, *34*, 1035–1043. [CrossRef]
55. Sridar, R.; Ramanane, U.U.; Rajasimman, M. ZnO nanoparticles–Synthesis, characterization and its application for phenol removal from synthetic and pharmaceutical industry wastewater. *Environ. Nanotechnol. Monit. Manag.* **2018**, *10*, 388–393. [CrossRef]
56. Li, R.; Chen, S.; Lou, Z.; Li, L.; Huang, T.; Song, Y.; Chen, D.; Shen, G. Fabrication of porous SnO2 nanowires gas sensors with enhanced sensitivity. *Sens. Actuators B Chem.* **2017**, *252*, 79–85. [CrossRef]
57. Ziarati, A.; Badiei, A.; Luque, R. Black hollow TiO2 nanocubes: Advanced nanoarchitectures for efficient visible light photocatalytic applications. *Appl. Catal. B Environ.* **2018**, *238*, 177–183. [CrossRef]
58. Kar, E.; Bose, N.; Dutta, B.; Banerjee, S.; Mukherjee, N.; Mukherjee, S. 2D SnO2 nanosheet/PVDF composite based flexible, self-cleaning piezoelectric energy harvester. *Energy Convers. Manag.* **2019**, *184*, 600–608. [CrossRef]
59. Peng, H.; Li, F.; Hua, Z.; Yang, K.; Yin, F.; Yuan, W. Highly sensitive and selective room-temperature nitrogen dioxide sensors based on porous graphene. *Sens. Actuators B Chem.* **2018**, *275*, 78–85. [CrossRef]
60. Muniandy, S.; Teh, S.J.; Appaturi, J.N.; Thong, K.L.; Lai, C.W.; Ibrahim, F.; Leo, B.F. A reduced graphene oxide-titanium dioxide nanocomposite based electrochemical aptasensor for rapid and sensitive detection of Salmonella enterica. *Bioelectrochemistry* **2019**, *127*, 136–144. [CrossRef] [PubMed]
61. Nadzirah, S.; Azizah, N.; Hashim, U.; Gopinath, S.C.; Kashif, M. Titanium dioxide nanoparticle-based interdigitated electrodes: A novel current to voltage DNA biosensor recognizes *E. coli* O157: H7. *PLoS ONE* **2015**, *10*, e0139766. [CrossRef] [PubMed]
62. Teng, Y.; Zhang, X.; Fu, Y.; Liu, H.; Wang, Z.; Jin, L.; Zhang, W. Optimized ferrocene-functionalized ZnO nanorods for signal amplification in electrochemical immunoassay of Escherichia coli. *Biosens. Bioelectron.* **2011**, *26*, 4661–4666. [CrossRef] [PubMed]
63. Purwidyantri, A.; Chen, C.-H.; Chen, L.-Y.; Chen, C.-C.; Luo, J.-D.; Chiou, C.-C.; Tian, Y.-C.; Lin, C.-Y.; Yang, C.-M.; Lai, H.-C. Speckled zno nanograss electrochemical sensor for staphylococcus epidermidis detection. *J. Electrochem. Soc.* **2017**, *164*, B205. [CrossRef]
64. Maduraiveeran, G.; Sasidharan, M.; Jin, W. Earth-abundant transition metal and metal oxide nanomaterials: Synthesis and electrochemical applications. *Prog. Mater. Sci.* **2019**, *106*, 100574. [CrossRef]
65. Wang, S.; Peng, T.; Meng, Q.; Zhu, X.; Guo, L.; Yao, K.; Wang, Z.; Zheng, P.; Ren, Z.; He, Z. Rapid and ultrasensitive detection of Salmonella typhimurium using a novel impedance biosensor based on SiO2@ MnO2 nanocomposites and interdigitated array microelectrodes. *Sens. Actuators B Chem.* **2020**, *324*, 128654. [CrossRef]
66. Patel, M.K.; Singh, J.; Singh, M.K.; Agrawal, V.V.; Ansari, S.; Malhotra, B. Tin oxide quantum dot based DNA sensor for pathogen detection. *J. Nanosci. Nanotechnol.* **2013**, *13*, 1671–1678. [CrossRef]
67. Zanet, V.; Vidic, J.; Auger, S.; Vizzini, P.; Lippe, G.; Iacumin, L.; Comi, G.; Manzano, M. Activity evaluation of pure and doped zinc oxide nanoparticles against bacterial pathogens and Saccharomyces cerevisiae. *J. Appl. Microbiol.* **2019**, *127*, 1391–1402. [CrossRef]
68. Auger, S.; Henry, C.; Péchaux, C.; Lejal, N.; Zanet, V.; Nikolic, M.V.; Manzano, M.; Vidic, J. Exploring the impact of Mg-doped ZnO nanoparticles on a model soil microorganism Bacillus subtilis. *Ecotoxicol. Environ. Saf.* **2019**, *182*, 109421. [CrossRef]
69. Auger, S.; Henry, C.; Péchoux, C.; Suman, S.; Lejal, N.; Bertho, N.; Larcher, T.; Stankic, S.; Vidic, J. Exploring multiple effects of Zn 0.15 Mg 0.85 O nanoparticles on Bacillus subtilis and macrophages. *Sci. Rep.* **2018**, *8*, 1–14. [CrossRef] [PubMed]
70. Vidic, J.; Stankic, S.; Haque, F.; Ciric, D.; Le Goffic, R.; Vidy, A.; Jupille, J.; Delmas, B. Selective antibacterial effects of mixed ZnMgO nanoparticles. *J. Nanoparticle Res.* **2013**, *15*, 1–10. [CrossRef] [PubMed]
71. Yang, Z.; Wang, Y.; Zhang, D. A novel multifunctional electrochemical platform for simultaneous detection, elimination, and inactivation of pathogenic bacteria based on the Vancomycin-functionalised AgNPs/3D-ZnO nanorod arrays. *Biosens. Bioelectron.* **2017**, *98*, 248–253. [CrossRef] [PubMed]
72. Iijima, S.; Ichihashi, T. Single-shell carbon nanotubes of 1-nm diameter. *Nature* **1993**, *363*, 603–605. [CrossRef]
73. Pérez-López, B.; Merkoçi, A. Carbon nanotubes and graphene in analytical sciences. *Microchim. Acta* **2012**, *179*, 1–16. [CrossRef]
74. Novoselov, K.S.; Geim, A.K.; Morozov, S.V.; Jiang, D.; Zhang, Y.; Dubonos, S.V.; Grigorieva, I.V.; Firsov, A.A. Electric field effect in atomically thin carbon films. *Science* **2004**, *306*, 666–669. [CrossRef] [PubMed]
75. McAllister, M.J.; Li, J.-L.; Adamson, D.H.; Schniepp, H.C.; Abdala, A.A.; Liu, J.; Herrera-Alonso, M.; Milius, D.L.; Car, R.; Prud'homme, R.K.; et al. Single Sheet Functionalized Graphene by Oxidation and Thermal Expansion of Graphite. *Chem. Mater.* **2007**, *19*, 4396–4404. [CrossRef]
76. Peigney, A.; Laurent, C.; Flahaut, E.; Bacsa, R.R.; Rousset, A. Specific surface area of carbon nanotubes and bundles of carbon nanotubes. *Carbon* **2001**, *39*, 507–514. [CrossRef]
77. Evtugyn, G.; Porfireva, A.; Shamagsumova, R.; Hianik, T. Advances in Electrochemical Aptasensors Based on Carbon Nanomaterials. *Chemosensors* **2020**, *8*, 96. [CrossRef]
78. Hu, J.; Zhang, Z. Application of Electrochemical Sensors Based on Carbon Nanomaterials for Detection of Flavonoids. *Nanomaterials* **2020**, *10*, 2020. [CrossRef]
79. Laghrib, F.; Bakasse, M.; Lahrich, S.; El Mhammedi, M.A. Electrochemical sensors for improved detection of paraquat in food samples: A review. *Mater. Sci. Eng. C* **2020**, *107*, 110349. [CrossRef]
80. Le, V.T.; Vasseghian, Y.; Dragoi, E.-N.; Moradi, M.; Mousavi Khaneghah, A. A review on graphene-based electrochemical sensor for mycotoxins detection. *Food Chem. Toxicol.* **2021**, *148*, 111931. [CrossRef]

81. Prattis, I.; Hui, E.; Gubeljak, P.; Kaminski Schierle, G.S.; Lombardo, A.; Occhipinti, L.G. Graphene for Biosensing Applications in Point-of-Care Testing. *Trends Biotechnol.* **2021**, *39*, 1065–1077. [CrossRef]
82. Smart, A.; Crew, A.; Pemberton, R.; Hughes, G.; Doran, O.; Hart, J.P. Screen-printed carbon based biosensors and their applications in agri-food safety. *TrAC Trends Anal. Chem.* **2020**, *127*, 115898. [CrossRef]
83. Arduini, F.; Micheli, L.; Scognamiglio, V.; Mazzaracchio, V.; Moscone, D. Sustainable materials for the design of forefront printed (bio)sensors applied in agrifood sector. *TrAC Trends Anal. Chem.* **2020**, *128*, 115909. [CrossRef]
84. Zia, Q.; Alawami, M.; Mokhtar, N.F.K.; Nhari, R.M.H.R.; Hanish, I. Current analytical methods for porcine identification in meat and meat products. *Food Chem.* **2020**, *324*, 126664. [CrossRef]
85. Kampeera, J.; Pasakon, P.; Karuwan, C.; Arunrut, N.; Sappat, A.; Sirithammajak, S.; Dechokiattawan, N.; Sumranwanich, T.; Chaivisuthangkura, P.; Ounjai, P.; et al. Point-of-care rapid detection of Vibrio parahaemolyticus in seafood using loop-mediated isothermal amplification and graphene-based screen-printed electrochemical sensor. *Biosens. Bioelectron.* **2019**, *132*, 271–278. [CrossRef] [PubMed]
86. Gupta, R.; Raza, N.; Bhardwaj, S.K.; Vikrant, K.; Kim, K.-H.; Bhardwaj, N. Advances in nanomaterial-based electrochemical biosensors for the detection of microbial toxins, pathogenic bacteria in food matrices. *J. Hazard. Mater.* **2021**, *401*, 123379. [CrossRef] [PubMed]
87. Pandey, A.; Gurbuz, Y.; Ozguz, V.; Niazi, J.H.; Qureshi, A. Graphene-interfaced electrical biosensor for label-free and sensitive detection of foodborne pathogenic *E. coli* O157: H7. *Biosens. Bioelectron.* **2017**, *91*, 225–231. [CrossRef]
88. Khan, M.S.; Misra, S.K.; Dighe, K.; Wang, Z.; Schwartz-Duval, A.S.; Sar, D.; Pan, D. Electrically-receptive and thermally-responsive paper-based sensor chip for rapid detection of bacterial cells. *Biosens. Bioelectron.* **2018**, *110*, 132–140. [CrossRef] [PubMed]
89. Cinti, S.; Arduini, F. Graphene-based screen-printed electrochemical (bio) sensors and their applications: Efforts and criticisms. *Biosens. Bioelectron.* **2017**, *89*, 107–122. [CrossRef]
90. Capobianco, J.A.; Armstrong, C.M.; Lee, J.; Gehring, A.G. Detection of pathogenic bacteria in large volume food samples using an enzyme-linked immunoelectrochemical biosensor. *Food Control* **2021**, *119*, 107456. [CrossRef]
91. Capobianco, J.A.; Lee, J.; Armstrong, C.M.; Gehring, A.G. Rapid detection of Salmonella enterica serotype Typhimurium in large volume samples using porous electrodes in a flow-through, enzyme-amplified immunoelectrochemical sensor. *Anal. Bioanal. Chem.* **2019**, *411*, 5233–5242. [CrossRef]
92. Jaiswal, N.; Pandey, C.M.; Soni, A.; Tiwari, I.; Rosillo-Lopez, M.; Salzmann, C.G.; Malhotra, B.D.; Sumana, G. Electrochemical genosensor based on carboxylated graphene for detection of water-borne pathogen. *Sens. Actuators B Chem.* **2018**, *275*, 312–321. [CrossRef]
93. Mathur, A.; Gupta, R.; Kondal, S.; Wadhwa, S.; Pudake, R.N.; Shivani; Kansal, R.; Pundir, C.S.; Narang, J. A new tactics for the detection of S. aureus via paper based geno-interface incorporated with graphene nano dots and zeolites. *Int. J. Biol. Macromol.* **2018**, *112*, 364–370. [CrossRef]
94. Xu, S.; Zhang, Y.; Dong, K.; Wen, J.; Zheng, C.; Zhao, S. Electrochemical DNA biosensor based on graphene oxide-chitosan hybrid nanocomposites for detection of Escherichia coli O157: H7. *Int. J. Electrochem. Sci.* **2017**, *12*, 3443–3458. [CrossRef]
95. Ma, X.; Jiang, Y.; Jia, F.; Yu, Y.; Chen, J.; Wang, Z. An aptamer-based electrochemical biosensor for the detection of Salmonella. *J. Microbiol. Methods* **2014**, *98*, 94–98. [CrossRef]
96. Mutreja, R.; Jariyal, M.; Pathania, P.; Sharma, A.; Sahoo, D.K.; Suri, C.R. Novel surface antigen based impedimetric immunosensor for detection of Salmonella typhimurium in water and juice samples. *Biosens. Bioelectron.* **2016**, *85*, 707–713. [CrossRef]
97. Mo, X.; Wu, Z.; Huang, J.; Zhao, G.; Dou, W. A sensitive and regenerative electrochemical immunosensor for quantitative detection of Escherichia coli O157:H7 based on stable polyaniline coated screen-printed carbon electrode and rGO-NR-Au@Pt. *Anal. Methods* **2019**, *11*, 1475–1482. [CrossRef]
98. Thakur, B.; Zhou, G.; Chang, J.; Pu, H.; Jin, B.; Sui, X.; Yuan, X.; Yang, C.-H.; Magruder, M.; Chen, J. Rapid detection of single *E. coli* bacteria using a graphene-based field-effect transistor device. *Biosens. Bioelectron.* **2018**, *110*, 16–22. [CrossRef]
99. Pandey, C.M.; Tiwari, I.; Singh, V.N.; Sood, K.; Sumana, G.; Malhotra, B.D. Highly sensitive electrochemical immunosensor based on graphene-wrapped copper oxide-cysteine hierarchical structure for detection of pathogenic bacteria. *Sens. Actuators B: Chem.* **2017**, *238*, 1060–1069. [CrossRef]
100. Zhu, F.; Zhao, G.; Dou, W. A non-enzymatic electrochemical immunoassay for quantitative detection of Escherichia coli O157:H7 using Au@ Pt and graphene. *Anal. Biochem.* **2018**, *559*, 34–43. [CrossRef]
101. Niu, X.; Zheng, W.; Yin, C.; Weng, W.; Li, G.; Sun, W.; Men, Y. Electrochemical DNA biosensor based on gold nanoparticles and partially reduced graphene oxide modified electrode for the detection of Listeria monocytogenes hly gene sequence. *J. Electroanal. Chem.* **2017**, *806*, 116–122. [CrossRef]
102. Ye, Y.; Yan, W.; Liu, Y.; He, S.; Cao, X.; Xu, X.; Zheng, H.; Gunasekaran, S. Electrochemical detection of Salmonella using an invA genosensor on polypyrrole-reduced graphene oxide modified glassy carbon electrode and AuNPs-horseradish peroxidase-streptavidin as nanotag. *Anal. Chim. Acta* **2019**, *1074*, 80–88. [CrossRef]
103. Jia, F.; Duan, N.; Wu, S.; Dai, R.; Wang, Z.; Li, X. Impedimetric Salmonella aptasensor using a glassy carbon electrode modified with an electrodeposited composite consisting of reduced graphene oxide and carbon nanotubes. *Microchim. Acta* **2016**, *183*, 337–344. [CrossRef]
104. Dinshaw, I.J.; Muniandy, S.; Teh, S.J.; Ibrahim, F.; Leo, B.F.; Thong, K.L. Development of an aptasensor using reduced graphene oxide chitosan complex to detect Salmonella. *J. Electroanal. Chem.* **2017**, *806*, 88–96. [CrossRef]

105. You, Z.; Qiu, Q.; Chen, H.; Feng, Y.; Wang, X.; Wang, Y.; Ying, Y. Laser-induced noble metal nanoparticle-graphene composites enabled flexible biosensor for pathogen detection. *Biosens. Bioelectron.* **2020**, *150*, 111896. [CrossRef]
106. Choi, H.K.; Lee, J.; Park, M.K.; Oh, J.H. Development of single-walled carbon nanotube-based biosensor for the detection of Staphylococcus aureus. *J. Food Qual.* **2017**, *2017*, 5239487. [CrossRef]
107. Bhardwaj, J.; Devarakonda, S.; Kumar, S.; Jang, J. Development of a paper-based electrochemical immunosensor using an antibody-single walled carbon nanotubes bio-conjugate modified electrode for label-free detection of foodborne pathogens. *Sens. Actuators B Chem.* **2017**, *253*, 115–123. [CrossRef]
108. Andrade, C.A.; Nascimento, J.M.; Oliveira, I.S.; de Oliveira, C.V.; de Melo, C.P.; Franco, O.L.; Oliveira, M.D. Nanostructured sensor based on carbon nanotubes and clavanin A for bacterial detection. *Colloids Surf. B Biointerfaces* **2015**, *135*, 833–839. [CrossRef]
109. Güner, A.; Çevik, E.; Şenel, M.; Alpsoy, L. An electrochemical immunosensor for sensitive detection of Escherichia coli O157: H7 by using chitosan, MWCNT, polypyrrole with gold nanoparticles hybrid sensing platform. *Food Chem.* **2017**, *229*, 358–365. [CrossRef]
110. Li, T.; Zhu, F.; Guo, W.; Gu, H.; Zhao, J.; Yan, M.; Liu, S. Selective capture and rapid identification of *E. coli* O157: H7 by carbon nanotube multilayer biosensors and microfluidic chip-based LAMP. *RSC Adv.* **2017**, *7*, 30446–30452. [CrossRef]
111. Saini, K.; Kaushal, A.; Gupta, S.; Kumar, D. Rapid detection of Salmonella enterica in raw milk samples using Stn gene-based biosensor. *3 Biotech* **2019**, *9*, 1–9. [CrossRef]
112. Hasan, M.R.; Pulingam, T.; Appaturi, J.N.; Zifruddin, A.N.; Teh, S.J.; Lim, T.W.; Ibrahim, F.; Leo, B.F.; Thong, K.L. Carbon nanotube-based aptasensor for sensitive electrochemical detection of whole-cell Salmonella. *Anal. Biochem.* **2018**, *554*, 34–43. [CrossRef]
113. Ngoensawat, U.; Rijiravanich, P.; Surareungchai, W.; Somasundrum, M. Electrochemical Immunoassay for Salmonella Typhimurium Based on an Immuno-magnetic Redox Label. *Electroanalysis* **2018**, *30*, 146–153. [CrossRef]
114. Farooq, U.; Ullah, M.W.; Yang, Q.; Aziz, A.; Xu, J.; Zhou, L.; Wang, S. High-density phage particles immobilization in surface-modified bacterial cellulose for ultra-sensitive and selective electrochemical detection of Staphylococcus aureus. *Biosens. Bioelectron.* **2020**, *157*, 112163. [CrossRef]
115. Lu, Y.; Liu, Y.; Zhao, Y.; Li, W.; Qiu, L.; Li, L. A novel and disposable enzyme-labeled amperometric immunosensor based on MWCNT fibers for Listeria monocytogenes detection. *J. Nanomater.* **2016**, *2016*, 3895920. [CrossRef]
116. Woznica, N.; Hawelek, L.; Fischer, H.E.; Bobrinetskiy, I.; Burian, A. The atomic scale structure of graphene powder studied by neutron and X-ray diffraction. *J. Appl. Crystallogr.* **2015**, *48*, 1429–1436. [CrossRef]
117. Jiang, H.; Yang, J.; Wan, K.; Jiang, D.; Jin, C. Miniaturized Paper-Supported 3D Cell-Based Electrochemical Sensor for Bacterial Lipopolysaccharide Detection. *ACS Sens.* **2020**, *5*, 1325–1335. [CrossRef]
118. Kurra, N.; Jiang, Q.; Nayak, P.; Alshareef, H.N. Laser-derived graphene: A three-dimensional printed graphene electrode and its emerging applications. *Nano Today* **2019**, *24*, 81–102. [CrossRef]
119. Lin, J.; Peng, Z.; Liu, Y.; Ruiz-Zepeda, F.; Ye, R.; Samuel, E.L.G.; Yacaman, M.J.; Yakobson, B.I.; Tour, J.M. Laser-induced porous graphene films from commercial polymers. *Nat. Commun.* **2014**, *5*, 5714. [CrossRef]
120. Lahcen, A.A.; Rauf, S.; Beduk, T.; Durmus, C.; Aljedaibi, A.; Timur, S.; Alshareef, H.N.; Amine, A.; Wolfbeis, O.S.; Salama, K.N. Electrochemical sensors and biosensors using laser-derived graphene: A comprehensive review. *Biosensors and Bioelectronics* **2020**, *168*, 112565. [CrossRef]
121. Shirasu, K.; Kitayama, S.; Liu, F.; Yamamoto, G.; Hashida, T. Molecular Dynamics Simulations and Theoretical Model for Engineering Tensile Properties of Single-and Multi-Walled Carbon Nanotubes. *Nanomaterials* **2021**, *11*, 795. [CrossRef]
122. García-Aljaro, C.; Cella, L.N.; Shirale, D.J.; Park, M.; Muñoz, F.J.; Yates, M.V.; Mulchandani, A. Carbon nanotubes-based chemiresistive biosensors for detection of microorganisms. *Biosens. Bioelectron.* **2010**, *26*, 1437–1441. [CrossRef]
123. Yamada, K.; Kim, C.-T.; Kim, J.-H.; Chung, J.-H.; Lee, H.G.; Jun, S. Single walled carbon nanotube-based junction biosensor for detection of Escherichia coli. *PLoS ONE* **2014**, *9*, e105767. [CrossRef]
124. Appaturi, J.N.; Pulingam, T.; Thong, K.L.; Muniandy, S.; Ahmad, N.; Leo, B.F. Rapid and sensitive detection of Salmonella with reduced graphene oxide-carbon nanotube based electrochemical aptasensor. *Anal. Biochem.* **2020**, *589*, 113489. [CrossRef]
125. Marin, M.; Nikolic, M.V.; Vidic, J. Rapid point-of-need detection of bacteria and their toxins in food using gold nanoparticles. *Compr. Rev. Food Sci. Food Saf.* **2021**. [CrossRef]
126. Li, Y.; Schluesener, H.J.; Xu, S. Gold nanoparticle-based biosensors. *Gold Bull.* **2010**, *43*, 29–41. [CrossRef]
127. Pingarrón, J.M.; Yanez-Sedeno, P.; González-Cortés, A. Gold nanoparticle-based electrochemical biosensors. *Electrochim. Acta* **2008**, *53*, 5848–5866. [CrossRef]
128. Raj, P.; Oh, M.H.; Han, K.; Lee, T.Y. Label-Free Electrochemical Biosensor Based on Au@ MoS_2–PANI for Escherichia coli Detection. *Chemosensors* **2021**, *9*, 49. [CrossRef]
129. Hassan, A.-R.H.A.-A.; de la Escosura-Muñiz, A.; Merkoçi, A. Highly sensitive and rapid determination of Escherichia coli O157: H7 in minced beef and water using electrocatalytic gold nanoparticle tags. *Biosens. Bioelectron.* **2015**, *67*, 511–515. [CrossRef]
130. Afonso, A.S.; Pérez-López, B.; Faria, R.C.; Mattoso, L.H.; Hernández-Herrero, M.; Roig-Sagués, A.X.; Maltez-da Costa, M.; Merkoçi, A. Electrochemical detection of Salmonella using gold nanoparticles. *Biosens. Bioelectron.* **2013**, *40*, 121–126. [CrossRef]
131. Eissa, S.; Zourob, M. Ultrasensitive peptide-based multiplexed electrochemical biosensor for the simultaneous detection of Listeria monocytogenes and Staphylococcus aureus. *Microchim. Acta* **2020**, *187*, 1–11. [CrossRef]

132. Wang, D.; Chen, Q.; Huo, H.; Bai, S.; Cai, G.; Lai, W.; Lin, J. Efficient separation and quantitative detection of Listeria monocytogenes based on screen-printed interdigitated electrode, urease and magnetic nanoparticles. *Food Control* **2017**, *73*, 555–561. [CrossRef]
133. Oliveira, M.D.; Andrade, C.A.; Correia, M.T.; Coelho, L.C.; Singh, P.R.; Zeng, X. Impedimetric biosensor based on self-assembled hybrid cystein-gold nanoparticles and CramoLL lectin for bacterial lipopolysaccharide recognition. *J. Colloid Interface Sci.* **2011**, *362*, 194–201. [CrossRef]
134. de Oliveira, T.R.; Martucci, D.H.; Faria, R.C. Simple disposable microfluidic device for Salmonella typhimurium detection by magneto-immunoassay. *Sens. Actuators B Chem.* **2018**, *255*, 684–691. [CrossRef]
135. Jiang, X.; Ding, W.; Lv, Z.; Rao, C. Highly sensitive electrochemical immunosensing for Listeria monocytogenes based on 3, 4, 9, 10-perylene tetracarboxylic acid/graphene ribbons as sensing platform and ferrocene/gold nanoparticles as amplifier. *Anal. Sci.* **2021**, 21P113, published online. [CrossRef]
136. Layqah, L.A.; Eissa, S. An electrochemical immunosensor for the corona virus associated with the Middle East respiratory syndrome using an array of gold nanoparticle-modified carbon electrodes. *Microchim. Acta* **2019**, *186*, 1–10. [CrossRef]
137. van Doremalen, N.; Bushmaker, T.; Karesh, W.B.; Munster, V.J. Stability of Middle East respiratory syndrome coronavirus in milk. *Emerg. Infect. Dis.* **2014**, *20*, 1263. [CrossRef]
138. Imran, M.; Ehrhardt, C.J.; Bertino, M.F.; Shah, M.R.; Yadavalli, V.K. Chitosan Stabilized Silver Nanoparticles for the Electrochemical Detection of Lipopolysaccharide: A Facile Biosensing Approach for Gram-Negative Bacteria. *Micromachines* **2020**, *11*, 413. [CrossRef]
139. Kalambate, P.K.; Gadhari, N.S.; Li, X.; Rao, Z.; Navale, S.T.; Shen, Y.; Patil, V.R.; Huang, Y. Recent advances in MXene–based electrochemical sensors and biosensors. *TrAC Trends Anal. Chem.* **2019**, *120*, 115643. [CrossRef]
140. Zhang, J.; Li, Y.; Duan, S.; He, F. Highly electrically conductive two-dimensional Ti3C2 Mxenes-based 16S rDNA electrochemical sensor for detecting Mycobacterium tuberculosis. *Anal. Chim. Acta* **2020**, *1123*, 9–17. [CrossRef]
141. Sinha, A.; Dhanjai; Tan, B.; Huang, Y.; Zhao, H.; Dang, X.; Chen, J.; Jain, R. MoS2 nanostructures for electrochemical sensing of multidisciplinary targets: A review. *TrAC Trends Anal. Chem.* **2018**, *102*, 75–90. [CrossRef]
142. Yu, T.; Breslin, C.B. Review—Two-Dimensional Titanium Carbide MXenes and Their Emerging Applications as Electrochemical Sensors. *J. Electrochem. Soc.* **2020**, *167*, 037514. [CrossRef]
143. Kalantar-zadeh, K.; Ou, J.Z. Biosensors based on two-dimensional MoS2. *Acs Sens.* **2016**, *1*, 5–16. [CrossRef]
144. Mishra, A.; Fatima, T.; Narang, J.; Shukla, S.K.; Rawal, R.; Mathur, A.; Jain, A.; Khanuja, M. Self-Assembled Two-Dimensional Molybdenum Disulfide Nanosheet Geno-Interface for the Detection of Salmonella. *ACS Omega* **2019**, *4*, 14913–14919. [CrossRef]
145. Singh, C.; Ali, M.A.; Kumar, V.; Ahmad, R.; Sumana, G. Functionalized MoS2 nanosheets assembled microfluidic immunosensor for highly sensitive detection of food pathogen. *Sens. Actuators B Chem.* **2018**, *259*, 1090–1098. [CrossRef]
146. Dang, S.; Zhu, Q.-L.; Xu, Q. Nanomaterials derived from metal–organic frameworks. *Nat. Rev. Mater.* **2017**, *3*, 1–14. [CrossRef]
147. Wang, Q.; Astruc, D. State of the art and prospects in metal–organic framework (MOF)-based and MOF-derived nanocatalysis. *Chem. Rev.* **2019**, *120*, 1438–1511. [CrossRef]
148. Meng, L.; Yu, B.; Qin, Y. Templated interfacial synthesis of metal-organic framework (MOF) nano-and micro-structures with precisely controlled shapes and sizes. *Commun. Chem.* **2021**, *4*, 1–10. [CrossRef]
149. Varsha, M.; Nageswaran, G. 2D Layered Metal Organic Framework Nanosheets as an Emerging Platform for Electrochemical Sensing. *J. Electrochem. Soc.* **2020**, *167*, 136502.
150. Gupta, A.; Sharma, A.L.; Deep, A. Sensitive impedimetric detection of *E. coli* with metal-organic framework (MIL-53)/polymer (PEDOT) composite modified screen-printed electrodes. *J. Environ. Chem. Eng.* **2021**, *9*, 104925. [CrossRef]
151. Sun, Z.; Peng, Y.; Wang, M.; Lin, Y.; Jalalah, M.; Alsareii, S.A.; Harraz, F.A.; Yang, J.; Li, G. Electrochemical Deposition of Cu Metal–Organic Framework Films for the Dual Analysis of Pathogens. *Anal. Chem. 2021 93*, 8994–9001.
152. Dai, G.; Li, Z.; Luo, F.; Ai, S.; Chen, B.; Wang, Q. Electrochemical determination of Salmonella typhimurium by using aptamer-loaded gold nanoparticles and a composite prepared from a metal-organic framework (type UiO-67) and graphene. *Microchim. Acta* **2019**, *186*, 1–9. [CrossRef]
153. Murasova, P.; Kovarova, A.; Kasparova, J.; Brozkova, I.; Hamiot, A.; Pekarkova, J.; Dupuy, B.; Drbohlavova, J.; Bilkova, Z.; Korecka, L. Direct culture-free electrochemical detection of Salmonella cells in milk based on quantum dots-modified nanostructured dendrons. *J. Electroanal. Chem.* **2020**, *863*, 114051. [CrossRef]
154. Jiang, D.; Yang, C.; Fan, Y.; Leung, H.-M.P.; Inthavong, K.; Zhang, Y.; Li, Z.; Yang, M. Ultra-sensitive photoelectrochemical aptamer biosensor for detecting *E. coli* O157: H7 based on nonmetallic plasmonic two-dimensional hydrated defective tungsten oxide nanosheets coupling with nitrogen-doped graphene quantum dots (dWO3•H2O@ N-GQDs). *Biosens. Bioelectron.* **2021**, *183*, 113214. [CrossRef] [PubMed]
155. Gu, C.; Kong, X.; Liu, X.; Gai, P.; Li, F. Enzymatic biofuel-cell-based self-powered biosensor integrated with DNA amplification strategy for ultrasensitive detection of single-nucleotide polymorphism. *Anal. Chem.* **2019**, *91*, 8697–8704. [CrossRef] [PubMed]
156. Gao, X.; Li, X.; Sun, X.; Zhang, J.; Zhao, Y.; Liu, X.; Li, F. DNA tetrahedra-cross-linked hydrogel functionalized paper for onsite analysis of dna methyltransferase activity using a personal glucose meter. *Anal. Chem.* **2020**, *92*, 4592–4599. [CrossRef] [PubMed]
157. Yin, X.; Hou, T.; Huang, B.; Yang, L.; Li, F. Aptamer recognition-trigged label-free homogeneous electrochemical strategy for an ultrasensitive cancer-derived exosome assay. *Chem. Commun.* **2019**, *55*, 13705–13708. [CrossRef]

nanomaterials

MDPI

Article

Laser-Tunable Printed ZnO Nanoparticles for Paper-Based UV Sensors with Reduced Humidity Interference

Georges Dubourg [1,*], Marko Radović [1] and Borislav Vasić [2]

[1] Center for Sensor Technologies, BioSense Institute, University of Novi Sad, Zorana Đinđića, 21101 Novi Sad, Serbia; marrad@biosense.rs
[2] Institute of Physics Belgrade, University of Belgrade, Pregrevica 118, 11080 Belgrade, Serbia; bvasic@ipb.ac.rs
* Correspondence: georges.dubourg@biosense.rs

Abstract: Development of paper-based sensors that do not suffer with humidity interference is desirable for practical environmental applications. In this work, a laser processing method was reported to effectively modulate the cross-sensitivity to humidity of ZnO-based UV (Ultraviolet) sensors printed on paper substrate. The results reveal that the laser induced zinc oxide (ZnO) surface morphology contributes to the super-hydrophobicity of the printed ZnO nanoparticles, reducing humidity interference while enhancing UV sensitivity. Herein, this conducted research highlights for the first time that laser processing is an attractive choice that reduces the cross-sensitivity to water vapor in the UV sensing response of ZnO-based devices printed on paper, paving the way to low-cost and sophisticated paper-based sensors.

Keywords: paper-based device; UV sensors; ZnO nanoparticles; humidity resistance

Citation: Dubourg, G.; Radović, M.; Vasić, B. Laser-Tunable Printed ZnO Nanoparticles for Paper-Based UV Sensors with Reduced Humidity Interference. *Nanomaterials* **2021**, *11*, 80. https://doi.org/10.3390/nano11010080

Received: 10 December 2020
Accepted: 27 December 2020
Published: 2 January 2021

1. Introduction

For a long time, cellulose fiber paper has been used as the main support for storing, displaying, transferring information and connecting people in the form of missives, flyers or books. In recent years, however, its function as a writing medium has been declining with the evolution of information and communication technologies. This evolution drastically changed how people work, communicate and learn, gradually replacing the paper substrate with electronic support, such as computer, TV, e-book and e-library. Nevertheless, this has generated a considerable amount of electronic waste resulting in severe environmental issues. In order to address the environmental concerns and end-of-life disposal challenges, paper was reinvented as a building component in flexible electronics because it is disposable, recyclable, inexpensive and one of the most abundant organic materials. Therefore, paper-based substrate has been explored with the aim of developing a variety of components, such as electronic and optoelectronic devices [1,2], electrochemical biosensors [3–5] and physical sensors [6,7]. Among them, physical sensors which transduce physical parameters, such as mechanical and optical signals, into processable electrical signals represent a major category of paper-based devices and might play an important role in the upcoming era of wearable electronics.

Various functional nanomaterials have been employed in order to enhance the paper-based sensor performance. Among them, the zinc oxide (ZnO) nanostructures are a popular choice due to their multiple sensing modalities [8–10]. For instance, its direct wide bandgap and 60 meV high exciton energy make ZnO nanostructures the ideal materials for UV sensing applications [11,12]. Due to the growing importance of detecting/protecting UV light application in various fields, various reports have been published on the fabrication of low-cost ZnO-based UV sensors on paper substrate [13–16]. Although many of the reported paper-based UV sensors work very well in laboratory scale proof of principle experiments, they are still limited by their cross-sensitivity to background conditions, such as relative humidity than can vary in outdoor conditions, impeding their practical use in applications

such as environmental monitoring. Indeed, it has been demonstrated that water vapor, present in the real environment for monitoring, strongly interacts with the surface or interface of a ZnO nanostructure, which leads to a significant fluctuation of its electrical and UV sensing properties [17–19]. Although the effect of humidity on UV sensing properties of ZnO nanostructure has been investigated [20–22], the elimination of cross-sensitivity of ZnO-based UV sensors to environmental humidity is still a major challenge. This is even more critical when they are made on paper substrate. As the paper is hygroscopic, the effect of moisture can cause additional significant fluctuations in the conductivity of paper-based devices. So far, the most applicable approaches to reduction of the influence of humidity include either coating paper with a superhydrophobic layer [23–27] or its chemical modification [28,29]. Even though those approaches are effective, they require additional processing steps, making the overall process more time-consuming and costlier. One interesting route to process paper substrate is by use of laser processing technique, which represents a simple, fast and scalable alternative to coating and chemical modification techniques and offers many advantages because of its capability of selective treatment and its fine spatial resolution [30–32]. It has been used to control the wetting properties of paper substrate for microfluidic applications [32–34]. In this work, we introduce the laser irradiation post-processing technique to withstand the influence of humidity and to improve the electrical properties of ZnO based UV detectors and screen-printed devices printed on paper substrate. Effects of the laser irradiation on the conductivity and UV sensing performance of the screen-printed ZnO nanoparticles (NPs) were studied in detail. Afterwards, both dark current and UV photocurrent of the laser treated ZnO UV sensors were measured in air with varied relative humidity (RH) to investigate the effect of water vapor on the ZnO film devices. Basic mechanisms for the observed behavior were discussed and correlated with results from structural analysis of the ZnO film. The results showed that the laser treated UV sensor had excellent compatibility between stability and sensitivity, response and recovery time, and reducing the impact of humidity.

2. Materials and Methods

The concept of the paper-based UV sensor is based on the resistive transduction principle, consisting of a nanostructured ZnO photosensitive layer deposited on interdigitated electrodes (IDE) that are printed on paper substrate, as shown in the Figure 1a.

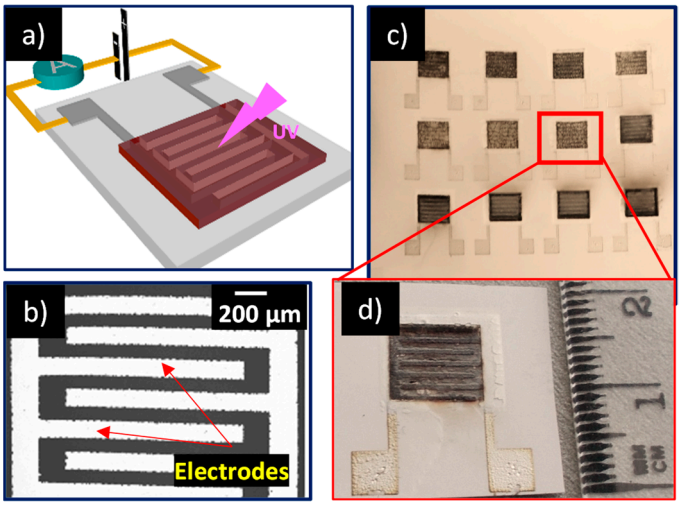

Figure 1. (**a**) Process sequence for fabrication of the paper-based devices; (**b**) SEM (Scanning electron microscope) image of the silver interdigitated electrodes; (**c**,**d**) Optical images of laser sintered devices fabricated on a paper substrate.

2.1. Device Fabrication

A simple, economic and scalable technological process, consisting of two screen-printing steps and a laser-postprocessing step, was used for the fabrication of the paper-based UV sensors. A schematic representation of the fabrication steps is described in the Figure S1. Firstly, a commercial silver paste (HPS-021LV, Novacentrix, Austin, TX, USA) was screen-printed with a semi-automatized screen-printer (EKRA 2H screen-printer, Dornstadt, Germany) on the paper substrate to design the IDEs and baked in an oven at 110 °C for 15 min. An individual digit of the IDE structure was 4 mm long and 170 µm wide. It was separated by a gap of 100 µm from the next digit, as shown in the Figure 1b exhibiting SEM (Scanning electron microscope, HITACHI TM3030, Tokyo, Japon) image of Ag interdigitated electrodes.

In order to fabricate the sensitive layer, based on commercial ZnO nanoparticles (Alfa Aesar™, particle size <25 nm, Kandel, Germany), a functional paste was developed [35]. The paste composition was optimized to meet the criteria: (i) used chemicals should be cost-efficient and environmentally friendly; (ii) paste components should be suitable for laser treatment (boiling point <500 °C); and (iii) paste should produce thick uniform film on top of the electrodes, with preserved properties of ZnO nanomaterial. Main components of the paste were solvent, binder, dispersant and the nanomaterial. Water as solvent was not suitable for final application of printed structure, so ethanol was used as solvent. Since the conducted research was focused on design of sensors with minimum humidity interference, we used PVP (Poly vinyl pyrrolidone) as binder because of its slightly better stability in higher humidity conditions in comparison to other commonly used binders, such as cellulose [36]. For the dispersant, we opted to use alpha-terpineol, which is environmentally friendly, has a relatively low boiling point and is suitable for laser treatment. First, 2 g of PVP (Sigma-Aldrich, St. Louis, MO, USA) was dissolved in 10 mL of ethanol. Afterwards, 1 g of ZnO nanopowder was dispersed in 400 µL of terpineol (Sigma-Aldrich, St. Louis, MO, USA), followed by the addition of 600 µL of PVP solution. High loading ratio of nanomaterial has proven to be optimal for the screen-printing of the sensitive layer, providing desired film thickness and uniformity.

Obtained suspensions were treated with ultrasonic homogenizer (Bandelin HD-70, Berlin, Germany), operating in continuous mode at 40% of total power. Duration of ultrasonic homogenization was 10 min.

2.2. Laser Treatment

The laser treatment of printed films was carried out by using a diode-pumped Nd:YAG laser cutter Rofin-Sinar Power Line D–100, operating in the NIR (Near-infrared) range at 1064 nm. Frequency of the laser pulse was set at 65 kHz, and the speed of the displacement was adjusted to 500 mm s^{-1} in order to obtain sufficient pulse overlapping. The laser fluence was varied by adjusting the laser current. One sample was kept untreated to be used as a reference, and two samples were treated with the input current values of 29 A and 30 A, corresponding to laser fluences of 0.21 J cm^{-2} and 0.23 J cm^{-2}, respectively. The Figure 1d shows the laser treated films sample with laser treated screen-printed ZnO nanoparticles. Figure 1c exhibits a matrix of laser treated samples, providing clear evidence that the developed process can be easily scaled-up for the large-scale fabrication of paper-based electronic devices.

2.3. Device Characterization

The morphology of the screen-printed ZnO film was examined by atomic force microscopy (AFM) in tapping mode. In order to precisely resolve grain boundaries, magnitude of AFM cantilever was recorded during the tapping mode imaging as well, since this signal is very sensitive to abrupt changes in the morphology. Surface roughness was calculated as a root mean square of the height distribution. The wetting characteristic of the sample was carried out by measuring contact angles using the sessile drop technique. A liquid droplet of about 2 µL in volume was dropped on the sample's surface with a micropipette.

The image of the liquid droplet was captured by a digital camera (uEye, IDS, Obersulm, Germany) attached to a microscope (Microzoom, Bausch and Lomb, Rochester, NY, USA) with 2.25× magnification and computed with the IDS camera manager software (IDS, Obersulm, Germany). The recorded droplet images were analyzed with the DropSnake Java plug-in for the ImageJ software (1.8.0, Wayne Rasband, Bethesda, MD, USA) based on B-spline snakes (active contours) to shape the drop [37].

3. Results and Discussion

3.1. Characterization of Laser-Treated ZnO Surface

Figure 2 exhibits top- and side-view SEM images of the ZnO film before and after laser treatment at 0.21 and 0.23 J cm^{-2} laser fluences, which clearly demonstrates that laser irradiation induces significant modifications of the film morphology. From SEM imaging of the untreated film, it can be established that nano-sized particles packed together by the dried organic additives formed a flat and uniform surface layer. When irradiated at 0.21 J cm^{-2}, the film exhibited bigger pores due to the formation of melted droplets. These droplets were formed during the breaking of the large agglomerates accomplished by laser thermal evaporation of organic components. With further increase of the laser fluence at 0.23 J cm^{-2}, the screen-printed film was transformed into solidified and dense ceramic material due to the complete release of the organic components and the sintering effect.

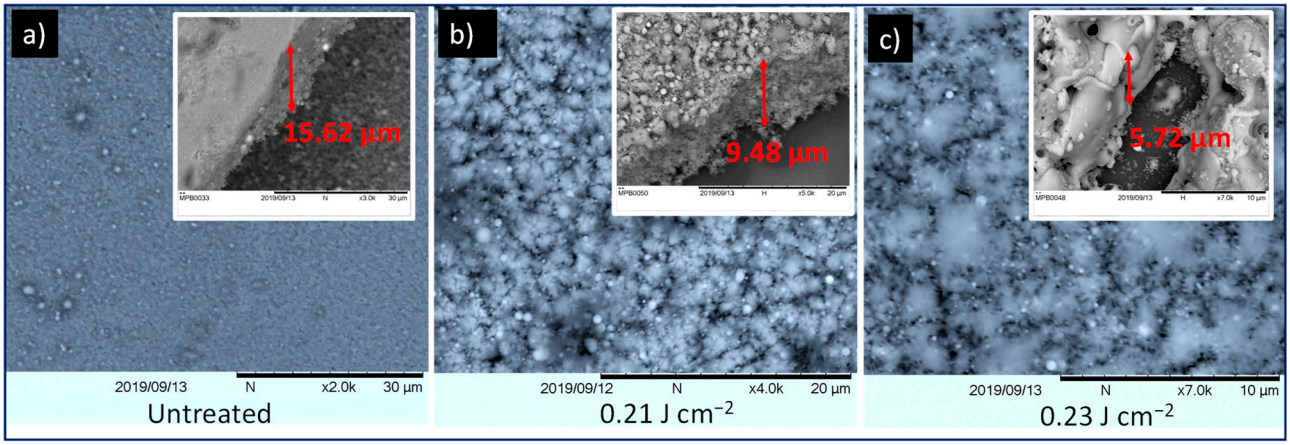

Figure 2. SEM images of (**a**) untreated screen-printed ZnO film, and laser-treated at (**b**) 0.21 J cm^{-2} and (**c**) 0.23 J cm^{-2}. Inset: side view of untreated and treated samples.

Additionally, the presented results demonstrate that the film thickness reduced from 15.6 µm to 9.5 µm and 6 µm after irradiation at 0.21, and 0.23 J cm^{-2}, respectively, which is in agreement with the profile analysis provided in the supporting information (Figure S2). This reduction in film thickness can be directly correlated to the removal of organic binder components with laser radiation and the densification of the screen-printed ZnO film during the sintering process. Furthermore, it can be noticed from the EDX (Energy-dispersive X-ray) characterization, shown in Figure S3, that the Zn and O signatures are present in the untreated and laser treated samples, while carbon signature is considerably reduced in the laser treated sample. This confirms that the laser irradiation does not change the chemical composition of the ZnO nanoparticles or remove organic components of the printed paste matrix.

Therefore, additional investigations were performed by atomic force microscopy (AFM) in tapping mode to explore the change of surface morphology in the laser sintered samples. Figure 3a presents images of the AFM magnitude of the untreated and all treated samples, which emphasize grains and grain boundaries. As can be seen, the morphology significantly changes from a flat surface with small grains in the case of the untreated sample, to very rough surfaces with large grains in the case of the treated samples.

Therefore, these images clearly represent the sintering process where small grains are merged into bigger ones. The underlying morphological changes during the sintering are summarized in the bottom row of Figure 3, in which Figure 3b shows characteristic height profiles from topographic images, while Figure 3c displays the surface roughness. An average grain diameter of the selected grains (encircled by dashed lines in the magnitude images) is presented partly in Figure 3d. The height profile of the untreated sample was a rather flat line, the surface roughness was around 30 nm, while the diameter of the selected grain was around 270 nm. On the other hand, the surface roughness of the treated samples were in the range of 200–300 nm, with some grains being larger than 2 µm.

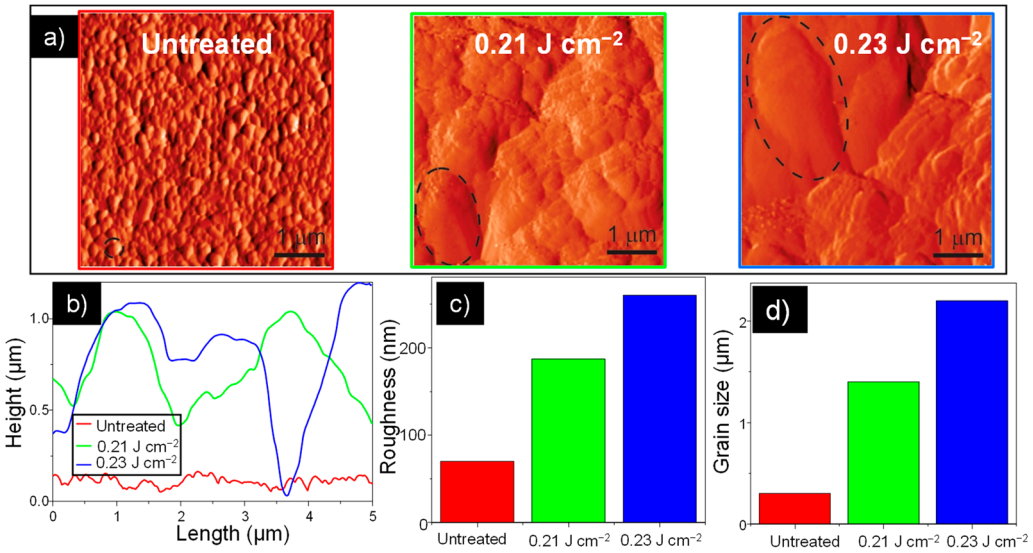

Figure 3. (**a**) AFM characterization of the untreated sample and samples treated at 0.21 and 0.23 J cm^{-2}. Inset: Corresponding 3D morphologies. (**b**) Surface profile from AFM analysis of the untreated and laser treated samples. (**c**) Roughness measurement of the investigated screen-printed films. (**d**) Grain size measurement of the investigated screen-printed films.

Figure 4 shows the contact angle of the untreated sample and samples treated with 0.21 and 0.23 J cm^{-2} laser fluence, where it can be noticed that hydrophobicity of the ZnO film increases with increase in the laser fluence. Clearly, a water droplet stands stable on the laser treated films, while it spreads out on the untreated sample. The wettability behavior of a surface is strongly related to the surface morphology [38]. From the AFM measurements, we established that morphology and roughness of the film surfaces change with the increase of the laser fluence. The surface of the untreated film (Figure 4a) with low surface roughness shows a low contact angle with hydrophilic behavior. With the rise of the surface roughness the contact angle increased, indicating a hydrophobic behavior for the sample treated at 0.21 J cm^{-2} and super hydrophobic behavior for the sample treated with higher laser fluence 0.23 J cm^{-2}. For porous nanostructured surfaces, the Cassie and Baxter (CB) model is usually applied for the description of wetting properties [39]. According to the CB model, the water contact angle on the porous surface is greatly influenced by the surface fraction of solid–liquid and liquid–air interfaces on the solid surface. In the CB wetting state, the large volume of air trapped between the grains prevents the water droplet from penetrating into the free space and the water droplet is suspended above the substrate unstably. Within such a framework, a hydrophilic surface can be modified into a hydrophobic one, and the contact angle increases with the ratio of water–air interface to the total area because air pockets formed below the water droplet minimize the interfacial energy. Considering that surface roughness of ZnO films increase with laser treatment, the fraction of interfacial area between air and liquid also increases. For highly rough surfaces, more air can be trapped within the interstices, increasing measured contact angle. The increased surface roughness and additional trapped air prevent further penetration of the

water droplet into the solid surface, giving rise to the observed shift from hydrophilicity to super-hydrophobicity.

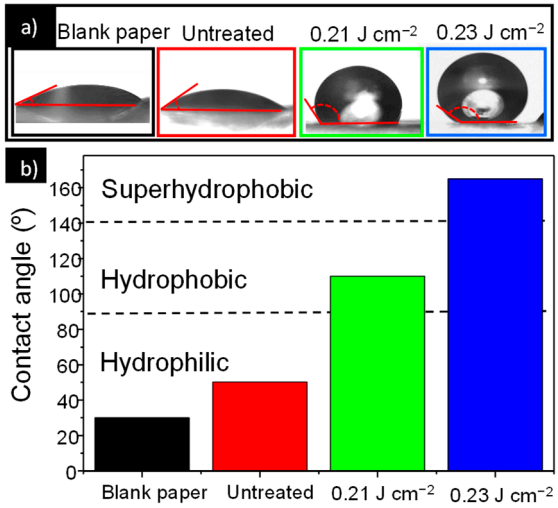

Figure 4. (**a**) Photographs of water droplet shape on the untreated and laser treated ZnO screen printed films. (**b**) Contact angle measured for untreated and laser treated samples.

3.2. UV Detection Performances

Figure 5a displays the dark current–voltage (I–V) characteristics, together with the photocurrent of the untreated samples and samples sintered with 0.21 J cm^{-2} and 0.23 J cm^{-2} laser fluences, measured in the −5 V to 5 V range at ambient humidity of 45%. Analysis of the obtained results clearly reveals that increase in laser fluence induces a significant increase in the dark current values, thus improving the conductivity of the printed ZnO film. Indeed, for the untreated sample, the profile of the I(V) curve corresponds to that of the material with poor conductivity with 3.42 nA at 5 V, whereas the I(V) curve of the sample treated with 0.23 J cm^{-2} has 5 orders of magnitude higher current (935 µA at 5 V). For porous nanomaterials, where nanoparticles are packed together, the conductivity is greatly affected by a mechanism governed by the grain-boundary resistance, since the resistance at these contacts is much higher than the resistance across the grains. The conduction channels in the ZnO–NP film include NP–NP junctions, and electrons must overcome the junction barriers to pass from one nanoparticle to another. Using AFM measurements, it was determined that during the sintering process, most of these grain boundaries vanished as the nanoparticles form neck like structures and the grains connected, reducing the junction barrier and creating a conductive path for electron transfer. In this case, the grain conductivity becomes dominant, leading to an observed increase in the current value.

Figure 5a also demonstrated that there was a significant increase in the photocurrent of all the samples when they were exposed to 360 nm wavelength at 10 mW cm^{-2}. This excitation wavelength was chosen to be in the vicinity of the optical band gap of ZnO (Eg = 305–395 nm) [40]. Moreover, it was noticed that a relatively high photocurrent (≈300 nA) was obtained at zero bias for the sample treated at 0.23 J cm^{-2}, offering the possibility to use this laser treated device as a self-powered, paper-based photodetector system. The Figure 5b depicts the photocurrent-to-dark current ratio (called the photoresponse) as a function of the time, which compares the switching characteristics of the investigated samples under a bias of 5 V. Figure 5b demonstrated that a significant increase in the photoresponse was observed under UV light illumination for the untreated samples, as well as for the samples treated at 0.21 and 0.23 J cm^{-2}, confirming the results from Figure 5a.

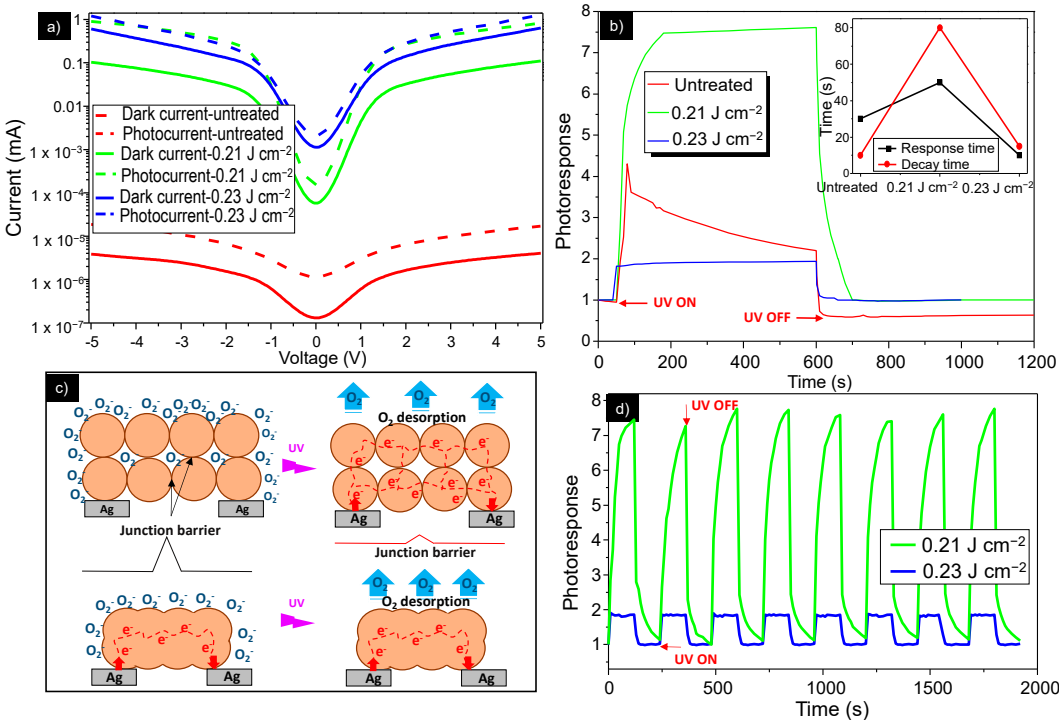

Figure 5. (**a**) I–V curves for uncoated and untreated samples and samples sintered at 0.21, and 0.23 J cm^{-2} with and without UV illumination. (**b**). Dynamic response behavior (response/recovery times) for the untreated and laser treated samples under UV illumination (**c**) Schematic diagram of the NP–NP junctions. (**d**) Time-resolved photoresponse of the ZnO device treated at 0.21 and 0.23 J cm^{-2} under a continuous UV light rectangle pulse.

However, the untreated device showed poor stability, with photoresponse decreasing gradually after the light source was switched on, while the laser treated samples showed good stability with constant photocurrent values under UV illumination, and a return to the initial value after switching off the light source. This can be attributed to some residual organic additives in the untreated screen-printed film, resulting in a poor conducting path for the electron transfer between nanoparticles, thus generating unstable conductivity. During the sintering process, the organic additives were removed from the film, creating better ZnO nanoparticle interconnection and thus the conducting path for electron transfer.

The device sintered at 0.21 J cm^{-2} shows better photosensitivity than the film sintered at 0.23 J cm^{-2}, which is due to its more efficient structure and morphology. The processes of generating and transporting carriers in the laser sintered devices are illustrated in the schematic diagram shown in Figure 5c. The photodetection property of the ZnO NPs-based screen-printed film is strongly influenced by two mechanisms: the adsorption and desorption of oxygen in the air. In the absence of photons, oxygen molecules adsorb on the surface of the ZnO nanoparticles as negatively charged ions, by capturing free electrons from the n-type ZnO. This process creates a low-conductivity depletion layer near the surface of the NPs. When the film was irradiated with UV light, electron-hole pairs were created in the depletion region and the negatively charged surface species traps the holes and releases the electrons into the conduction band of ZnO, so the current gradually increases until saturation. The conduction channels in the ZnO NPs detectors also include NP–NP junctions. Electrons must get over the junction barrier to pass from one NP to another. These barriers formed by the surface depletion layers can govern the charge transport within the film under UV illumination.

When treated at 0.23 J cm^{-2}, the film becomes more compact and bulkier, with bigger grains, lower porosity and thickness reducing surface-to-volume ratio of the film structure compared with the structure of the film treated at 0.21 J cm^{-2}. This facilitates the penetration of oxygen species into the inner film layers, ensuring the participation of the nanoparticles

from whole film in the UV sensing mechanism. Therefore, under illumination, the film treated with 0.23 J cm^{-2} fluence provides less active surface area and lower rate of oxygen desorption, resulting in a lower photocurrent. Additionally, the structure of the NP–NP junction is beneficial for the electrons to flow through the nanoparticle networks under UV light illumination, giving rise to the increase in photocurrent.

The inset in Figure 5b shows decay and rise time of the untreated and laser treated devices, defined respectively as the time required for photocurrent to drop from 90% to 10% and rise from 10% to 90% of its maximum value. The sample treated at 0.23 J cm^{-2} had a shorter response time than the sample treated at 0.21 J cm^{-2}, with decay and rise time of 10 s, which is comparable with other paper-based UV-detectors [8,41].

Furthermore, in order to examine the repeatability of the screen-printed paper-based ZnO UV detectors, the time-resolved photoresponse at 5 V bias with multiple UV on/off cycles was measured, in which both the turn-on and turn-off times of the UV light equaled 2 min. The Figure 5d shows height cycles of photocurrent switching, demonstrating very good repeatability and sensitivity of the two laser treated photodetectors.

3.3. Suppressed Response to Humidity by Laser-Post Processing Treatment

The influence of humidity was evaluated by calculating the device's response given by the ratio of the initial electrical resistance (R_0) at zero humidity, used as a baseline, to the electrical resistance when humidity is introduced (R_m), measured between the IDE. The inclusion of an uncoated paper allowed us to assess whether the ZnO screen printed film coating suppresses the water vapor absorption. The results shown in Figure 6a disclose the strong response differences between different samples, clearly indicating the effects of the screen-printed films and laser surface modification. For the uncoated paper, an important rise of the response is observed when humidity increases, with two times increased response with increasing RH from 0 to 10%, and at 3 orders of magnitude higher at moderate humidity levels (60%) than at 0% RH. The untreated ZnO sample shows a lower sensitivity to humidity than the uncoated sample. However, the sensitivity to humidity of the untreated sample was still significant, at 2 orders of magnitude higher at moderate humidity levels (60%) than at 0% RH. It was evident that the samples treated with laser exhibit a negligible response to humidity, revealing a very poor sensitivity to humidity of the laser treated ZnO films. This difference in humidity sensitivity between the untreated and laser treated samples can be directly correlated to their different surface wettability properties. The inset in Figure 6a depicts the relationship of the contact angle and response to humidity in the investigated samples. It was noticed that the samples with hydrophobic surfaces were sensitive to humidity, while humidity did not affect the laser treated samples with hydrophilic surfaces. Indeed, when the sensor film was hydrophilic, the water nucleation barrier was low, yielding high nucleation rate due to the strong attraction forces between the surface and the water molecules. This implies that water vapor is strongly adsorbed onto the sample surface, resulting in high humidity response. When the sensor film was hydrophobic, the energy barrier was high, thus minimizing the water vapor adsorption onto the film surface, which resulted in roughness induced non-wetting properties and no humidity interference.

Figure 6b showed the UV photoresponse of the investigated samples cross-linked with different humidity levels of 0%, 45% and 80%. It was noticed that the photoresponse of the untreated samples were greatly affected by the presence of water molecules, whereas the effect of the humidity on the photoresponse of the laser treated samples can be neglected. Indeed, the photoresponse of the untreated sample decreased with the humidity increase. This was due to the fact that water molecules replaced the previously surface adsorbed ionized oxygen species, and hence released electrons into the conduction band, a process which partially annihilates the depletion layer, leading to a rise in the dark current, as shown in the Figure 6a. Under the UV illumination, the dissociated H_2O molecules on the surface of the ZnO film capture both electrons and holes generated by UV light, leading to a decrease of carrier density and thus lower photoconductivity. At low RH <50%, the effect

of O_2 desorption is more pronounced, so that the photoresponse slightly decreased with the humidity but it was still detectable. At high RH, around 80%, the effect of the dissociated H_2O capturing electrons and holes becomes more significant due to a discrete water layer formed on the ZnO film surface, which generates a humidity-induced degradation of ZnO-based photodetector with a photoresponse almost undetectable. As seen in Figure 6c, in the case of the laser treated samples, the photoresponse does not change with the humidity level, due to the roughness engineered hydrophobic surface that hampers water molecules to be absorbed at the surface of the ZnO film, as previously explained.

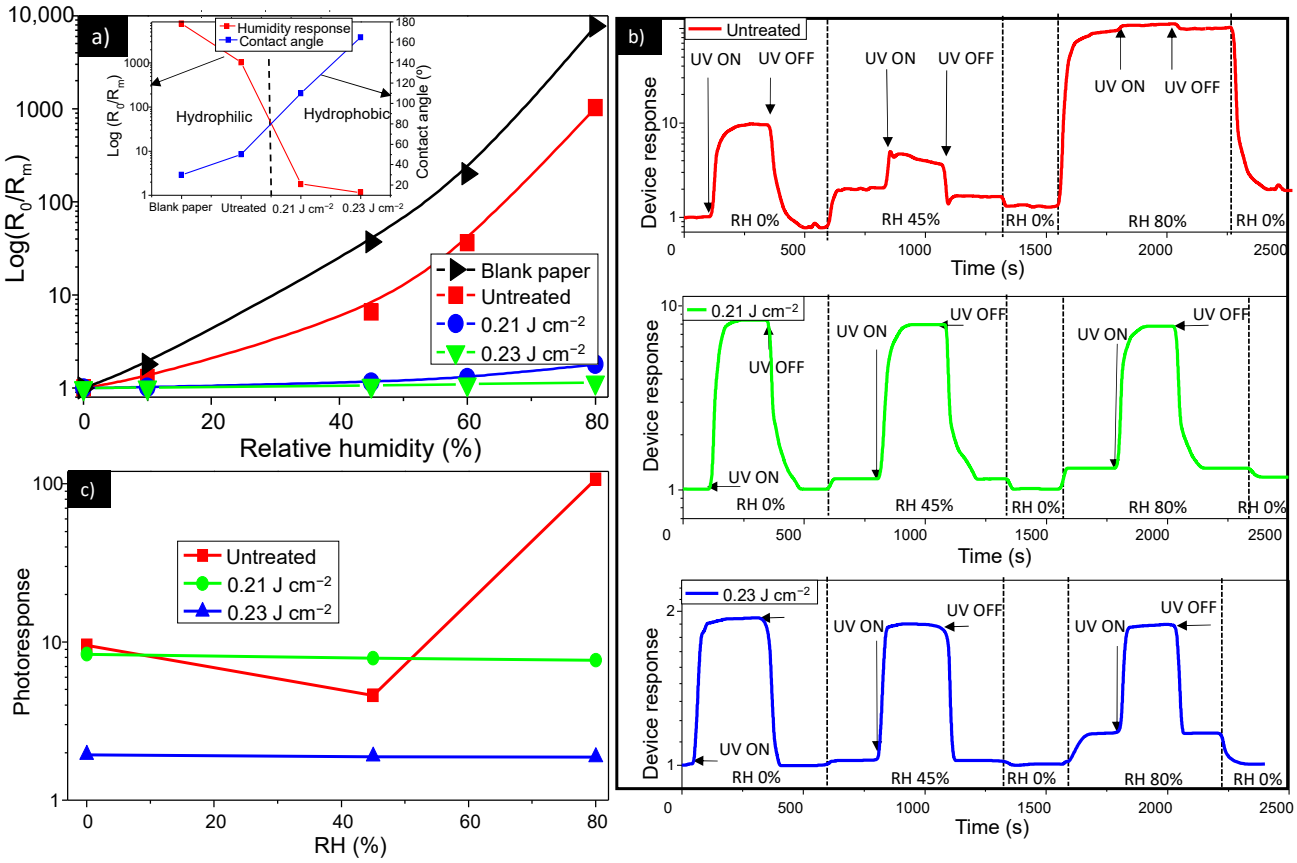

Figure 6. (**a**) Electrical resistance changes for the untreated and laser treated devices as a function of RH (Relative Humidity). Inset: Humidity response at 60% and contact angle as a function of the laser fluence. (**b**) Dynamic response of untreated and treated ZnO sensor to UV light at various humidity levels. (**c**) Photoresponse of the untreated and laser treated samples as a function of RH.

The laser-profiling of the sensitive layer surface roughness provides us with a powerful tool for the management of the film wettability properties, with high impact on tuning of the device sensitivity toward humidity. The undertaken approach can be easily optimized for fabrication of humidity-sensitive ZnO film that can be used for humidity sensors or for fabrication of paper-based ZnO film with no humidity interference that can be used for other electronic devices like UV detectors.

4. Conclusions

In summary, we developed a new strategy to reduce humidity interference on paper-based UV sensor. The proposed approach is fast, cost-effective, scalable, easy-to-operate and paper-friendly, since they do not require annealing steps at high temperatures. The effects of the laser fluence on morphology, electrical properties, UV and humidity sensing properties were disclosed. The ZnO film conductivity and UV photoresponse were improved and the influence of the humidity was considerably reduced by properly adjusting

the laser fluence. It was found that this phenomenon is correlated to the change of the morphology and structure of the ZnO film generated by the laser irradiation. Additionally, the resulting UV sensors showed good repeatability and relatively short response time. Therefore, the possibility of fabricating paper-based sensing devices with no humidity impact in a rapid and large-scale manner paves the way to low-cost solutions of sophisticated paper-based electronics with low environmental footprint.

Supplementary Materials: The following are available online at https://www.mdpi.com/2079-4991/11/1/80/s1, Figure S1: Process sequence of the humidity sensors, Figure S2: Thickness profile of the ZnO films, Figure S3: EDX profiles of the untreated and treated ZnO films.

Author Contributions: Conceptualization, G.D.; data curation, G.D. and B.V.; formal analysis, G.D., M.R. and B.V.; investigation, G.D.; methodology, G.D. and M.R.; resources, M.R. and B.V.; supervision, G.D.; validation, G.D. and M.R.; visualization, G.D., M.R. and B.V.; writing—original draft preparation, G.D.; writing—review and editing, M.R. and B.V. All authors have read and agreed to the published version of the manuscript.

Funding: This work was supported by the Serbian Ministry of Education, Science and Technological Development [Grant numbers No. 451-03-68/2020-14/200358], the ANTARES project that has received funding from the European Union's Horizon 2020 research and innovation program [Grant numbers No. 739570] and the Institute of Physics Belgrade, through the grant of the Ministry of Education, Science, and Technological Development of the Republic of Serbia.

Data Availability Statement: The data presented in this study are available on request from the corresponding author.

Conflicts of Interest: The authors declare no conflict of interest.

References

1. Ha, D.; Fang, Z.; Zhitenev, N.B. Paper in Electronic and Optoelectronic Devices. *Adv. Electron. Mater.* **2018**, *4*, 1700593. [CrossRef]
2. Bordbar, M.M.; Tashkhourian, J.; Hemmateenejad, B. Structural Elucidation and Ultrasensitive Analyses of Volatile Organic Compounds by Paper-Based Nano-Optoelectronic Noses. *ACS Sens.* **2019**, *4*, 1442–1451. [CrossRef] [PubMed]
3. Ratajczak, K.; Stobiecka, M. High-performance modified cellulose paper-based biosensors for medical diagnostics and early cancer screening: A concise review. *Carbohydr. Polym.* **2020**, *229*, 115463. [CrossRef] [PubMed]
4. Samir Kamel, S.; Khattab, T.A. Recent Advances in Cellulose-Based Biosensors for Medical Diagnosis. *Biosensors* **2020**, *10*, 67. [CrossRef] [PubMed]
5. Pradela-Filho, L.A.; Noviana, E.; Araújo, D.A.G.; Takeuchi, R.M.; Santos, A.L.; Henry, C.S. Rapid Analysis in Continuous-Flow Electrochemical Paper-Based Analytical Devices. *ACS Sens.* **2020**, *5*, 274–281. [CrossRef]
6. Ummartyotin, S.; Manuspiya, H. A critical review on cellulose: From fundamental to an approach on sensor technology. *Renew. Sustain. Energy Rev.* **2015**, *41*, 402–412. [CrossRef]
7. Vicente, A.T.; Araújo, A.; Mendes, M.J.; Nunes, D.; Oliveira, M.J.; Sanchez-Sobrado, O.; Ferreira, M.P.; Águas, H.; Fortunato, E.; Martins, R.J. Multifunctional cellulose-paper for light harvesting and smart sensing applications. *Mater. Chem. C* **2018**, *6*, 3143–3181. [CrossRef]
8. Sahoo, K.; Mohanty, B.; Biswas, A.; Nayak, J. Role of hexamethylenetetramine in ZnO-cellulose nanocomposite enabled UV and humidity sensor. *Mater. Sci. Semicond. Process.* **2020**, *105*, 104699. [CrossRef]
9. Zhang, G.; Liao, Q.; Ma, M.; Gao, F.; Zhang, Z.; Kang, Z.; Zhang, Y. Uniformly assembled vanadium doped ZnO microflowers/bacterial cellulose hybrid paper for flexible piezoelectric nanogenerators and self-powered sensors. *Nano Energy* **2018**, *52*, 501–509. [CrossRef]
10. Chen, L.; Cui, J.; Sheng, X.; Xie, T.; Xu, T.; Feng, X. High-performance photoelectronic sensor using mesostructured ZnO nanowires. *ACS Sens.* **2017**, *2*, 1567–1572. [CrossRef]
11. Martinez, A.G.; Santana, G.; Güell, F.; Martínez-Alanis, P.R.; Dutt, A. Photoluminescence of ZnO Nanowires: A Review. *Nanomaterials* **2020**, *10*, 857. [CrossRef] [PubMed]
12. Lee, M.E.; Armani, A.M. Flexible UV exposure sensor based on UV responsive polymer. *ACS Sens.* **2016**, *1*, 1251–1255. [CrossRef]
13. Carvalho, J.T.; Dubceac, V.; Grey, P.; Cunha, I.; Fortunato, E.; Martins, R.; Clausner, A.; Zschech, E.; Pereira, L. Fully Printed Zinc Oxide Electrolyte-Gated Transistors on Paper. *Nanomaterials* **2019**, *9*, 169. [CrossRef] [PubMed]
14. Liao, Q.; Zhang, Z.; Zhang, X.; Mohr, M.; Zhang, Y.; Fecht, H.J. Flexible piezoelectric nanogenerators based on a fiber/ZnO nanowires/paper hybrid structure for energy harvesting. *Nano Res.* **2014**, *7*, 917. [CrossRef]
15. Gullapalli, H.; Vemuru, V.S.M.; Kumar, A.; Botello-Mendez, A.; Vajtai, R.; Terrones, M.; Nagarajaiah, S.; Ajayan, P.M. Flexible piezoelectric ZnO–paper nanocomposite strain sensor. *Small* **2010**, *6*, 1641. [CrossRef]
16. Pimentel, A.; Samouco, A.; Nunes, D.; Araújo, A.; Martins, R.; Fortunato, E. Ultra-Fast Microwave Synthesis of ZnO Nanorods on Cellulose Substrates for UV Sensor Applications. *Materials* **2017**, *10*, 1308. [CrossRef]

17. Hsu, C.L.; Li, H.H.; Hsueh, T.J. Water-and humidity-enhanced UV detector by using p-type La-doped ZnO nanowires on flexible polyimide substrate. *ACS Appl. Mater. Interfaces* **2013**, *5*, 11142–11151. [CrossRef]
18. Li, Y.B.; Valle, F.D.; Simonnet, M.; Yamada, I.; Delaunay, J. Competitive surface effects of oxygen and water on UV photoresponse of ZnO nanowires. *J. Appl. Phys. Lett.* **2009**, *94*, 023110. [CrossRef]
19. Qiu, X.; Tang, R.; Zhu, J.; Oiler, J.; Yu, C.; Wang, Z.; Yu, H. The effects of temperature, relative humidity and reducing gases on the ultraviolet response of ZnO based film bulk acoustic-wave resonator. *Sens. Actuators B* **2011**, *151*, 360–364. [CrossRef]
20. Liu, Y.-J.; Zhang, H.-D.; Zhang, J.; Li, S.; Zhang, J.-C.; Zhu, J.-W.; Gong, M.-G.; Wang, X.-X.; Long, Y.-Z. Effects of Ce doping and humidity on UV sensing properties of electrospun ZnO nanofibers. *J. Appl. Phys.* **2017**, *122*, 105102. [CrossRef]
21. Lai, C.; Wang, X.X.; Zhao, Y.; Fong, H.; Zhu, Z.T. Effects of humidity on the ultraviolet nanosensors of aligned electrospun ZnO nanofibers. *RSC Adv.* **2013**, *3*, 6640–6645. [CrossRef]
22. Nobbs, J. The effect of water vapour on the photoconductivity of zinc oxide. *J. Phys. Chem. Solids* **1968**, *29*, 439–450. [CrossRef]
23. Gao, L.; Chao, L.; Hou, M.; Liang, J.; Chen, Y.; Yu, H.-D.; Huang, W. Flexible, transparent nanocellulose paper-based perovskite solar cells. *NPJ Flex. Electron.* **2019**, *3*, 4. [CrossRef]
24. Mates, J.E.; Schutzius, T.M.; Bayer, I.S.; Qin, J.; Waldroup, D.E.; Megaridis, C.M. Water-Based Superhydrophobic Coatings for Nonwoven and Cellulosic Substrates. *Ind. Eng. Chem. Res.* **2014**, *53*, 222–227. [CrossRef]
25. Bollstrom, R.; Pettersson, F.; Dolietis, P.; Preston, J.; Oster-backa, R.; Toivakka, M. Impact of humidity on functionality of on-paper printed electronics. *Nanotechnology* **2014**, *25*, 094003. [CrossRef]
26. Ren, F.; Guo, H.; Guo, Z.; Jin, Y.; Duan, H.; Ren, P.; Yan, D. Highly Bendable and Durable Waterproof Paper for Ultra-High Electromagnetic Interference Shielding. *Polymers* **2019**, *11*, 1486. [CrossRef]
27. Ogihara, H.; Xie, J.; Okagaki, J.; Saji, T. Simple Method for Preparing Superhydrophobic Paper: Spray-Deposited Hydrophobic Silica Nanoparticle Coatings Exhibit High Water-Repellency and Transparency. *Langmuir* **2012**, *28*, 4605–4608. [CrossRef]
28. De Medeiros, M.S.; Chanci, D.; Martinez, R.V. Moisture-insensitive, self-powered paper-based flexible electronics. *Nano Energy* **2020**, *78*, 105301. [CrossRef]
29. Baidya, A.; Ganayee, M.A.; Jakka Ravindran, S.; Tam, K.C.; Das, S.K.; Ras, R.H.A.; Pradeep, T. Organic Solvent-Free Fabrication of Durable and Multifunctional Superhydrophobic Paper from Waterborne Fluorinated Cellulose Nanofiber Building Blocks. *ACS Nano* **2017**, *11*, 11091–11099. [CrossRef]
30. Yao, Y.; Duan, X.; Niu, M.; Luo, J.; Wang, R.; Liu, T. One-Step Process for Direct Laser Writing Carbonization of $NH_4H_2PO_4$ Treated Cellulose Paper and Its Use for Facile Fabrication of Multifunctional Force Sensors with Corrugated Structures. *Cellulose* **2019**, *26*, 7423–7435. [CrossRef]
31. Khan, M.; Chantal, G. Laser processing for bio-microfluidics applications (part I). *Anal. Bioanal. Chem.* **2006**, *385*, 1351–1361. [CrossRef] [PubMed]
32. Balliu, E.; Andersson, H.; Engholm, M.; Ohlund, T.; Nilsson, H.E.; Olin, H. Selective laser sintering of inkjet-printed silver nanoparticle inks on paper substrates to achieve highly conductive patterns. *Sci. Rep.* **2018**, *8*, 10408. [CrossRef] [PubMed]
33. Hiep, D.H.; Tanaka, Y.; Matsubara, H.; Ishizaka, S. Fabrication of paper-based microfluidic devices using a laser beam scanning technique. *Anal. Sci.* **2020**, *36*, 1275–1278. [CrossRef] [PubMed]
34. Le, S.; Zhou, H.; Nie, J.; Cao, C.; Yang, J.; Pan, H.; Li, J.; Zhang, Y. Fabrication of paper devices via laser-heating-wax-printing for high-tech enzyme-linked immunosorbent assays with low-tech pen-type pH meter readout. *Analyst* **2017**, *142*, 511–516. [CrossRef]
35. Dubourg, G.; Radović, M. Multifunctional Screen-Printed TiO_2 Nanoparticles Tuned by Laser Irradiation for a Flexible and Scalable UV Detector and Room-Temperature Ethanol Sensor. *ACS Appl. Mater. Interfaces* **2019**, *11*, 6257–6266. [CrossRef]
36. Barański, A.; Dutka, D.; Dziembaj, R.; Konieczna-Molenda, A.; Łagan, J.M. Effect of Relative Humidity on the Degradation Rate of Cellulose. Methodology Studies. *Restaurator* **1970**, *25*, 68–74. [CrossRef]
37. Stalder, A.F.; Kulik, G.; Sage, D.; Barbieri, L.; Hoffmann, P. A snake-based approach to accurate determination of both contact points and contact angles. *Colloid Surf. A* **2006**, *286*, 92–103. [CrossRef]
38. Li, S.; Huang, J.; Chen, Z.; Chen, G.; Lai, Y. A review on special wettability textiles: Theoretical models, fabrication technologies and multifunctional applications. *J. Mater. Chem. A* **2017**, *5*, 31. [CrossRef]
39. Cassie, A.B.D.; Baxter, S. Wettability of porous surfaces. *Trans. Faraday Soc.* **1944**, *40*, 546–551. [CrossRef]
40. Tan, S.T.; Chen, B.J.; Suna, X.W.; Fan, W.J. Blueshift of optical band gap in ZnO thin films grown by metal-organic chemical-vapor deposition. *J. Appl. Phys.* **2005**, *98*, 013505. [CrossRef]
41. Fang, F.; Futter, J.; Markwitz, A.; Kennedy, J. UV and humidity sensing properties of ZnO nanorods prepared by the arc discharge method. *Nanotechnology* **2009**, *24*, 245502. [CrossRef] [PubMed]

Processing and Application of Ceramics 14 [2] (2020) 102–112
https://doi.org/10.2298/PAC2002102D

Influence of oxygen vacancy defects and cobalt doping on optical, electronic and photocatalytic properties of ultrafine $SnO_{2-\delta}$ nanocrystals

Zorana D. Dohčević-Mitrović[1,*], Vinicius D. Araújo[2], Marko Radović[3], Sonja Aškrabić[1], Guilherme R. Costa[4], Maria Ines B. Bernardi[4], Dejan M. Djokić[1], Bojan Stojadinović[1], Marko G. Nikolić[5]

[1]*Nanostructured Matter Laboratory, Institute of Physics Belgrade, University of Belgrade, Pregrevica 118, 11080 Belgrade, Serbia*
[2]*NanoA-UACSA, Universidade Federal Rural de Pernambuco, UFRPE, Cabo de Santo Agostinho, PE, Brazil*
[3]*University of Novi Sad, Group for Nano and Microelectronics, Biosense Institute, Novi Sad, Serbia*
[4]*Instituto de Física de São Carlos, Universidade de São Paulo, USP, 13560-970, São Carlos – SP, Brasil*
[5]*Institute of Physics Belgrade, University of Belgrade, P.O. Box 68, Pregrevica 118, 11080 Belgrade, Serbia*

Received 12 November 2019; Received in revised form 21 February 2020; Accepted 15 March 2020

Abstract

Ultrafine pure and cobalt doped $SnO_{2-\delta}$ nanocrystals ($Sn_{1-x}Co_xO_{2-\delta}$, $0 \leq x \leq 0.05$) were synthesized by microwave-assisted hydrothermal method. The as-prepared nanocrystals have single phase tetragonal rutile structure. With increase of Co content ($x > 0.01$), Co entered into SnO_2 lattice in mixed Co^{2+}/Co^{3+} state. Pronounced blue shift of the band gap with cobalt doping originated from the combined effect of quantum confinement and Burnstain-Moss shift. Raman and photoluminescence study revealed oxygen deficient structure of $SnO_{2-\delta}$ for which the prevalent defects are in the form of in-plane oxygen vacancies. Co-doping induced decrease of in-plane oxygen vacancy concentration and luminescence quenching. $SnO_{2-\delta}$ exhibited significantly better photocatalytic activity under UV light irradiation, than Co-doped samples due to better UV light absorption and increased concentration of in-plane oxygen vacancies which, as shallow donors, enable better electron-hole separation and faster charge transport.

Keywords: *SnO_2 nanopowders, wet-chemical synthesis, defects, optical properties, photocatalysis*

I. Introduction

Tin oxide (SnO_2) is an n-type semiconductor with large band gap (3.6 eV) at room temperature. Because of its unique electronic, optical and electrochemical properties, SnO_2 is widely used in dye-sensitized solar cells, transparent conductive electrodes, solid state sensors, lithium-ion batteries and catalysis [1–7]. During the past decade, SnO_2 nanostructures have become one of the most important oxide nanostructures due to their exceptional properties and potential applications which are strongly influenced by size effects and morphology [8].

In the past decade various efforts were devoted to the synthesis of SnO_2 nanostructures with controlled size and morphology. SnO_2 nanostructures like thin films, nanobelts, nanotubes or nanowires, nanodisks and nanocrystals have been prepared using different methods, such as carbothermal reduction process, hydrothermal and solvothermal, chemical vapour condensation, laser ablation, sol-gel and molten salt techniques [9–18]. However, for most of these methods relatively high temperatures are required during the synthesis process and the samples are usually subjected to additional thermal treatment in order to achieve good crystallinity. In recent years hydrothermal approaches appeared to be widely applied as SnO_2 nanostructures can be obtained with different morphologies and tunable size at mild temperatures [8,19]. Microwave-assisted hydrothermal

*Corresponding author: tel: +381 113713024,
e-mail: *zordoh@ipb.ac.rs*

synthesis (MAH) became a very promising method for obtaining size and morphology controllable oxide nanostructures due to the unique advantages, such as fast heating rate and uniform heating without superheating of the solvent, which results in small particle size, narrow size distribution and high purity of the obtained nanopowders. Therefore, MAH appeared to be very convenient method for obtaining ultrafine SnO_2 nanopowders [19,20].

SnO_2 nanostructures are generally less studied as potential photocatalysts compared to TiO_2 and ZnO, despite its crystalline structure being similar to TiO_2 and good properties such as high photochemical stability, non-toxic nature, strong oxidizing power, and low-cost [21]. In order to improve the photocatalytic efficiency of SnO2, selective doping with metal ions, transition metals (gold, manganese, silver and iron) and rare–earth elements (Ce, Sm, Gd) was performed and well presented in the review paper by Al-Hamdi *et al.* [21]. Among the transition metals, cobalt is rarely applied as dopant. In fact, there are only few papers dedicated to potential applicability of Co-doped SnO_2 nanostructures as photocatalysts [22–24], but none of them investigated the synergic influence of defective nature and Co-doping on photocatalytic properties of very fine SnO_2 nanocrystals. It is well known that photocatalytic efficiency of metal oxide nanostructures can be influenced by the presence of intrinsic defects such as oxygen vacancies [25–28]. The presence of oxygen vacancies strongly influences the charge recombination process and the band gap structure. Namely, oxygen vacancies introduce the defect levels (near conduction or valence band) inside the gap and behave as trapping centres for photogenerated carriers preventing the fast recombination. Besides, oxygen vacancies can facilitate the transferring of charge carriers to adsorbed species (OH^- or water molecules and dissolved oxygen present on the surface of the catalyst) and enhance the formation of reactive radicals which are responsible for improved photocatalytic activity of oxide nanostructures [26,27]. Moreover, the formation of defect states inside the gap reduces the band gap and extends the absorption to visible light [25,27]. The prominent intrinsic defects in SnO_2 nanostructures are oxygen vacancies as well, which form donor/acceptor states inside the SnO_2 gap, influencing its electronic structure and making it conductive [4]. As oxygen vacancies play a critical role in many new physical phenomena, it is important to investigate associated changes in the optical and electronic properties of pure and Co-doped SnO_2 nanomaterials which can have a strong impact on photocatalytic activity of these materials.

In the work presented here, ultrafine, nonstoichiometric pristine and Co-doped $SnO_{2-\delta}$ nanopowders were synthesized via simple and cost effective microwave-assisted hydrothermal method. This paper intends to explore how defective structure and Co-doping provoke changes of optical and electronic properties of $SnO_{2-\delta}$ nanocrystals influencing the photocatalytic performances.

II. Experimental procedure

2.1. Materials preparation

$Sn_{1-x}Co_xO_{2-\delta}$ (where x = 0, 1, 3 and 5 mol%) nanopowders were synthesized by microwave-assisted hydrothermal method using $SnCl_4 \cdot 5\,H_2O$ (98%, Aldrich), $CoCl_2 \cdot 6\,H_2O$, NaOH and HCl as starting precursors. Initially, 1 ml of hydrochloric acid was added to 10 ml of distilled water at 50 °C resulting in a solution with pH between 0 and 1. Next, 17.529 g of $SnCl_4 \cdot 5\,H_2O$ was added and the mixed solution was homogenized under stirring with simultaneous increasing of the water amount to approximately 50 ml. In a case of the doped samples, 0.119 g, 0.357 g and 0.595 g of $CoCl_2 \cdot 6\,H_2O$ were added to obtain 1, 3 and 5 mol% Co-doped samples, respectively. NaOH was added dropwise under vigorous stirring until the pH of the solution was adjusted to 8. The mixed solution was placed in a 110 ml sealed Teflon autoclave and subjected to microwave heating, applying 2.45 GHz of microwave radiation at a maximum power of 800 W. The as-prepared solution was heated at 140 °C for 10 min using heating rate of 14 °C/min and then air-cooled to room temperature. The as-prepared undoped and Co-doped $SnO_{2-\delta}$ nanopowders were submitted to dialysis in order to be separated from the solution and then dried at 80 °C for 12 h.

2.2. Materials characterization

The crystalline structure and average crystallite size of the $Sn_{1-x}Co_xO_{2-\delta}$ samples were evaluated using X-ray diffraction (XRD) measurements. The measurements were carried out using an automatic X-ray diffractometer (Rigaku, Rotaflex RU200B) with CuKα radiation (50 kV, 100 mA, λ = 1.5405 Å) in a θ–2θ configuration using a graphite monochromator. The 2θ scanning range was between 20 and 70°, with a step size of 0.02°. Microstructural analysis was made by transmission electron microscopy (TEM) FEI Titan 60-300 operating at voltages between 60 and 300 kV, using a field emission gun (FEG) with an objective lens (Super Twin) and a corrector that allows resolution of 0.08 nm.

Micro-Raman scattering measurements were performed at room temperature in the backscattering configuration on Tri Vista 557 Raman system equipped with a nitrogen-cooled CCD detector, using 532 nm laser line of optically pumped semiconductor laser (Coherent Verdi G) as an excitation source. UV-visible diffuse reflectance spectra were acquired with a Cary 5G spectrophotometer in the 200–800 nm range. Diffuse reflectance spectra were transformed into the absorbance spectra by the Kubelka-Munk method. The ellipsometric measurements were performed using high resolution variable angle spectroscopic ellipsometer (SOPRA GES5E-IRSE) of the rotating polarizer type. The data

were collected at room temperature in the UV-Vis spectral range with a resolution of 0.02 eV, for the incidence angle of 70°. Photoluminescence emission measurements were performed at room temperature using Spex Fluorolog spectrofluorometer with C31034 cooled photomultiplier under Xenon lamp excitation at 380 nm.

2.3. Photocatalytic experiments

The photocatalytic activity of the $Sn_{1-x}Co_xO_{2-\delta}$ samples, for the degradation of methylene blue (MB) as model pollutant, was tested under UV illumination. The different samples with the same photocatalyst amount (150 mg/l) were immersed in 20 ml of an aqueous solution of methylene blue (5.0 mg/l). The beakers were placed in a photo-reactor at controlled temperature (15 °C), under magnetic stirring, and were illuminated by six 15 W UV lamps (TUV Philips, maximum intensity at 254 nm). The solution was placed in the dark for 60 min to reach the adsorption/desorption equilibrium before UV light exposure. Blank experiment without UV irradiation demonstrated no adsorption of MB dye on the surface of the $Sn_{1-x}Co_xO_{2-\delta}$ samples. The photocatalytic experiments were conducted at the natural pH = 6 of MB dye. At regular time intervals 2 ml aliquots were taken, centrifuged to remove any catalyst particles and the concentration of the dye was determined by UV-Vis absorption spectrophotometer (Shimadzu-UV-1601 PC) monitoring the variation of absorbance at 663 nm.

The formation of hydroxyl radicals ($OH^{\bullet}$) on the surface of the $SnO_{2-\delta}$ sample under the UV light illumination was examined by photoluminescence (PL) technique using terephthalic acid (TA) as a probe molecule. The detailed experimental procedure was described in reference [29]. TA is known to react with $OH^{\bullet}$ radicals induced on the photocatalyst's surface where it produces highly fluorescent 2-hydroxyterephthalic acid which shows an intense PL peak at around 425 nm. The intensity of this peak is proportional to the amount of $OH^{\bullet}$ radicals [30,31] produced in the photocatalytic process. The changes of the 425 nm PL peak intensity were measured at room temperature using 315 nm excitation.

III. Results and discussion

3.1. Crystal structure and morphology

Figure 1a shows XRD patterns of the $Sn_{1-x}Co_xO_{2-\delta}$ ($0 \le x \le 0.05$) nanopowders, whereas the Rietveld refined XRD spectra of the $SnO_{2-\delta}$ and $Sn_{0.95}Co_{0.05}O_{2-\delta}$ samples are presented in Figs. 1b and 1c. The XRD patterns of all the samples revealed single phase tetragonal structure (cassiterite phase). The XRD peaks at 26.6, 33.8, 51.9 and 65.8° can be assigned to (110), (101), (211) and (301) planes, which are in good agreement with literature data (ICDS № 9163). No secondary phases like Co oxides, Co clusters or other tin oxide phases were observed. Moreover, broad diffraction peaks of low intensities compared to those of bulk SnO_2, point to low crystallinity and small crystallite size of the SnO_2 nanoparticles.

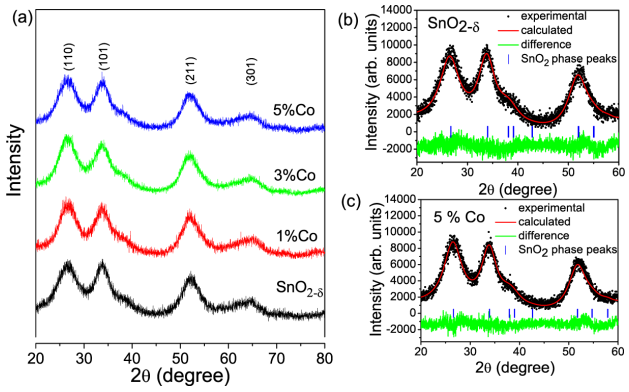

Figure 1. XRD patterns of $Sn_{1-x}Co_xO_{2-\delta}$ nanocrystals ($0 \le x \le 0.05$) indexed to tetragonal rutile structure of SnO_2 (a), Rietveld refined XRD spectra of $SnO_{2-\delta}$ (b) and $Sn_{0.95}Co_{0.05}O_{2-\delta}$ (c) nanoparticles

The average lattice parameters and unit cell volume obtained from the Rietveld refinement data are given in Table 1. These results showed an expansion of the SnO_2 unit cell with increasing cobalt content up to 5%. This variation originates from the substitution of smaller Sn^{4+} cations (0.83 Å) with larger Co^{2+} cations in high spin state (0.89 Å) [32]. The slight shrinkage of the unit cell observed for the 5% Co-doped sample can be related to the presence of increased amount of smaller Co^{3+} cations (*ls*: 0.68 Å or *hs*: 0.75 Å). The average crystallite size (D) of the $Sn_{1-x}Co_xO_{2-\delta}$ nanocrystals was calculated with the Scherrer formula using the 110 reflection and their values are reported in Table 1. Obviously, the mean crystallite sizes of the undoped and Co-doped samples are less than Bohr exciton radius (2.7 nm for SnO_2) [33] and with increased Co-doping the crystallite size of the $Sn_{1-x}Co_xO_{2-\delta}$ nanocrystals decreases. Such a trend implies that Co-doping has an inhibiting effect on the crystal growth. This inhibiting effect of Co on the crystal grains growth was already confirmed in the work of Babu *et al.* [34].

TEM images of the undoped and Co-doped $SnO_{2-\delta}$ samples are presented in Fig. 2. TEM images revealed

Table 1. Lattice parameters (a, c), unit cell volume (V) and average crystallite size (D) of the $Sn_{1-x}Co_xO_{2-\delta}$ nanocrystals

Sample	$a = b$ [Å]	c [Å]	V [Å^3]	D [nm]
$SnO_{2-\delta}$	4.722 ± 0.002	3.180 ± 0.003	70.905	2.5
$Sn_{0.99}Co_{0.01}O_{2-\delta}$	4.747 ± 0.002	3.201 ± 0.003	72.131	2.4
$Sn_{0.97}Co_{0.03}O_{2-\delta}$	4.759 ± 0.002	3.206 ± 0.002	72.609	2.3
$Sn_{0.95}Co_{0.05}O_{2-\delta}$	4.744 ± 0.002	3.186 ± 0.002	71.703	2.2

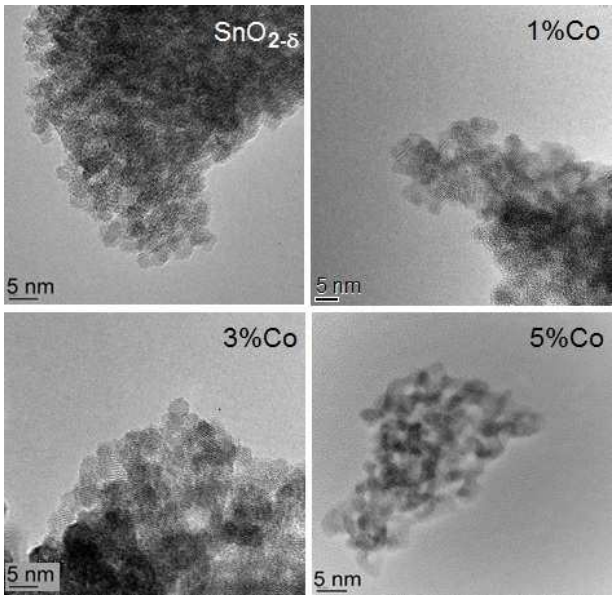

Figure 2. TEM images of $Sn_{1-x}Co_xO_{2-\delta}$ ($0 \le x \le 0.05$) nanoparticles

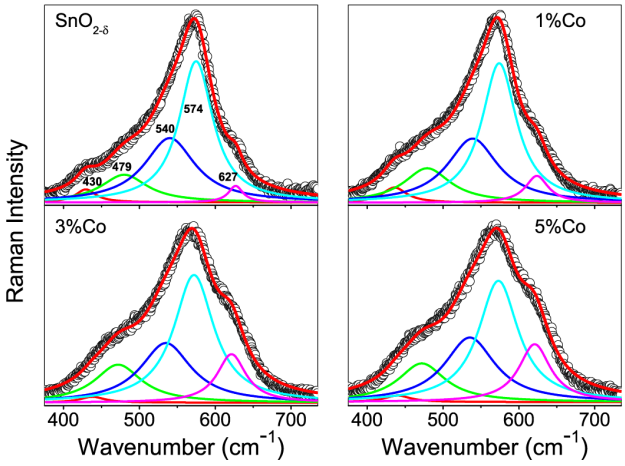

Figure 3. Deconvoluted room-temperature Raman spectra of $Sn_{1-x}Co_xO_{2-\delta}$ nanoparticles

that the undoped $SnO_{2-\delta}$ sample is composed of single crystalline nanoparticles of very small size and quasi-spherical shape. The morphology of the $Sn_{1-x}Co_xO_{2-\delta}$ nanoparticles remained the same with Co-doping. The particles are of spherical shape with the size less than 3 nm, which is in good agreement with the results obtained from XRD data. The observed agglomeration of the $Sn_{1-x}Co_xO_{2-\delta}$ nanoparticles can be ascribed to small crystallite sizes.

3.2. Raman analysis

SnO_2 tetragonal rutile crystalline structure (space group $P4_2/mnm$) has four active Raman modes (non-degenerate A_{1g}, B_{1g}, B_{2g} modes, and a doubly degenerated E_g mode), two active infrared modes (A_{2u} and E_u) and two silent modes (A_{2g}, B_{1u}) [35]. The positions of A_{1g}, B_{1g}, B_{2g} and E_g Raman modes in SnO_2 single crystal under ambient conditions are 634, 123, 776 and 475 cm^{-1}, respectively, and the A_{1g} and E_g modes are of much higher intensity compared to B_{1g} and B_{2g} modes [35].

The Raman spectra of nanocrystalline, non-stoichiometric $SnO_{2-\delta}$ are modified in comparison with single-crystal or polycrystalline SnO_2, because Raman spectroscopy is more sensitive to intrinsic defects and confinement effect than conventional XRD technique. Namely, the position, bandwidth and intensity of Raman modes are size dependent, i.e. Raman modes are broadened, of lower intensity and shifted towards lower or higher energies depending on phonon dispersion curves. Besides, new modes of defect origin can appear [36,37]. The room temperature Raman spectra of the $Sn_{1-x}Co_xO_{2-\delta}$ nanocrystals are presented in Fig. 3 and they are deconvoluted using Lorentzian profiles (full lines in Fig. 3).

In the Raman spectrum of the pure $SnO_{2-\delta}$, the most prominent mode is located at ~574 cm^{-1}. This mode is characteristic for non-stoichiometric $SnO_{2-\delta}$ and it is not present in the Raman spectra of SnO_2 single-crystal [35]. Density functional calculations performed by Liu *et al.* [38] have shown that this mode arises from in-plane oxygen vacancies (V_{Oin}) in the surface region of $SnO_{2-\delta}$ nanoparticles, intensity of which is proportional to their concentration. In very fine nanoparticles this mode has the highest intensity due to the increased concentration of oxygen vacancies. Raman mode at ~627 cm^{-1} can be ascribed to the A_{1g} mode of rutile SnO_2 structure. This mode is of lower intensity, broadened and shifted to lower wave numbers compared to the bulk counterpart, due to the phonon confinement effect [37]. As the crystallite size of the undoped $SnO_{2-\delta}$ is smaller than the Bohr exciton radius, the size effect can be very pronounced in this sample. Another broad Raman mode at ~479 cm^{-1} is assigned to E_g mode and it is shifted to higher wavenumbers with size decrease of $SnO_{2-\delta}$ nanocrystals [37]. Besides these modes, additional modes at around 430 and 540 cm^{-1} appear. These new modes are usually seen in very fine SnO_2 nanoparticles [37–39], nanotubes [40] or nanoribbons [41] because of the increased degree of local disorder, i.e. loss in long-range order due to the large number of lattice vacant positions, especially at the surface of nanoparticles. These modes are of high intensity in small nanoparticles and disappear with particle size increase. According to some literature data, due to the relaxation of the selection rules in nanostructured SnO_2, the mode at 540 cm^{-1} is assigned to the Raman forbidden mode (B_{1u}) [40,41], whereas the new mode at around 430 cm^{-1} can be assigned to the oxygen vacancy clusters (V_C) [39]. The A_{1g} and E_g modes exhibited redshift and broadening with Co-doping. The redshift and broadening of these modes are expected with substitution of Sn^{4+} ions with larger Co^{2+} ions and decreased crystallite size due to the phonon confinement effect. The positions and intensities of the A_{1g}, E_g and oxygen vacancy related modes (V_{Oin} and V_C) are presented in Fig. 4. As it can be seen from Fig. 4, the intensity of A_{1g} mode increases with increased Co concentration, whereas the intensity of E_g

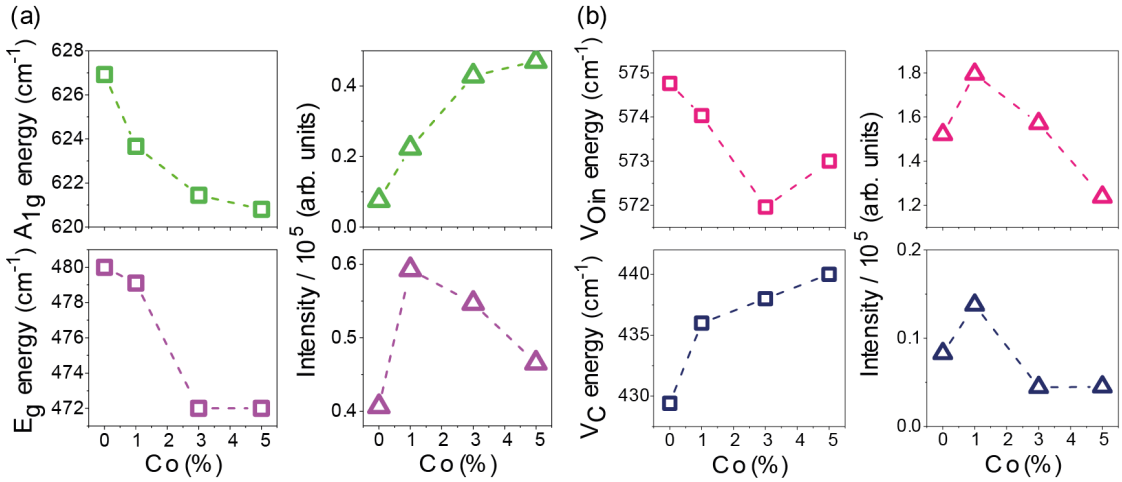

Figure 4. Positions and intensities of A_{1g} and E_g (a) and vacancy (V_{Oin} and V_C) (b) Raman modes

mode is higher in the Co-doped samples compared to the undoped $SnO_{2-\delta}$. The E_g mode intensity slightly decreased in samples doped with higher Co content, as a consequence of lattice distortion and reduction in lattice space symmetry. The position of the Raman mode ascribed to in-plane oxygen vacancies (574 cm^{-1}) did not change significantly, whereas the Raman mode related to vacancy clusters (430 cm^{-1}) shifts to higher energies with Co-doping. The intensity of both modes decreased in the $Sn_{0.97}Co_{0.03}O_{2-\delta}$ sample and this trend is more evident for the $Sn_{0.95}Co_{0.05}O_{2-\delta}$ sample. The intensity reduction of oxygen vacancy related modes in these samples implies that the concentration of oxygen vacancies decreased. The decrease of the oxygen vacancy concentration is expected if the part of Co cations were in Co^{3+} state or if some Co cations were interstitially incorporated in $SnO_{2-\delta}$ lattice [33,42].

In order to see if Co cations substituted Sn^{4+} in Co^{2+} state or the part of them was in Co^{3+} state, UV-Vis absorption measurements were performed and the absorption spectra of the $Sn_{1-x}Co_xO_{2-\delta}$ samples are presented in Fig. 5. In the UV range, the absorption spectrum of $SnO_{2-\delta}$ displays a strong absorption due to

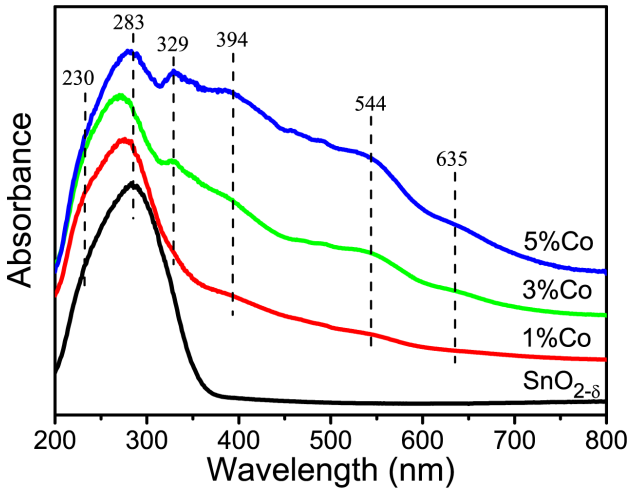

Figure 5. UV-Vis spectra of $Sn_{1-x}Co_xO_{2-\delta}$ nanoparticles

the SnO_2 interband transition. Two peaks at 230 and 283 nm are superimposed giving the broad band which might correspond to the surface Sn^{4+} species and to the $Sn^{4+} \rightarrow Sn^{2+}$ intervalence charge transfer, respectively [43]. In Co-doped samples the broad band is shifted to lower wavelength implying the band gap increase with Co-doping. In the absorption spectra of the $Sn_{0.97}Co_{0.03}O_{2-\delta}$ and $Sn_{0.95}Co_{0.05}O_{2-\delta}$ samples, new bands appear. The band around 329 nm can be assigned to the partial change of oxidation state of Co^{2+} to Co^{3+} [44], whereas the broad band around 400 nm can be ascribed to $^1A_{1g} \xrightarrow{\nu_2} {}^1T_{2g}$ transition of low spin Co^{3+} ions in octahedral environment [45]. The intensity of these bands increased in the $Sn_{0.95}Co_{0.05}O_{2-\delta}$ sample pointing to the increased concentration of Co^{3+} ions. The bands around 544 and 635 nm can be related to $^4A_2(F) \xrightarrow{\nu_2} {}^4T_1(P)$ transition of tetrahedral Co^{2+} species [45]. Therefore, from the absorption spectra of the $Sn_{0.97}Co_{0.03}O_{2-\delta}$ and $Sn_{0.95}Co_{0.05}O_{2-\delta}$ samples it can be deduced that part of Co cations entered into SnO_2 lattice in Co^{3+} state, concentration of which increased with the increased dopant content. This result supports the finding obtained from the refined XRD spectrum of the $Sn_{0.95}Co_{0.05}O_{2-\delta}$ sample, since the shrinkage of the unit cell was ascribed to the increased amount of Co^{3+} cations.

Our conclusions derived from absorption measurements are well-supported by recently published work of Roy *et al.* [46] concerning Co-doped SnO_2 nanocrystals. From the XPS study, Roy *et al.* [46] confirmed the mixed valence nature of Co ions in the host lattice and they have found that the relative concentration of Co^{3+} exceeds that of Co^{2+} with the increase of dopant content. This study also showed that Co incorporation into SnO_2 leads to the reduction of oxygen vacancies which is consistent with our Raman study.

3.3. Optical and electronic properties

The investigation of complex dielectric function by spectroscopic ellipsometry offers an insight into the

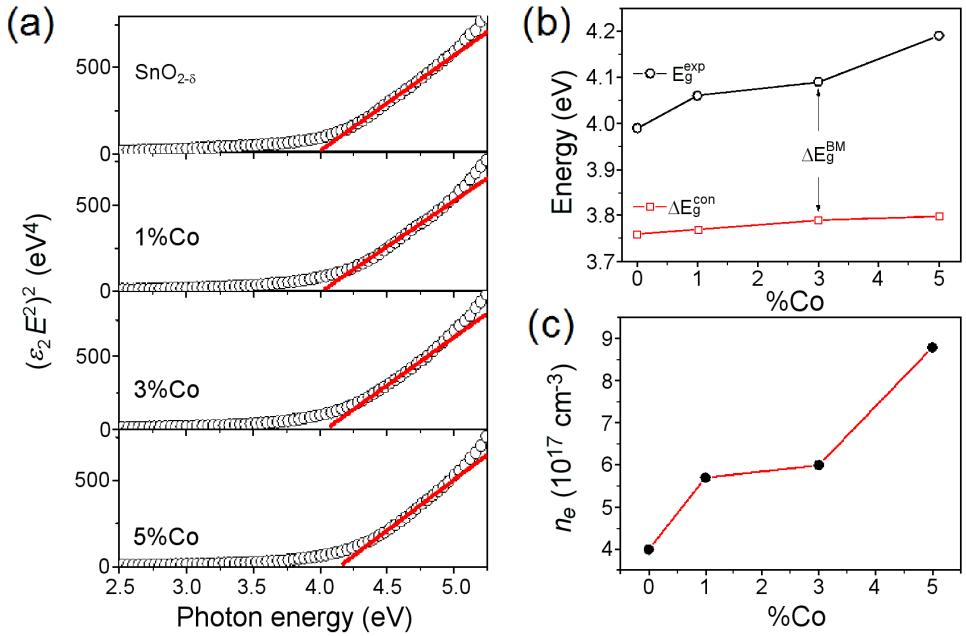

Figure 6. Determination of the direct band gap for $Sn_{1-x}Co_xO_{2-\delta}$ nanoparticles using Tauc law(a); variation of the band gap energy obtained from ellipsometric measurements (E_g^{exp}) and from quantum confinement model (ΔE_g^{con}) (b) and concentration of charge carriers n_e for $Sn_{1-x}Co_xO_{2-\delta}$ samples (c)

most important optical properties of the nanomaterials, such as, optical band gap, interband and intraband transitions, defect electronic states. The imaginary part of dielectric function is directly related to the electronic density of states and in a case of nanopowders it can be deduced from the ellipsometric measurements by applying two-phase model approximation (in our case: $SnO_{2-\delta}$ nanocrystals/air). In order to investigate the optical band gap behaviour and the influence of Co dopant on the absorption edge in $SnO_{2-\delta}$ nanocrystals we applied the Tauc model for direct band gap transition [47], knowing that SnO_2 is a direct band gap material [48]. In this case general expression for $\varepsilon_2(E)$ is:

$$(\varepsilon_2 \cdot E^2)^2 = a(E - E_g) \tag{1}$$

where E is the photon energy, E_g is the band gap and a is the constant related to the density of states for the conduction band. The Tauc plots of the $Sn_{1-x}Co_xO_{2-\delta}$ samples obtained from ellipsometric measurements are presented in Fig. 6a. Linear extrapolation to zero absorption (straight lines in Fig. 6a) gives the band gap energy values of the $Sn_{1-x}Co_xO_{2-\delta}$ samples.

In Fig. 6b, the dependence of the band gap energy (from Fig. 6a) on dopant content for the $Sn_{1-x}Co_xO_{2-\delta}$ samples is represented with open circles. It is obvious that Co-doping induces an increase of the E_g. Also, it is important to notice that all investigated samples have the band gap values higher than that for bulk SnO_2. Such changes in electronic properties of SnO_2 nanomaterials can be a consequence of the quantum confinement effect. This effect causes an increase of the band gap value due to the stronger localization of electronic states inside the volume of nanocrystals. The band gap energy shift, caused by this effect, can be calculated according to the following relation [49]:

$$\Delta E_g^{con} = E_g + \frac{\hbar^2 \pi^2}{2\mu \cdot D^2} \tag{2}$$

where E_g is the band gap value for the bulk SnO_2 (3.6 eV), D is the crystallite radius and μ is the reduced effective mass of the electron-hole pair. From the XRD results it was obtained that the average crystallite size of the undoped $SnO_{2-\delta}$ nanocrystals is lower than Bohr exciton radius, and that it has a tendency of further decrease with Co-doping. Therefore, it is reasonable to take into account the quantum confinement effect in order to properly analyse the band gap behaviour of the $Sn_{1-x}Co_xO_{2-\delta}$ samples. Taking the D values from Table 1 and knowing that $\mu = 0.38m_0$ [48], the band gap values (ΔE_g^{con}) that arise from the quantum confinement effect were calculated using Eq. 2. The ΔE_g^{con} values are presented in Fig. 6b with open squares. Comparing the ΔE_g^{con} values with E_g^{exp} ones it is obvious that observed band gap increase of the $Sn_{1-x}Co_xO_{2-\delta}$ samples cannot be ascribed only to the quantum confinement effect.

Another effect that can cause a shift of optical absorption edge to higher energies is the Burstein-Moss effect, which becomes more relevant in doped semiconductors (like transparent conducting oxides) with high charge carrier concentration. The Burstein-Moss effect is already registered in doped SnO_2 thin films [50,51]. According to this effect, the widening of the optical gap is caused by metallic doping and increase of carrier density which leads to the filling of empty semiconductor electronic states in the vicinity of Fermi level and its shift to higher energies. Assuming parabolic bands and

spherical Fermi surface the band gap shift due to the Burstein-Moss effect can be calculated by simple relation [4]:

$$\Delta E_g^{BM} = \frac{h^2}{2\mu}\left(3\pi^2 \cdot n_e\right)^{2/3} \quad (3)$$

where h is Planck constant, μ is the reduced effective mass and n_e is the carrier concentration.

Additional charge, i.e. increased charge carrier density in pure and doped $SnO_{2-\delta}$ nanocrystals, can originate from the donor type defects like oxygen vacancies and Co-dopants. Raman spectra have already evidenced defective structure of $SnO_{2-\delta}$, whereas Co^{2+} dopants bring additional charge when substituting Sn^{4+} ions. Hence, the observed increase of the E_g from Fig. 6b can be ascribed to the Burstein-Moss shift (ΔE_g^{BM}). Combining Eqs. 2 and 3 it is possible to estimate the concentration of charge carriers (n_e) in the $Sn_{1-x}Co_xO_{2-\delta}$ samples and the obtained values are presented in Fig. 6c. These calculated values are in good agreement with literature data for SnO_2 thin films [52]. As can be seen from Fig. 6c, doping of $SnO_{2-\delta}$ nanocrystals with Co ions causes an increase of the charge carriers concentration and shift of the optical absorption edge toward UV region, making the investigated material more conductive and at the same time more transparent.

It is well known that large number of defects, such as oxygen vacancies or vacancy clusters, can be formed at the SnO_2 nanoparticles surface and subsurface [21]. Intrinsic oxygen vacancies can be of three types: in-plane (V_{Oin}), bridging (V_{OB}) and subbridging (V_{OSB}) vacancies [36,38]. These vacancies can be in different charge states, i.e. vacancies which trap one, two or none electrons, so called F^+, F^0 and F^{++} centres, and they can form defect levels inside the $SnO_{2-\delta}$ gap [53]. Among the optical spectroscopy methods, photoluminescence (PL) spectroscopy is convenient method to investigate the defect structure of the pure and Co-doped $SnO_{2-\delta}$ samples.

Room temperature PL spectra of the $SnO_{2-\delta}$, $Sn_{0.99}Co_{0.01}O_{2-\delta}$ and $Sn_{0.95}Co_{0.05}O_{2-\delta}$ samples using a wavelength of 380 nm for excitation are presented in Fig. 7a. The PL spectrum of $SnO_{2-\delta}$ is deconvoluted into four Gaussian peaks centred at 510, 575, 470 and 446 nm (inset of Fig. 7a). In the deconvoluted PL spectrum of the undoped $SnO_{2-\delta}$ two bands dominate: broad intense band centred at around 510 nm and another band of lower intensity at around 575 nm. Since the excitation and emissions are both lower than the band gap of $SnO_{2-\delta}$, neither of these PL bands can be ascribed to the recombination of the Sn $4p$ conduction electrons with a holes from a O $2p$ band. The broad green luminescence around 510 nm is already seen in SnO_2 thin films [10] and nanoparticles [36] and it was attributed to the in-plane oxygen vacancy defects [36]. Therefore, the strong PL peak at 510 nm (2.45 eV) is ascribed to V_{Oin} defects. This finding is in accordance with corresponding Raman spectrum in which the most prominent Raman mode originates from in-plane oxygen vacancies. Another PL band at 575 nm (2.15 eV) can be ascribed to the isolated bridging oxygen vacancy defects, i.e. singly ionized F^+ defects [53]. The PL bands around 470 and 440 nm were seen in SnO_2 nanopowders [54]. These PL bands obtained with similar excitation line as in our case were ascribed to have excitonic origin [54]. It is well known that excitonic bands are formed near the band edge and they are usually of much narrower bandwidth than PL bands which originate from defect structures. As the band gap of the $SnO_{2-\delta}$ sample is around 4 eV, it can be concluded that PL bands at 446 and 470 nm lie deeper in the gap. Hence, it is unlikely that these two bands originate from some excitonic states. Performing density functional calculation for defective $SnO_{2-\delta}$ nanocrystals, Liu *et al.* [38] have shown that PL peaks at 446 and 470 nm originate from the subbridging oxygen vacancies, V_{OSB}. Schematic model for different relaxation processes in the $SnO_{2-\delta}$ nanocrystals is presented in Fig. 7b.

Co-doping induced complete reduction of PL intensity. Even the smallest percent of Co-doping (see Fig. 7a) almost completely quenched the luminescence. By integrating the spectra of the $Sn_{1-x}Co_xO_{2-\delta}$ samples from Fig. 7a, the areas within the boundary of emission were calculated for both undoped and doped samples in order to compare the quantum efficiencies. As the spectra were recorded under the identical excitation/absorption

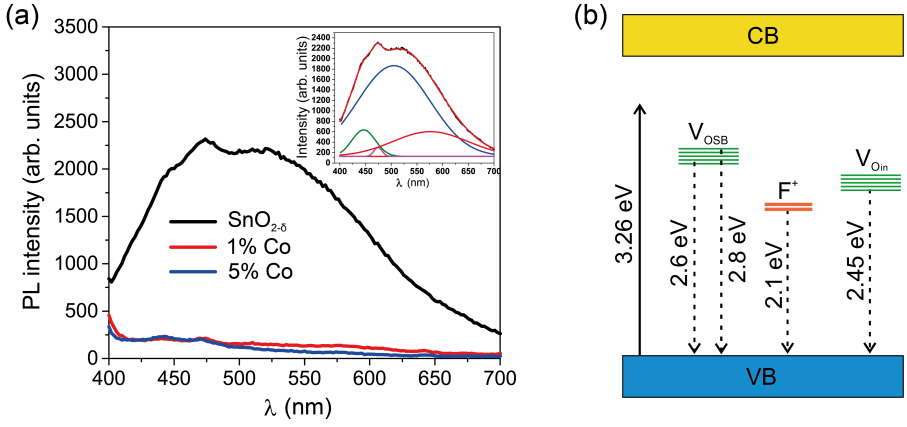

Figure 7. Room-temperature PL spectra of $Sn_{1-x}Co_xO_{2-\delta}$ nanoparticles (a) and the schematic of relaxation mechanism (b)

conditions, the drop in quantum yield value was estimated to be nearly 93%, which evidently implies that cobalt doping drastically quenches the photoluminescence of $SnO_{2-\delta}$. It has been already demonstrated that Co ions act as luminescence quenchers for metal oxides like TiO_2 or ZnO, decreasing the intensity of PL emission by forming the large number of nonradiative centres [55,56]. Therefore, it can be inferred that Co-doping of the $SnO_{2-\delta}$ nanocrystals increases the nonradiative recombination processes.

3.4. Photocatalytic performances

The degradation of MB under the UV light in the presence of the $Sn_{1-x}Co_xO_{2-\delta}$ samples is shown in Fig. 8a. The blank experiment in the absence of the catalyst (black curve) displayed almost no photocatalytic degradation of MB under UV irradiation. The $SnO_{2-\delta}$ nanoparticles exhibited high photocatalytic activity as the degradation of MB was completed after 6 h. The photocatalytic efficiency of the $SnO_{2-\delta}$ nanoparticles is much better than the ones of bulk SnO_2 [53] and is comparable to other reported works on SnO_2 nanoparticles [24,57]. Photoinduced degradation of MB was significantly slower in the presence of Co-doped samples. After 6 h, the MB degradation of 50% was obtained in the presence of the $Sn_{0.99}Co_{0.01}O_{2-\delta}$ catalyst, whereas significant decrease of photocatalytic activity was registered for the $Sn_{0.97}Co_{0.03}O_{2-\delta}$ and $Sn_{0.95}Co_{0.05}O_{2-\delta}$ samples. The obtained results are in accordance with the solitary work of Entradas *et al.* [22] who showed that increased Co-doping resulted in the decreased photocatalytic activity of SnO_2. The experimental kinetic data for $SnO_{2-\delta}$ catalyst were fitted to the rate equation of a pseudo first-order reaction $\ln(C/C_0) = kt$, where k is the rate constant and C_0 and C are the initial dye concentration and that at time t. The reaction kinetics for the $SnO_{2-\delta}$ catalyst (inset of Fig. 8a) follows the first order and the reaction rate constant estimated from the slope of the linear fit is 0.323 h^{-1}. The degradation process of MB is initiated when the electron-hole pairs are formed on the $SnO_{2-\delta}$ surface under the UV irradiation. Photogenerated electrons and holes, if not recombined, can migrate to the catalyst surface and react with adsorbed oxygen, water molecules or hydroxyl anions generating hydroxyl ($OH^\bullet$), superoxide ($O_2^{\bullet-}$) or ($HO_2^\bullet$) radicals. These reactions can be presented by Eq. 4–8:

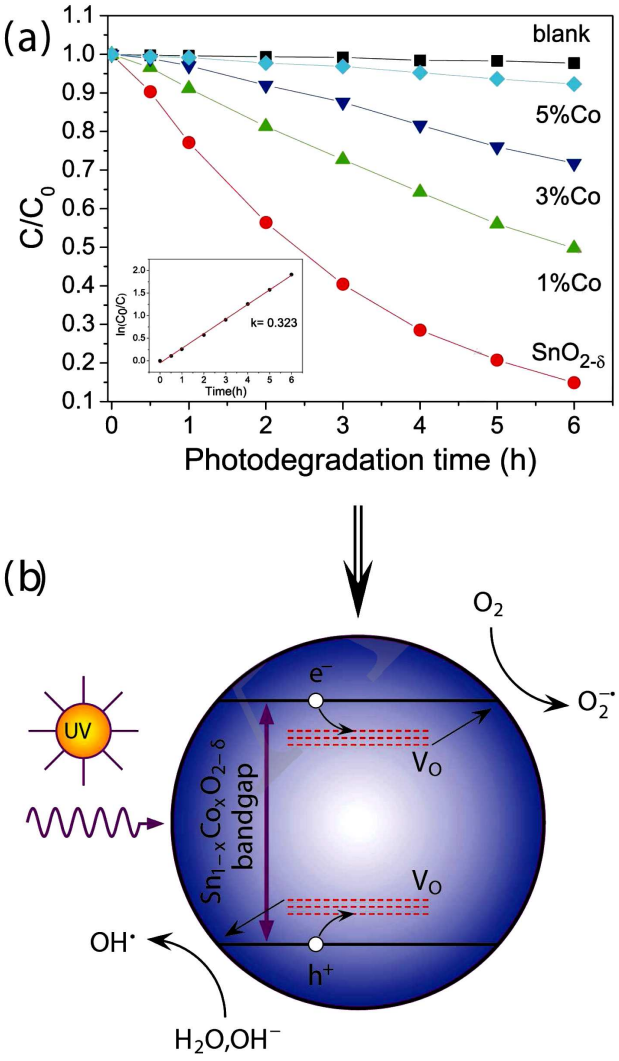

Figure 8. Photocatalytic degradation of MB in the presence of $Sn_{1-x}Co_xO_{2-\delta}$ samples (inset: pseudo first-order reaction kinetics of $SnO_{2-\delta}$ sample) (a) and illustration of proposed photodegradation mechanism under UV light illumination (b)

$$SnO_2 + h\nu \longrightarrow SnO_2(e^-_{cb} + h^+_{vb}) \quad (4)$$

$$e^-_{cb} + O_{2ads} \longrightarrow O_2^{\bullet-} \quad (5)$$

$$h^+_{vb} + H_2O \longrightarrow H^+ + OH^\bullet \quad (6)$$

$$h^+_{vb} + OH^- \longrightarrow OH^\bullet \quad (7)$$

$$O_2^{\bullet-} + H^+ \longrightarrow HO_2^\bullet \quad (8)$$

The photocatalytic efficiency of semiconductors like SnO_2 can be enhanced by introducing lattice defects such as oxygen vacancies because these defects can be active sites on the photocatalyst surface and delay the recombination of photogenerated electrons and holes [21,58]. The as-prepared $SnO_{2-\delta}$ nanopowders are very much oxygen deficient as confirmed by Raman results. The oxygen vacancies can form defect states inside the gap influencing the electronic structure of $SnO_{2-\delta}$ nanoparticles, as already seen from PL spectrum. By applying complementary techniques such as ultraviolet photoelectron spectroscopy and ion-scattering spectroscopy, Cox *et al.* [59] analysed oxygen vacancy electronic states on the SnO_2 surface and they showed that in-plane oxygen vacancies V_{Oin} form defect electronic states inside the SnO_2 gap near the conduction band behaving like F^+ centre donor states. Bridging/subbridging oxygen vacancies form states near the valence band [59] playing the role of hole acceptors. These donor/acceptor states can serve as carrier traps for electrons and holes ensuring better charge separation efficiency and suppression of *e-h* recombination process. Besides, doubly ionized (F^{++}) or singly ionized (F^+)

in-plane or subbridging vacancies formed at the surface of the catalyst facilitate charge transfer to adsorption species like H_2O or O_2, forming reactive radicals responsible for dye degradation. The holes, h^+_{vb}, trapped by oxygen vacancies at the nanoparticle surface react with adsorbed H_2O or OH^- groups to form $OH^\bullet$ radicals (Eqs. 6 and 7). Besides, electrons, e^-_{cb}, can be trapped by surface F^{++} vacancies which convert to F^+. Molecular oxygen adsorbed on the $SnO_{2-\delta}$ surface can capture electrons located on F^+ states [58] to form $O_2^{\bullet-}$ radicals:

$$e^-_{cb} + F^{++} \longrightarrow F^+ \quad (9)$$

$$F^+ + O_2 \longrightarrow O_2^{\bullet-} + F^{++} \quad (10)$$

Therefore, it is reasonable to assume that in-plane and subbridging/bridging oxygen vacancies in different charge states play significant role in enhancing the photocatalytic efficiency of $SnO_{2-\delta}$. The proposed mechanism of photodegradation process is presented in Fig. 8b.

Among the reactive radicals, $OH^\bullet$ radicals are considered to be the most important oxidative agent in photocatalytic reactions on metal-oxide nanostructures. They have one of the highest oxidation potentials among the oxidizing species (2.8 V) and can rapidly attack pollutants on the semiconductor surface. These radicals are considered as non-selective oxidizing species, since they can oxidize almost all electron rich organic molecules because of its electrophilic nature. $OH^\bullet$ radicals are usually formed by the reaction between the holes and OH^- or water molecules present on the surface of the catalyst (Eqs. 6 and 7). The formation of $OH^\bullet$ radicals on the surface of UV-illuminated $SnO_{2-\delta}$ was tested by performing the experiment with terephthalic acid, described in detail in section 2.3. The concentration of $OH^\bullet$ radicals was estimated from the intensity change of the PL peak attributed to 2-hydroxyterephtalic acid which is known to be proportional to the amount of $OH^\bullet$ radicals formed [30,31]. Figure 9 showed that intensity of PL peak at around 430 nm gradually increased with the prolonged irradiation time pointing to the higher formation rate of hydroxyl radicals. This result indicates that increased formation of $OH^\bullet$ radicals has a great effect on the photocatalytic activity of $SnO_{2-\delta}$. Further investigations will be directed to the estimation of the optimal SnO_2 concentration and the influence of solution pH on the SnO_2 photocatalytic properties. In that sense, more detailed mechanism study needs to be performed.

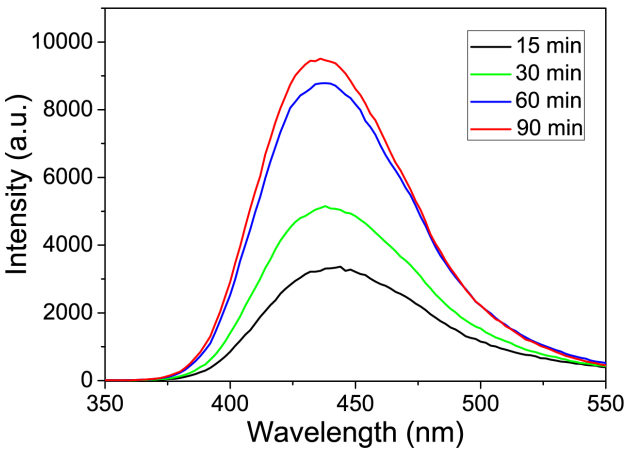

Figure 9. PL intensity change of 430 nm peak observed during UV illumination of $SnO_{2-\delta}$ sample in the solution of terephthalic acid and recorded at different time

With Co-doping the photocatalytic performances of $SnO_{2-\delta}$ were deteriorated. The reasons can be found in increased number of nonradiative centres with increasing cobalt concentration which act as trapping centres, immobilizing the fast transfer of photo-generated electrons to the nanoparticle surface. However, one of the main reasons can be found in the decreased concentration of oxygen vacancies which promotes the charge separation enhancing at the same time the photocatalytic activity. Also, the increased band gap of the Co-doped samples decreases the number of photons with sufficient energy to initiate photocatalytic processes, i.e. less UV energy is absorbed.

IV. Conclusions

Single phase ultrafine $Sn_{1-x}Co_xO_{2-\delta}$ nanocrystals, of a tetragonal (cassiterite-type) crystal structure, were prepared using a simple microwave-assisted hydrothermal synthesis at low temperature without the addition of any surfactant. Rietveld refinement of the XRD data showed that Co cations entered substitutionally into $SnO_{2-\delta}$ lattice and the unit cell volume increased up to $x = 0.05$. The slight shrinkage of the unit cell of the $Sn_{0.95}Co_{0.05}O_{2-\delta}$ sample was ascribed to the increased amount of Co^{3+} cations. The average crystallite size of the $SnO_{2-\delta}$ nanocrystals was less than Bohr exciton radius and it was found to decrease with increasing Co-doping level. UV-Vis absorption measurements confirmed that Co cations entered into the $SnO_{2-\delta}$ lattice in mixed valence state for higher dopant content ($x > 0.01$) and the concentration of Co^{3+} cations increased in the $Sn_{0.95}Co_{0.05}O_{2-\delta}$ sample. Raman spectra revealed oxygen deficient structure of the $SnO_{2-\delta}$ nanocrystals, whereas the oxygen vacancy concentration decreased with increased Co-doping. Further, Co-doping brought significant changes in the optical and electronic properties of tin oxide. $SnO_{2-\delta}$ nanocrystals exhibited blue shift of the band gap energy, compared to the bulk counterpart, due to the combined phonon confinement and the Burstein-Moss effects. The optical band gap energy increased with increasing Co concentration. The luminescence process in $SnO_{2-\delta}$ nanocrystals mainly originated from oxygen vacancy related defects and it was completely quenched in the Co-doped nanocrystals due to the increased nonradiative recombination processes. The oxygen-deficient $SnO_{2-\delta}$ was efficient for the light-induced degradation of methylene blue. Enhanced photocatalytic activity of $SnO_{2-\delta}$ can be ascribed to the

oxygen vacancies-assisted better charge separation and faster charge transport to adsorbed species. On the other hand, deteriorated photocatalytic performances of Co-doped $SnO_{2-\delta}$ nanopowders can be ascribed to the decreased oxygen vacancy concentration and less amount of absorbed UV light because of the band gap widening.

Acknowledgement: The authors acknowledge funding by the Institute of Physics Belgrade, through the grant by the Serbian Ministry of Education, Science and Technological Development. V.D. Araújo and M.I.B. Bernardi wish to thank Brazilian agencies FAPESP, FACEPE and CNPq for financial support.

References

1. H. Park, S. Alhammadi, K. Bouras, G. Schmerber, F. Gérald, D. Aziz, S. Abdelilah, J. Chan-Wook, P. Chinho, K. Woo Kyoung, "Nd-doped SnO_2 and ZnO for application in Cu(InGa)Se_2 solar cells", *Sci. Adv. Mater.*, **9** (2017) 2114–2120.
2. J. Lee, N.H. Kim, Y.S. Park, "Characteristics of SnO_2:Sb films as transparent conductive electrodes of flexible inverted organic solar cells", *J. Nanosci. Nanotechnol.*, **16** (2016) 4973–4977.
3. Y. Chen, J. Lu, S. Wen, L. Lu, J. Xue, "Synthesis of SnO_2/MoS_2 composites with different component ratios and their applications as lithium ion battery anodes", *J. Mater. Chem. A*, **2** (2014) 17857–17866.
4. M. Batzill, U. Diebold, "The surface and materials science of tin oxide", *Prog. Surf. Sci.*, **79** (2005) 47–154.
5. K. Singh, R. Malakar, R. Narzary, K. Priyanka, M. Biplob, "Hydrogen sensing properties of pure and composites of ZnO and SnO_2 particles: Understanding sensing mechanism", *Sens. Lett.*, **15** (2017) 771–778.
6. Z. Zhao, B. Wang, J. Ma, W. Zhan, L. Wang, Y. Guo, Y. Guo, G. Lu, "Catalytic combustion of methane over Pd/SnO_2 catalysts", *Chinese J. Catal.*, **38** (2017) 1322–1329.
7. J.T. Wiswall, M.S. Wooldridge, H.G. Im, "An experimental investigation of catalytic oxidation of propane using temperature controlled Pt, Pd, SnO_2, and 90% SnO_2–10% Pt catalysts", *Catal. Sci. Technol.*, **3** (2013) 618–625.
8. J.S. Chen, X.W.D. Lou, "SnO_2-based nanomaterials: synthesis and application in lithium-Ion batteries", *Small*, **9** (2013) 1877–1893.
9. M.O. Orlandi, A.J. Ramirez, E.R. Leite, E. Longo, "Morphological evolution of tin oxide nanobelts after phase transition", *Cryst. Growth Des.*, **8** (2008) 1067–1072.
10. J. Jeong, S.-P. Choi, C.I. Chang, D.C. Shin, J.S. Park, B.-T. Lee, Y.-J. Park, H.-J. Song, "Photoluminescence properties of SnO_2 thin films grown by thermal CVD", *Solid State Commun.*, **127** (2003) 595–597.
11. Y. Wang, M.H. Wu, Z. Jiao, J.Y. Lee, "One-dimensional SnO_2 nanostructures: facile morphology tuning and lithium storage properties", *Nanotechnology*, **20** (2009) 345704.
12. Z.R. Dai, Z.W. Pan, Z.L. Wang, "Growth and structure evolution of novel tin oxide diskettes", *J. Am. Chem. Soc.*, **124** (2002) 8673–8680.
13. X. Li, Q. Yu, C. Yu, Y. Huang, R. Li, J. Wang, F. Guo, Y. Zhang, S. Gao, L. Zhao, "Zinc-doped SnO_2 nanocrystals as photoanode materials for highly efficient dye-sensitized solar cells", *J. Mater. Chem. A*, **3** (2015) 8076–8082.
14. Y. Liu, F. Yang, X. Yang, "Size-controlled synthesis and characterization of quantum-size SnO_2 nanocrystallites by a solvothermal route", *Colloid Surf. A*, **312** (2008) 219–225.
15. Y.K. Liu, C.L. Zheng, W.Z. Wang, Y.J. Zhan, G.H. Wang, "Production of SnO_2 nanorods by redox reaction", *J. Cryst. Growth*, **233** (2001) 8–12.
16. J.Q. Hu, Y. Bando, Q.L. Liu, D. Golberg, "Laser-ablation growth and optical properties of wide and long single-crystal SnO_2 ribbons", *Adv. Funct. Mater.*, **13** (2003) 493–496.
17. H.Q. Cao, X.Q. Qiu, Y. Liang, L. Zhang, M.J. Zhao, Q.M. Zhu, "Sol-gel template synthesis and photoluminescence of n- and p-type semiconductor oxide nanowires", *Chem. Phys. Chem.*, **7** (2006) 497–501.
18. Y.K. Liu , C.L. Zheng , W.Z. Wang , C.R. Yin , G.H. Wang, "Synthesis and characterization of rutile SnO_2 nanorods", *Adv. Mater.*, **13** (2001) 1883–1887.
19. D. Chen, S. Huang, R. Huang, Q. Zhang, T.-T. Lee, E. Cheng, Z. Hu, Z. Chen, "Highlights on advances in SnO_2 quantum dots: insights into synthesis strategies, modifications and applications", *Mater. Res. Lett.*, **6** (2018) 462–488.
20. P.G. Mendes, M.L. Moreira, S.M. Tebcherani, M.O. Orlandi, J. Andrés, M.S. Li, N. Diaz-Mora. J.A. Varela. E. Longo, "SnO_2 nanocrystals synthesized by microwave-assisted hydrothermal method: towards a relationship between structural and optical properties", *J. Nanopart. Res.*, **14** (2012) 750–13.
21. A.M. Al-Hamdi, U. Rinner, M. Sillanpää, "Tin dioxide as a photocatalyst for water treatment: A review", *Process Saf. Environ.*, **107** (2017) 190–205.
22. T. Entradas, J.F. Cabrita, S. Dalui, M.R. Nunes, O.C. Monteiro, A.J. Silvestre, "Synthesis of sub-5 nm Co-doped SnO_2 nanoparticles and their structural, microstructural, optical and photocatalytic properties", *Mater. Chem. Phys.*, **147** (2014) 563–571.
23. R. Mani, K. Vivekanandan, K. Vallalperuman, "Synthesis of pure and cobalt (Co) doped SnO_2 nanoparticles and its structural, optical and photocatalytic properties", *J. Mater. Sci. Mater. Electron.*, **28** (2017) 4396–4402.
24. D. Chandran, L.S. Nair, S. Balachandran, K. Rajendra Babu, M. Deepa, "Structural, optical, photocatalytic, and antimicrobial activities of cobalt-doped tin oxide nanoparticles", *J. Sol-Gel Sci. Technol.*, **76** (2015) 582–591.
25. Y. Cao, L. Huang, Y. Bai, K. Jermsittiparsert, R. Hosseinzadeh, H. Rasoulnezhad, G. Hosseinzadeh, "Synergic effect of oxygen vacancy defect and shape on the photocatalytic performance of nanostructured TiO_2 coating", *Polyhedron*, **175** (2020) 114214.
26. X. Xu, X. Ding, X. Yang, P. Wang, S. Li, Z. Lu, H. Chen, "Oxygen vacancy boosted photocatalytic decomposition of ciprofloxacin over Bi_2MoO_6: Oxygen vacancy engineering, biotoxicity evaluation and mechanism study", *J. Hazar. Mater.*, **364** (2019) 691–699.
27. Q. Zhang, X. Zhao, L. Duan, H. Shen, R. Liu, "Controlling oxygen vacancies and enhanced visible light photocatalysis of CeO_2/ZnO nanocomposites", *J. Photoch. Photobio. A*, **392** (2020) 112156.
28. B. Matovic, J. Lukovic, B. Stojadinović, S. Aškrabić, A. Zarubica, B. Babic, Z. Dohčević-Mitrović, "Influence of Mg doping on structural, optical and photocatalytic performances of ceria nanopowders", *Process. Appl. Ceram.*,

11 (2017) 304–310.
29. Z. Dohčević-Mitrović, S. Stojadinović, L. Lozzi, S. Aškrabić, M. Rosić, N. Tomić, N. Paunović, S. Lazović, M.G. Nikolić, S. Santucci, "WO_3/TiO_2 composite coatings: Structural, optical and photocatalytic properties", *Mater. Res. Bull.*, **83** (2016) 217–224.
30. T.M. Su, Z.L. Liu, Y. Liang, Z.Z. Qin, J. Liu, Y.Q. Huang, "Preparation of PbYO composite photocatalysts for degradation of methyl orange under visible-light irradiation", *Catal. Comm.*, **18** (2012) 93–97.
31. K. Ishibashi, A. Fujishima, T. Watanabe, K. Hashimoto, "Detection of active oxidative species in TiO_2 photocatalysis using the fluorescence technique", *Electrochem. Commun.*, **2** (2000) 207–210.
32. D. Menzel, A. Awada, H. Dierke, J. Schoenes, F. Ludwig, M. Schilling, "Free-carrier compensation in ferromagnetic ion-implanted SnO_2:Co", *J. Appl. Phys.*, **103** (2008) 07D106.
33. E.J.H. Lee, C. Ribeiro, T.R. Giraldi, E. Longo, E.R. Leite, J.A. Varela, "Photoluminescence in quantum-confined SnO_2 nanocrystals: Evidence of free exciton decay", *Appl. Phys. Lett.*, **84** (2004) 1745–1747.
34. B. Babu, Ch.V. Reddy, J. Shim, R.V.S.S.N. Ravikumar, J. Park, "Effect of cobalt concentration on morphology of Co-doped SnO_2 nanostructures synthesized by solution combustion method", *J. Mater. Sci. Mater. Electron.*, **27** (2016) 5197–5203.
35. P.S. Peercy, B. Morosin, "Pressure and temperature dependences of the Raman-active phonons in SnO_2", *Phys. Rev. B*, **7** (1973) 2779–2786.
36. V. Bonu, A. Das, S. Amirthapandian, S. Dhara, A.K. Tyagi, "Photoluminescence of oxygen vacancies and hydroxyl group surface functionalized SnO_2 nanoparticles", *Phys. Chem. Chem. Phys.*, **17** (2015) 9794–9801.
37. A. Diéguez, A. Romano-Rodríguez, A. Vilà, J.R. Morante, "The complete Raman spectrum of nanometric SnO_2 particles", *J. Appl. Phys.*, **90** (2001) 1550–1557.
38. L.Z. Liu, J.K. Xu, X.L. Wu, T.H. Li, J.C. Shen, P.K. Chu, "Optical identification of oxygen vacancy types in SnO_2 nanocrystals", *Appl. Phys. Lett.*, **102** (2013) 031916.
39. K.N. Yu, Y. Xiong, Y. Liu, C. Xiong, "Microstructural change of nano-SnO_2 grain assemblages with the annealing temperature", *Phys. Rev. B*, **55** (1997) 2666–2671.
40. Y. Liu, M. Liu, "Growth of aligned square-shaped SnO_2 tube arrays", *Adv. Funct. Mater.*, **15** (2005) 57–62.
41. F. Wang, X. Zhou, J. Zhou, T.-K. Sham, Z. Ding, "Observation of single tin dioxide nanoribbons by confocal Raman microspectroscopy", *J. Phys. Chem. C*, **111** (2007) 18839–18843.
42. C. Van Komen, A. Thurber, K.M. Reddy, J. Hays, A. Punnoose, "Structure-magnetic property relationship in transition metal (M = V, Cr, Mn, Fe, Co, Ni) doped SnO_2 nanoparticles", *J. Appl. Phys.*, **103** (2008) 07D141.
43. D.A. Popescu, J.-M. Herrmann, A. Ensuque, F. Bozon-Verduraz, "Nanosized tin dioxide: Spectroscopic (UV-VIS, NIR, EPR) and electrical conductivity studies", *Phys. Chem. Chem. Phys.*, **3** (2001) 2522–2530.
44. I. Rossetti, B. Bonelli, G. Ramis, E. Bahadori, R. Nasi, A. Aronne, S. Esposito, "New insights into the role of the synthesis procedure on the performance of Co-based catalysts for ethanol steam reforming", *Top. Catal.*, **61** (2018) 734–1745.
45. Y. Brik, M. Kacimi, M. Ziyad, F. Bozon-Verduraz, "Titania-supported cobalt and cobalt-phosphorus catalysts: Characterization and performances in ehane oxidative dehydrogenation", *J. Catal.*, **202** (2001) 118–128.
46. S. Roy, A.G. Joshi, S. Chatterjee, A.K. Ghosh, "Local symmetry breaking in SnO_2 nanocrystals with cobalt doping and its effect on optical properties", *Nanoscale*, **10** (2018) 10664–10682.
47. A.S. Ferlauto, G.M. Ferreira, J.M. Pearce, C.R. Wronski, R.W. Collins, X. Deng, G. Ganguly, "Analytical model for the optical functions of amorphous semiconductors from the near-infrared to ultraviolet: Applications in thin film photovoltaics", *J. Appl. Phys.*, **92** (2002) 2424–2436.
48. P.D. Borges, L.M.R. Scolfaro, H.W. Leite Alves, E.F. da Silva Jr., "DFT study of the electronic, vibrational, and optical properties of SnO_2", *Theor. Chem. Acc.*, **126** (2010) 39–44.
49. L. Brus, "Electronic wave functions in semiconductor clusters: experiment and theory", *J. Phys. Chem.*, **90** (1986) 2555–2560.
50. S. Dalui, S. Rout, A.J. Silvestre, G. Lavareda, L.C.J. Pereira, P. Brogueira, O. Conde, "Structural, electrical and magnetic studies of Co:SnO_2 and (Co,Mo):SnO_2 films prepared by pulsed laser deposition", *Appl. Surf. Sci.*, **278** (2013) 127–131.
51. H.S. So, J.-W. Park, D.H. Jung, K.H. Ko, H. Lee, "Optical properties of amorphous and crystalline Sb-doped SnO_2 thin films studied with spectroscopic ellipsometry: Optical gap energy and effective mass", *J. Appl. Phys.*, **118** (2015) 085303.
52. A. Oprea, E. Moretton, N. Bârsan, W.J. Becker, J. Wöllenstein, U. Weimar, "Conduction model of SnO_2 thin films based on conductance and Hall effect measurements", *J. Appl. Phys.*, **100** (2006) 033716.
53. A. Kar, M.A. Stroscio, M. Dutta, J. Kumari, M. Meyyappan, "Growth and properties of tin oxide nanowires and the effect of annealing conditions", *Semicond. Sci. Technol.*, **25** (2010) 024012.
54. I.I. Gontia, M. Baibarac, I. Baltog, "Photoluminescence and Raman studies on tin dioxide powder and tin dioxide/single-walled carbon-nanotube composites", *Phys. Status Solidi B*, **248** (2011) 1494–1498.
55. B. Choudhury, A. Choudhury, "Luminescence characteristics of cobalt doped TiO_2 nanoparticles", *J. Lumin.*, **132** (2012) 178–184.
56. S. Yamamoto, "Photoluminescence quenching in cobalt doped ZnO nanocrystals", *J. Appl. Phys.*, **111** (2012) 094310.
57. S.P. Kim, M.Y. Choi, H.C. Choi, "Photocatalytic activity of SnO_2 nanoparticles in methylene blue degradation", *Mater. Res. Bull.*, **74** (2016) 85–89.
58. X. Pan, M.-Q. Yang, X. Fu, N. Zhang, Y.-J. Xu, "Defective TiO_2 with oxygen vacancies: synthesis, properties and photocatalytic applications", *Nanoscale*, **5** (2013) 3601–3614.
59. D.F. Cox, T.B. Fryberger, S. Semancik, "Oxygen vacancies and defect electronic states on the SnO_2(110)-1 × 1", *Phys. Rev. B*, **38** (1988) 2072–2083.

Journal of Physics D: Applied Physics

PAPER

SnO_2 nanosheets with multifunctional properties for flexible gas-sensors and UVA light detectors

To cite this article: Marko Radovi *et al* 2019 *J. Phys. D: Appl. Phys.* **52** 385305

IOP Publishing Journal of Physics D: Applied Physics
J. Phys. D: Appl. Phys. **52** (2019) 385305 (7pp) https://doi.org/10.1088/1361-6463/ab2d1b

SnO_2 nanosheets with multifunctional properties for flexible gas-sensors and UVA light detectors

Marko Radović[1], Georges Dubourg[1], Zorana Dohčević-Mitrović[2], Bojan Stojadinović[2], Jelena Vukmirović[3], Nataša Samardžić[4] and Miloš Bokorov[5]

[1] University of Novi Sad, Group for Nano and Microelectronics, Biosense Institute, Novi Sad, Serbia
[2] Laboratory for Nanocomposite Structures and Bio-Vibrational Spectroscopy, Institute of Physics, University of Belgrade, Belgrade, Serbia
[3] University of Novi Sad, Faculty of Technology, Novi Sad, Serbia
[4] University of Novi Sad, Faculty of Technical Sciences, Novi Sad, Serbia
[5] University of Novi Sad, University Center for Electronic Microscopy, Novi Sad, Serbia

E-mail: marrad@biosense.rs

Received 10 April 2019, revised 11 June 2019
Accepted for publication 26 June 2019
Published 19 July 2019

Abstract

The presented research introduces an innovative bottom-up approach, involving synthesis, characterization and application of SnO_2 nanomaterials in advanced technologies. SnO_2 nanosheets are synthesized with a hydrothermal method and screen-printed on a flexible substrate with interdigitated electrodes. The obtained measurements reveal that the synthesized material has a rutile crystal structure with preferable (1 1 0) orientation and oxygen-defects, unique morphology and good electric conductivity. Multifunctional performance is evaluated for gas and ultraviolet A (UVA; 365 nm) light sensing. The designed sensor shows a better response to ethanol in comparison to 2-propanol and acetone, indicating the selectivity feature among the investigated volatile organic compounds. Photocurrent measurements reveal a good photoconversion rate, suitable for UVA monitoring.

Keywords: SnO_2, oxygen vacancies, electrical properties, gas sensors, light sensors

(Some figures may appear in colour only in the online journal)

1. Introduction

Metal oxides stand out as a landmark in materials science due to their unique properties, widely exploited in basic research and technological applications. Among these materials, tin oxide (SnO_2) is a prime example of multifunctionality, since it possesses low electrical resistance combined with high optical transparency in the visible spectrum. Such a feature is highly demanded for optoelectronic devices (solar cells, light emitting diodes (LEDs) and smart windows) [1–5]. Also, SnO_2 based materials are recognized for their outstanding surface related catalytic properties, leaving high impact on gas-sensing performance and broad applications in sensing technologies [6–8]. Chemical gas sensors based on tin oxide films, coupled with heater elements, gave rise to the golden era in the evolution of commercial products for monitoring of various types of gases, over the past three decades. However, with the recent advancement of sensor network technologies and increased need for sensor array devices, focus on the application of tin oxide sensors has shifted to cost-efficient platforms, low power consumption (room temperature operating conditions) and to the sub ppm detection range. Significant efforts are being continuously invested in nanomaterials design to improve sensors sensitivity and selectivity.

Chemical routes for the synthesis of SnO_2 nanomaterials have been evolving in parallel with wide adoption and application of these materials in advanced technologies. Among such processes, the hydrothermal method has proven to be

the most versatile, reliable, repeatable, clean and environmentally-friendly technique for obtaining SnO_2 nanomaterials with targeted properties. The portfolio of the hydrothermal method in synthesis of tin oxide-based nanomaterials extends over different types of dimensionality and morphologies, like nanocrystals [9, 10], nanowires [11], nanorods [12, 13], nanoneedles [14, 15], nanosheets [14–20], snowflakes [21] and nanoflowers [22]. An accumulated library of knowledge points to the fact that low dimensional 0D and 1D materials usually have a larger specific surface area than the 3D microstructures, which is highly desired in sensor applications, but they have poor thermal stability. For example, nanoparticles easily tend to form agglomerates, transforming into polycrystalline material and discarding their unique properties related to their nanostructured nature, whereas nanosheet structures are highly effective in mitigating the agglomeration, yielding better structural integrity. Also, synthesis of SnO_2 nanosheets has gained a lot of research interest in recent years since they exhibit exceptional selectivity feature towards ethanol sensing [15–17, 20, 23], compared to the other nanostructures. Two of the biggest problems facing hydrothermal synthesis of tin oxide nanosheets is the precise control of the oxidation state of Sn ions over the exposed surfaces and control of impurities concentration (highly reduced SnO phase) [24]. Optimization of hydrothermal parameters for synthesis of SnO_2 into clean and single phase nanosheet morphology is one of the foundations for their successful application in sensors technologies.

Recent technological developments imposed strong demands for the integration of multifunctional properties of nanomaterials into a single device [25, 26], where metal oxides like SnO_2 hold great potential to meet market demands. Still, many precise and sophisticated technologies used for the fabrication of state-of-art devices involve complex processes which are not compatible with large scale production. Therefore, alternative approaches need to be developed to meet the high demand of such devices, like low-cost and mass producible multifunctional platforms. A major challenge for successful integration of nanomaterials in new technologies lies in the preservation of the material fundamental properties through the functionalization process. This challenge is conditioned with the low production cost of the final device. Lots of research activities are currently dedicated to the development of flexible electronics [27], aiming to take advantage over traditional rigid platforms in cost, mechanical flexibility, biocompatibility and biodegradability.

The main idea behind the conducted research was to uncover versatile surface properties of SnO_2 nanomaterials and to develop a simple and potentially scalable bottom-up approach for implementation of such unique properties into sensing devices, by combining hydrothermal synthesis and screen-printing functionalization. Basic parameters of the hydrothermal method, such as the precursor type, pH value and reaction temperature, were optimized for obtaining SnO_2 nanopowders with the desired structural, morphological, electrical and sensing properties. Functional paste for the screen-printing of synthesized nanomaterial was specially formulated in order to preserve materials fundamental features without the need for an additional high-temperature curing step. The undertaken approach revealed great potential for the application of SnO_2 nanosheets, with enhanced surface features, in alcohol gas-sensing and UVA photodetection.

2. Experimental

The hydrothermal method was used to synthesize SnO_2 powder. The starting precursors were tin(IV) chloride pentahydrate ($SnCl_4{\cdot}5H_2O$) (Acros Organics, Belgium), sodium hydroxide (NaOH) (Sigma-Aldrich, USA) and hydrochloric acid (HCl) (Centrohem, Serbia). Initially, HCl and distilled water were mixed and stirred on a magnetic stirrer, at 50 °C, for 30 min, to produce the solution with a pH between 0 and 1. Further, $SnCl_4 \times 5H_2O$ (17.529 g) was added and the mixed solution was homogenized under constant stirring. The NaOH solution was added dropwise until the the pH value of the solution reached 9. After this process, a whitish liquid was formed and transferred to the autoclave and heated to 180 °C for 12 h. The obtained powders were filtered and dried.

Fabrication of an interdigitated electrodes (IDE) structure and functionalization of the synthesized powders was achieved by screen-printing, using an EKRA 2H screen printer. Silver IDEs were printed using commercial Novacentrix Metalon paste with 75% of Ag loading. The SnO_2-based screen-printing paste, used for deposition of the sensitive layer, was prepared by dispersing 2 g of SnO_2 synthesized nanoparticles into 400 μl of terpineol (Sigma-Aldrich). To this dispersion, 600 ml of polyvinyl pyrrolidone (Sigma-Aldrich) ethanol solution (1 g/10 ml) was added. Then, dispersion was treated with an ultrasonic horn for 5 min and the obtained paste was left at room temperature to dry for 24 h. The dried film was treated at 100 °C for 2 h.

X-ray diffraction (XRD) measurements were performed on a Rigaku MiniFlex600 system in the 20° to 80° range, with 0.03° scan step. Scanning electron microscopy (SEM) images were taken with JEOL JSM 6460 LV microscope. Micro-Raman measurements were performed on a Tri Vista 557 Raman system equipped with a nitrogen-cooled charge-coupled device (CCD) detector, using a 532 nm laser line (Coherent Verdi G) as an excitation source. Electrical analysis was performed using the impedance spectroscopy measurements on SP-200 Biologic potentiostat/galvanostat, in the 10 Hz–7 MHz frequency range. DC measurements were collected on a Yokogawa–Hewlett–Packard 4145A semiconductor probe analyzer. Gas-sensing performance was evaluated using a custom-built chamber equipped with nitrogen purging inlet/outlet, evaporator and fan. Photocurrent measurements were collected using a custom-built set-up with high power LED, operating at 365 nm with power of 100 mW.

3. Results and discussion

XRD spectra of the synthesized SnO_2 powder is shown in figure 1(a). The diffraction peaks can be indexed to tetragonal rutile phase characteristics for tin oxide, with corresponding Miller indices denoted for each diffraction peak according to

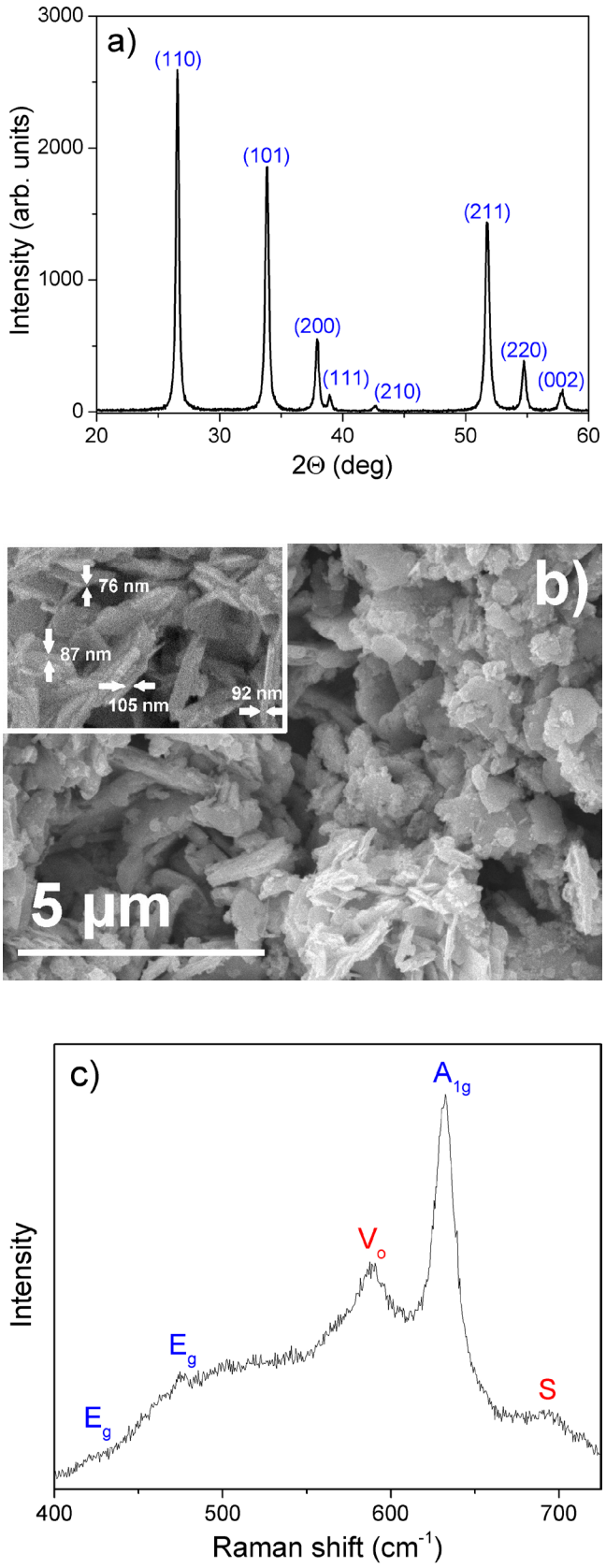

Figure 1. Structural and morphological characterization. (a) XRD spectra of the synthesized SnO_2 powder. (b) Large area SEM image of the nanosheets. The inset shows magnified image with denoted sheet thicknesses. (c) Raman spectra of the synthesized SnO_2 nanosheets.

JCPDS card 21-1250. No traces of impurities or other phases were observed. Sharp and narrow diffraction peaks suggest good crystallinity of powders composed of larger crystallites, even though the low hydrothermal temperature was used. The most intense peak in the diffraction spectra comes from the (1 1 0) plane, unlike the reported spectra for some sintered and crystalline SnO_2 samples, where (1 0 1) peak is dominant [28]. Calculation of the relative ratios between the intensities of the main diffraction peaks in figure 1(a), in comparison with the literature data [28], leads to the assumption that synthesized crystallites have a preferable (1 1 0) orientation. Such an assumption is justified with several theoretical and experimental studies [29–31], which demonstrated that (1 1 0) is the most stable surface of tin oxide with the lowest formation energy.

The morphology and particle size of the SnO_2 powders were investigated by the SEM technique. An SEM micrograph of the SnO_2 nanosheets is given in figure 1(b). The inset of figure 1(b) shows a magnified SEM image with determined thicknesses of several representative nanosheets. As shown, synthesized SnO_2 powder is composed of nanosheets whose lateral dimensions are in the 1 μm–10 μm range and the thickness of the individual sheets is around 100 nm.

Based on analysis of XRD and SEM results, it can be noted that selected parameters of the synthesis process produce exposed surfaces of the SnO_2 nanosheets with dominant (1 1 0) surface termination, which is most suitable for gas-sensing applications [31].

Figure 1(c) presents Raman spectra of the synthesized SnO_2 nanosheets in the 400 cm^{-1}–750 cm^{-1} range.

The most prominent peak and two weak features are assigned to first order Raman active phonons of SnO_2 rutile structure (triply-degenerate Eg mode and doubly-degenerate A2g mode) [32]. A very interesting feature in the presented spectra is the appearance of the defect-related mode (Vo) at 580 cm^{-1} attributed to the formation of oxygen vacancies and surface mode (*S*) at 690 cm^{-1} which is activated by surface structural disorder [32, 33]. Reported results by Diéguez *et al* [32] and Rumyantseva *et al* [33] provide clear evidence that the Raman intensity of these modes is strongly related to surface oxygen species, with a strong influence on the gas-sensing properties of SnO_2 nanomaterials. A pronounced Vo peak in the measured spectrum is a fingerprint of the high concentration of the oxygen vacancies in the synthesized nanosheets with high potential for applications in sensing technologies.

After successful synthesis and characterization, the SnO_2 nanosheets were functionalized into sensor components using versatile screen-printing technology. A PET substrate was chosen as a flexible platform for integration of a sensor transducer and sensitive layer, because this material is extensively used in modern food and beverage packaging technology. Transducer fabrication was performed by screen-printing of Ag paste in the form of IDEs on the PET substrate. Printed silver paste was cured at 200 C for 1 h and the resulting IDE structure has 200 microns width of individual digits and 100 microns gap between the digits. The effective surface area of

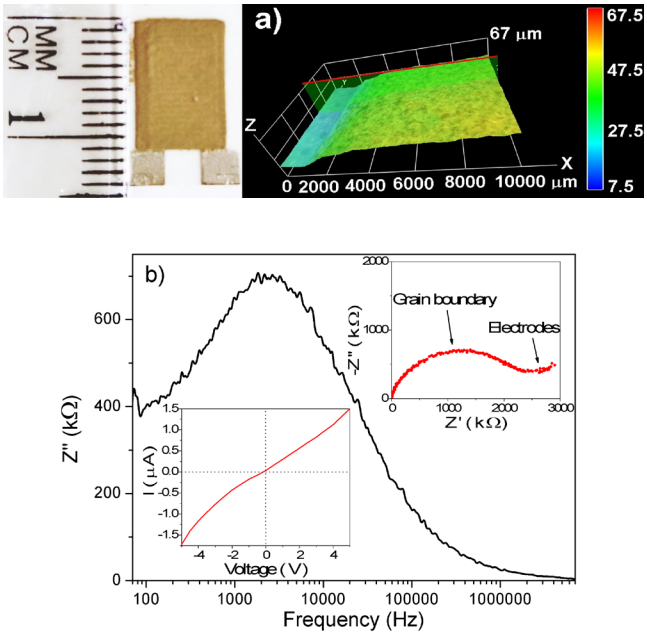

Figure 2. (a) (Left) Image of the printed SnO_2 nanosheets on the IDE electrodes and PET substrate. (Right) 3D profile of the screen-printed film, determined with optical profilometry. (b) Imaginary part of complex impedance as a function of frequency. The upper right inset presents the Cole–Cole plot extracted from the impedance measurements. The lower left inset shows DC characterization in the form of $I(V)$ curves.

the electrodes is 28 mm^2. Next, the paste with SnO_2 nanoparticles was screen-printed on top of the electrodes. The resulting printed device, exhibited in figure 2(a), is featured by thickness of 32 μm and has a uniform coverage of the IDE structure, with a relatively flat surface as presented in the 3D optical profile image.

AC electrical characterization of the designed sensor device was performed using the impedance spectroscopy measurements in the 10 Hz–7 MHz frequency range and the obtained results are shown in figure 2(b). Electrical response of polycrystalline materials is commonly described using an approximate microstructure model combining grain regions, grain boundaries regions and electrodes [6]. The dependence of the imaginary part of the impedance (Z'') with frequency revealed a single broad peak. The appearance of such peaks in the impedance spectrum is a signature of relaxation processes that occur during the current transport and they can be described with the mentioned microstructure model. The main peak in the imaginary part of impedance is centered at a frequency of 2.6 kHz, which could be used for extracting the value of electronic relaxation time in the material $\tau = 1/f \approx 0.4$ ms. A relatively long relaxation time is favourable for photovoltaic and photocatalitic applications, since it can ensure a longer lifetime of photo or thermally generated electron-hole pairs. In the upper right inset of figure 2(b), the Cole–Cole plot extracted from impedance measurements is shown. The single semicircle arc observed in the Cole–Cole plot can be attributed to grain boundary electrical resistance and the onset of the uncomplete arc can be ascribed to the contribution of the electrode resistance (for the frequencies below 100 Hz) [34, 35]. The origin of the dominant grain boundary resistance can be explained by taking into account the results of the SEM measurements, where it was established that the synthesized powder consists of nanosheets with a lot of contact surfaces between individual particles. Additional charge is accumulated at the opposite sides of the contact surfaces, disrupting the electron flow between the nanosheets and giving rise to the so-called interfacial polarization in impedance measurements. The intersection of the Cole–Cole plot with the Z' axis occurs near the origin, which reveals negligible grain resistance ($R_g \approx 0$).

From the diameter of the existing semicircle (figure 2(b), inset), we could estimate grain boundary resistance $R_{gb} \approx 2.7$ kΩ, as well as microscopic electrical conductivity:

$$\sigma_{gb} = \frac{1}{R_{gb}}\left(\frac{L}{A}\right) \approx 20.25\ \mathrm{S\,m^{-1}}.$$

Furthermore, the capacitance of grain boundary $C_{gb} \approx 0.14$ μF is calculated from the value of relaxation time and grain boundary resistance [18].

DC electrical characterization is shown in the lower left inset of figure 2(b), as the $I(V)$ curve measured in the −5 V to +5 V range. The curve has a linear response in the wide voltage range, indicating ohmic contacts between the printed film and electrode surface. The prepared device exhibits very good current values in comparison to similar resistive oxide-based sensors [6–8, 35], which represents a very good starting point for application of the synthesized SnO_2 nanomaterial in sensing devices. DC conductivity $\sigma_{DC} = 6.7\ \mathrm{S\,m^{-1}}$ of nanosheets was calculated from $I(V)$ measurements. From direct comparison of AC/DC measurements, it can be noted that the main contribution to electrical resistance in the DC regime also comes from the detected interfacial polarization, which can be observed as a low frequency tail of the main peak in the Z'' spectrum in figure 2(b).

Afterwards, the gas-sensing performance of the SnO_2 printed device was investigated. In figure 3(a), the dynamic gas response curves are shown, for the SnO_2 nanosheets, towards different concentrations of ethanol (from 10 ppm to 500 ppm), measured at room temperature and low relative humidity (10% RH). Sensor response is defined as the ratio between air (Ra) and target gas (Rg) resistivities ($S = \mathrm{Ra/Rg}$). Variations in sensor response are typical for n-type semiconductor materials and the sensor shows a high response for the investigated ppm concentrations of ethanol. The response and recovery times are shown in the inset of figure 3(a). The printed sensor has average response times and relatively good and stable recovery times, even at higher levels of ethanol vapor, which is very important for sensing performance.

For practical applications, the ethanol concentration of 50 ppm is of great interest, since it is the concentration usually measured by breath analyzers and food decay monitors [36, 37]. Therefore, we have conducted selectivity testing to establish the influence of the most common interfering VOC gases and humidity on the performance of the designed sensor. In figure 3(b), time resolved gas responses of the SnO_2 nanosheets towards 30% RH and 50 ppm of ethanol, 2-propanol and acetone vapor are compared. The obtained results

Table 1. Comparison of the gas sensing performance of hydrothermally synthesized SnO_2 nanomaterials. In the table, morphology, hydrothermal temperature, transducer design, response and recovery times, sensor response, selectivity and operating temperature are presented from the literature data.

Morphology	ht temp (°C)	transducer	Resp/Rec time	Response	Selectivity feature	Operating temp	Ref
SnO_2/graphene composite	120	Ceramic + Au IDE	/	15	NH_3	RT	[40]
SnO_2@rGO composite	180	Al_2O_3 + Au IDE	61 s/330 s	47.6%	CH_4	150 C	[41]
Porous nanotubes	160	Al_2O_3 tube + Au electrodes	6 s/20 s	7.5	/	/	[42]
Porous nanosheets	120	Al_2O_3 tube + Au electrodes	<10 s	6	Ethanol	300 C	[17]
Flower-like structures	180	/	20 s/15 s	87	No	250 C	[43]
Nanoneedles and nanosheets	180	Al_2O_3 tube + Au electrodes	6 s–21 s	33–65	Ethanol	240 C	[15]
Hollow spheres	120	/	5 s	11	No	350 C	[44]
Nanosheets	180	PET + Ag IDE	100 s/40 s	1.3	Ethanol	RT	This work

clearly show that humidity has the strongest influence on the sensor performance at room temperature. A recent study [38] has demonstrated that activation of ethanol sensing on the SnO_2 surface is driven by low levels of humidity, but the intricate detection mechanism is quite different for ethanol and humidity, offering the tool for eliminating the influence of humidity by calibration. In comparison with other VOC gases, the investigated sensor has a higher response towards ethanol with faster response/recovery times, whereas the response is significantly lower for 2-propanol and acetone.

The inset of figure 3(b) shows variation in sensor response for different VOC concentrations. The limit of detection (LOD) for ethanol was obtained from the linear fit of experimental data, shown in the inset of figure 3(b), and the calculated value of 1.5 ppm suggests that SnO_2 nanosheets have very good operating sensitivity in the 1 ppm to 500 ppm range. Reported DFT calculations [30, 31] have established that a SnO_2 (1 1 0) surface has the highest adsorption affinity for gas molecules and therefore offer very good sensing characteristics. Keeping in mind the above mentioned findings, it can be stated that good sensitivity and selectivity originate from unique surface termination, morphology and defect structure of the synthesized SnO_2 nanosheets. In comparison with the previously reported data on hydrothermally synthesized SnO_2 nanomaterials, presented in table 1, the obtained results in the presented research suggest that the undertaken approach offers relatively good sensing characteristics of the synthesized nanosheets. One of the most important advancements in the presented research can be viewed through utilization of low cost technology for sensor fabrication and in the use of low hydrothermal temperature with no subsequent calcination steps for obtaining the high quality SnO_2 nanosheets, with ethanol selectivity feature.

In order to fully exploit the potential offered by the hydrothermally synthesized SnO_2 nanosheets, time-resolved photoconductivity measurements of the same sensor were performed, as shown in figure 4. Analysis of the obtained measurements and comparison with literature data [39] revealed that synthesized SnO_2 nanosheets produce high photocurrent

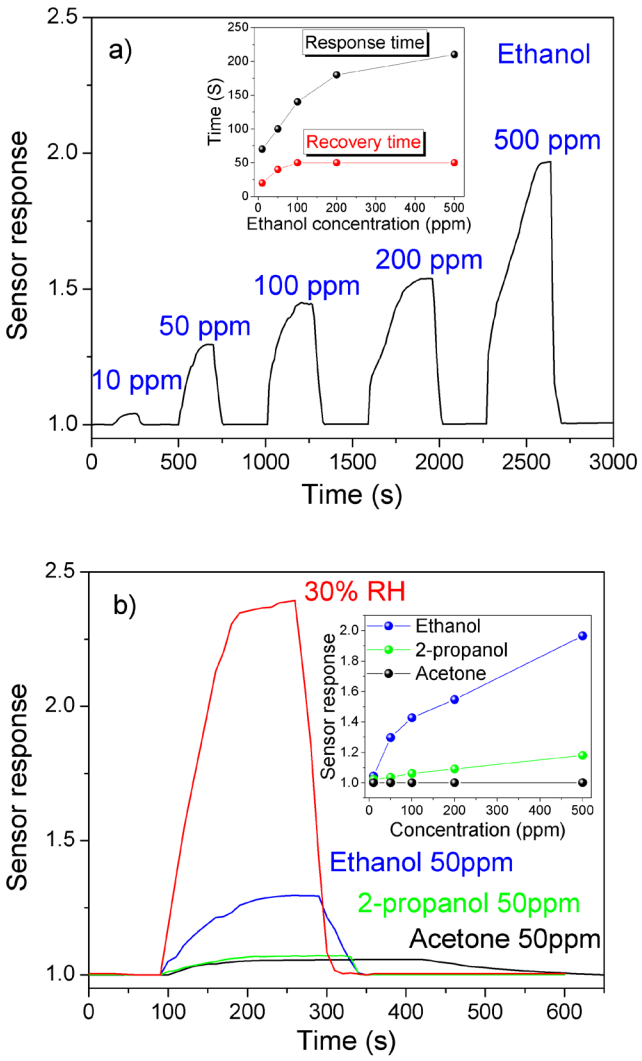

Figure 3. Characterization of gas sensing properties. (a) Time resolved gas sensing measurements of the SnO_2-based sensor for different concentrations of ethanol, at room temperature. (b) Dynamic response of the investigated sensor towards 30% RH and 50 ppm of ethanol, 2-propanol and acetone. The inset shows variation in sensor response for different VOC concentrations.

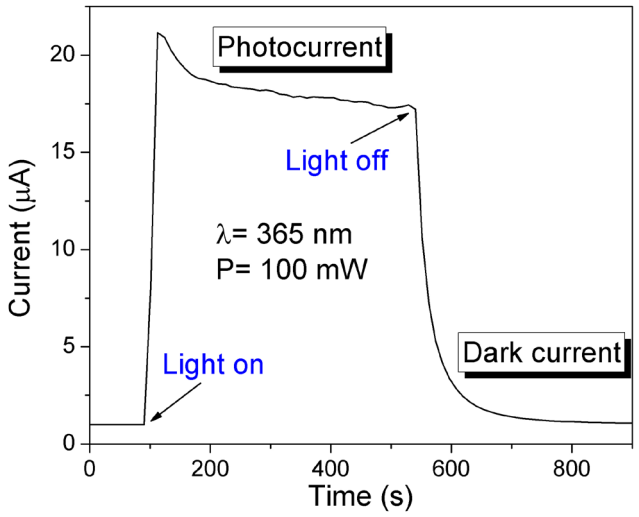

Figure 4. Time-resolved photocurrent response of the screen printed SnO_2 nanosheets.

values and that the sensor exhibits good photoconversion rates suitable for UVA (315 nm–400 nm) radiation monitoring, but the rise and decay times (22 s and 67 s) are average and not suitable for fast photodetection.

The major influence on the good photoconversion properties of SnO_2 nanosheets can be ascribed to specific surface morphology and the formation of oxygen vacancies in the crystal lattice, which was detected with SEM measurements and Raman spectroscopy. Previous studies [29, 30] demonstrated that oxygen vacancies introduce additional electronic states above the O 2p valence band, which can have a strong impact on the measured electronic relaxation time (figure 2(b)), the lifetime of the photogenerated electron–hole pair and the observed good photoconversion rate for the UVA radiation.

4. Conclusion

In summary, SnO_2 powder, with a unique structure, shape and surface morphology, was synthesized by the hydrothermal method. Results from XRD, SEM and Raman measurements revealed that the synthesized sample exhibits a rutile crystal structure, with a crystallite size in the micrometer range and that the investigated powder consists of plane-shaped nanosheets with a high concentration of oxygen vacancies. Paste with SnO_2 nanosheets was screen-printed on a flexible PET substrate with IDEs. AC measurements revealed only a single relaxation time characteristic for interfacial polarization, which originates from the contact surfaces between SnO_2 nanosheets. DC measurements showed that the designed device exhibits very good conductivity with linear dependence of the sensor current with applied voltage. Gas-sensing performance was evaluated at room temperature through the detection of humidity and VOC vapors. The designed sensor showed good response to ethanol in comparison to 2-propanol and acetone indicating selectivity feature of the SnO_2 nanosheets. Moreover, photocurrent measurements showed that the printed flexible sensor has very good photoconversion rate suitable for the UVA radiation detection and monitoring.

Acknowledgments

This work was supported by the Serbian Ministry of Education, Science and Technological Development through projects III44006, III45021 and OI171032.

ORCID iDs

Marko Radović https://orcid.org/0000-0001-7565-4015

References

[1] Wang D, Liu S, Shao M, Zhao J, Gu Y, Li Q, Zhang X, Zhao J and Fang J 2018 *Materials* **11** 1774
[2] Bakr Z H, Wali Q, Ismail J, Elumalai N K, Uddin A and Jose R 2018 *Electrochim. Acta* **263** 524
[3] Ghodsi V and Radovanovic P V 2018 *Chem. Mater.* **30** 3578
[4] Vasanthi V, Kottaisamy M, Anitha K and Ramakrishnan V 2018 *Mater. Sci. Semicond. Process.* **85** 141
[5] Huang H, Ng N, Wu Y and Kong L 2015 *Mater. Des.* **88** 38
[6] Kaur M, Gupta S K, Betty C A, Saxena V, Katti V R, Gadkari S C and Yakhmi J V 2005 *Sensors Actuators* B **107** 360
[7] Das S and Jayaraman V 2015 *Prog. Mater. Sci.* **67** 161
[8] Ambardekar V, Bandyopadhyay P P and Majumder S B 2018 *J. Alloys Compd.* **752** 440
[9] Wu S, Cao H, Yin S, Liu X and Zhang X 2009 *J. Phys. Chem.* C **113** 17893
[10] Kong Z, Liu D, Liu X, Fu A, Wang Y, Guo P and Li H 2019 *J. Nanosci. Nanotechnol.* **19** 850
[11] Yann J, Xu M, Zhang F, Ruan X, Yun J, Zhangn Z and Liao F 2016 *Mater. Lett.* **165** 243
[12] Guo C, Cao M and Hu C 2004 *Inorg. Chem. Commun.* **7** 929
[13] Zhao B, Fan B, Shao G, Zhao W and Zhang R 2015 *ACS Appl. Mater. Interfaces* **7** 18815
[14] Li Y, Liu T and Zhang H 2016 *Mater. Lett.* **176** 9
[15] Xu L, Zeng W and Li Y 2018 *Appl. Surf. Sci.* **457** 1064
[16] Sun P, Cao Y, Liu J, Sun Y, Ma J and Lu G 2011 *Sensors Actuators* B **156** 779
[17] Guo J, Zhang J, Ju D, Xu H and Cao B 2013 *Powder Technol.* **250** 40
[18] Tao T, He L, Li J and Zhang Y 2015 *Mater. Lett.* **138** 45
[19] Wan W, Li Y, Ren X, Zhao Y, Gao F and Zhao H 2018 *Nanomaterials* **8** 112
[20] Yan S, Liang X, Song H, Ma S and Lu Y 2018 *Ceram. Int.* **44** 358
[21] Li Y 2018 *Physica* E **96** 54
[22] Zhang W, Zeng W, Miao B and Wang Z C 2015 *Appl. Surf. Sci.* **355** 631
[23] Zhao C, Gong H, Lan W, Ramachandran R, Xu H, Liu S and Wang F 2018 *Sensors Actuators* B **258** 492
[24] Chen J S and Lou X V 2013 *Small* **9** 1877
[25] Paulowicz I *et al* 2015 *Adv. Electron. Mater.* **1** 1500081
[26] Manikandan K, Dhanuskodi S, Thomas A R, Maheswari N, Muralidharan G and Sastikumar D 2016 *RSC Adv.* **6** 90559

[27] Han S T, Peng H, Sun Q, Venkatesh S, Chung K S, Lau S C, Zhou Y and Roy V A L 2017 *Adv. Mater.* **29** 1700375
[28] Floriano E A, de Andrade Scalvi L A, Sambrano J R and Geraldo V 2010 *Mater. Res.* **13** 437
Hu J, Bando Y, Liu Q and Golberg D 2003 *Adv. Funct. Mater.* **13** 493
[29] Cox D F, Fryberger T B and Semancik S 1989 *Surf. Sci.* **224** 121
[30] Mäki-Jaskari M A and Rantala T T 2002 *Phys. Rev.* B **65** 245428
[31] Chen Y, Wang X, Shi C, Li L, Qin H and Hu J 2015 *Sensors Actuators* B **220** 279
[32] Diéguez A, Romano-Rodríguez A, Vila A and Morante J R 2001 *J. Appl. Phys.* **90** 1550
[33] Rumyantseva M N, Gaskov A M, Rosman N, Pagnier T and Morante J R 2005 *Chem. Mater.* **17** 893
[34] Barsoukov E and Macdonald J R 2005 *Impedance Spectroscopy: Theory, Experiment, and Applications* (New York: Wiley)
[35] Ponce M A, Bueno P R, Varela J, Castro M S and Aldao C M 2008 *J. Mater. Sci.: Mater. Electron.* **19** 1169
[36] Righettoni M, Amann A and Pratsinis S E 2015 *Mater. Today* **18** 163
[37] Matindoust S, Baghaei-Nejad M, Abadi M H S, Zou Z and Zheng L R 2016 *Sens. Rev.* **36** 169
[38] Zhu H, Li Q, Ren Y, Gao Q, Chen J, Wang N, Deng J and Xing X 2018 *Small* **14** 1703974
[39] Zhai T, Fang X, Liao M, Xu X, Zeng H, Yoshio B and Golberg D 2009 *Sensors* **9** 6504
[40] Lin Q, Li Y and Yang M 2012 *Sensors Actuators* B **173** 139
[41] Navazani S, Shokuhfar A, Hassanisadi M, Askarieh M, Carlo A D and Agresti A 2018 *Talanta* **181** 422
[42] Zhang J, Guo J, Xu H and Cao B 2013 *ACS Appl. Mater. Interfaces* **5** 7893
[43] Zhou Q, Chen W, Li J, Tang C and Zhang H 2015 *Mater. Lett.* **161** 499
[44] Wang B, Sun L and Wang Y 2018 *Mater. Lett.* **218** 290

ACS APPLIED MATERIALS & INTERFACES

Research Article

Cite This: ACS Appl. Mater. Interfaces 2019, 11, 6257−6266

www.acsami.org

Multifunctional Screen-Printed TiO_2 Nanoparticles Tuned by Laser Irradiation for a Flexible and Scalable UV Detector and Room-Temperature Ethanol Sensor

Georges Dubourg* and Marko Radović

BioSense Institute-Research and Development Institute for Information Technologies in Biosystems, University of Novi Sad, Dr Zorana Đinđića 1, Novi Sad 21000, Serbia

Supporting Information

ABSTRACT: Recently, multifunctional devices printed on flexible substrates, with multisensing capability, have found new demand in practical fields of application, such as wearable electronics, soft robotics, interactive interfaces, and electronic skin design, revealing the vital importance of precise control of the fundamental properties of metal oxide nanomaterials. In this paper, a novel low-cost and scalable processing strategy is proposed to fabricate all-printed multisensing devices with UV- and gas-sensing capabilities. This undertaken approach is based on the hierarchical combination of the screen-printing process and laser irradiation post-treatment. The screen-printing is used for the patterning of silver interdigitated electrodes and the active layer based on anatase TiO_2 nanoparticles, whereas the laser processing is utilized to fine-tune the UV and ethanol-sensing properties of the active layer. Different characterization techniques demonstrate that the laser fluence can be adjusted to optimize the morphology of the TiO_2 film by increasing the contribution from volume porosity, to improve its electrical properties and enhance its UV photoresponse and ethanol-sensing characteristics at room temperature. Furthermore, results of the UV and ethanol-sensing investigation show that the optimized UV and ethanol sensors have good repeatability, relatively fast response/recovery times, and excellent mechanical flexibility.

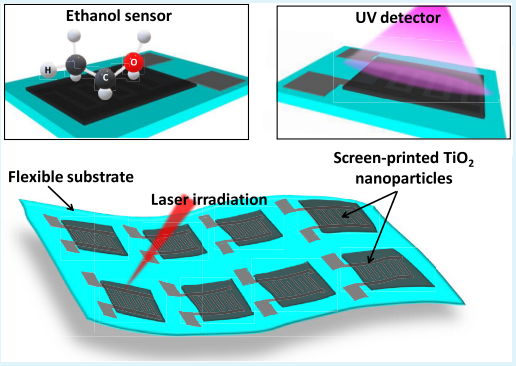

KEYWORDS: *laser processing, multifunctional sensors, flexible substrates, screen-printing, titanium dioxide*

1. INTRODUCTION

Metal oxides (MOx) represent an important class of materials since they can be easily shaped to provide them with specific features and improved mechanical, chemical, electrical, and optical properties. It is then clearly understandable why they have attracted a lot of attention in a wide range of applications, including optoelectronics, gas-sensing devices,[1−4] and more recently in the development of multifunctional devices able to perform several of these tasks.[5−8] Their conjunction with printing technologies and flexible substrates can offer the potential for scalable and low-cost fabrication and open new opportunities for various sensing applications in wearable and flexible multisensing devices, including watches, glasses, patches, bandages, food packaging, and other fields that are currently difficult to reach with traditional semiconductor technology. A major challenge for the fabrication of flexible devices based on MOx materials is to lower the processing temperature to make it compatible with flexible substrates such as plastics, as most plastic substrates degrade at ∼150 °C. Indeed, annealing process at an elevated temperature is an important step when processing MOx material since it contributes to enhancement of specific properties and thus enables integration in functional devices. Typically, this step ensures the removal of residual solvents and organic binders, improves the chemical homogeneity of the MOx-based film, controls its stoichiometry, composition, phase structure, and microstructure, and improves the interfacial adhesion of the film/substrate and interparticle connection. The thermal treatment of MOx nanomaterials is generally carried out in an oven or furnace at temperatures ranging from 300 to 1000 °C, which are clearly incompatible with thermally sensitive substrates like cellulose, textile, and polymers. Some solutions have been explored to overcome this problem, including near-infrared,[9,10] microwave,[11,12] and laser treatments.[13,14] Among them, laser sintering offers many advantages because of its capability of selective treatment and localized thermal effect, its fine spatial resolution, along with the possibility to be processed in ambient atmosphere. Over the past decade, laser irradiation has been employed in conjunction with diverse MO films and nanostructures. For instance, laser treatment was used to improve the gas-sensing and photocatalytic properties of nickel oxide.[15,16] Effect of the laser irradiation on ZnO and

Received: November 16, 2018
Accepted: January 17, 2019
Published: January 17, 2019

DOI: 10.1021/acsami.8b19976
ACS Appl. Mater. Interfaces 2019, 11, 6257−6266

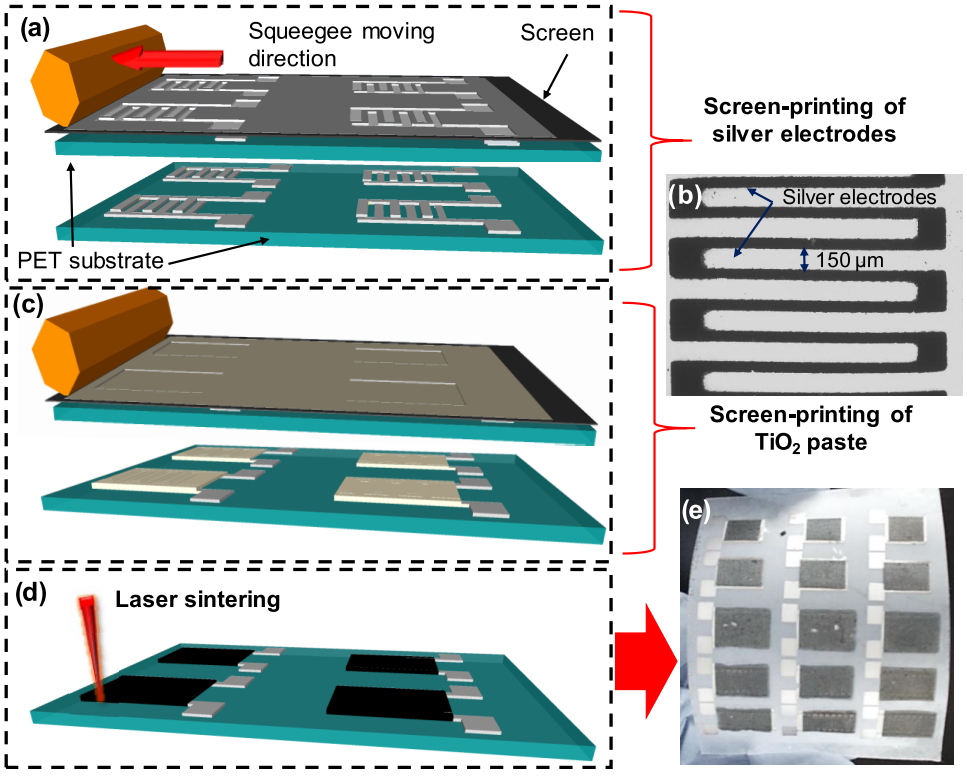

Figure 1. Schematic representation of a multisensor platform design: (a), (c), and (d) process sequence of the flexible devices, (b) SEM image of the silver electrodes, and (e) optical image of 3 × 5 sintered device matrix fabricated on a PET substrate.

SnO_2 was also studied to enhance their electrical and optical properties and surface morphology for transparent electrodes,[17,18] field effect transistor,[19,20] and gas sensor applications.[21−23] Furthermore, interaction of the laser irradiation with TiO_2 was extensively explored but with attention importantly on the enhancement of its dye-sensitized solar cells and photocatalytic performance through optimization of basic parameters of the laser treatment method[24−28] even though TiO_2 has other outstanding properties. Indeed, it was identified to be the appropriate material in many fields, including water purification, photocatalysis,[29,30] UV and gas sensors,[31−33] dye-sensitized solar cells,[34] light-emitting diodes,[35] and in biomedical engineering[36] because of its unique electrical, physical, chemical, and optical properties. Hence, to fully exploit the unique properties of TiO_2, especially those related to its sensing capabilities, it is essential to investigate the effect of the laser irradiation on the sensing behavior of TiO_2, which is a key element for its integration in flexible and wearable multifunctional devices.

In this present work, we introduce a novel approach for tailoring the UV- and ethanol-sensing capabilities of screen-printed anatase TiO_2 nanoparticles. The entire process includes two screen-printing steps and low-temperature laser post-treatment, indicating the possibility of arbitrary substrates and low-cost and large-area fabrication of multisensing devices. Effects of the laser irradiation on UV- and gas-sensing performances on the screen-printed TiO_2 nanoparticles have been studied in detail, and it was found that a substantial improvement of the photoresponse and ethanol sensitivity can be obtained by simply adjusting the laser fluence. Basic mechanisms for the observed behavior are discussed and correlated with results from surface analysis and electrical characterization of the TiO_2 laser-treated film. Photo- and gas-sensing characteristics, including repeatability, response times, and mechanical stability, are carefully examined to demonstrate the actual performance of the printed devices to be used as a flexible multisensing platform.

2. EXPERIMENTAL PROCEDURE

Multifunctional sensors were fabricated in a resistive configuration consisting of a TiO_2-based active layer deposited on interdigitated electrodes (IDE) previously patterned on a flexible substrate. The fabrication process of the flexible UV and ethanol sensors, made of a single common active material (anatase TiO_2 nanoparticles) is shown in Figure 1. Briefly, we selected a lightweight and economical poly(ethylene terephthalate) (PET) substrate as a flexible building platform for the sensor design. Then, to preserve the attractiveness of the sensors as low-cost and potentially mass-produced devices, we developed a simple and economic technological process consisting of two screen-printing steps for the deposition of silver electrodes and paste with TiO_2 nanomaterial. Initially, commercial silver paste (HPS-021LV, Novacentrix) was screen-printed with a semiautomatized screen printer (EKRA 2H screen-printer, Dornstadt, Germany) on the PET substrate to create the interdigitated electrodes (Figure 1a). After printing, the samples were heated in an oven at 110 °C for 15 min. The individual digit of the IDE structure is 4 mm long and 100 μm wide, and it is separated by a gap of 100 μm from the next digit, as shown in Figure 1b, exhibiting scanning electron microscopy (SEM) image of Ag-interdigitated electrodes. The next step involved the screen-printing of the TiO_2-based paste on top of the IDE. For this purpose, a TiO_2-based paste was prepared and then screen-printed to cover locally the surface of the electrodes (Figure 1c). The functional paste based on TiO_2 nanoparticles was prepared following the previously published procedure,[37] where commercial anatase TiO_2 nanopowder, poly(vinylpyrrolidone) (PVP), and terpineol were used. First, PVP from Sigma-Aldrich (2 g) was dissolved in ethanol (10 mL). Next, anatase TiO_2 (1 g) nanopowder (Sigma-Aldrich, particle size <25 nm) was dispersed in terpineol (400 μL) (Sigma-Aldrich), followed by addition of PVP solution (600 μL). Obtained suspensions

DOI: 10.1021/acsami.8b19976
ACS Appl. Mater. Interfaces 2019, 11, 6257−6266

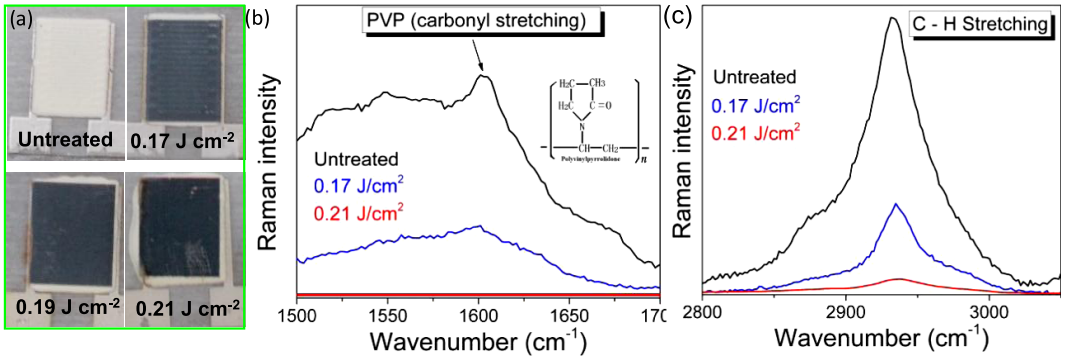

Figure 2. (a) Optical images of untreated and laser-sintered samples. (b) Raman spectra of the untreated sample and samples treated at 0.17 and 0.21 J cm^{-2} in the spectral range between 1000 and 1800 cm^{-2}. (c) Raman spectra of the untreated sample and samples treated at 0.17 and 0.21 J cm^{-2} in the spectral range between 2800 and 3200 cm^{-2}.

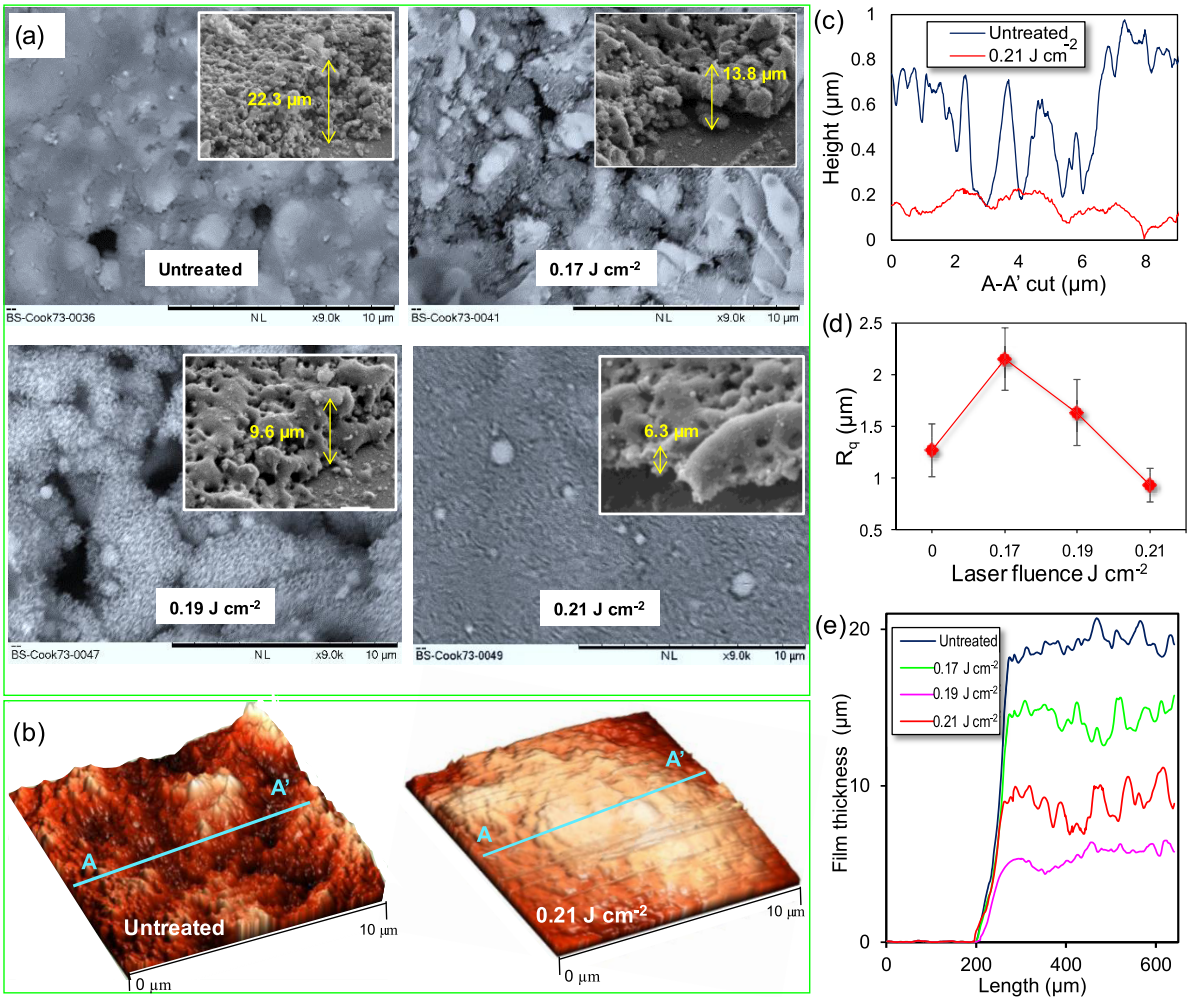

Figure 3. (a) SEM images of untreated and laser-treated screen-printed TiO_2 films, inset: side view of untreated and treated samples. (b) AFM characterization of the untreated sample and sample treated at 0.21 J cm^{-2}. (c) Thickness profile from AFM analysis of the untreated sample and sample treated at 0.21 J cm^{-2}. (d) Root mean square roughness of the investigated films as a function of the laser fluence. (e) Thickness profile dependence on laser fluence for the different TiO_2 films.

were treated with ultrasonic horn for 10 min, respectively. After screen-printing, the sample with the resulting patterned TiO_2-based paste was dried at ambient temperature for 2 days.

Afterward, a laser-processing step was employed to control precisely the properties of the screen-printed TiO_2 films in a large-scale manner (Figure 1d). The laser treatment of printed films was carried out by using a diode-pumped Nd:YAG laser cutter Rofin-Sinar Power Line D-100, operating in the NIR range at 1064 nm. The length of the line scanned by the laser was designed to be 5 mm, with line intervals of 10 μm. The laser beam was precisely focused on the surface of the screen-printed film and the laser pulse was set with a frequency of 65 kHz and a speed of displacement of 500 mm s^{-1} to obtain sufficient pulse overlapping. Afterward, the laser fluence was varied by adjusting the laser pump current. Basically, three samples were treated with input current values of 27, 28, and 29 A corresponding to laser fluences of 0.17, 0.19, and 0.21 J cm^{-2},

DOI: 10.1021/acsami.8b19976
ACS Appl. Mater. Interfaces 2019, 11, 6257−6266

respectively, and one sample was kept untreated to be used as a reference. Figure 1e shows a matrix of laser-treated films made of TiO_2 nanoparticles, providing clear evidence that the developed process is convenient for the large-scale fabrication of functional sensors.

Micro-Raman spectroscopy measurements were performed in the 1000−3000 cm^{-1} range, on the Jobin Yvon T64000 spectrometer, equipped with a nitrogen-cooled CCD detector and the solid-state Nd:YAG laser, operating at λ = 532 nm.

The morphology of the screen-printed TiO_2 film was examined by a scanning electron microscope (HITACHI TM3030) and atomic force microscopy (AFM). Images from AFM were collected with an NTEGRA prima microscope, operating in semicontact mode. The thickness profiles were measured from SEM images with the software three-dimensional (3D) image Viewer (HITACHI) and roughness characteristics of the film were obtained from the multiprofile analyses provided in the Supporting Information (Figure S1 and Table S1) and measured with the same software. Profile analysis of the AFM measurements was performed from the two-dimensional AFM images provided in the Supporting Information (Figure S2) using Gwyddion software. The electrical properties of the sensors were measured by using a Yokogawa−Hewlett-Packard semiconductor probe analyzer and optical transmission measurements with a UV−vis spectrometer (DSH-L6-L6S). The photoactivation of the devices was carried out with a 365 nm light-emitting diode in a faraday cage and characterized with the same semiconductor probe analyzer. For the ethanol-sensing characterization, the contact pads of the printed devices were connected to wires, fixed on a plastic holder, and placed on the top of a closed 15 cl plastic chamber composed of an inlet for ethanol solution injection, controllable N_2 flow system, evaporator, and fan for ethanol vapor circulation. The sensing operation was performed at 25 °C, and the ethanol gas-sensing characterization was monitoring using the semiconductor probe analyzer.

3. RESULTS AND DISCUSSION

3.1. Structural Characterization. Figure 2a shows optical images of untreated samples and samples sintered at laser fluences of 0.17, 0.19, and 0.21 J cm^{-2}. It can be seen that laser sintering introduces a change in the apparent color of printed films, from white for the untreated TiO_2 to gray for the samples treated with laser fluence of 0.17 J cm^{-2} and as the laser fluence increased the samples become black.

Observed changes in contrast can originate from carbonization of organic binders present in the paste, during the laser treatment or from microscale reorganization of the surface roughness and porosity. To gain a better insight into chemical composition of the laser-treated film and to directly monitor changes in carbon content, Raman spectroscopy measurements were performed in the spectral range where organic (carbohydrate) molecules have distinct fingerprint modes, before and after laser treatment. From the analysis of the obtained results (Figure 2b), it can be clearly seen that laser treatment induces a dramatic decrease in the carbonyl stretching peak at 1605 cm^{-1},[38] which is characteristic for PVP polymers, providing clear evidence of complete degradation and removal of PVP component (chemical structure given in Figure 2b). In the case of a C−H bond at 2935 cm^{-1}, we can see a very weak peak in the spectrum (Figure 2c) even after treatment at the highest laser fluence. Such findings point out that after laser sintering, there are some traces of organic components in the investigated film, which probably originate from terpineol component that was used in the paste matrix. Most important is to highlight the fact that the characteristic peak of graphite or similar compounds was not detected, indicating that darkening of the samples does not originate from the formation of carbon allotropes such as graphite but probably from the microscale reorganization of the surface roughness and porosity that strongly diffuses the incident light. In addition, it can be noticed from the EDX characterization shown in Figure S3 that the Ti and O signatures are present in the untreated and laser-treated samples, which confirms that the laser irradiation does not change the chemical composition of the TiO_2 nanoparticles.

Therefore, additional investigations were performed with SEM measurement to evaluate the change of the film morphology in the laser-sintered samples. Figure 3a exhibits top- and side-view images of the TiO_2 film before and after laser treatment at various laser fluences, which clearly demonstrate that increase in laser fluence induces significant modifications of the film morphology. From SEM image of the untreated film, it can be established that micron-sized particles, in the form of clusters, constitute the surface layer. These agglomerates are formed from individual nanoparticles held together by the dried organic additives. When irradiated at 0.17 W cm^{-2}, the film roughness increases, exhibiting bigger pores due to the formation of melted droplets. These droplets are formed during the breaking of the large agglomerates accomplished by laser thermal evaporation of organic components, but the investigated film still lacks better interconnection between the individual TiO_2 particles. With further increase of the laser fluence, laser treatment leads to sintering of the anatase nanoparticles and the printed film becomes denser due to the formation of necking between individual nanoparticles, introducing better mutual connectivity. Figure 3a reveals that the film sintered at 0.19 J cm^{-2} still has a rough film, but the formation of solid layers becomes dominant, due to the complete release of the organic components and the sintering effect. When irradiated at 0.21 J cm^{-2}, the screen-printed film is transformed into solidified, uniform, and dense ceramic material.

These results are confirmed by the 3D AFM images of the untreated sample and film treated with 21 J cm^{-2} laser fluence exhibited in Figure 3b. Indeed, in this figure, it can be clearly observed that the surface of the untreated sample consists of agglomerated micron-sized particles, whereas the laser-treated films exhibit a finer surface structure with particles in the nanometer range, in agreement with SEM measurements. Direct comparison of AFM images offers clear evidence that laser treatment induces breaking of large agglomerates into nanoparticles and provides a powerful tool for fine tuning of surface corrugation. In Figure 3c are compared typical line profiles from AFM measurements, taken along the $A-A'$ direction, as denoted in the corresponding 3D images. The observed behavior points out that variations in the line profile of the sintered sample are less pronounced in comparison to the untreated sample, suggesting that the laser-treated surface has improved surface ordering, lower roughness, and much finer morphology.

Figure 3d shows the root mean square roughness R_q as a function of the laser fluence obtained from multiprofile analyses. It can be noticed that the roughness of the TiO_2 film is increased when the film is treated at 0.17 J cm^{-2} and then decreased when the surface is treated at higher laser fluences due to the densification of the TiO_2 film, confirming results deducted from SEM and AFM images.

Figure 3e shows the thickness profile of the investigated samples. The presented results demonstrate that the film thickness is reduced from 20 to 13.00, 10, and 6 μm after irradiation at 0.17, 0.19, and 0.21 J cm^{-2}, respectively, which

DOI: 10.1021/acsami.8b19976
ACS Appl. Mater. Interfaces 2019, 11, 6257−6266

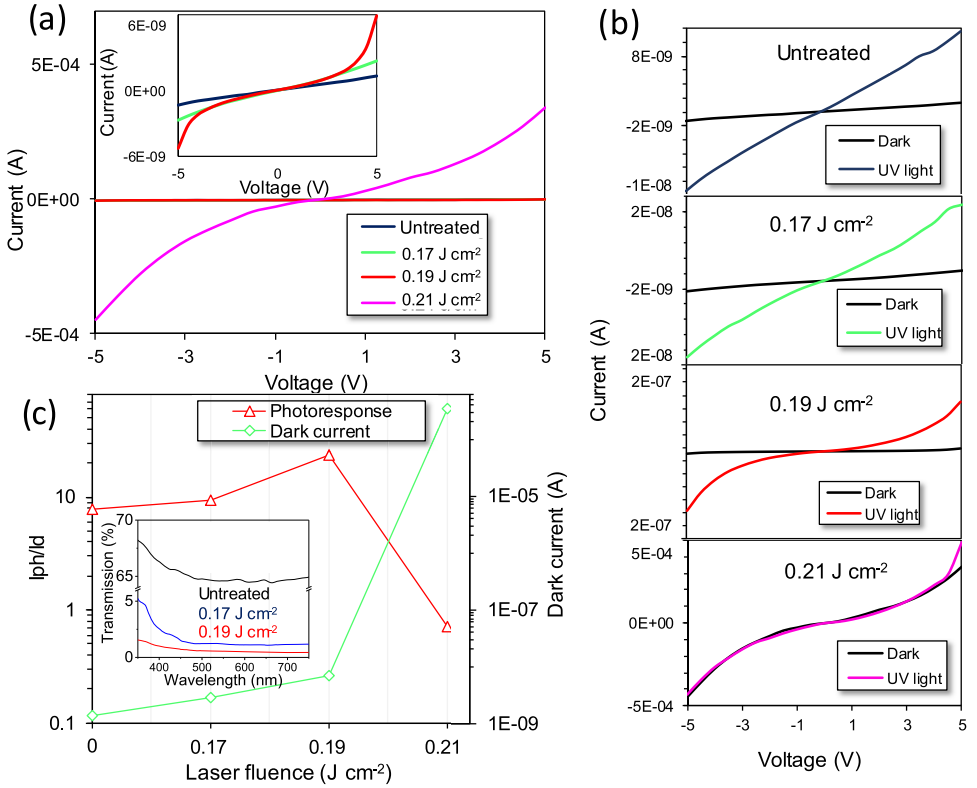

Figure 4. (a) Dark Current vs voltage curves for untreated samples and samples sintered at 0.17, 0.19, and 0.21 J cm^{-2} laser fluences, the inset is the $I-V$ curve of untreated and treated samples. (b) Current vs voltage curves under UV illumination for untreated samples and samples sintered at 0.17, 0.19, and 0.21 J cm^{-2} laser fluences. (c) Photoresponse and dark current as a function of the laser fluence. Inset: optical transmission of the untreated sample and samples treated at 0.17 and 0.19 J cm^{-2} in the 350−750 nm wavelength range.

can be directly correlated to the removal of organic binder components with laser radiation and the densification of the screen-printed TiO_2 film during the sintering process.

3.2. UV Detection Performance. UV sensors are employed today in a wide range of applications, including healthcare, space technology, and environmental monitoring. Those applications require often large-scale and low-cost fabrication processes and certain flexibility to allow their integration into wearable and flexible devices that are capable of working under inherent bending. Today, this could be achieved through printing technology; hence, several studies regarding printed photodetectors on flexible substrates based on various metal oxide materials have been reported.[39,40] However, there is still a lack of a scalable and routine process to allow their integration into a large and flexible surface. The process proposed in our work is fast, scalable, low cost, and does not require high-temperature steps, which is fully compatible with flexible substrate technologies. As described previously, our method consists of only two screen-printing steps and a post-treatment step by laser sintering to optimize the UV photosensitivity of the TiO_2 screen-printing film.

To evaluate the potential of the resulting samples to be used as a UV detector, direct current (DC) electrical charaterization was performed for the untreated samples and samples sintered at 0.17, 0.19, and 0.21 J cm^{-2} laser fluences. Figure 4a shows $I(V)$ curves of the investigated sensors, measured in the −5 to 5 V range. All measured curves exhibit a typical semiconductor response, with an evident deviation from linear current−voltage behavior.

Figure 4a clearly reveals that increase in laser fluence induces a significant increase in the current values, thus improving the conductivity of the printed TiO_2 film. Indeed, for the untreated sample, the profile of the $I(V)$ curve corresponds to that of the material with poor conductivity (1.36 nA at 5 V), whereas the $I(V)$ curve of the sample treated with 0.21 J cm^{-2} has a 3 orders of magnitude higher current (341 μA at 5 V). For porous nanomaterials, wherein nanoparticles are packed together, DC transport properties of the film are generally governed by the grain-boundary resistance, since the resistance at these contacts is much higher than the resistance across a single nanoparticle. During sintering process, most of these grain boundaries vanish as the nanoparticles form necklike structures and the grains connect together. In this case, the grain conductivity becomes dominant,[41] leading to an observed increase in the current values. Another contribution to the DC conductivity comes from formation of oxygen vacancies in TiO_2 nanoparticles with laser treatment, since these defects introduce additional electronic states inside the band gap (donor impurities).[37]

Afterward, to define the best sintering process for the device to be used as a UV detector, photocurrent measurements were performed for the fabricated TiO_2-printed devices before and after laser treatment at 0.17, 0.19, and 0,21 J cm^{-2}. To highlight the UV detection capabilities of the devices, all samples were studied by measuring the current−voltage ($I-V$) relationships at 365 nm wavelength illumination at 20 mW cm^{-2} light intensity and plotted in Figure 4b together with the dark current for comparison. Figure 4b clearly demonstrates that a significant increase in the current is observed under UV light illumination for the untreated samples and samples treated at 0.17 and 0.19 J cm^{-2} whereas no significant rise of current can be noticed for the sample treated at 0.21 J cm^{-2}.

DOI: 10.1021/acsami.8b19976
ACS Appl. Mater. Interfaces 2019, 11, 6257−6266

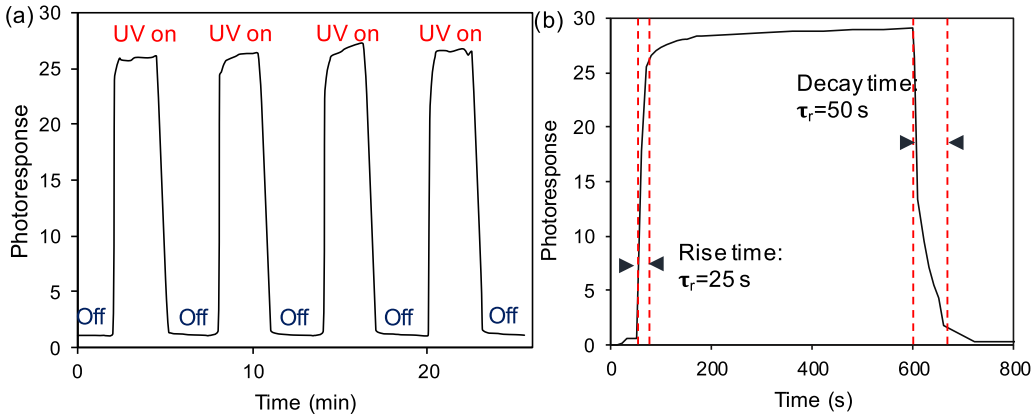

Figure 5. (a) Time-resolved photoresponses of the TiO_2 device under a continuous UV light rectangle pulse (b) Highlights of the dynamic response behavior (response/recovery times) for the photodetector under UV illumination.

This is confirmed in Figure 4c, showing the photocurrent-to-dark current ratio called the photoresponse and the dark current of the TiO_2 film as a function of the laser fluence. The photoresponse is improved as the the laser fluence is raised to 0.19 J cm^{-2} and subsequently deteriorated for higher laser fluence, whereas the dark current is still rising as the laser fluence is increased until 0.21 J cm^{-2}.

This result can be attributed to several competing parameters that determine the photoresponse efficiencies of the investigated samples, such as: (i) good semiconducting properties of the film, with additional contribution of oxygen-vacancy defect electronic states and (ii) the rough structure of the TiO_2 film that ensures a high number of surface trap states, thus prolonging the lifetime of photogenerated carriers.

Indeed, the highest value of photocurrent was obtained for a sintering fluence of 0.19 J cm^{-2}. This is due to the removal of the organic binder inducing the interconnection of the TiO_2 nanoparticles, which is consistent in the SEM picture from Figure 3a. Formation of necking between individual nanoparticles provides more fluent electron transfer paths across the surface of the film. Moreover, the screen-printed film with TiO_2 nanoparticles still has a rough film, which increases light scattering effects and thus improves the light-harvesting efficiencies.

If the film is treated with laser fluence lower than 0.19 J cm^{-2}, the sintering process increases the porosity and roughness of the film compared with the untreated sample. However, the TiO_2 film still retains the organic binder and lack of interconnection between the TiO_2 particles, resulting to a lower photoresponse.

In the opposite case, if the film is treated with a laser fluence higher than 0.19 J cm^{-2}, the film becomes more compact and bulky with low porosity and roughness. This morphological change in the film surface induces a better electrical conductivity but also a low photoresponse due to degradation of the active surface area. Thus, there is a competition between increasing conductivity and decreasing the active surface area with high laser fluence. Then, to improve the photoresponse of the UV sensor, there is an intermediate laser fluence found in our case at 0.19 J cm^{-2}.

Moreover, the optical transmission shown in the inset of Figure 4c, measured for the untreated samples and samples with highest photoresponse (0.17 and 0.19 J cm^{-2}), in the 350−750 nm wavelength range, support the obtained results. In fact, measurements reveal a significant drop in transmission of the incident light for the laser-treated samples. This drop originates from diffuse light scattering induced by surface roughness reorganization, and it was noticed as a change in colorization of the samples from white to black. Measured transmission spectra for all investigated samples have strong optical absorption at the middle of UVA (315−400 nm) part of the spectrum, which can be attributed to absorption of the PET substrate. Optical absorption onset for a laser-treated sensor is slightly shifted toward the visible range due to increased concentration of oxygen vacancies and defect electronic states in the band gap of titania,[37] giving rise to better photoresponse and high photocurrent values in comparison to those of an untreated sensor.

Next, the stability of the UV sensor based on TiO_2 sintered with 0.19 J cm^{-2} laser fluence was evaluated by measuring its time-dependent responses (photocurrent-to-dark current ratio) under a bias of 5 V with periodically repeating a 365 nm UV illumination (alternating dark and light conditions) with an on/off interval of 5 min. Four repeat cycles under an on/off light intensity of 20 mW cm^{-2} are displayed in Figure 5a, in which the UV response was observed to be consistent and repeatable over the weeks, as shown in Figure S4. Next, the time response of the UV sensors was estimated. The rise time (τ_r) and decay time (τ_d) are defined as the rise time ranging from 10 to 90% and the fall time ranging from 90 to 10% of the maximum photocurrent.

Figure 5b shows the more detailed transient photoresponse of the device from Figure 5a. The photoresponse rises to 90% of the peak value in 25 s, whereas it takes a longer time (50 s) to recover the initial value on turning off the UV light due to the decay process in which photogenerated electrons recombine with holes in the valence band.

3.3. Ethanol-Sensing Performance. In addition to UV sensors, the same screen-printed TiO_2 film can be improved to be used as an ethanol sensor by simply adjusting the laser fluence of the post-treatment process.

Indeed, previous studies have shown that TiO_2 is an appealing material for ethanol sensing, due to its wide-band gap semiconductor properties and high surface reactivity to gases. Various methods have been explored to optimize ethanol-sensing properties of TiO_2, such as the use of nanostructured TiO_2-like nanowires, nanotubes, or/and by doping it with noble metals, like silver, iron, platinum.[42−45] Moreover, all of these examples of TiO_2-based ethanol sensors either work at temperatures above 150 °C or/and require a

DOI: 10.1021/acsami.8b19976
ACS Appl. Mater. Interfaces 2019, 11, 6257−6266

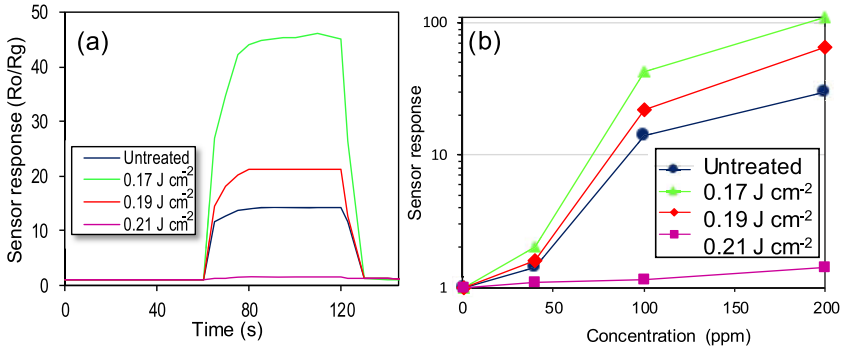

Figure 6. (a) Time-resolved ethanol responses of untreated and treated TiO_2 films at 100 ppm. (b) Gas response of untreated and laser-treated TiO_2 films as a function of ethanol concentration.

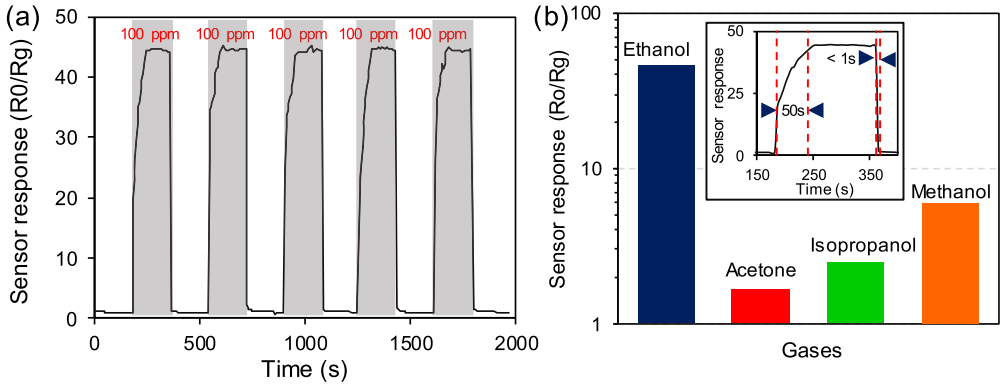

Figure 7. (a) Sensor response of the sample treated at 0.17 J cm^{-2} under dynamic cycles between 0 and 100 ppm concentrations of ethanol at 25 °C. (b) Response characteristics of the TiO_2 sensor, measured at room temperature for various volatile organic pollutants under the same concentration of 100 ppm. Inset: highlight of the dynamic response behavior (response/recovery times) for the sensor under an ethanol concentration of 100 ppm.

high calcination temperature, which limits their integration into flexible substrates. Here, we propose a robust solution for producing ethanol sensors based on TiO_2 nanoparticles printed on a flexible substrate, operating at room temperature. The pulsed laser treatment is introduced for the first time to replace the calcination step and improve ethanol-sensing properties of TiO_2 by controlling the morphology and structure of TiO_2 screen-printed films.

To investigate the influence of the laser treatment on the response of the devices, the sensor response and recovery as a function of time toward 100 ppm ethanol were measured at room temperature (25 °C) for untreated and treated samples. Here, the gas sensor response is given by the ratio of the initial electrical resistance in air to the electrical resistance when ethanol vapor is introduced (R_0/R_g). Figure 6a clearly demonstrates that the highest response for 100 ppm ethanol vapor was measured for the sample treated at 0.17 mJ cm^{-2}; then, the response decreases as the laser fluence increases. This trend is confirmed by Figure 6b exhibiting the sensor response for all samples as a function of the ethanol concentration wherein it can be noticed that by increasing the ethanol concentration, the response value increases for all samples except for that treated with the higher laser fluence where no significant change can be observed. Moreover, the highest response was also measured for the sample treated with the lowest laser fluence for all ethanol concentrations.

The rise of the response to ethanol of the sample treated with laser power of 0.17 J cm^{-2} compared to the untreated sample is due to its higher porosity and roughness and higher conductivity, as evidenced from the SEM images from Figure 3a and electrical characterization from Figure 4a. Then, by further increasing the laser fluence to 0.19 J cm^{-2}, the response decreases while the conductivity increases and the film still maintains its porous and rough surface but to a lesser extent.

At laser fluence of 0.21 J cm^{-2}, the sensor response is almost null due to the complete loss of surface porosity, roughness, and formation of a bulky and dense film with a lower surface-to-volume ratio, which is consistent with the SEM and AFM observation from Figure 3a,b. In this case, laser treatment not only produces rise of the conductivity but also leads to reduction of the sensing area that is directly related to the detected drop of the sensor response. Here, it is interesting to notice that improvement of the film conductivity does not have a significant influence on the gas sensitivity of the fabricated sensors unlike the UV detectors where sustainable improvement of the UV sensitivity is achieved through compromise between the surface morphology of the film and its electrical conductivity. Indeed, the key structural parameters to determine the gas-sensing properties are the amount of activated adsorption sites and the gas-diffusion ability of the sensitive film. A rough surface with a small grain size will create a higher specific surface area than a compact layer with sintered nanoparticles. Moreover, an open and porous structure will allow the diffusion and distribution of gas molecules into the volume of the film, where the inner grains can contribute to the improvement of gas-sensing properties.

These results clearly demonstrate the capacity of the laser radiation to interact with the surface structures and

DOI: 10.1021/acsami.8b19976
ACS Appl. Mater. Interfaces 2019, 11, 6257–6266

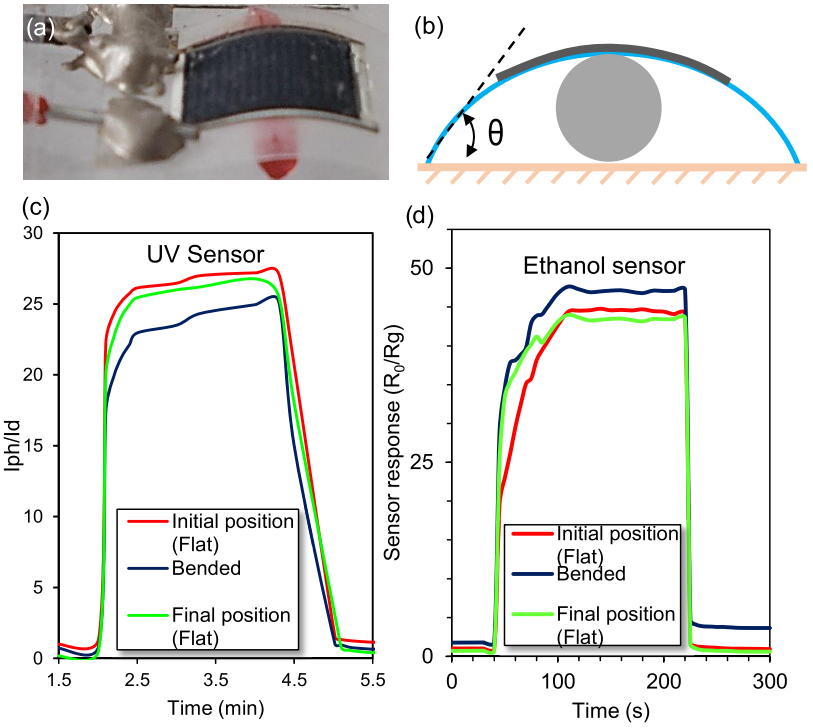

Figure 8. (a) Optical image of the fabricated flexible TiO_2-based sensor. (b) The schematic image of the direction of the bending of the sensor and the corresponding curvature angle. (c) Time-resolved UV sensor responses of 0.19 J cm^{-2} treated TiO_2 film under UV light and bending conditions. (d) Time-resolved ethanol responses of 0.17 J cm^{-2} treated TiO_2 film at 100 ppm under bending condition.

morphologies of the MOx-based nanomaterials and to fine-tune their multifunctionality.

Afterward, to confirm the potential of the fabricated sensor to be used as an ethanol sensor, repeatability, which is an important parameter in terms of reliability of sensors, was evaluated for the sample treated with the optimized laser fluence of 0.17 J cm^{-2}. Figure 7a illustrates the gas response evolutions of the laser-treated sample in 5 cycles toward 100 ppm ethanol at room temperature. The reproducibility of the sensor reveals that it maintains its initial response amplitude without a clear decrease upon five cycle's successive sensing tests at 100 ppm ethanol, which is confirmed by the measurements performed for 5 weeks, shown in Figure S4.

Selectivity is another important aspect of the gas-sensing performance. Thereupon, to explore the selectivity of the TiO_2 sensors, other volatile organic pollutants (VOPs), including acetone, isopropanol, and methanol, were also measured under the same conditions and the results are shown in Figure 7b. It can be seen that among all different targeted gases tested with the same concentration of 100 ppm, the response of the TiO_2 sensor to ethanol is the highest, indicating that the TiO_2-based sensor has comparatively favorable selectivity to ethanol.

Moreover, a fast response and recovery time are also commonly desired characteristics. Herein, the response time is the time taken by a sensor to achieve 90% of the maximum response and the recovery time is the time needed for the sensor to drop to 10% of its initial response. The inset in Figure 7b shows the more detailed sensor response, and recovery of this device exhibits a fast response and a recovery time of less than 1 min.

3.4. Flexibility Performance. Mechanical stability is essential to flexible electronic devices, especially for applications where high stability over the mechanical deformation is required, such as wearable electronics and smart food packaging. Therefore, the influence of the mechanical strain on the sensor response behavior has to be investigated. Sensing measurements were then performed when the sensors were bended at 40° and after returning to the flat position. The optical image of the screen-printed TiO_2 sensor under bending at 40° is shown in Figure 8a. The schematic image of the direction of the bending-induced mechanical strain in the sensor is described in Figure 8b. Figure 8c shows the real-time photoresponse of the sensor sintered at 0.19 J cm^{-2} under a 365 nm light illumination (20 mW cm^{-2}) at room temperature when the sensor is in its initial position, bent at 40°, and after its return to the flat position. From the obtained results, it can be concluded that the sensors' response showed negligible effect over the mechanical strain. The same measurements were also performed at room temperature for the device sintered at 0.17 J cm^{-2} at 100 ppm ethanol concentration, as exhibited in Figure 8d. This figure clearly demonstrates that, as in the previous case, the effect of the mechanical strain can be neglected. Thus, these results clearly indicate that bending of the sensor did not affect the sensing performance of the fabricated devices.

4. CONCLUSIONS

In summary, we have developed a new strategy for producing low-cost, scalable, flexible, and multifunctional devices for UV detection and ethanol sensing, which is based on printed TiO_2 nanoparticles with laser-tunable properties. The main idea behind the undertaken approach is the association of two different techniques: screen-printing and laser treatment process. The first technique is coherent for the patterning of multisensing devices that consist of a TiO_2 active layer deposited on the top of silver interdigitated electrodes. The second one is particularly adapted for the post-treatment of the active layers on flexible substrates and allows to perform

DOI: 10.1021/acsami.8b19976
ACS Appl. Mater. Interfaces 2019, 11, 6257–6266

simultaneously and selectively the sintering of TiO_2 patterned films in a single step. Both approaches are fast, cost-effective, and do not require annealing steps at high temperatures, which makes them compatible with any kind of flexible substrates. The effects of the laser fluence on morphology, electrical properties, and UV-sensing and gas-sensing properties are disclosed. The UV photoresponse and ethanol response were improved by properly adjusting the laser fluence. It was found that this phenomenon is correlated to the change of the morphology and structure of the TiO_2 film generated by the laser irradiation. In addition, the resulting UV and ethanol sensors showed good repeatability, relatively fast response time, and good mechanical flexibility. Therefore, the possibility to fabricate multifunctional devices with tunable properties, in a rapid and large-scale manner, paves the way to low-cost solutions of sophisticated multisensing technologies, printed on flexible substrates.

■ ASSOCIATED CONTENT

Supporting Information

The Supporting Information is available free of charge on the ACS Publications website at DOI: 10.1021/acsami.8b19976.

Multiprofile analysis of the SEM images from Figure 3a of the untreated sample and samples treated at 0.17, 0.19, and 0.21 J cm^{-2}; roughness measurements obtained from the multiprofile analysis; 2D AFM images of the untreated sample and sample treated at 0.21 J cm^{-2} ; energy dispersive X-ray analysis of the untreated and treated samples at 0.21 J cm^{-2} ; ethanol (100 ppm) and UV response (20 mW cm^{-2}) of the devices over the weeks (PDF)

■ AUTHOR INFORMATION

Corresponding Author

*E-mail: georges.dubourg@biosense.rs.

ORCID

Georges Dubourg: 0000-0002-7216-5168

Marko Radović: 0000-0001-7565-4015

Author Contributions

G.D. conceived the idea and designed and performed the experiments. M.R. contributed in material preparation (TiO_2 paste) and optical and structural characterization; G.D. and M.R. analyzed the data. G.D. wrote the manuscript.

Funding

This work is supported by the Serbian Ministry of Education, Science and Technological Development through the project III44006 and OI171032.

Notes

The authors declare no competing financial interest.

■ ACKNOWLEDGMENTS

The authors would like to acknowledge Dr Borislav Vasić for AFM measurements.

■ REFERENCES

(1) Yu, X.; Marks, T. J.; Facchetti, A. Metal Oxides for Optoelectronic Applications. *Nat. Mater.* **2016**, *15*, 383−396.

(2) Jeong, J. K. The Status and Perspectives of Metal Oxide Thin-Film Transistors for Active Matrix Flexible Displays. *Semicond. Sci. Technol.* **2011**, *26*, No. 034008.

(3) Miller, D. R.; Akbar, S. A.; Morris, P. A. Nanoscale Metal Oxide-Based Heterojunctions for Gas Sensing: a Review. *Sens. Actuators, B* **2014**, *204*, 250−272.

(4) Gogurla, N.; Sinha, A. K.; Santra, S.; Manna, S.; Ray, K. Multifunctional Au-ZnO Plasmonic Nanostructures for Enhanced UV Photodetector and Room Temperature NO Sensing Devices. *Sci. Rep.* **2014**, *4*, No. 6483.

(5) Mishra, Y. K.; Modi, G.; Cretu, V.; Postica, V.; Lupan, O.; Reimer, T.; Paulowicz, I.; Hrkac, V.; Benecke, W.; Kienle, L. Direct Growth of Freestanding ZnO Tetrapod Networks for Multifunctional Applications in Photocatalysis, UV Photodetection, and Gas Sensing. *ACS Appl. Mater. Interfaces* **2015**, *7*, 14303−14316.

(6) Postica, V.; Hölken, I.; Schneider, V.; Kaidas, V.; Polonskyi, O.; Cretu, V.; Tiginyanu, I.; Faupel, F.; Adelung, R.; Lupan, O. Multifunctional Device Based on ZnO: Fe Nanostructured Films with Enhanced UV and Ultra-Fast Ethanol Vapour Sensing. *Mater. Sci. Semicond. Process.* **2016**, *49*, 20−33.

(7) Postica, V.; Gröttrup, J.; Adelung, R.; Lupan, A.; Mishra, K.; de Leeuw, N. H.; Ababii, N.; Carreira, J. F. C.; Rodrigues, J.; Sedrine, N. B.; Correia, M. R.; Monteiro, T.; Sontea, V.; Mishra, Y. K. Multifunctional Materials: A Case Study of the Effects of Metal Doping on ZnO Tetrapods with Bismuth and Tin Oxides. *Adv. Funct. Mater.* **2017**, *27*, No. 1604676.

(8) Chen, S.; Liu, H.; Liu, S.; Wang, P.; Zeng, S.; Sun, L.; Liu, L. Transparent and Waterproof Ionic Liquid-Based Fibers for Highly Durable Multifunctional Sensors and Strain-Insensitive Stretchable Conductors. *ACS Appl. Mater. Interfaces* **2018**, *10*, 4305−4314.

(9) Watson, T.; Mabbett, I.; Wang, H.; Peter, L.; Worsley, D. Ultrafast Near Infrared Sintering of TiO_2 Layers on Metal Substrates for Dye-Sensitized Solar Cells. *Prog. Photovoltaics* **2011**, *19*, 482−486.

(10) Jeong, H.; Kim, J. Y.; Koo, B.; Son, H. J.; Kim, D.; Ko, M. J. Rapid Sintering of MoS2 Counter Electrode Using Near-Infrared Pulsed Laser for Use in Highly Efficient Dye-Sensitized Solar Cells. *J. Power Sources* **2016**, *330*, 104−110.

(11) Croquesel, J.; Bouvard, D.; Chaix, J.-M.; Carry, C. P.; Saunier, S.; Marinel, S. Direct Microwave Sintering of Pure Alumina in a Single Mode Cavity: Grain Size and Phase Transformation Effects. *Acta Mater.* **2016**, *116*, 53−62.

(12) Mathew, C. T.; Vidya, S.; Koshy, J.; Solomon, S.; Thomas, J. K. Enhanced Infrared Transmittance Properties in Ultrafine $MgAl_2O_4$ Nanoparticles Synthesised by a Single Step Combustion Method, Followed by Hybrid Microwave Sintering. *Infrared Phys. Technol.* **2015**, *72*, 153−159.

(13) Palneedi, H.; Park, J. H.; Maurya, D.; Peddigari, M.; Hwang, G. T.; Annapureddy, V.; Kim, J. W.; Choi, J. J.; Hahn, B. D.; Priya, S.; Lee, K. J.; Ryu, J. Laser Irradiation of Metal Oxide Films and Nanostructures: Applications and Advances. *Adv. Mater.* **2018**, *30*, No. 1705148.

(14) Joe, D. J.; Kim, S.; Park, J. H.; Park, D. Y.; Lee, H. E.; Im, T. H.; Choi, I.; Ruoff, R. S.; Lee, K. J. Laser−Material Interactions for Flexible Applications. *Adv. Mater.* **2017**, *29*, No. 1606586.

(15) Soleimanpour, A. M.; Khare, S. V.; Jayatissa, A. H. *ACS Appl. Mater. Interfaces* **2012**, *4*, 465−4657.

(16) Molaei, R.; Bayati, M. R.; Alipour, H. M.; Nori, S.; Narayan, J. Enhanced Photocatalytic Efficiency in Zirconia Buffered n-NiO/p-NiO Single Crystalline Heterostructures by Nanosecond Laser Treatment. *J. Appl. Phys.* **2013**, *113*, No. 233708.

(17) Lee, D.; Pan, H.; Ko, S. H.; Park, H. K.; Kim, E.; Grigoropoulos, C. P. Non-Vacuum, Single-Step Conductive Transparent ZnO Patterning by Ultra-Short Pulsed Laser Annealing of Solution-Deposited Nanoparticles. *Appl. Phys. A.* **2012**, *107*, 161−171.

(18) Ganz, D.; Reich, A.; Aegerter, M. A. Laser Firing of Transparent Conducting SnO_2 Sol-Gel Coatings. *J. Non-Cryst. Solids* **1997**, *218*, 242−246.

(19) Maeng, J.; Heo, S.; Jo, G.; Choe, M.; Kim, S.; Hwang, H.; Lee, T. The Effect of Excimer Laser Annealing on ZnO Nanowires and Their Field Effect Transistors. *Nanotechnology* **2009**, *20*, No. 095203.

DOI: 10.1021/acsami.8b19976
ACS Appl. Mater. Interfaces 2019, 11, 6257−6266

(20) Zhao, X. H.; Wang, M. J.; Zhang, Q.L.; Yang, H.; Hu, L.; Yu, D. Improving Sintering Characteristic and Dielectric Properties of Kermanite ($Ca_2MgSi_2O_7$) Ceramics by Bi_2O_3–B_2O_3 Addition. *Mater. Lett.* **2014**, *122*, 9–12.
(21) Zhu, B. L.; Xie, C. S.; Wang, A. H.; Wu, J.; Wu, R.; Liu, J. Laser Sintering ZnO Thick Films for Gas Sensor Application. *J. Mater. Sci.* **2007**, *42*, 5416–5420.
(22) Zhang, H.; Wu, S.; Liu, J.; Cai, Y.; Liang, C. Laser Irradiation-Induced Au–ZnO Nanospheres with Enhanced Sensitivity and Stability for Ethanol Sensing. *Phys. Chem. Chem. Phys.* **2016**, *18*, 22503–22508.
(23) Cai, Z. X.; Li, X. Y.; Zeng, X. Y. Direct Fabrication of SnO_2-Based Thick Film Gas Sensor Using Micropen Direct Writing and Laser Microcladding. *Sens. Actuators, B* **2009**, *137*, 340–344.
(24) Huang, T.; Lu, J.; Xiao, R.; Wu, Q.; Yang, W. Enhanced Photocatalytic Properties of Hierarchical Three-Dimensional TiO_2 Grown on Femtosecond Laser Structured Titanium Substrate. *Appl. Surf. Sci.* **2017**, *403*, 584–589.
(25) Hadi, A.; Alhabradi, M.; Chen, Q.; Liu, H.; Guo, W.; Curioni, M.; Cernik, R.; Liu, Z. Rapid Fabrication of Mesoporous TiO_2 Thin Films by Pulsed Fibre Laser for Dye Sensitized Solar Cells. *Appl. Surf. Sci.* **2018**, *428*, 1089–1097.
(26) Kim, H.; Kushto, G. P.; Arnold, C. B.; Kafafi, Z. H.; Piqué, A. Laser Processing of Nanocrystalline TiO_2 Films for Dye-Sensitized Solar Cells. *Appl. Phys. Lett.* **2004**, *85*, 464–466.
(27) Pu, M. J.; Chen, J. Z.; Cheng, I. C. KrF Excimer Laser Irradiated Nanoporous TiO_2 Layers for Dye-Sensitized Solar Cells: Influence of Laser Power Density. *Ceram. Int.* **2013**, *39*, 6183–6188.
(28) Yoon, J.; Jin, M.; Lee, M. Laser-Induced Control of TiO2 Porosity for Enhanced Photovoltaic Behavior. *Adv. Mater.* **2011**, *23*, 3974–3978.
(29) Ochiai, T.; Tago, S.; Hayashi, M.; Tawarayama, H.; Hosoya, T.; Fujishima, A. TiO_2-Impregnated Porous Silica Tube and Its Application for Compact Air- and Water-Purification Units. *Catalysts* **2015**, *5*, 1498–1506.
(30) Mushtaq, F.; Asani, A.; Hoop, M.; Chen, X. Z.; Ahmed, D.; Nelson, B. J.; Pané, S. Highly Efficient Coaxial TiO_2-PtPd Tubular Nanomachines for Photocatalytic Water Purification with Multiple Locomotion Strategies. *Adv. Funct. Mater.* **2016**, *26*, 6995–7002.
(31) Gao, Y.; Xu, J.; Shi, S.; Dong, H.; Cheng, Y.; Wei, C.; Zhang, X.; Yin, S.; Li, L. TiO_2 Nanorod Arrays Based Self-Powered UV Photodetector: Heterojunction with NiO Nanoflakes and Enhanced UV Photoresponse. *ACS Appl. Mater. Interfaces* **2018**, *10*, 11269–11279.
(32) Krško, O.; Plecenik, T.; Roch, T.; Grančič, B.; Satrapinskyy, L.; Truchlý, M.; Ďurina, P.; Gregor, M.; Kúš, P.; Plecenik, A. Flexible Highly Sensitive Hydrogen Gas Sensor Based on a TiO_2 Thin Film on Polyimide Foil. *Sens. Actuators, B* **2017**, *240*, 1058–1065.
(33) Dubourg, G.; Segkos, A.; Katona, J.; Radović, M.; Savić, S.; Niarchos, G.; Tsamis, C.; Crnojević-Bengin, V. Fabrication and Characterization of Flexible and Miniaturized Humidity Sensors Using Screen-Printed TiO_2 Nanoparticles as Sensitive Layer. *Sensors* **2017**, *17*, No. 1854.
(34) Chandiran, A. K.; Zakeeruddin, S. M.; Humphry-Baker, R.; Nazeeruddin, M. K.; Graetzel, M.; Sauvage, F. Investigation on the Interface Modification of TiO_2 Surfaces by Functional Co-Adsorbents for High-Efficiency Dye-Sensitized Solar Cells. *ChemPhysChem* **2017**, *18*, 2724–2731.
(35) Zhu, P.; Zhu, H.; Qin, W.; Dantas, B. H.; Sun, W.; Tan, C. K.; Tansu, N. Narrow-Linewidth Red-Emission Eu^{3+}-Doped TiO_2 Spheres for Light-Emitting Diodes. *J. Appl. Phys.* **2016**, *119*, No. 124305.
(36) Wu, S.; Weng, Z.; Liu, X.; Yeung, K. W. K.; Chu, P. K. Functionalized TiO2 Based Nanomaterials for Biomedical Applications. *Adv. Funct. Mater.* **2014**, *24*, 5464–5481.
(37) Radović, M.; Dubourg, G.; Kojić, S.; Dohčević-Mitrović, Z.; Stojadinović, B.; Bokorov, M.; Crnojević-Bengin, V. Laser Sintering of Screen-Printed TiO_2 Nanoparticles for Improvement of Mechanical and Electrical Properties. *Ceram. Int.* **2018**, *44*, 10975–10983.
(38) Borodko, Y.; Habas, S. E.; Koebel, M.; Yang, P.; Frei, H.; Somorjai, G. A. Probing the Interaction of Poly(vinylpyrrolidone) with Platinum Nanocrystals by UV–Raman and FTIR. *J. Phys. Chem. B* **2006**, *110*, 23052–23059.
(39) Xie, C.; Yan, F. Flexible Photodetectors Based on Novel Functional Materials. *Small* **2017**, *13*, No. 1701822.
(40) Zhai, T. Y.; Li, L.; Wang, X.; Fang, X. S.; Bando, Y.; Golberg, D. Recent Developments in One-Dimensional Inorganic Nanostructures for Photodetectors. *Adv. Funct. Mater.* **2010**, *20*, 4233–4248.
(41) Barsan, N.; Weimar, U. J. Conduction model of metal oxide gas sensors. *J. Electroceramics* **2001**, *7*, 143–167.
(42) Meng, D.; Yamazaki, T.; Kikuta, T. Preparation and Gas Sensing Properties of Undoped and Pd-Doped TiO_2 Nanowires. *Sens. Actuators, B* **2014**, *190*, 838–843.
(43) Hu, P.; Du, G.; Zhou, W.; Cui, J.; Lin, J.; Liu, H.; Liu, D.; Wang, J.; Chen, S. Enhancement of Ethanol Vapor Sensing of TiO2 Nanobelts by Surface Engineering. *ACS Appl. Mater. Interfaces* **2010**, *2*, 3263–3269.
(44) Vijayalakshmi, K.; Jereil, S. D. Enhanced Ethanol Sensing Performance of Fe: TiO_2 Nanowires and their Mechanism of Sensing at Room Temperature. *Ceram. Int.* **2015**, *41*, 3220–3226.
(45) Zhu, Z.; Kao, C. T.; Wu, R. J. A Highly Sensitive Ethanol Sensor Based on Ag@TiO_2 Nanoparticles at Room Temperature. *Appl. Surf. Sci.* **2014**, *320*, 348–355.

DOI: 10.1021/acsami.8b19976
ACS Appl. Mater. Interfaces 2019, 11, 6257–6266

Ceramics International 44 (2018) 10975–10983

Contents lists available at ScienceDirect

Ceramics International

journal homepage: www.elsevier.com/locate/ceramint

Laser sintering of screen-printed TiO_2 nanoparticles for improvement of mechanical and electrical properties

M. Radović[a,*], G. Dubourg[a], S. Kojić[b], Z. Dohčević-Mitrović[c], B. Stojadinović[c], M. Bokorov[d], V. Crnojević-Bengin[a]

[a] Nano and Microelectronics Group, BioSense Institute, Novi Sad, Serbia
[b] Faculty of Technical Sciences, University of Novi Sad, Serbia
[c] Laboratory for Nanocomposite Structures and Biovibrational Spectroscopy, Institute of Physics Belgrade, University of Belgrade, Serbia
[d] University Laboratory for Electronic Microscopy, University of Novi Sad, Serbia

ARTICLE INFO

Keywords:
A. Sintering
B. Microstructure-final
C. Mechanical properties
D. TiO_2

ABSTRACT

Conducted research presents a rapid and cost-effective approach to technological processing of screen-printed films with anatase TiO_2 nanoparticles, by utilizing the high fluence laser radiation. The influence of laser sintering on the screen-printed films was characterized with optical and scanning electron microscopy, energy-dispersive X-ray (EDX) spectroscopy, Raman spectroscopy, nanoindenter measurements and current vs voltage measurements. Investigation of surface morphology of screen-printed films revealed that higher laser fluences caused significant decrease in film thickness, trough evaporation of organic additives used in the paste matrix. EDX mapping of carbon content in untreated and laser sintered surface confirmed removal of organic additives. Laser sintering stimulated breaking of large agglomerates into much finer nano-sized particles and promoted formation of necking between individual grains. Crystal structure and vibrational properties of anatase TiO_2 nanoparticles was monitored with Raman spectroscopy before and after laser sintering. Obtained results point out that anatase polymorph was preserved during the sintering process, without appearance of other phases. From observation of the behavior of the most intense E_g Raman active mode it was deduced that laser sintering provoked a formation of structural defects i.e. oxygen vacancies in TiO_2 nanoparticles, whose concentration increased in the samples treated with higher laser fluences. Mechanical properties of untreated and laser sintered samples were investigated with nanoindenter measurements using several load forces, in order to carefully probe the Young modulus and mechanical hardness. From the analysis of collected data, we established that overall improvement of the mechanical properties with laser sintering originates from formation of very dense ceramic layer with enhanced interconnectivity between individual TiO_2 nanoparticles. Measurements of current vs voltage characteristics clearly demonstrated that increase in laser fluence leads to drastic increase in current values and improvement of electric conductivity.

1. Introduction

Recent technological and industrial advancements have imposed a staggering need for robust, scalable, cost-effective and innovative solutions for processing of coatings (thick and thin films), foils, bulk surfaces and other types of functional materials. Driven by the needs for cleaner energy, environmental protection and efficient health care, some of the classical energy sources such as UV radiation [1–3], plasma [4–6] and laser radiation [7–9], have found new fields of application in present days. Among these technologies, laser surface texturing has emerged as a versatile tool for improvement of solar cells efficiency [10–12], photocatalytic performance [13], biosensing applications [14,15] and even textile processing [16,17]. Constant development introduced a large variety of laser sources for functionalization of surfaces, ranging from UV region to NIR wavelengths, that can operate in a constant flux or in a pulse mode. Pulsed lasers have recently gained a lot of attention since their pulses can be tuned down to nanosecond [18], picosecond [19] and femtosecond [20,21] intervals. One of the most important advantages of laser processing over the other above mentioned technologies, lies in its spatial resolution. With an appropriate choice of optics or optical fibers, a laser spot can be reduced to micron sizes, enabling very precise localized heating of the target surface without damaging the substrate, which is especially suitable for flexible substrates [22]. Laser processing is also a very effective tool for

* Correspondence to: Biosense Institute, Dr. Zorana Đinđića 1, 21000 Novi Sad, Serbia.
E-mail address: marrad@bioisense.rs (M. Radović).

https://doi.org/10.1016/j.ceramint.2018.03.181
Received 13 March 2018; Received in revised form 20 March 2018; Accepted 20 March 2018
Available online 21 March 2018

rapid prototyping (excluding the need for stencils and masks), and can be easily optimized for roll-to-roll and other types of large scale production methods.

Titanium based materials (Ti metal and TiO_2) have been extensively studied for their interaction with laser radiation because of several fascinating effects that were observed. Laser treatment of Ti metal surfaces and TiO_2 films leads to the appearance of laser-induced periodic surface structures (LIPSS) with improved morphological and optical characteristics [23,24]. Another interesting effect was observed during laser treatment of TiO_2 nanoparticles in reducing (Ar) ambient or in colloidal suspension, when the interaction of the laser plume with the target produces the so called "black titania", with a very interesting structural, photovoltaic and photocatalytic properties [25,26]. Most common polymorphs of TiO_2: rutile (tetragonal, *P*42/*mnm*), anatase (tetragonal, *I*41/*amd*), and brookite (orthorombic, *Pbca*/mmm), are particulary suited for laser treatment because all these structural phases exhibit an optical band gap in the visible region. Having established the abovementioned facts, it is clearly understandable why most of the research attention is devoted to enhancement of the dye sensitized solar cells (DSSC) performance trough optimization of basic parameters of the laser treatment method [13,22,27–29].

Available database provides an extensive coverage of literature about the improvement of optical and photovoltaic properties of nanostructured TiO_2 films and coatings with various laser treatment methods. In order to take full advantage of these methods, it is essential to evaluate an effect of laser sintering on the behavior of TiO_2 nanoparticles and to gain better insight into fundamental features of investigated oxide material. The vital importance of this evaluation is based on the fact that mechanical properties, in terms of hardness and elastic modulus, are the key elements that assure both the structural integrity and reliability in various fields of applications.

The aim of this work was to investigate the influence of laser sintering on morphology, structural, mechanical and electrical transport characteristics of the screen-printed films with TiO_2 nanoparticles. One of the first milestones was to achieve controllable technological process for laser sintering of screen-printed nanoparticles, which would induce removal of organic components of the paste (dispersant and binder) and promote sintering of titanium dioxide into dense ceramic material. In the first phase of research we investigated the influence of laser sintering on chemical composition of printed paste matrix and crystallinity of TiO_2 nanoparticles, using EDX and Raman spectroscopy. EDX mapping of untreated and laser sintered surface revealed that laser sintering causes decrease of carbon content and appearance of non-stoichiometry. Raman spectra of treated films showed that anatase crystal structure was preserved, but oxygen deficiency increased in the samples treated with higher laser fluence. From the analysis of SEM images and nanoindenter measurements we established that increase in the laser fluence led to decrease of film thickness and better interconnectivity between TiO_2 nanoparticles, resulting in increase in Young modulus and mechanical hardness. Within such framework, it is possible to offer a cost-effective solution for rapid and large-scale fabrication of ceramic films and coatings on different substrates that could find potential application in electronic devices and advanced technologies.

2. Experimental

One of the main ideas behind the conducted research was to use a simple technology for the functionalization of TiO_2 nanoparticles, such as screen-printing, and to combine it with laser sintering for thermal treatment and improvement of various physical properties of the printed films (Fig. 1). Undertaken multidisciplinary approach can be easily optimized for large scale production of solar cells, sensors and photocatalytic devices [13,22,30]. We deliberately chose a common microscope glass slide as substrate (Fig. 1) and easily accessible commercial TiO_2 nanoparticles, in order to emphasize the low-cost aspect of the utilized technologies and to make it easily applicable to other nanomaterials and substrates.

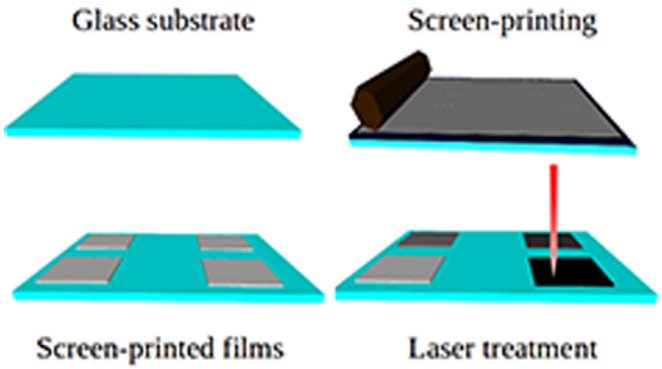

Fig. 1. Schematic representation of multidisciplinary approach undertaken in this research: preparation of microscope glass slide as substrate, screen printing process for the deposition of TiO_2 nanoparticles, and laser sintering of the printed films as a post-processing step.

For the preparation of the functional paste, 2 g of PVP (Sigma-Aldrich) were initially dissolved in 10 ml of ethanol (Sigma-Aldrich). 1 g of anatase TiO_2 nanopowder (Sigma-Aldrich, particle size < 25 nm) was dispersed in 400 µl of terpineol (Sigma-Aldrich), followed by addition of 600 µl of PVP solution. Obtained suspensions were treated with ultrasonic horn for 10 min. Thus prepared paste was deposited on the cleaned microscope-glass substrate using a low-cost screen printing technique (Fig. 1) with EKRA 2H semi-industrial screen printer, in order to obtain a matrix of screen printed films on the glass substrate.

The next step was to apply a very precise and rapid processing technology, such as high-power laser radiation (Fig. 1), and to optimize the parameters of laser treatment of the target surface, with the aim of achieving a controllable sintering of the screen-printed films and improving desired properties of the nanomaterials. The laser treatment of printed films was carried out by using a diode-pumped Nd:YAG laser cutter Rofin-Sinar Power Line D–100, operating in the NIR range at 1064 nm. In order to accomplish a uniform sintering of the surface on the entire sample, the length of the line scanned by the laser was designed to be 5 mm, with line intervals of 20 µm. Frequency of the laser pulse was set at 65 kHz, and, in order to obtain sufficient pulse overlapping, the speed of displacement was adjusted to 1000 mm/s. Afterwards, the laser fluence was varied by adjusting the laser pump current. Several samples were prepared. One sample was kept untreated, in order to serve as a reference, while 4 remaining samples were treated with input current values of 25 A, 26 A, 27 A and 28 A, which correspond to laser fluences of 0.15 J/cm^2, 0.17 J/cm^2, 0.19 J/cm^2 and 0.21 J/cm^2, respectively.

Optical microscopy/profilometry measurements were performed with Huvitz HRM-300 microscope, equipped with Bioimager automatized stage. SEM images were collected on JEOL JSM 6460 LV device in the backscattering geometry. EDX measurements were carried out on Hitachi TM3030 electron microscope, coupled with Bruker Xflash EDX detector. The micro-Raman spectra were collected using Jobin Yvon T64000 spectrometer, equipped with a nitrogen-cooled CCD detector. The $\lambda = 532$ nm line of solid state Nd:YAG laser was used as an excitation source, with an incident laser power less than 40 mW, in order to minimize the heating effects. Investigation of mechanical properties was performed on Agilent G200 nanoindenter. Current vs voltage curves were measured on Yokogawa-Hewlett-Packard 4145A semiconductor probe analyzer.

3. Results and discussion

Fig. 2a), b), c) and d) present the images of untreated and laser sintered samples taken with 500× magnification on optical profilometer. These images show that laser sintering introduces a shift in the

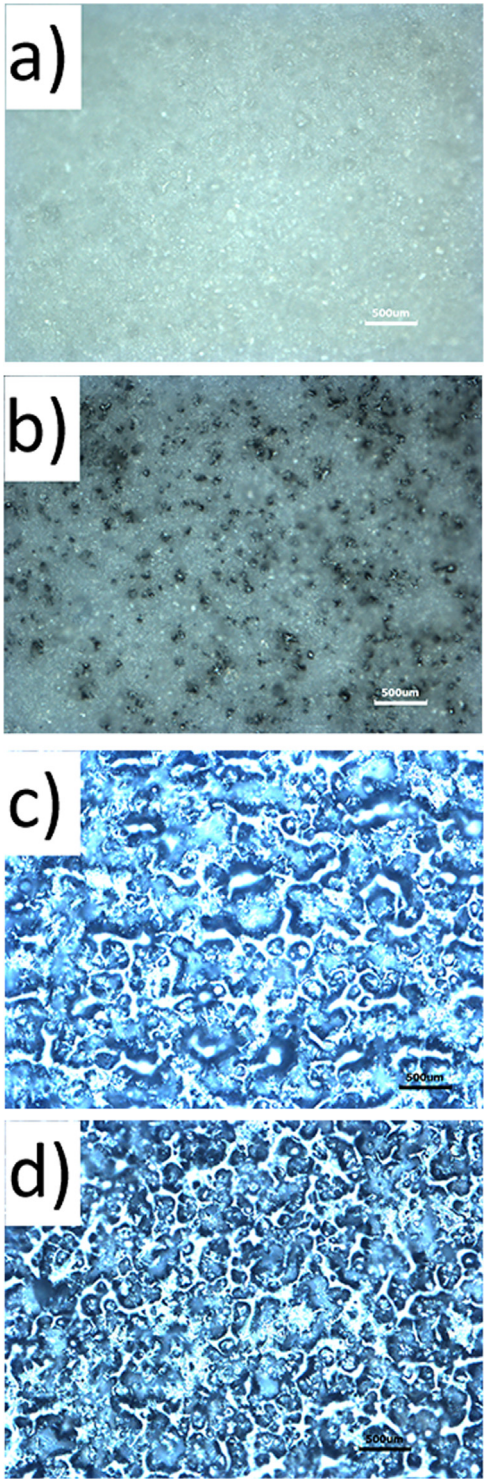

Fig. 2. Comparison of optical microscopy images between a) untreated and samples sintered with b) 0.15 J/cm^2, c) 0.17 J/cm^2 and d) 0.19 J/cm^2 laser fluences, taken with 500× magnification.

apparent color of printed films, from white for the untreated TiO_2 to black for the sample treated with laser fluence of 0.19 J/cm^2. The sample treated with the highest laser fluence shows significant changes in the topology, manifested as a formation of new, melted structures that exhibit better interconnectivity of the material in the surface layer. The change in contrast in these images reveals that laser sintered surface strongly diffuses the incident light, due to micro-scale reorganization of the surface roughness and porosity. It is important to mention that the laser sintering with fluence higher than 0.19 J/cm^2 results in the ablation of printed films, leading to loss of the nanomaterial and formation of large voids on the film surface. Similar fluence threshold (200 mJ/cm^2) for ablation of the screen printed TiO_2 nanoparticles was reported by Pu et al. [28]. For this reason, the highest laser fluence that was used in this research was set at 0.19 J/cm^2.

SEM measurements were performed in order to gain better insight into the influence of laser sintering on the microstructure of screen printed films. Fig. 3a), b), c) and d) present the captured images of the surface morphologies for the untreated and laser sintered samples. Variation in the film thickness with an increasing laser fluence was determined from the profile images shown in the right part of the Fig. 3a), b), c) and d). The insets in Fig. 3a), b), c) and d) show high magnification SEM images. The SEM image of the untreated screen-printed film reveals a porous surface containing micron sized particles (see the inset of Fig. 3a)) that are much larger than the original anatase nanoparticles (20–30 nm) used for the preparation of the paste. Such clusters are formed by agglomeration of individual TiO_2 nanoparticles, held-together by dried organic binder and dispersant.

In a recent study [22], the same effect was observed for similar paste with ethyl cellulose and terpineol matrix. It is important to mention that in the presented research we used pure anatase TiO_2 nanoparticles, unlike in the majority of previous studies, where P-25 TiO_2 nanoparticles (Evonink Degussa P-25) were used [22,27,31,32]. The P-25 mixture is composed of anatase and rutile phases in the 80%: 20% ratio, for which it is difficult to uncouple the contributions from individual phases to the investigated physical properties. Therefore, pure anatase nanoparticles were chosen in order to easily follow the behavior of a single TiO_2 polymorph during laser treatment. Furthermore, it is interesting to note that for temperatures higher than 500 °C this polymorph starts to transform into rutile phase [33]. Such feature of the material is a good indicator of the local distribution of temperatures in printed films during laser treatment.

Increase in laser fluence induces observable modifications of the surface morphology in the form of melted droplets, as shown in Fig. 3c) and d). The appearance of melted droplets in the printed film is a direct result of breaking of large agglomerates. These agglomerates are reduced into much finer nanoparticles (see inset in Fig. 3d)), whose dimensions are close to the initial size of anatase nanoparticles used in the paste preparation. Breaking of the agglomerates is accomplished by laser thermal evaporation of organic components (PVP and terpineol) whose evaporation temperatures are below 500 °C [22,34]. Additionally, the laser treatment produced sintering of the TiO_2 nanomaterial, which can be observed as formation of necking between individual nanoparticles and better mutual connectivity (inset in Fig. 2d)). In this sintered material, a higher compactness of TiO_2 nanoparticles can be detected, accompanied by dramatic increase in specific surface area. All of the mentioned features reveal great potential for practical applications of the laser sintered films.

The values of film thickness were estimated using the profile SEM images of printed films shown in Fig. 3. The obtained results are shown in Fig. 4 and compared with values obtained from optical profilometry of images shown in Fig. 2a), b), c) and d). Both techniques gave very similar values and the same trend. Film thickness for the untreated sample was around 40 μm, whereas with the laser sintering the film thickness decreased to 10 μm. Decrease in film thickness can be directly correlated to removal of organic binder components with laser radiation, taking into account the fact that oxide material has much higher evaporation temperature. Evaporation of organic additives supports closer packing of the nanoparticles, and formation of dense ceramic material, resulting in the observed film thickness decrease.

Chemical composition and spatial distribution of constitutional elements in laser sintered films was investigated with EDX spectroscopy. Large area EDX maps of the untreated and the laser sintered film were measured using SEM microscope, equipped with EDX detector. SEM image of the investigated area is presented in Fig. 5a), showing

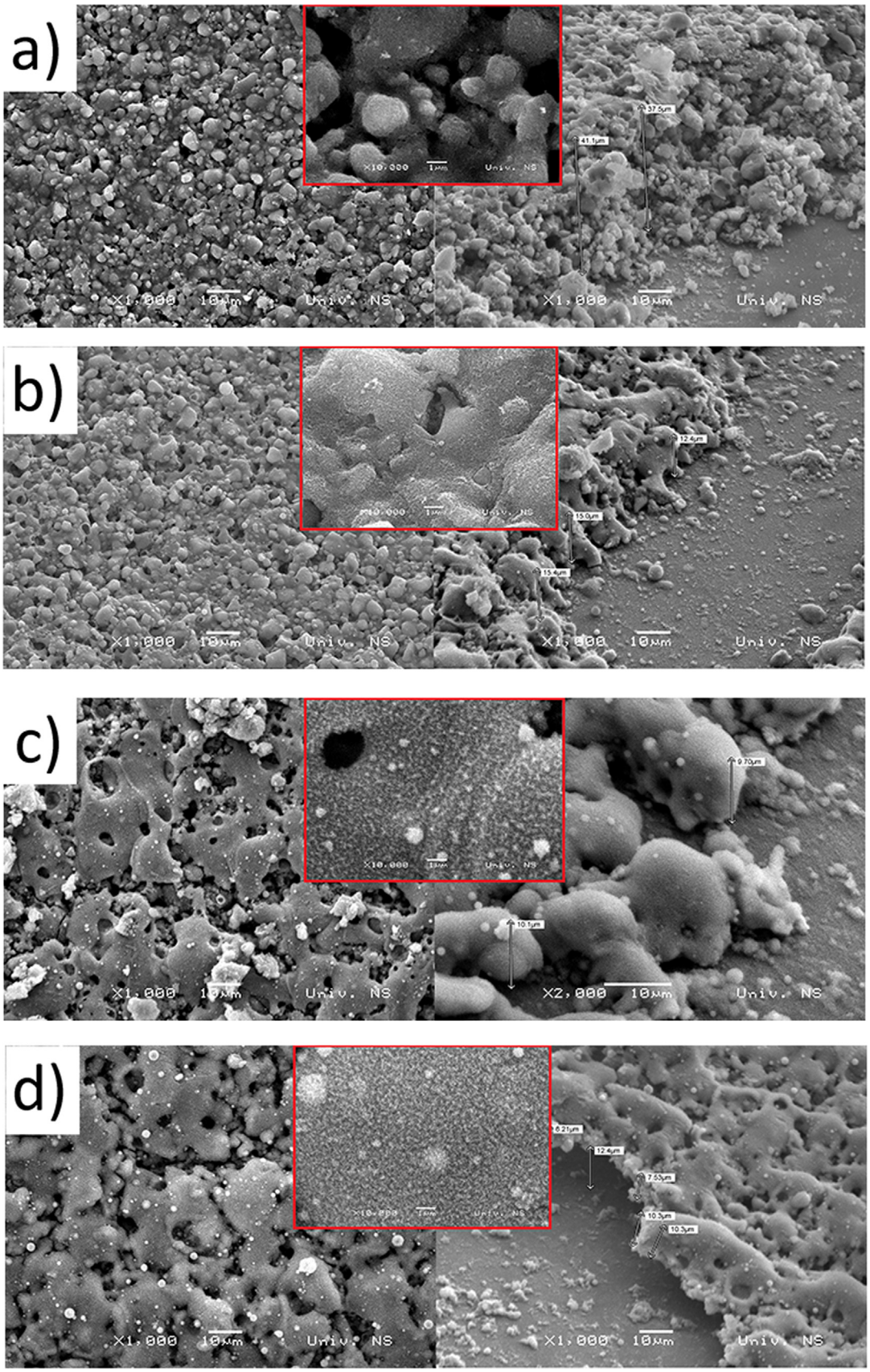

Fig. 3. SEM images of a) untreated and laser sintered screen-printed films with TiO_2 nanoparticles, using b) 0.15 J/cm^2, c) 0.17 J/cm^2 and d) 0.19 J/cm^2 laser fluences.

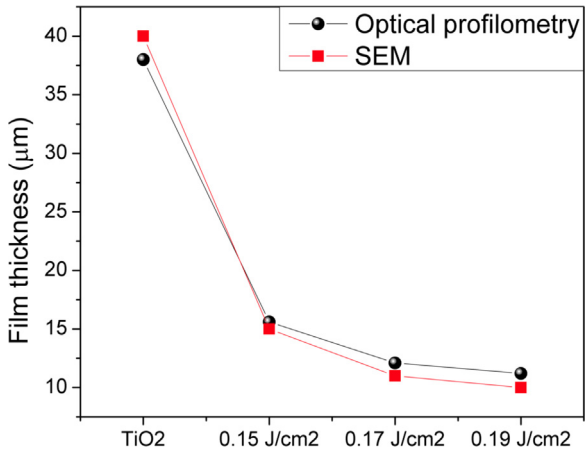

Fig. 4. Variation in film thickness with laser fluence, determined from optical profilometry and SEM images.

laser sintered (0.19 J/cm^2) surface on the left side, and untreated film on the right side. The main features in measured EDX spectra were assigned to titanium (Ti), oxygen (O) and carbon (C) species. Other impurities were not detected. Ti and O signature originates from the oxide nanoparticles, whereas C signature corresponds to the organic additives used for the paste matrix. Fig. 5b), c), d) present the corresponding C, O and Ti EDX maps of the untreated surface and film sintered at 0.19 J/cm^2. When comparing the presented maps with the SEM image, one can clearly see that laser treatment leads to significant changes in the spatial distribution of carbon atoms. Carbon content is lower in the laser sintered surface than in the untreated part. The O map (Fig. 5c) shows a slight decrease in the oxygen content in the sintered surface, whereas Ti map does not show any visible changes in distribution of this element. Lower concentration of O species in treated surface is a signature of non-stoichiometry. Deviation from ideal stoichiometry can originate from a formation of oxygen vacancies in anatase TiO_2 structure, caused by high energy laser radiation. Obtained data lead us to conclusion that the process of laser sintering of screen-printed films induces evaporation of carbon components in the printed film and preserves chemical composition of the oxide nanoparticles. The results also indicate that there is still a certain presence of carbon species in the treated film, and that laser sintering did not entirely remove organic components of the printed paste matrix.

Raman spectroscopy represents a very powerful tool for investigation of nanostructured materials and surfaces. It provides the essential information about crystalline phase and degree of crystallinity of TiO_2 nanoparticles in the printed paste matrix. Moreover, it could be viable tool for assessing the TiO_2 nanocrystals stoichiometry.Fig. 6a) presents Raman spectra of untreated and laser sintered samples, in the spectral region where the first order anatase TiO_2 phonon modes are dominant. Within the spectrum of untreated TiO_2 five distinct modes can be ascribed to phonon modes of anatase TiO_2 crystal structure. Raman modes positioned at 145, 197 and 639 cm^{-1} belong to E_g modes, whereas modes at 398 cm^{-1} and 517 cm^{-1} correspond to the B_g phonon modes [35,36]. Among these modes, E_g mode at around 145 cm^{-1} exhibited noticeable changes. This mode is broader and shifted to higher frequencies with respect to its bulk counterpart. Such behavior can be ascribed to the quantum size effects, strain or non-stoichiometry [37,38]. All Raman modes of anatase crystal structure can be observed in laser treated samples too, providing clear evidence that in these samples, besides the anatase phase, the presence of other phases was not detected. Therefore, it can be concluded that during the laser treatment, local sintering temperature did not exceed 500 °C that instigates transition towards rutile structure [33]. The intensity of this mode, as well as signal-to-noise ratio, decreased in the films treated with higher laser fluence. The SEM analysis of the samples indicated

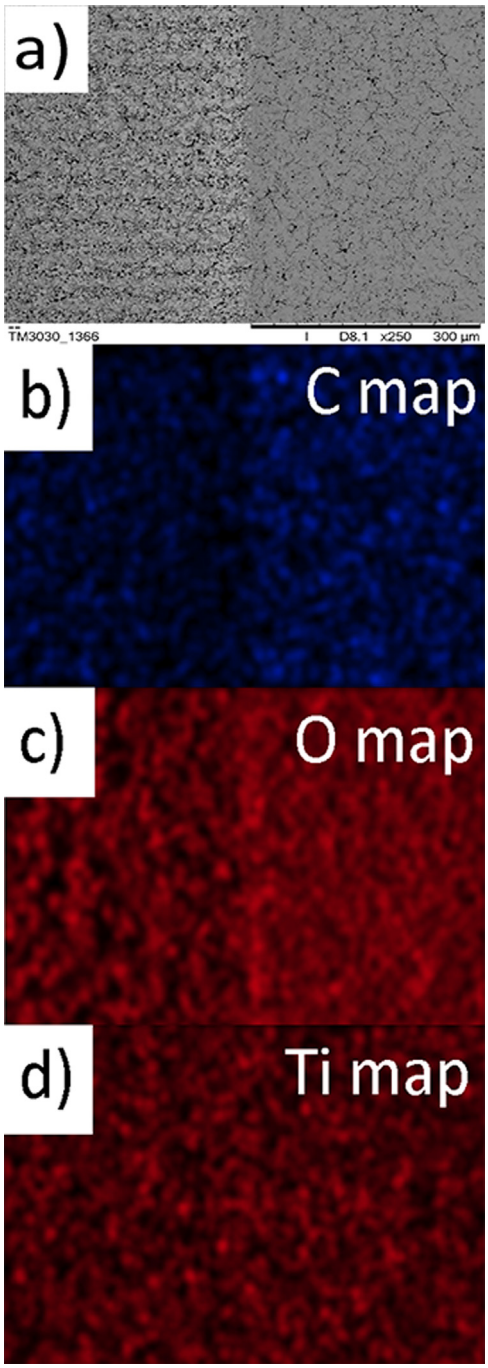

Fig. 5. a) SEM image of the laser sintered (left) and untreated surface (right) of screen-printed film. Laser fluence used for sintering was set at 0.19 J/cm^2. b), c) and d) Corresponding carbon, oxygen and titanium EDX maps of untreated and treated parts. (For interpretation of the references to color in this figure, the reader is referred to the web version of this article.)

transformation of the surface morphology, i.e an appearance of much finer nanoparticles with higher specific surface area and enhanced porosity. The observed changes in the Raman spectra of films treated with higher laser fluence can be ascribed to increased porosity. However, another reason for the changes can be found in the formation of oxygen vacancies and lack of Ti-O bonds, particularly at the samples` surface. Oxygen vacancies are the most prevalent defects in metal oxides like TiO_2, and their formation is more favorable in anatase than in rutile phase [39]. Furthermore, a novel treatment of hydrogenation of TiO_2 surface, which provoked high disorder in surface layers, led to formation of stable reduced TiO_2, followed by drastic change in color, e.

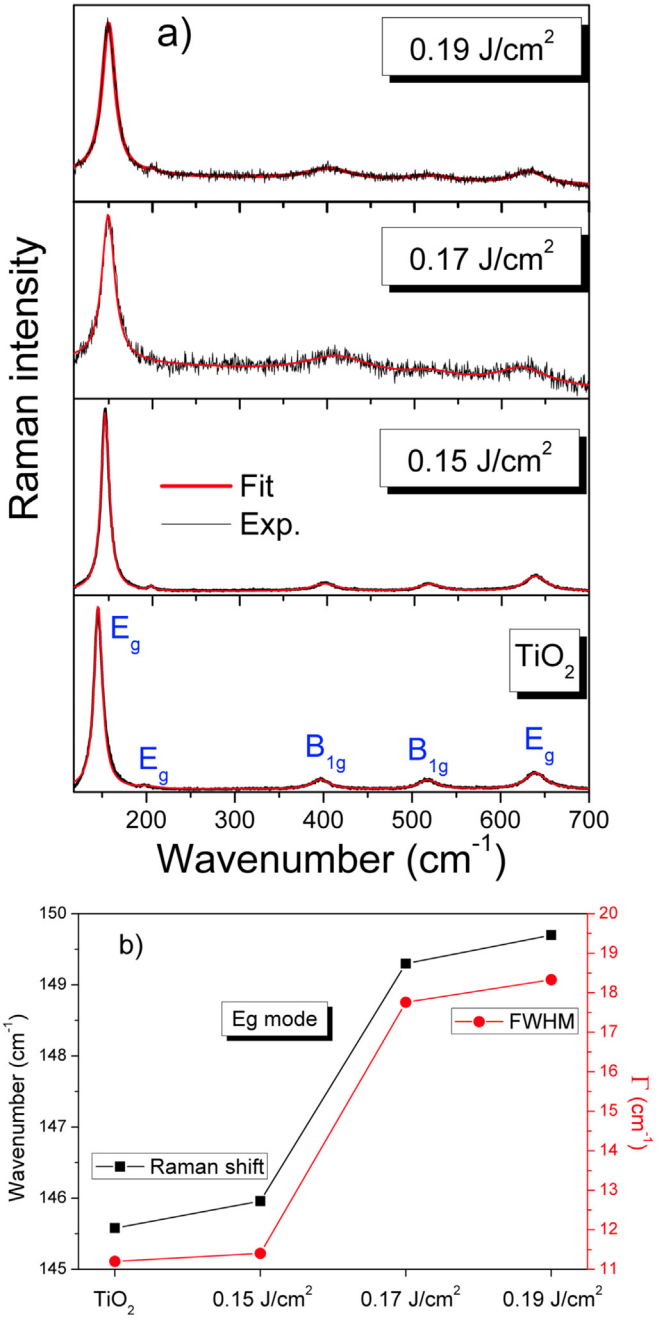

Fig. 6. a) First-order Raman spectra (black curve), together with Lorentzian fits (red curve) for the untreated and laser treated samples. b) Variation in the most-intense Eg mode position and linewidth with the laser fluence. (For interpretation of the references to color in this figure legend, the reader is referred to the web version of this article.)

g., darkening of the nanomaterial [40,41]. Based on these findings, it is reasonable to assume that during the laser treatment of TiO_2 films, oxygen vacancy defects are formed in the surface layer, as confirmed by EDX map of O species (Fig. 5c)). Also, formation of oxygen vacancies is accompanied by color change of treated samples from white to black, as observed in the optical microscopy images (see Fig. 2).

Deconvolution of the Raman spectra was performed by Lorentzian profile (red curves in Fig. 6a)). The main effect of the laser sintering manifested as an increase in linewidth and blueshift of the TiO_2 phonon modes. Pronounced blueshift and broadening of E_g mode at 145 cm^{-1} was detected in the films treated with higher laser fluence. In their paper, Parker and Siegel [42] demonstrated that shift and broadening of Raman modes in anatase and rutile polymorphs can be solely

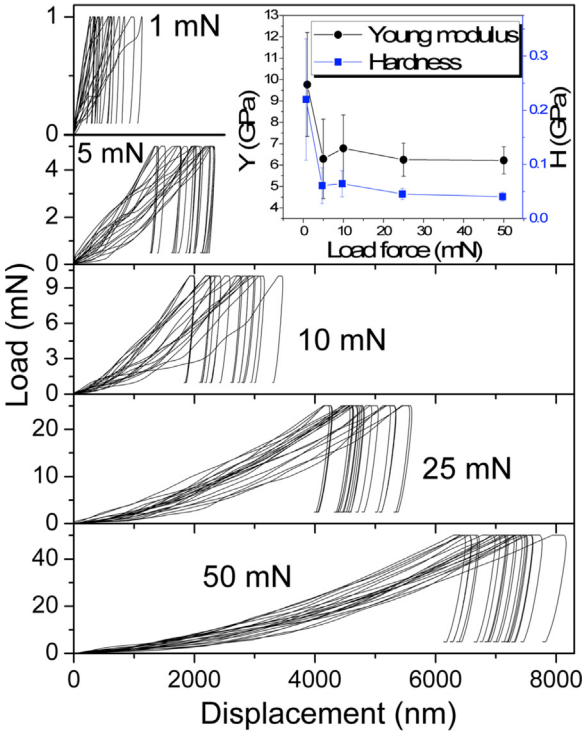

Fig. 7. Load versus displacement curves for untreated sample, measured at 1 mN, 5 mN, 10 mN, 25 mn and 50 mN.

ascribed to oxygen stoichiometry, which can be quantitatively assessed by nondestructive Raman spectroscopy. The appearance of oxygen vacancies as defects, directly influences local crystal symmetry and affects the force constants of the E_g mode, leading to a frequency blueshift and increase in phonon damping. The Fig. 6b) presents values of the frequency and linewidth for the most intense E_g mode. Keeping in mind the quantitative estimation of O/Ti ratio from Ref. [42], and knowing the position and bandwidth of E_g mode (Fig. 6b)), we can estimate that the O/Ti ratio is about 1.99 for the sample treated with the lowest laser fluence, whereas for the sample treated with the highest laser fluence this ratio decreased to 1.96. Obtained information reveals that laser treatment preserves crystal structure of TiO_2 nanoparticles and induces formation of structural defects in the form of oxygen vacancies, concentration of which increases in the samples treated with higher laser fluence.

Mechanical properties of untreated and laser sintered screen-printed films with TiO_2 nanoparticles were studied using nano-indentation technique. Aiming to obtain better statistics and more reliable data, Young modulus and hardness were carefully probed using several load-forces, and several measurements points on the surface of samples. The Fig. 7 shows 20 load-displacement curves, measured for each load (1 mN, 5 mN, 10 mN, 25 mN and 50 mN), only for the untreated sample. Values of load-forces are chosen to discriminate the influence of the glass substrate on the resulting characteristics of the investigated samples. For each load-force, 20 measurements were taken in rectangular array on different spots on the surface of investigated sample. The adopted approach offers a proper insight into mechanical properties, because localized defects, impurities and irregularities can very often produce an incorrect conclusion about Young modulus and hardness. Based on the obtained measurements for the untreated sample, one can see that, with an increase in the applied load, the curves shift to higher values of displacements on sample surface (higher penetration depth). This is due to the fact that TiO_2 nanoparticles in as-printed film are loosely bound by the paste matrix.

Values of Young modulus and hardness are calculated from the averaged load-displacement curves, using the Oliver-Pharr method [43]

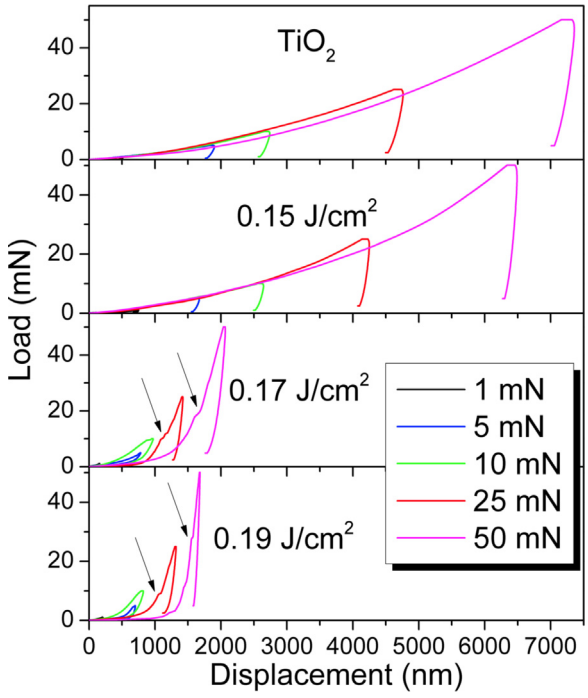

Fig. 8. Averaged load vs displacement curves for the untreated and laser treated samples, measured at 1 mN, 5 mN, 10 mN, 25 mn and 50 mN.

for each load-force and the results are presented in the inset of Fig. 7. With increase in the applied load, the values of Young modulus and hardness decrease. Large standard deviations and very low displacement into sample surface for 1 mN and 5 mN suggest that the measurements performed at these values of load forces are not reliable. This can be expected, since these are the lowest load forces that can be probed with nanoindenter.

Following the investigation of untreated sample, special attention was devoted to the influence of laser sintering on mechanical properties of screen-printed films. For the purpose of quantitative analysis, we averaged 20 measurements obtained for each load-force (like in Fig. 7), and also for each laser fluence that was used for sintering. The Fig. 8 presents comparison of the obtained averaged load displacement curves for untreated and laser sintered samples. From Fig. 8 it can be easily noticed that, with the increasing laser fluence, the curves shift towards lower penetration depth compared to untreated film. For sample treated with the highest laser fluence, the load–displacement curve shows maximum shifting toward lower penetration depth, which directly confirms our assumption that laser treatment process induces localized sintering and hardening of the printed film with TiO_2 nanoparticles. For the samples treated with laser fluences of 0.17 J/cm^2 and 0.19 J/cm^2, and for the highest load-forces (25 mN and 50 mN), we can detect deviation from the expected behavior in load displacement curves as the non-uniform increase in displacement and appearance of critical points (marked with arrows in Fig. 8). Such features can originate from surface roughness, local defects and non-homogeneities in the printed film [44]. Appearance of these defects can produce false values of Young modulus and hardness so it is not advisable to calculate mechanical parameters from the curves possessing such features.

Having in mind that measurements for the lowest applied loads are not reliable and that for the highest applied loads critical points affect the measurements, we chose the curves measured at 10 mN for the calculation and comparison of mechanical parameters for the untreated and laser sintered films. Young modulus and hardness were calculated from the measured load–displacement curves at 10 mN load and their values are presented in the Fig. 9. The obtained values for hardness provide information about the resistance of the screen-printed film to

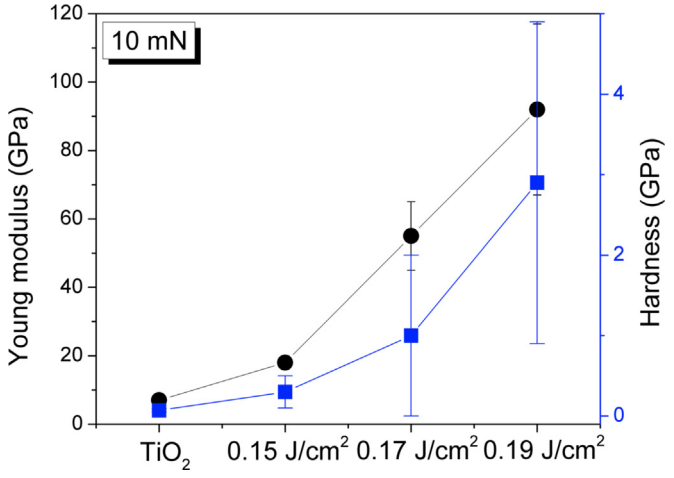

Fig. 9. Comparison of Young modulus and hardness values for untreated and laser treated samples. Presented values were calculated for 10 mN maximum load, from the curves presented in Fig. 7.

deformation caused by applied load force, whereas the Young modulus can be interpreted as the ability of the printed film to recover in its initial shape and form (stiffness of the material). For the untreated sample we obtained the lowest values of modulus, reflecting the low connectivity between the grains in the screen-printed matrix. For sample treated with highest laser fluence we measured substantial increase in Young modulus and hardness values. Presented results are in good agreement with SEM measurements, since it was established that the first stage of laser sintering process induces formation of necking between nanoparticles, yielding a dense and compact TiO_2 layer. The observed process strongly resembles a transition of micro-porous powdered material towards a solid ceramic one.

The significant increase in modulus and hardness values with laser treatment shows that sintered surfaces exhibit very good recovery characteristics and improved resistance to applied load. Compared to literature data for films prepared with pulsed magnetron sputtering (hardness H = 8 GPa, Young modulus E = 170 GPa) [45], modified physical vapor deposition technique (H: 0.1–4.4 GPa, E: 20–122 GPa) [46], nanocellulose composites (H = 3.4 GPa) [47] and for dip coating (H = 0.69 GPa) [48], the values obtained in the presented research reveal that the applied laser treatment produced successful sintering of the oxide nanoparticles into ceramic material. It is important to keep in mind the fact that applied technological processes in this work are by far cost-effective than the ones reported in the literature. Gaillard et al. [46] reported 4.4 GPa value for the hardness of anatase polymorph, but this value was obtained after additional sintering of the laser treated TiO_2 film. Anatase is a very interesting material, because it is stable at lower temperatures (< 500 °C) and ambient pressure, so it mainly occurs in nanocrystalline form. For this reason, it is very important to characterize its fundamental mechanical properties in order to expand the scope of applications of anatase polymorph in advanced technologies. For temperatures higher than 500 °C, anatase starts to transform into rutile polymorph, which naturally possesses much higher hardness and Young modulus [49]. At very high temperatures and pressures, achieved by laser sintering in diamond cell, anatase can transform into cotunnite polymorph, the hardest known oxide [50]. This polymorph exhibits extremely high hardness and Young modulus, comparable even to the artificial diamond. The 2.9 GPa obtained in this research, for the film treated with 0.19 J/cm^2, is lower than the one reported for the films developed with pulsed magnetron sputtering [45] and sintered laser treated film [46]. This is probably due to the fact that not all organic additives were removed during the laser treatment process, as we have seen from the EDX maps. Analysis of the conducted research and comparison with literature database provides substantial room for

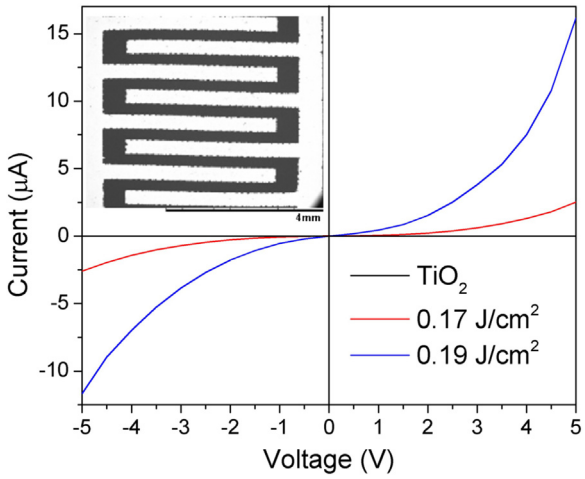

Fig. 10. Current vs voltage curves for untreated and samples sintered at 0.17 J/cm^2 and 0.19 J/cm^2 laser fluences, measured in the − 5 to 5 V range. The inset shows SEM image of the screen-printed interdigitated electrodes.

further improvement.

Formation of necking between individual nanoparticles is one of the most important features of the sintering process, with strong impact on the application of these materials in advanced technologies. Electronic transport in devices based on semiconductor oxide nanomaterials is essentially dependent on the formation of necking and good connectivity among nanoparticles [51]. Aiming to investigate the effect of laser fluence on conductivity of screen-printed films, we measured the current versus voltage characteristics in the DC regime. For successful and reliable measurements, the first step was to prepare the Ag interdigitated electrodes on glass substrate with screen-printing technique. The SEM image of interdigitated electrodes is shown in the inset of Fig. 10. The next step was to print the prepared paste with anatase TiO_2 nanoparticles on top of the electrodes and, finally, printed films were laser sintered using the same parameters in order to obtain identical values of the laser fluence. The Fig. 10 shows I(V) curves for the untreated and samples sintered with 0.17 J/cm^2 and 0.19 J/cm^2 laser fluences, measured in the − 5 to 5 V range. All measured curves exhibit typical semiconductor response, with an evident deviation from linear behavior originating from non-ohmic contacts between printed paste matrix and silver electrodes.

Fig. 10 clearly demonstrates that increase in laser fluence induces significant increase in the current values. For untreated sample, the profile of I(V) curve corresponds to the material with poor conductivity (9 nA at 5 V), whereas for the sample treated with 0.19 J/cm^2 we have order of magnitude higher current (16.6 μA at 5 V). Generally, DC transport properties of the porous nanomaterial, where nanoparticles are packed together, are governed by the grain-boundary resistance, since the resistance at these contacts is much higher than the resistance across single nanoparticle [52]. During sintering process, most of these grain boundaries disappear as the nanoparticles form neck-like structures and the grains connect together. In this case, the grain conductivity becomes dominant, and increase in current values can be detected, as shown in Fig. 10. Improvement of DC conductivity with laser sintering is essential for optimum performance of these materials in gas sensors and photovoltaic devices.

4. Conclusion

Analysis of the obtained results clearly indicates that laser treatment leads to significant improvement of mechanical properties of the screen-printed films. Laser induced evaporation of organic components in the paste matrix enabled total reorganization of the surface morphology, through breaking of the agglomerates into more compact and denser material with nanostructured surface roughness. The investigation of chemical composition in untreated and laser sintered films with EDX spectroscopy, revealed that carbon content is lower in the laser treated film due to evaporation of organic additives. The investigation of crystal structure and vibrational properties, performed with Raman spectroscopy, pointed out that anatase crystal structure is preserved during the laser sintering without presence of other phases, and that implementation of higher laser fluences led to increased non-stoichiometry in the TiO_2 nanoparticles. Nanoindenter measurements were carried out at several applied loads (1 mN, 5 mN, 10 mN, 25 mN and 50 mN), in order to carefully probe the Young modulus and mechanical hardness. Based on refined measurements, it was established that laser treatment induces sintering and hardening of the oxide material into dense ceramic coating with enhanced resistance to mechanical deformation and recovery characteristics. Benefiting from improved mechanical properties and formation of necking between individual nanoparticles during laser sintering process, a dramatic increase in DC conductivity was detected. Combination of the two simple technologies (screen-printing and laser processing) in the presented research offers a cost-effective solution to design and fabrication of semiconductor electrical devices with enhanced mechanical properties.

Acknowledgment

This work is supported by the Serbian Ministry of Education, Science and Technological Development through the projects III44006 and OI171032.

References

[1] J.M. Boyce, Modern technologies for improving cleaning and disinfection of environmental surfaces in hospitals, Antimicrob. Resist. Infect. 5 (2016) 1–10.
[2] W. Ke, G. Fang, J. Wan, H. Tao, Q. Liu, L. Xiong, P. Qin, J. Wang, H. Lei, G. Yang, M. Qin, X. Zhao, Y. Yan, Efficient hole-blocking layer-free planar halide perovskite thin-film solar cells, Nat. Commun. 6 (2015) 6700 (1-7).
[3] S. Zen, Y. Inoue, R. Ono, Low temperature (150 °C) fabrication of high-performance TiO_2 films for dye-sensitized solar cells using ultraviolet light and plasma treatments of TiO_2 paste containing organic binder, J. Appl. Phys. 117 (2015) 103302 (1-5).
[4] V.D. Dao, L.L. Larina, H.S. Choi, Suppression of charge recombination in dye-sensitized solar cells using the plasma treatment of fluorine-doped tin oxide substrates, J. Electrochem. Soc. 162 (2015) H903–H909.
[5] O.V. Penkov, M. Khadem, W.S. Lim, D.E. Kim, A review of recent applications of atmospheric pressure plasma jets for materials processing, J. Coat. Technol. Res. (2015).
[6] L.T. Phan, S.M. Yoon, M.W. Moon, Plasma-based nanostructuring of polymers: a review, Polymers 9 (2017) 417 (1-24).
[7] C.P. Eduardo, A.C.C. Aranha, A. Simões, M.S. Bello-Silva, K.M. Ramalho, M. Esteves-Oliveira, P.M. de Freitas, J. Marotti, J. Tunér, Laser treatment of recurrent herpes labialis: a literature review, Lasers Med. Sci. (2013).
[8] F. Mangano, L. Chambrone, R. van Noort, C. Miller, P. Hatton, C. Mangano, Direct metal laser sintering titanium dental implants: a review of the current literature, Int. J. Biomater. (2014) (Article ID461534).
[9] C. Kerse, H. Kalaycıoğlu, P. Elahi, B. Çetin, D.K. Kesim, Ö. Akçaalan, S. Yavaş, M.D. Aşık, B. Öktem, H. Hoogland, R. Holzwarth, F.O. Ilday, Ablation-cooled material removal with ultrafast bursts of pulses, Nature 537 (2016) 84–88.
[10] G. Mincuzzi, A.L. Palma, A. Di Carlo, T.M. Brown, Laser processing in the manufacture of dye-sensitized and perovskite solar cell technologies, ChemElectroChem 3 (2016) 9–30.
[11] M. Colina, A. Morales-Vilches, C. Voz, I. Martín, P. Ortega, A. Orpella, G. López, R. Alcubilla, Laser induced forward transfer for front contact improvement in silicon heterojunction solar cells, Appl. Surf. Sci. 336 (2015) 89–95.
[12] J.A. Spechler, K.A. Nagamatsu, J.C. Sturm, C.B. Arnold, Improved efficiency of hybrid organic photovoltaics by pulsed laser sintering of silver nanowire network transparent electrode, ACS Appl. Mater. Interfaces 7 (2015) 10556–10562.
[13] T. Huang, J. Lu, R. Xiao, Q. Wu, W. Yang, Enhanced photocatalytic properties of hierarchical three-dimensional TiO_2 grown on femtosecond laser structured titanium substrate, Appl. Surf. Sci. 403 (2017) 584–589.
[14] C. Fenzl, P. Nayak, T. Hirsch, O.S. Wolfbeis, H.N. Alshareef, A.J. Baeumner, Laser-scribed graphene electrodes for aptamer-based biosensing, ACS Sens. 2 (2017) 616–620.
[15] A. Kuchmizhak, E. Pustovalov, S. Syubaev, O. Vitrik, Y. Kulchin, A. Porfirev, S. Khonina, S. Kudryashov, P. Danilov, A. Ionin, On-fly femtosecond-laser fabrication of self-organized plasmonic nanotextures for chemo- and biosensing applications, ACS Appl. Mater. Interfaces 8 (2016) 24946–24955.
[16] O. Hung, C.A. Kan, Study of CO_2 laser treatment on colour properties of cotton-

based fabrics, Coatings 7 (2017) 131 (1-14).
[17] R. Nayak, R. Padhye, The use of laser in garment manufacturing: an overview, Fash. Text. 3 (2016) 5 (1-16).
[18] D.V. Ta, A. Dunn, T.J. Wasley, R.V. Kay, J. Stringer, P.J. Smith, C. Connaughton, J.D. Shephard, Nanosecond laser textured superhydrophobic metallic surfaces and their chemical sensing applications, Appl. Surf. Sci. 357 (2015) 248–254.
[19] H. Zhang, J. Di, M. Zhou, Y. Yan, R. Wang, An investigation on the hole quality during picosecond laser helical drilling of stainless steel 304, Appl. Phys. A 119 (2015) 745–752.
[20] K. Sugioka, J. Xu, D. Wu, Y. Hanada, Z. Wang, Y. Cheng, K. Midorikawa, Femtosecond laser 3D micromachining: a powerful tool for the fabrication of microfluidic, optofluidic, and electrofluidic devices based on glass, Lab Chip 14 (2014) 3447–3458.
[21] G.D. Tsibidis, C. Fotakis, E. Stratakis, From ripples to spikes: a hydrodynamical mechanism to interpret femtosecond laser-induced self-assembled structures, Phys. Rev. B 92 (2015) 041405 (1-6).
[22] A. Hadi, M. Alhabradi, Q. Chen, H. Liu, W. Guo, M. Curioni, R. Cernik, Z. Liu, Rapid fabrication of mesoporous TiO_2 thin films by pulsed fibre laser for dye sensitized solar cells, Appl. Surf. Sci. 428 (2018) 1089–1097.
[23] T.M. Tanvir Ahmmed, C. Grambow, A. Kietzig, Fabrication of micro/nano structures on metals by femtosecond laser micromachining, Micromachines 5 (2014) 1219–1253.
[24] B. Hopp, T. Smausz, M. Lentner, J. Kopniczky, C. Tápai, T. Gera, T. Csizmadia, M. Ehrhardt, P. Lorenz, K. Zimmer, Stability investigation of laser darkened metal surfaces, Appl. Phys. A 123 (2017) 598 (1-8).
[25] M. Tian, M. Mahjouri-Samani, G. Eres, R. Sachan, M. Yoon, M.F. Chisholm, K. Wang, A.A. Puretzky, C.M. Rouleau, D.B. Geohegan, G. Duscher, Structure and formation mechanism of black TiO_2 nanoparticles, ACS Nano 9 (2015) 10482–10488.
[26] X. Chen, L. Liu, F. Huang, Black titanium dioxide (TiO_2) nanomaterials, Chem. Soc. Rev. 44 (2015) 1861–1885.
[27] H. Kim, G.P. Kushto, C.B. Arnold, Z.H. Kafafi, A. Piqué, Laser processing of nanocrystalline TiO_2 films for dye-sensitized solar cells, Appl. Phys. Lett. 85 (2004) 464–466.
[28] M.J. Pu, J.Z. Chen, I.C. Cheng, KrF excimer laser irradiated nanoporous TiO_2 layers for dye-sensitized solar cells: influence of laser power density, Ceram. Int. 39 (2013) 6183–6188.
[29] M.A. Gondal, A.M. Ilyas, U. Baig, Pulsed laser ablation in liquid synthesis of ZnO/TiO_2 nanocomposite catalyst with enhanced photovoltaic and photocatalytic performance, Ceram. Int. 42 (2016) 13151–13160.
[30] G. Dubourg, A. Segkos, J. Katona, M. Radović, S. Savić, G. Niarchos, C. Tsamis, V. Crnojević-Bengin, Fabrication and characterization of flexible and miniaturized humidity sensors using screen-printed TiO_2 nanoparticles as sensitive layer, Sensors 17 (2017) 1854 (1-13).
[31] J. Kim, J. Kim, M. Lee, Laser welding of nanoparticulate TiO_2 and transparent conducting oxide electrodes for highly efficient dye-sensitized solar cell, Nanotechnology 21 (2010) 345203 (6pp).
[32] H. Pan, S. Hwan Ko, N. Misra, C.P. Grigoropoulos, Laser annealed composite titanium dioxide electrodes for dye-sensitized solar cells on glass and plastics, Appl. Phys. Lett. 94 (2009) 071117.
[33] C. Perego, R. Revel, O. Durupthy, S. Cassaignon, J.P. Jolivet, Thermal stability of TiO_2-anatase: impact of nanoparticles morphology on kinetic phase transformation, Solid State Sci. 12 (2010) 989–995.
[34] F. Haaf, A. Sanner, F. Straub, Polymers of *N*-vinylpyrrolidone: synthesis, characterization and uses, Polym. J. 17 (1985) 143–152.
[35] T. Ohsaka, F. Izumi, Y. Fujiki, Raman spectrum of anatase, TiO_2, J. Raman Spec. 7 (1978) 321.
[36] J.-G. Li, T. Ishigaki, X. Sun, Anatase, brookite, and rutile nanocrystals via redox reactions under mild hydrothermal conditions: phase-selective synthesis and physicochemical properties, J. Phys. Chem. C 111 (2007) 4969–4976.
[37] W.F. Zhang, Y.L. He, M.S. Zhang, Z. Yin, Q. Chen, Raman scattering study on anatase TiO_2 nanocrystals, J. Phys. D: Appl. Phys. 33 (2000) 912–916.
[38] A.L. Bassi, D. Cattaneo, V. Russo, C.E. Bottani, E. Barborini, T. Mazza, P. Piseri, P. Milani, F.O. Ernst, K. Wegner, S.E. Pratsinis, Raman spectroscopy characterization of titania nanoparticles produced by flame pyrolysis: the influence of size and stoichiometry, J. Appl. Phys. 98 (2005) 074305.
[39] B.J. Morgan, G.W. Watson, Intrinsic n-type defect formation in TiO_2: a comparison of rutile and anatase from GGA + *U* calculations, J. Phys. Chem. C 114 (2010) 2321–2328.
[40] X. Chen, L. Liu, P.Y. Yu, S.S. Mao, Increasing solar absorption for photocatalysis with black hydrogenated titanium dioxide nanocrystals, Science 331 (2011) 746–750.
[41] X. Pan, M.-Q. Yang, X. Fu, N. Zhang, Y.-J. Xu, Defective TiO2 with oxygen vacancies: synthesis, properties and photocatalytic applications, Nanoscale 5 (2013) 3601–3614.
[42] J.C. Parker, R.W. Siegel, Calibration of the Raman spectrum to the oxygen stoichiometry of nanophase TiO2, Appl. Phys. Lett. 57 (1990) 943–945.
[43] W.C. Oliver, G.M. Pharr, Measurement of hardness and elastic modulus by instrumented indentation: advances in understanding and refinements to methodology, J. Mater. Res. 19 (2011) 3.
[44] L. Qian, M. Li, Z. Zhou, H. Yang, X. Shi, Comparison of nano-indentation hardness to microhardness, Surf. Coat. Technol. 195 (2005) 264–271.
[45] O. Zywitzki, T. Modes, H. Sahm, P. Frach, K. Goedicke, D. Glöß, Structure and properties of crystalline titanium oxide layers deposited by reactive pulse magnetron sputtering, Surf. Coat. Technol. 180–181 (2004) 538–543.
[46] Y. Gaillard, V.J. Rico, E. Jimenez-Pique, A.R. González-Elipe, Nanoindentation of TiO_2 thin films with different microstructures, J. Phys. D: Appl. Phys. 42 (2009) 145305 (9pp).
[47] C. Schütz, J. Sort, Z. Bacsik, V. Oliynyk, E. Pellicer, A. Fall, L. Wågberg, L. Berglund, L. Bergström, G. Salazar-Alvarez, Hard and transparent films formed by nanocellulose-TiO_2 nanoparticle hybrids, PLos One 7 (2012) e45828.
[48] H. Yaghoubi, N. Taghavinia, E.K. Alamdari, A.A. Volinsky, Nanomechanical properties of TiO_2 granular thin films, Appl. Mater. Interface 2 (2010) 2629–2636.
[49] M.J. Mayo, R.W. Siegel, A. Narayanasamy, W.D. Nix, Mechanical properties of nanophase TiO_2 as determined by nanoindentation, J. Mater. Res. 5 (1990) 1073–1082.
[50] R. Ahuja, L.S. Dubrovinsky, High-pressure structural phase transitions in TiO_2 and synthesis of the hardest known oxide, J. Phys.: Condens. Matter 14 (2002) 10995–10999.
[51] N. Barsan, U. Weimar, Conduction model of metal oxide gas sensors, J. Electroceram. 7 (2001) 143.

Processing and Application of Ceramics 12 [4] (2018) 326–334
https://doi.org/

Preparation of TiO_2 and ZnO dispersions for inkjet printing of flexible sensing devices

Nejra Omerović[1,*], Marko Radović[1], Slavica M. Savić[1], Jaroslav Katona[2]

[1]*University of Novi Sad, BioSense Institute, Nano and Microelectronics Group, Dr Zorana Đinđića 1, 21000 Novi Sad, Serbia*
[2]*University of Novi Sad, Faculty of Technology Novi Sad, Bulevar cara Lazara 1, 21000 Novi Sad, Serbia*

Received 29 June 2018; Received in revised form 30 September 2018; Accepted 29 October 2018

Abstract

Research presented in this article focuses on the preparation of functional dispersions for inkjet printing of nanoparticles as sensitive layers. The stable suspensions of MO_x (M = Ti, Zn) were prepared using gum arabic (GA) and Solsperse® 40000 (SO) as dispersants. A special attention was paid to the monitoring of particle size evolution during the planetary ball milling of dispersions, so that optimum ratio between milling time and particle size can be determined. After adjusting the printing parameters, prepared inks were printed on the flexible PET substrate with interdigitated electrodes (IDE). Films printed with TiO_2 ink stabilized by GA exhibited highly cracked surface which resulted in low current values, whereas ZnO ink stabilized by SO yielded crack-free surface and much higher current values. All investigated samples showed linear current behaviour in the range from -5 to 5 V, indicating formation of ohmic contacts between electrodes and nanoparticles, but ZnO ink produced the highest current values. Gas sensing properties, tested at room temperature at several humidity levels and for different types of alcohols, revealed that printed sensor exhibits modest sensitivity for low humidity levels and slightly higher affinity towards methanol gas. Photo sensitivity measurement showed very high photocurrent values with strong potential for optoelectronic applications.

Keywords: *ZnO, TiO_2, inkjet printing, sensors*

I. Introduction

Although the most common use of the inkjet printing is in conventional applications such as graphics, text printing or marking, over the last decades the technology has been guided to manufacture novel functional surfaces and components with applications for advanced technologies. This is due to the ability of the inkjet printing to digitally control the ejection of ink droplets of defined volume and precisely position them onto a substrate [1–3]. Inkjet printing is a contactless process which means that wide range of fluids can be used and optimized for a variety of substrates, even non-flat, rigid or flexible ones. Besides this flexibility, short production time, low-cost and very efficient use of materials can be listed as main advantages of the inkjet printing [2–5].

Inkjet printing is one of the most versatile tools for functionalization of MO_x (metal oxides) nanomaterials into electronic components and devices [6]. Due to their unique structure, morphology, chemical, optical and electrical properties, MO_x nanomaterials have wide scope of applications in advanced technologies. Using suitable dispersions, these nanomaterials are printed as components for solar cells [7,8], photodetectors [9], gas sensors [10] and biosensors [11,12]. Cost-effective solutions to ambient monitoring, based on printed MO_x nanomaterials, have strong impact on modern food production industry, which is today the fastest growing market for inkjet printing technology. Food decay process is often followed by the emission of volatile organic compounds (VOC) like alcohols [13], therefore a lot of attention is focused on the development of highly efficient sensors, operating at room temperature and having high sensitivity [14]. Smart packaging technology often requires sensor operation at different humidity levels, ranging from low to high, for mushrooms, maize, grains, spices and tomatoes [15]. Significant efforts have

* Corresponding authors: tel: +381 21 485 2138,
e-mail: *nejra@biosense.rs*

been devoted to the optimization of breathalyser devices for monitoring concentration of ethanol vapour in human breath [16]. One of the advantages for application of the inkjet technology in diagnostic devices is the ability to rapidly produce low cost solutions printed on common paper substrate [17]. All these challenges have spanned together chemistry, physics, material science, biology and engineering in a joint multidisciplinary research of sensor design and applications. The most important challenges for printing of MO_x nanomaterials are preservation of the material fundamental properties trough the printing process and to provide conditions for maximum efficiency of the materials performance.

The aim of this work was to demonstrate the possibility of the inkjet printing of stable homogeneous aqueous suspensions of MO_x onto flexible, environmentally friendly, low-cost substrates addressing the requirements of flexible electronics for a cost-efficient, high-output manufacturing and opening the route towards the flexible, eco-designed mass production. The investigations on the optimum concentration of dispersants and the mechanism determining the dispersion behaviour of MO_x in aqueous dispersants solution were performed. The main goal of this work is to analyse the influences of different quantity of dispersants and milling conditions on the printing quality parameters of the ink using different substrates.

II. Experimental procedure

Fabrication of basic components of sensor devices such as transducer and sensitive layer was performed with simple and cost-effective inkjet printing technique. A schematic representation of sensor fabrication with inkjet technology is shown in Fig. 1. Transducer used in this work is composed of IDE printed with commercial Ag ink on flexible substrate. The sensitive layer with MO_x nanoparticles is printed as rectangular film on top of the electrodes. Utilization of the inkjet printing offers very precise patterning on various types of substrates with efficient use of nanomaterials and also provides substantial operating flexibility since it does not require use of masks and other complicated processing steps.

For the preparation of functional inks we have used commercially available titanium oxide (TiO_2, anatase, 99.7%, Sigma Aldrich, US) and zinc oxide (ZnO, 99+%, Alfa Aesar, US) nanopowders. For the matrix preparation we have used gum arabic (GA, polyanionic hydrocolloide, Sigma Aldrich, US), *Solsperse*® 40000 (SO, anionic phosphate alkoxylated polymer, Lubrizol, US); *Byk*®-028 (antifoaming agent, BYK Additives & Instruments, Germany); 1,2-propylene glycol ($C_3H_8O_2$, Centrohem, Serbia), n-propanol (C_3H_8O, Kemika, Croatia). Printing of the interdigitated electrodes was performed using the Ag nanoparticle ink *SunTronic*® *Jet Silver* (SunChemical, UK).

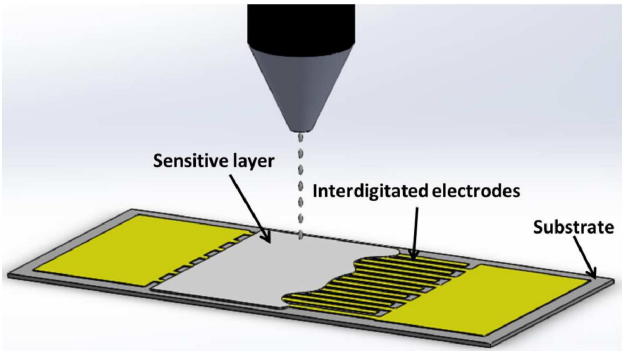

Figure 1. A schematic representation of fabricated sensor

The dispersions were homogenized by means of Ultraturrax T-25 homogenizer (IKA, Germany). The ball milling was performed using planetary ball mill PM 100 (Retsch, Germany) with YSZ (yttrium stabilized zirconia) 50 ml jar and balls of 2 mm in diameter. Viscosity of prepared inks was determined with RheoStress 600HP rheometer (Thermo Haake, Germany). Surface tension was measured with Sigma 703D tensiometer (KSV Instruments, Finland). Particle size determination was performed with Zetasizer Nano ZS (Malvern Instruments Ltd, UK), which works on the dynamic light scattering principle. Printing of the prepared inks was performed with Fuji Dimatix DMP-3000 (Fujifilm, Japan) semi-industrial inkjet printer. The optical images were collected using Huvitz HRM-300 optical microscope (Huvitz, South Korea). Atomic force microscopy (AFM) measurements were performed on NTEGRA prima (NDMT, Russia) microscope in semicontact mode. Characterization of DC electrical properties was done on Yokogawa-Hewlett-Packard 4145A semiconductor analyser (Yokogawa Electronic, Japan). Humidity sensing characterization was performed using appropriate setup. Gas sensing properties of different alcohols (methanol, ethanol and propanol) were investigated using custom-built setup consisting of the chamber with mounted gas inlet/outlet for N2 purging and equipped with fan and evaporator. Photocurrent measurements were made in the custom built setup equipped with high power light emitting diode operating at 365 nm.

III. Results and discussion

Design and optimization of functional inks, that can be used for inkjet printing of nanomaterials, can be considered as a bottom-up approach to achieve higher technological level, with the strong impact on the application of these materials in advanced technologies. Undertaken approach to the preparation of functional ink can be divided into 3 simple steps as shown in Fig. 2.

The primary dispersions of MO_x were prepared by dispersing either TiO_2 or ZnO nanopowder in a continuous phase. As the continuous phase, aqueous solution

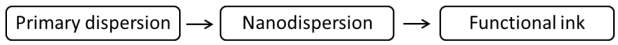

Figure 2. Basic steps used for preparation of functional ink for inkjet printing of TiO_2 and ZnO nanoparticles

Table 1. Chemical compositions of TiO_2 primary dispersions

Dispersion	TiO_2 [wt.%]	GA [wt.%]	SO [wt.%]	*Byk*® [wt.%]	H_2O [wt.%]	TiO_2 in H_2O [wt.%]	Dispersant in H_2O [wt.%]	TiO_2 : dispersant ratio
GATO-1	14.71	14.71			70.58	17.24	17.24	1 : 1
GATO-3.6	15.24	4.23		0.08	80.44	15.93	5.00	3.6 : 1
GATO-2.25	15.92	7.07		0.09	76.92	17.15	8.42	2.25 : 1
SOTO-45.2	15.82		0.35	0.35	83.48	15.93	0.42	45.2 : 1
SOTO-12.5	15.67		1.25	0.37	82.71	15.93	1.49	12.5 : 1

Table 2. Chemical compositions of ZnO primary dispersions

Dispersion	ZnO [wt.%]	GA [wt.%]	SO [wt.%]	*Byk*® [wt.%]	H_2O [wt.%]	ZnO in H_2O [wt.%]	Dispersant in H_2O [wt.%]	ZnO : dispersant ratio
GAZO-1	14.68	14.68		0.12	70.53	17.22	17.22	1 : 1
GAZO-3.6	15.25	4.24		0.04	80.47	15.93	5.00	3.6 : 1
SOZO-38.6	15.82		0.41	0.26	83.51	15.93	0.48	38.6 : 1

of dispersant GA or SO, in appropriate concentration, was used. The appearance of foam during homogenization imposed addition of suitable weight of antifoaming agent Byk®-028 in the continuous phase. The dispersions were homogenized by means of Ultraturrax T-25 homogenizer during 10 min at 15000 rpm and room temperature. The obtained dispersions with corresponding ratios are denoted as GATO (in the case of GA and TiO_2), SOTO (SO and TiO2), GAZO (GA and ZnO) and SOZO (SO and ZnO). The compositions of TiO_2 and ZnO primary dispersions are shown in Tables 1 and 2, respectively.

It is important to mention that for the preparation of dispersions with acceptable particle size and stability, the required concentration of SO is much lower compared to GA concentration, because of different structures and stabilization mechanisms of dispersants.

The primary dispersions, immediately after preparation, were further homogenized in planetary ball mill. The ball milling was performed using YSZ (yttrium stabilized zirconia) 50 ml jar and YSZ balls of 2 mm in diameter. For milling, 16.5 ml of primary dispersion was used. The milling conditions for prepared dispersions are shown in Table 3. TiO_2 and ZnO dispersions with higher concentration of GA in the formulation (GATO-1 and GAZO-1) were milled at 250 rpm for 180 min, and the particle sizes were simultaneously measured after 15, 30, 60, 90, 120, 150 and 180 min, in order to determine an optimum milling time.

Table 3. The milling conditions for TiO_2 and ZnO dispersions

Dispersion		Milling speed [rpm]	Milling time [min]
TiO_2	GATO-1	250	180
	GATO-3.6	250	90
	GATO-2.25	250 + 350	90 + 90
	SOTO-45.2	250	180
	SOTO-12.5	250	90
ZnO	GAZO-1	250	180
	GAZO-3.6	250	90
	SOZO-38.6	250	90

The primary dispersions, with GA as a dispersant, were prepared with the GA : TiO_2 and GA : ZnO ratio 1 : 1 and treated in planetary ball mill at 250 rpm for 180 min. Evolution of average particle size as a function of milling time is presented in Fig. 3. The milling of dispersions up to 90 min resulted in the significant reduction of the average particle size, which was the main goal of using planetary ball mill for the preparation of functional inks. For TiO_2 dispersion (GATO-1) the average particle size is reduced from 600 nm at the beginning to 420 nm after 90 min of milling, while in the case of ZnO dispersion (GAZO-1) the average particle size is reduced from 460 nm at the beginning to 330 nm after 90 min of milling. Prolonged milling time up to 180 min resulted in negligible changes of the average particle size for both dispersions. Therefore, milling time of 90 min can be considered as an optimal compromise between invested energy and achieved particle size.

Very important issue that needs to be addressed is the long term stability of the prepared dispersions. The particle size measurements during three weeks after preparation of dispersion, served as an indicator of colloidal

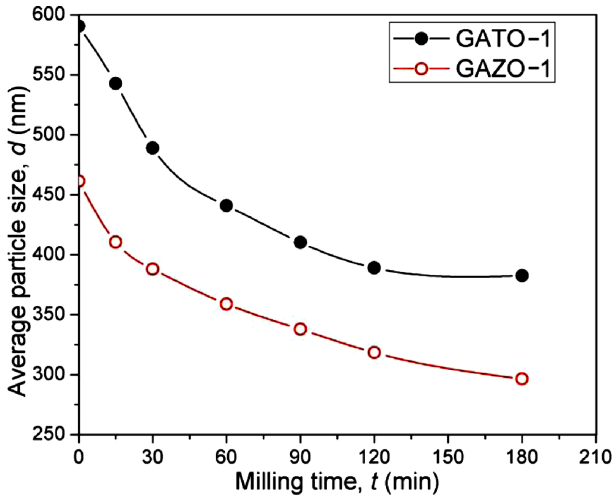

Figure 3. Variation in average particle size with milling time for GATO-1 and GAZO-1 primary dispersions

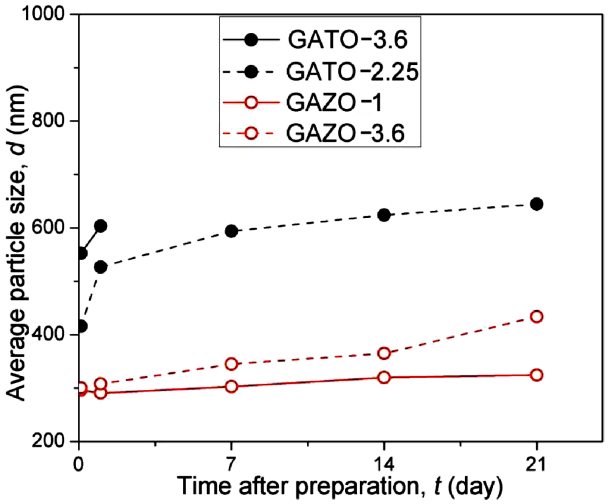

Figure 4. The average particle size of TiO_2 and ZnO primary dispersions stabilized with GA

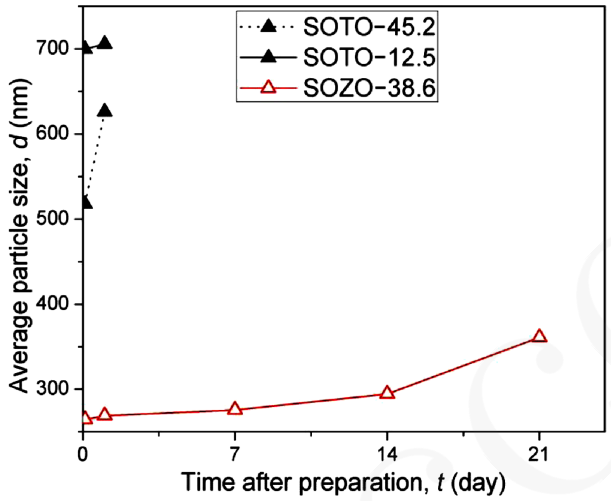

Figure 5. The average particle size of TiO_2 and ZnO primary dispersions stabilized with SO

stability. The dispersions GATO-1 and GAZO-1 showed good stability within the three weeks, but these dispersions were not used for functional inks preparation due to the high concentration of gum arabic, which is expected to have a strong influence on the properties of printed structures. Therefore, TiO_2 and ZnO primary dispersions with lower GA concentration (GATO-3.6 and GAZO-3.6) were prepared by milling at 250 rpm for 90 min. The average particle sizes, measured for TiO_2 and ZnO primary dispersions stabilized with GA, are displayed in Fig. 4. As can be seen (Fig. 4) the average particle size in TiO_2 dispersion GATO-3.6, after milling for 90 min is around 550 nm which means that the particle size is not decreased to the expected value. On the other hand, the average particle size in ZnO dispersion GAZO-3.6, after milling for 90 min, is around 300 nm, which is close to the achieved particle size in dispersion GAZO-1 after the same milling time.

It can also be seen (Fig. 4) that the average particle size of GATO-3.6 dispersion has increased for 10%, up to around 600 nm after one day, which indicated very unstable dispersion, while the average particle size of GAZO-3.6 dispersion stayed almost unchanged. During the third week, the average particle size of GAZO-3.6 was increased for 44%, up to around 430 nm. Although the new dispersion GAZO-3.6 displayed slightly worse stability compared to dispersion GAZO-1, due to the lower concentration of used dispersant, the GAZO-3.6 dispersion was used for functional ink preparation. In order to obtain more stable TiO_2 dispersion with smaller average particle size, the new dispersion GATO-2.25 was prepared. The dispersion GATO-2.25 was milled 180 min in total (90 min at 250 rpm + 90 min at 350 rpm). As can be seen in Fig. 4, smaller particles of TiO_2 dispersion were obtained with optimized milling conditions. The average particle size of the GATO-2.25 dispersion after 180 min of milling is around 400 nm. Although the GATO-2.25 dispersion, similarly as the GATO-3.6 dispersion, shows instability in the first 24 h after milling, it was used for functional ink formulation because of the smaller average particle size.

In order to examine how to prepare stable nanodispersions with SO as dispersant, two TiO_2 primary dispersions (SOTO-45.2 and SOTO-12.5) and one ZnO primary dispersion (SOZO-38.6) were prepared. The obtained results of the particle size measurements for TiO_2 and ZnO primary dispersions stabilized with SO are shown in Fig. 5. As can be seen, the dispersion SOZO-38.6 displayed good stability for the first two weeks, and a more significant increase in the particle size during the third week, up to around 350 nm, which is around 35% of the value obtained immediately after milling. The average particle size of the SOTO-12.5 dispersion is higher than that of the SOTO-45.2 dispersion, but dispersion SOTO-12.5 showed better stability during the time. The dispersions SOTO-12.5 and SOZO-38.6 were used for functional ink preparation.

Finally, two TiO_2 dispersions (GATO-2.25 and SOTO-12.5) and two ZnO dispersions (GAZO-3.6 and SOZO-38.6) were selected for functional ink preparation. Thus, four inkjet inks were prepared: two inks with TiO_2 nanoparticles (IJ-GATO-2.25 and IJ-SOTO-12.5) and two inks with ZnO nanoparticles (IJ-GAZO-3.6 and IJ-SOZO-38.6) according to the formulations from Table 4. The functional inks were prepared by diluting stable TiO_2 and ZnO nanodispersions with water and adding 1,2-propylene glycol (PG) and n-propanol (PrOH) in ratio PG : PrOH = 43 : 7. The water, PG and PrOH ratio in the formulations was H_2O : PG : PrOH = 50 : 43 : 7 which gives required values of viscosity and surface tension (η = 6.40 mPa s and σ = 36.20 mN/m) for printing. The formulations of the prepared inkjet inks are shown in Table 4.

The weight of PG-PrOH mixture, equal to the total weight of water in the formulation, was added to the previously diluted nanodispersion. Finally, inks were homogenized during 5 min at 15000 rpm and room tem-

Table 4. The formulations of inks used for inkjet printing of nanoparticles

Ink	MO_x [wt.%]	GA [wt.%]	SO [wt.%]	*Byk*® [wt.%]	PG [wt.%]	PrOH [wt.%]	H_2O [wt.%]	MO_x : dispersant ratio
TiO_2 – IJ-GATO-2.25	4.81	2.14		0.03	40	6.51	46.51	2.25 : 1
TiO_2 – IJ-SOTO-12.5	4.50		0.40	0.10	40.85	6.67	47.52	12.5 : 1
ZnO – IJ-GAZO-3.6	4.45	1.24		0.01	40.54	6.60	47.14	3.6 : 1
ZnO – IJ-SOZO-38.6	4.51		0.12	0.07	40.96	6.69	47.65	38.6 : 1

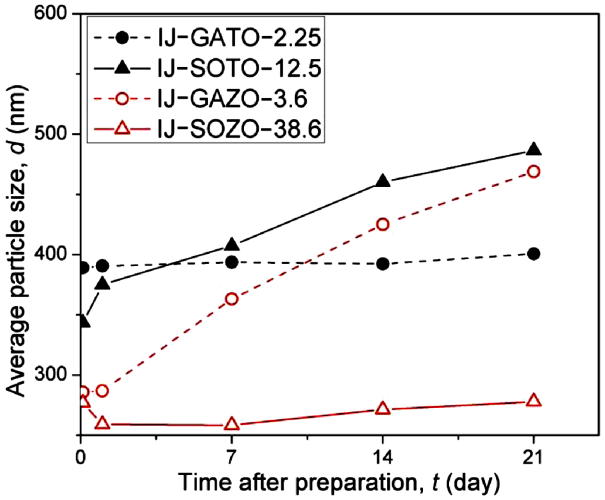

Figure 6. Stability test of the prepared inks, presented as variation in particle size during three weeks after preparation

perature by Ultraturrax T-25 homogenizer. The stability test of the prepared inks was conducted by measuring particle size during three weeks after preparation and the results are shown in Fig. 6. Negligible changes in particle size for inks IJ-GATO-2.25 and IJ-SOZO-38.6 can be observed, indicating good stability of these inks.

Based on the performed particle size measurements it can be concluded that the inks IJ-GATO-2.25 and IJ-SOZO-38.6 showed the best stability. In order to remove large particle aggregates and to reduce the risk of printhead nozzle clogging, prepared inks were filtered through 1 μm syringe filter (Whatman, UK) and loaded in the cartridge reservoir.

After successful preparation of inks, next step in the research was to optimize the printing parameters aiming to obtain a controllable and effective process for printing of nanoparticles that can be used for fabrication of sensitive sensor layers. By adjusting basic parameters of piezoelectric inkjet printer, such as jetting voltage, frequency and waveform, stable ink droplets, with an appropriate drop speed at 0.5 mm distance from the nozzle plate, were obtained. All prepared inks were printable and able to form stable droplets during jetting, except the TiO_2 ink stabilized with SO (IJ-SOTO-12.5), which showed the worst stability test after 3 weeks of aging.

Dropwatcher images of the IJ-SOZO-38.6 ink droplets ejection from the nozzles of printhead are shown in Fig. 7. It can be seen that after the drop leaves the nozzle it has a ligament, called tail, which ideally merges into the main drop without creating satellites (formation of satellites usually leads to the reduction in print quality).

In order to obtain continuous and homogeneous layer during inkjet printing, it was necessary to determine the optimal drop spacing by studying the behaviour of the printed ink drops on the substrate surfaces. An array of single ink drops on Si, polyimide (Kapton®), PET and paper substrates was printed at a mutual distance of 100 μm as shown in Fig. 8. The measured average drop diameter is 34 μm for Si, 32 μm for Kapton® and 40 μm for PET substrate. It must be noted that no coffee ring effect (a pattern left by a puddle of particle-laden liquid after it evaporates) was observed for all investigated substrates, since appearance of this feature can lead to the degradation of the print quality. The printing of uniform layer on Si and Kapton® surfaces resulted in a formation of irregular structures due to the hydrophobic nature of these surfaces. For printing of sensitive layer of MO_x nanoparticles we have chosen PET substrate because it is hydrophilic and can be heated up to 200 °C. Taking into account the measured average drop diameter on the PET substrate, drop spacing which is half of the droplet size (20 μm) was used as the optimal value, aiming to create sufficient overlapping between individual droplets so that continuous layers can be printed.

The fabrication of the sensor transducer was performed by printing interdigitated electrodes (IDE) on flexible PET substrate, using commercial silver ink. The

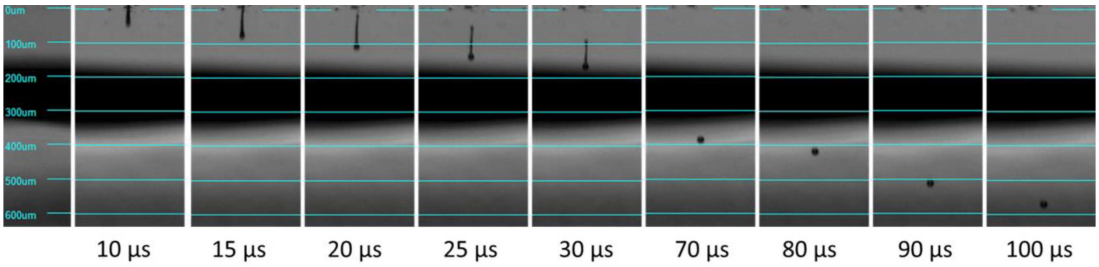

Figure 7. Dropwatcher images of the IJ-SOZO-38.6 ink droplets ejection from the nozzles of piezoelectric inkjet printhead

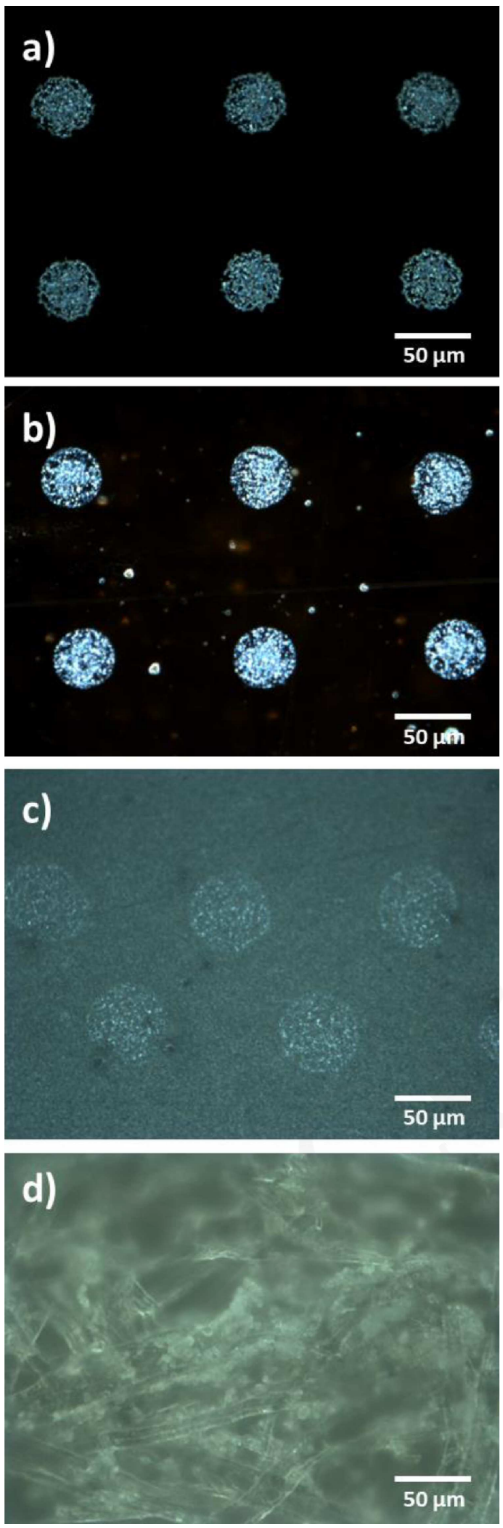

Figure 8. Optical images of individual drops of IJ-SOZO-38.6 ink printed on: a) Si, b) Kapton®, c) PET and d) paper substrate

optical image of the printed electrodes is given in Fig. 9. During the printing of the silver ink, the substrate was heated up at 40 °C, a step necessary for achievement of precisely resolved structures for electrical characterization. After printing, the IDE were gradually heated up to 200 °C and kept for 1 h to attain sintered Ag nanoparticles. The distance between fingers of IDE structure,

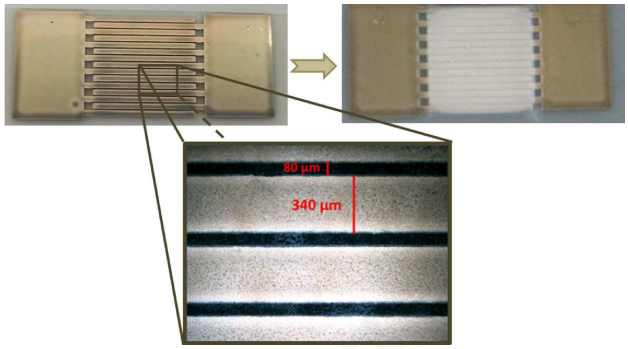

Figure 9. Optical images of IDE printed with Ag ink, along with image of the sensitive layer printed with IJ-SOZO-38.6 ink

after sintering, was around 80 µm, whereas the width of the individual finger was around 340 µm. PET substrate was chosen since it can withstand temperatures up to 200 °C allowing the sintering of printed electronic components and because of its flexibility, biodegradability and availability. In the second step rectangular layers of functional TiO_2 and ZnO inks were printed on top of the electrodes and they represent a sensitive sensor layer. By printing, a layer of liquid ink on the substrate was obtained, which was transformed into functional electronic element by evaporating volatile components of dispersion. After printing, the obtained sensors with rectangular (5 × 5 mm) sensitive layer were gradually heated up at 100 °C and kept at that temperature for 2 h to achieve evaporation of organic additives.

The successful preparation of inks with nanoparticles and optimization of printing parameters enabled printing of multilayer MO_x structures for sensing applications. Optical images of films printed with 10 layers using IJ-SOZO-38.6 and IJ-GATO-2.25 inks, together with corresponding AFM images of the printed nanoparticles are shown in Fig. 10. From the presented

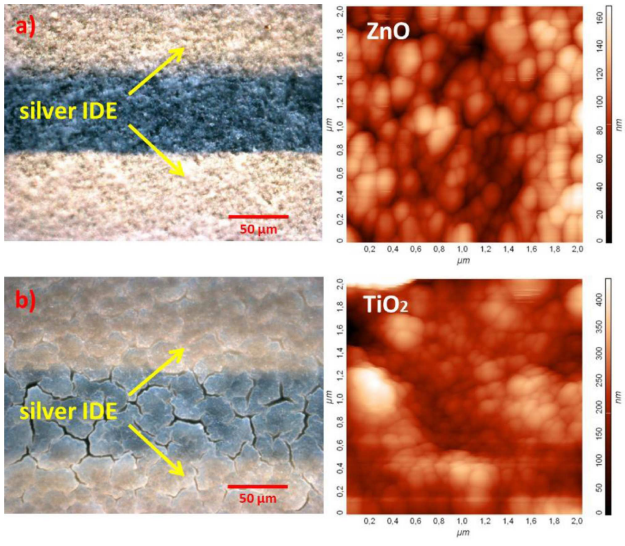

Figure 10. Optical images of films printed with 10 layers on top of IDE, using: a) IJ-SOZO-38.6 and b) IJ-GATO-2.25 inks, along with corresponding AFM images of printed ZnO and TiO_2 nanoparticles

optical images it can be clearly seen that ZnO ink (IJ-SOZO-38.6) produces consistent and homogeneous layer without cracks. The layer printed with TiO_2 ink (IJ-GATO-2.25) exhibits significant cracks on the surface of the film. The AFM images reveal nanostructured nature of printed films, where nanoparticles form large agglomerates. The agglomeration process is also observed during the preparation of the functional inks since the size of particles in primary dispersion is much larger than the initial size reported by manufacturers (TiO_2 APS < 25 nm; ZnO APS 40–100 nm). The particle size determined by the dynamic light scattering in primary dispersion is very similar to the size of agglomerates observed in AFM images, indicating that once the particles are stabilized in dispersion their size does not alter significantly during the inkjet printing process and after thermal treatment of the printed films.

The electrical characterization of the printed sensors was performed by measuring current vs. voltage ($I(V)$) curves in the -5 to 5V range. In Fig. 11, $I(V)$ curves are compared for sensors printed with 10 layers of IJ-SOZO-38.6, IJ-GAZO-3.6 and IJ-GATO-2.25 inks. From the presented measurements it is evident that sensors printed with IJ-GAZO-3.6 and IJ-GATO-2.25 inks possess very high resistivity (very low current) which renders these samples not quite suitable for practical applications. Sensor printed with IJ-SOZO-38.6 ink exhibits significantly higher current values and linear voltage dependence pointing out that inkjet printed ZnO nanoparticles have ohmic contacts with silver electrodes. In the inset of Fig. 11 $I(V)$ curve for IJ-SOZO-38.6 ink without ZnO nanoparticles is shown, which displays essentially different behaviour compared to other presented results. The curve profile for the ink without nanoparticles presents clear evidence that the main contribution to the DC conductivity of printed film originates from ZnO nanoparticles. From the comparison of presented curves in Fig. 11, one can easily conclude that only sensor printed with IJ-SOZO-38.6 ink can be used for sensing purposes.

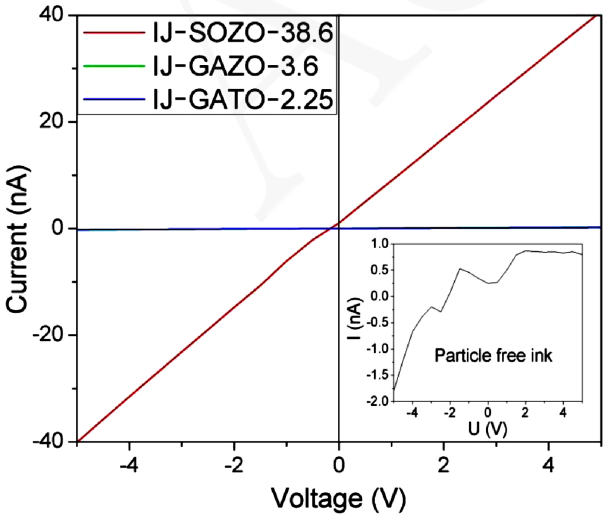

Figure 11. $I(V)$ curves for sensors printed with IJ-SOZO-38.6, IJ-GAZO-3.6 and IJ-GATO-2.25 inks (inset shows $I(V)$ curve for IJ-SOZO-38.6 ink without ZnO nanoparticles)

Transient response curves to different relative humidity levels, of the sensor printed with 10 layers of IJ-SOZO-38.6 ink are shown in Fig. 12. In the inset of Fig. 12 response/recovery curves are given for sensor response to different types of alcohol vapours with the same 50 ppm concentration. The performance of the printed sensor was tested at room temperature. Sensor response can be defined as [18]:

$$S = \frac{R_a}{R_g} \tag{1}$$

where R_a is sensor's resistivity in ambient gas and Rg is sensor's resistivity in the presence of target gas. From the dynamic response behaviour, presented in Fig. 12, it can be easily confirmed that for lower humidity levels sensor has relatively modest response, which is expected for ZnO nanoparticles [19]. For extremely high humidity conditions (RH = 90%) sensor response becomes drastic, most probably because of the several layers of physisorbed water on the surface of nanoparticles. For porous structures made of MO_x nanoparticles, in the low RH conditions where water molecules do not cover the reactive surface completely, dominant transport mechanism is based on the electronic conduction [20,21]. In the case of high relative humidity the physisorbed water covers the surface completely and the conduction mechanism is based on the proton transport between adjacent hydrogen sites. Such transport mechanism is independent of the properties of ZnO nanomaterial, so the sensor response becomes significantly higher as seen in Fig. 12.

Response/recovery time profiles of the same inkjet printed sensor to 50 ppm of methanol, propanol and ethanol vapours are shown in the inset of Fig. 12. Measurements are performed at RT and very low humid-

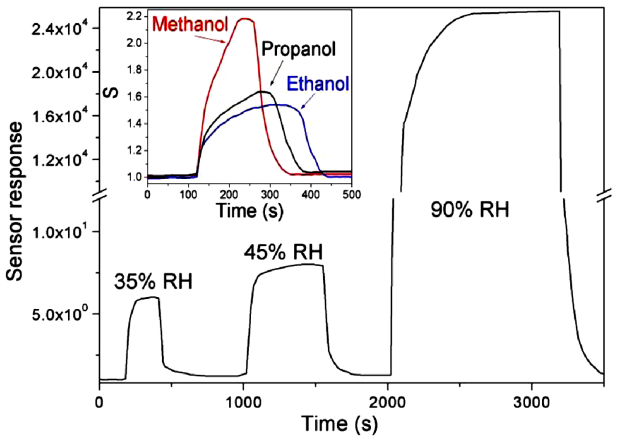

Figure 12. Transient response curves to different levels of relative humidity of the sensor printed with 10 layers of IJ-SOZO-38.6 ink (inset shows response/recovery time profiles of the sensor to 50 ppm ethanol, propanol and methanol vapour, measured at RT and 8% RH)

ity levels (8% *RH*) in order to determine true sensor response to alcohol vapours without interference of humidity. The target analyte concentration was set at 50 ppm, since it is typical concentration of alcohol vapour that can be detected during the food decay process [13], and tested with breath analyser [16]. Displayed responses reveal that printed SOZO sensor exhibits sensitivity to all tested alcohol vapours, and slight affinity to methanol gas. For methanol vapour sensor has the highest and the fastest response, whereas for propanol and ethanol vapour the response is lower with notably longer response and recovery times. By comparison of the gas sensitivity results we have concluded that designed sensors have good sensing characteristics, operating at room temperature, but the cross-sensitivity between the humidity and VOC vapours remains the big challenge for further optimization of this type of devices.

Inkjet printing of porous MO_x nanostructures can offer cutting-edge technology for photosensitive devices [9] and solar cells [7], due to their unique electronic structure and optical properties. Measurement of photocurrent for the sensor printed with 10 layers of IJ-SOZO-38.6 ink is given in Fig. 13. Light emitting diode (LED) operating at 365 nm with the power of 100 mW is used as excitation source. The wavelength of LED source is chosen to be in the visible spectral range and in the vicinity of the optical band gap of ZnO [22]. From the presented time-resolved response it can be seen that investigated sensor shows very high response to the incident light. By comparison with literature data for photocurrent values of ZnO based materials [23–25], one important fact can be established and that is very good photosensitivity with very high photocurrent values. These results offer great potential for application of the inkjet printed ZnO nanoparticles in solar cell devices where high photoconversion rates are required. It should be emphasized that rise and decay times (τ_r = 240 s; τ_d = 210 s) are longer than for previously published data [26], and these findings render sensor with ZnO nanoparticles not suitable for photosensitive devices, where fast response is required. Longer rise/decay times are probably the result of IDE configuration, and further optimization of the electrode design can lead to the improved photocurrent response.

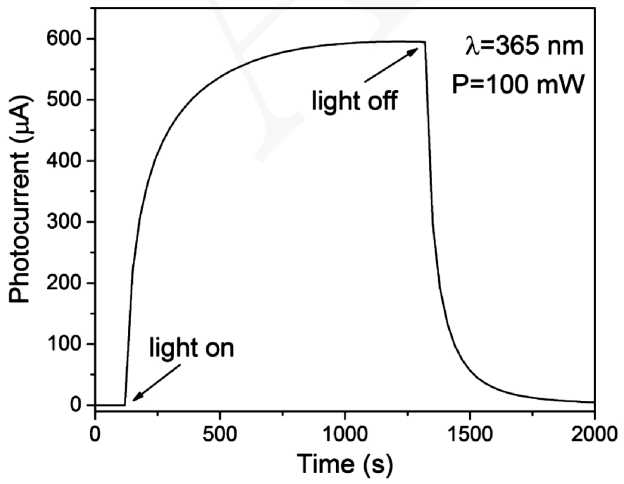

Figure 13. Photocurrent time resolved response of the sensor printed with 10 layers of IJ-SOZO-38.6 ink (excitation wavelength was 365 nm and LED power was set to 100 mW)

IV. Conclusions

A bottom-up approach to the inkjet fabrication of sensitive layers for sensing devices is demonstrated in this article. Main focus of the conducted research is optimization of functional dispersions for inkjet deposition of MO_x nanoparticles. PET substrate with Ag IDE was chosen as flexible transducer platform. On top of the electrodes multiple layers of prepared inks were printed in order to produce porous MO_x nanostructures for sensing applications. DC electrical transport characterization proved to be very useful for discrimination of the quality of the printed films since the IJ-GAZO-3.6 (gum arabic as dispersant and ZnO nanoparticles with ratio 1 : 3.6) and IJ-GATO-2.25 (gum arabic as dispersant and TiO_2 nanoparticles with ratio 1 : 2.25) inks showed much lower current values compared to the sensor printed with the IJ-SOZO-38.6 (*Solsperse*® 40000 as dispersant and ZnO nanoparticles with ratio 1 : 38.6) ink. Gas sensing measurements revealed that the sensor printed with the IJ-SOZO-38.6 ink had modest response to normal ambient humidity levels and very high response to extreme *RH* levels. The tested sensor had slight affinity to methanol vapour in comparison to propanol and ethanol at the 50 ppm concentration. The photocurrent measurements showed very good response to the excitation light with high photocurrent values, bringing strong impact on practical application of the inkjet printed flexible sensing devices.

Acknowledgement: This work was supported by the Serbian Ministry of Education, Science and Technological Development through projects III46010 and III44006.

References

1. B. Derby, "Inkjet printing ceramics: From drops to solid", *J. Eur. Ceram. Soc.*, **31** [14] (2011) 2543–2550.
2. J. Alamán, R. Alicante, J.I. Peña, C. Sánchez-Somolinos, "Inkjet printing of functional materials for optical and photonic applications", *Materials*, **9** [11] (2016) 910.
3. A. Friederich, J.R. Binder, W. Bauer, "Rheological control of the coffee stain effect for inkjet printing of ceramics", *J. Am. Ceram. Soc.*, **96** [7] (2013) 2093–2099.
4. B. Andò, S. Baglio, A.R. Bulsara, T. Emery, V. Marletta, A. Pistorio, "Low-cost inkjet printing technology for the rapid prototyping of transducers", *Sensors*, **17** [4] (2017) 748.
5. M. Rieu, M. Camara, G. Tournier, J.P. Viricelle, C. Pijolat, N.F. de Rooij, D. Briand, "Fully inkjet printed SnO_2 gas sensor on plastic substrate", *Sensors Actuators B*, **236** (2016) 1091–1097.

6. P. Calvert, "Inkjet printing for materials and devices", *Chem. Mater.*, **13** [10] (2001) 3299–3305.
7. Y. Oh, H.G. Yoon, S-N. Lee, H-K. Kim, J. Kim, "Inkjet-printing of TiO_2 co-solvent ink: From uniform ink-droplet to TiO_2 photoelectrode for dye-sensitized solar cells", *J. Electrochem. Soc.*, **159** [1] (2012) B34–B38.
8. A. Karpinski, S. Berson, H. Terrisse, M.M. Granvalet, S. Guillerez, L. Brohan, M. Richard-Plouet, "Anatase colloidal solutions suitable for inkjet printing: Enhancing lifetime of hybrid organic solar cells", *Solar Energy Mater. Solar Cells*, **116** (2013) 27–33.
9. B. Cook, Q. Liu, J. Butler, K. Smith, K. Shi, D. Ewing, M. Casper, A. Stramel, A. Elliot, J. Wu, "Heat-assisted inkjet printing of tungsten oxide for high-performance ultraviolet photodetectors", *ACS Appl. Mater. Interf.*, **10** [1] (2018) 873–879.
10. T. Järvinen, G.S. Lorite, A-R. Rautio, K.L. Juhász, Á. Kukovecz, Z. Kónya, K. Kordas, G. Toth, "Portable cyber-physical system for indoor and outdoor gas sensing", *Sensors Actuators B*, **252** (2017) 983–990.
11. A. Määttänen, U. Vanamo, P. Ihalainen, P. Pulkkinen, H. Tenhu, J. Bobacka, J. Peltonen, "A low-cost paper-based inkjet-printed platform for electrochemical analyses", *Sensors Actuators B*, **177** (2013) 153–162.
12. N. Komuro, S. Takaki, K. Suzuki, D. Citterio, "Inkjet printed (bio)chemical sensing devices", *Anal. Bioanal. Chem.*, **405** [17] (2013) 5785–5805.
13. D. Dong, C. Zhao, W. Zheng, W. Wang, X. Zhao, L. Jiao, "Analyzing strawberry spoilage via its volatile compounds using longpath Fourier transform infrared spectroscopy", *Sci. Reports*, **3** (2013) 2585.
14. D. Sebők, L. Janovák, D. Kovács, A. Sápi, D.G. Dobó, Á. Kukovecz, Z. Kónya, I. Dékány, "Room temperature ethanol sensor with sub-ppm detection limit: Improving the optical response by using mesoporous silica foam", *Sensors Actuators B*, **243** (2017) 1205–1213.
15. S. Yildirim, B. Röcker, M.K. Pettersen, J. Nilsen-Nygaard, Z. Ayhan, R. Rutkaite, T. Radusin, P. Suminska, B. Marcos, "Active packaging applications for food", *Compr. Rev. Food Sci. Food Safety*, **17** [1] (2018) 165–199.
16. M.A.G. Wallace, J.D. Pleil, "Evolution of clinical and environmental health applications of exhaled breath research: Review of methods and instrumentation for gas-phase, condensate, and aerosols", *Anal. Chim. Acta*, **1024** (2018) 18–38.
17. E. Bihar, Y. Deng, T. Miyake, M. Saadaoui, G.G. Malliaras, M. Rolandi, "A Disposable paper breathalyzer with an alcohol sensing organic electrochemical transistor", *Sci. Reports*, **6** (2016) 27582.
18. L.-J. Bie, X.-N. Yan, J. Yin, Y.-Q. Duan, Z.-H. Yuan, "Nanopillar ZnO gas sensor for hydrogen and ethanol", *Sensors Actuators B*, **126** [2] (2007) 604–608.
19. G. Niarchos, G. Dubourg, G. Afroudakis, M. Georgopoulos, V. Tsouti, E. Makarona, V. Crnojevic-Bengin, C. Tsamis, "Humidity sensing properties of paper substrates and their passivation with ZnO nanoparticles for sensor applications", *Sensors*, **17** [3] (2017) 516.
20. Z. Wang, L. Shi, F. Wu, S. Yuan, Y. Zhao, M. Zhang, "The sol-gel template synthesis of porous TiO_2 for a high performance humidity sensor", *Nanotechnology*, **22** [27] (2011) 275502.
21. J. Bai, B. Zhou, "Titanium dioxide nanomaterials for sensor applications", *Chem. Rev.*, **114** [19] (2014) 10131–10176.
22. E.A. Meulenkamp, "Synthesis and growth of ZnO nanoparticles", *J. Phys. Chem. B*, **102** [29] (1998) 5566–5572.
23. D. Lin, H. Wu, W. Zhang, H. Li, W. Pan, "Enhanced UV photoresponse from heterostructured Ag-ZnO nanowires", *Appl. Phys. Lett.*, **94** (2009) 172103.
24. M. Furuta, Y. Kamada, M. Kimura, S. Shimakawa, T. Kawaharamura, D. Wang, C. Li, S. Fujita, T. Hirao, "Photocurrent and persistent photoconductivity in zinc oxide thin-film transistors under ultraviolet-light irradiation", *Jpn. J. Appl. Phys.*, **50** (2011) 110204.
25. F. Zahedi, R.S. Dariani, S.M. Rozeti, "Structural, optical and electrical properties of ZnO thin films prepared by spray pyrolysis: Effect of precursor concentration", *Bull. Mater. Sci.*, **37** [3] (2014) 433–439.
26. V.K. Dwivedi, P. Srivastava, G. Vijaya Prakash, "Photoconductivity and surface chemical analysis of ZnO thin films deposited by solution-processing techniques for nano and microstructure fabrication", *J. Semicond.*, **34** [3] (2013) 033001.

sensors

MDPI

Article

Fabrication and Characterization of Flexible and Miniaturized Humidity Sensors Using Screen-Printed TiO_2 Nanoparticles as Sensitive Layer

Georges Dubourg [1,*], Apostolos Segkos [2], Jaroslav Katona [3], Marko Radović [1], Slavica Savić [1], Georgios Niarchos [1], Christos Tsamis [2] and Vesna Crnojević-Bengin [1]

1 Nano and Microelectronics Group, BioSense Institute, 21000 Novi Sad, Serbia; marrad@biosense.rs (M.R.); slavicas@biosense.rs (S.S.); niarchos@uns.ac.rs (G.N.); bengin@uns.ac.rs (V.C.-B.)

2 Institute of Nanoscience and Nanotechnology, NCSR "Demokritos", Patriarhou Gregoriou & Neapoleos, 15310 Aghia Paraskevi, Greece; a.segkos@inn.demokritos.gr (A.S.); c.tsamis@inn.demokritos.gr (C.T.)

3 Faculty of Technology, University of Novi Sad, 21000 Novi Sad, Serbia; jkatona@uns.ac.rs

* Correspondence: georgesdubourg@uns.ac.rs; Tel.: +381-214-852-137

Received: 30 June 2017; Accepted: 27 July 2017; Published: 11 August 2017

Abstract: This paper describes the fabrication and the characterization of an original example of a miniaturized resistive-type humidity sensor, printed on flexible substrate in a large-scale manner. The fabrication process involves laser ablation for the design of interdigitated electrodes on PET (Poly-Ethylene Terephthalate) substrate and a screen-printing process for the deposition of the sensitive material, which is based on TiO_2 nanoparticles. The laser ablation process was carefully optimized to obtain micro-scale and well-resolved electrodes on PET substrate. A functional paste based on cellulose was prepared in order to allow the precise screen-printing of the TiO_2 nanoparticles as sensing material on the top of the electrodes. The current against voltage (I–V) characteristic of the sensor showed good linearity and potential for low-power operation. The results of a humidity-sensing investigation and mechanical testing showed that the fabricated miniaturized sensors have excellent mechanical stability, sensing characteristics, good repeatability, and relatively fast response/recovery times operating at room temperature.

Keywords: humidity sensors; flexible substrate; TiO_2 nanoparticles; screen-printing; laser ablation

1. Introduction

Humidity sensors are employed today in a wide range of applications, including environmental monitoring, automotive, industrial process, healthcare, agriculture, and increasing indoor air quality in smart buildings. Several kinds of humidity sensors are available based on different transduction principles, such as resistive, capacitive, optical, and surface acoustic wave [1–4]. However, resistive-type sensors have the advantage to be cheaper and easier to read out over the other ones.

Typically, rigid substrates like ceramic, glass, or silicon are used as the fundamental building blocks of humidity sensors; but, recent advancements in the field of printed electronics show increased potential for the substitution of rigid substrates by flexible ones, since the latter potentially reduce the cost of sensors and offer good mechanical flexibility. Examples of flexible sensors integrating additional electronic functions like readout electronics [5,6], thermal compensation systems [7], and other sensors [8,9] have opened a new route towards multi-functional sensors fabricated on flexible substrate. Despite that, silicon technology is still attractive for the fabrication of sensors due to its mass-production capability, its high degree of miniaturization resulting in high integration density, and, consequently its considerable cost reduction for sensor devices [10,11]. Indeed, as given in the paper of Moore in 1965 [12]: "With unit cost falling as the number of components per circuit rises", the cost of one sensor must also decrease as more sensors are put on the substrate.

In addition, due to their very small size, silicon-based devices can be integrated with a flexible substrate. For example, a silicon strain sensor and multiplexed silicon non-volatile memory were transferred onto flexible substrate for wearable electronics [13,14]. Miniaturization is then an important issue in printed electronics, which needs to be assessed to consider it a valuable alternative to silicon technology.

In the case of resistive-type sensors, the size of a device depends mainly on the surface area covered by the electrodes. Low-cost printing technologies such as ink-jet or screen-printing are forecasted to dominate the printed electronics era, since they allow high-volume production [15,16]. However, for electrode designs, the line resolution/width achievable by printing technologies cannot reach micro-scale features generally higher than 100 µm, resulting in a large surface area. Thus, alternative technologies need to be considered to obtain miniaturized devices. Photolithography coming from expensive CMOS (Complementary Metal–Oxide–Semiconductor) technologies allows the design of micro-scale electrodes with high resolution in a large-scale manner, and this technology can be also employed for the mass production fabrication of sensors on flexible substrate [17–20]. Nevertheless, chemical and baking steps are required in photolithography, which limits it to chemically resistant substrates such as polyimide.

Laser technology is gaining interest as another alternative micropatterning technique due to its high precision and the possibility to use it in open air without clean room facilities. This process was used for the fabrication of ozone sensors, and was compared with photolithography in [21]. It was shown that this method can reach features of up to 60 µm. However, smaller features should be obtained to enhance its potential for sensor fabrication.

Furthermore, to take advantage of miniaturization, it is important to select an adequate sensing material. Among the various sensing materials, metal oxide nanomaterials possess good properties such as chemical and physical stability and high mechanical strength, and they have a high surface-to-volume ratio that makes them a perfect candidate for sensor applications. In recent years, TiO_2 has received wide attention and has found applications in many promising areas, such as photovoltaics, photocatalysis, and sensors [22–26]. Many examples of humidity sensors based on TiO_2 can be found in the literature [27–30]. The ability of the sensing material to be integrated in industrial production depends on the fabrication route used for its deposition and patterning. In the case of humidity sensors, the most standard methods to deposit TiO_2 are the spin-coating, dip coating, or microdroper processes [27–31], which are suitable for prototypes, but cannot be considered for large-scale process. In fabrication route selection, several factors must be considered, such as costs, throughput, and reproducibility, and the procedure ought to be compatible with the substrate, especially in terms of temperature. The screen-printing process meets all of the above, which has been demonstrated in [32,33], where the screen-printing of TiO_2 nanomaterials was used for dye-sensitized solar cells and electrodes.

In this context, the aim of this work was to introduce a cost-efficient and low-temperature procedure that allows the large scale fabrication of humidity sensors on flexible PET(Poly-Ethylene Terephthalate) substrate. The undertaken multidisciplinary approach combines expertise in materials science and chemistry, and fabrication processes and sensor characterization, aiming to present comprehensive bottom-up research in the field of flexible electronics and sensors. One of the main goals of the conducted research is not only to introduce an innovative technology process for the fabrication of sensor devices, but also to provide a proof-of-concept through extensive mechanical testing and a humidity response characterization of the fabricated miniaturized sensors.

2. Materials and Methods

2.1. Fabrication

The concept of the sensor is based on the resistive transduction principle, which consists in the deposition of a TiO_2-based sensitive layer on interdigitated electrodes (IDE) previously patterned on a

flexible substrate (Figure 1). PET substrate was chosen as a flexible building block for the sensor design, because this material is biodegradable, cost effective, and widely available. The underlying principle of the sensor's operation lies in fact that the absorption of water molecules by the sensitive film results in an increase of the film's electrical conductance. The conductance change as function of the humidity level can be easily quantified by measuring the resistance between the interdigitated electrodes.

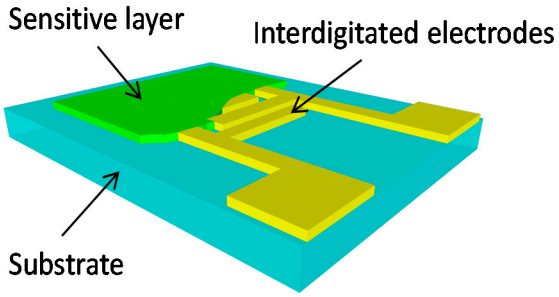

Figure 1. Schematic model of resistive-type chemical sensor.

Keeping the intended final application closely in mind, we aimed to develop a simple and economic technological process for the fabrication of humidity sensors, in order to be able to preserve their attractiveness as low-cost, potentially mass-produced devices. The fabrication process of the sensors proposed in this work is fast, compatible with roll-to-roll technologies, and does not require the high-cost of the semiconductor manufacturing equipment and high temperature steps normally used for silicon or ceramic fabrication.

The process sequence for the fabrication of the flexible humidity sensors is schematically illustrated in Figure 2. Initially, a gold layer was deposited by electron beam evaporation on a commercial PET substrate (Figure 2a). Afterwards, the resulting layer was directly patterned by laser ablation using a short pulse laser (Nd:YAG-1064 nm, Rofin) in order to create micro-scale interdigitated electrodes (Figure 2b). The next step is the patterning of the sensitive layer on top of the IDE in a low-cost manner. For this purpose, a TiO_2-based paste was prepared and then screen-printed (Figure 2c) in order to cover locally the surface of the electrodes (Figure 2d).

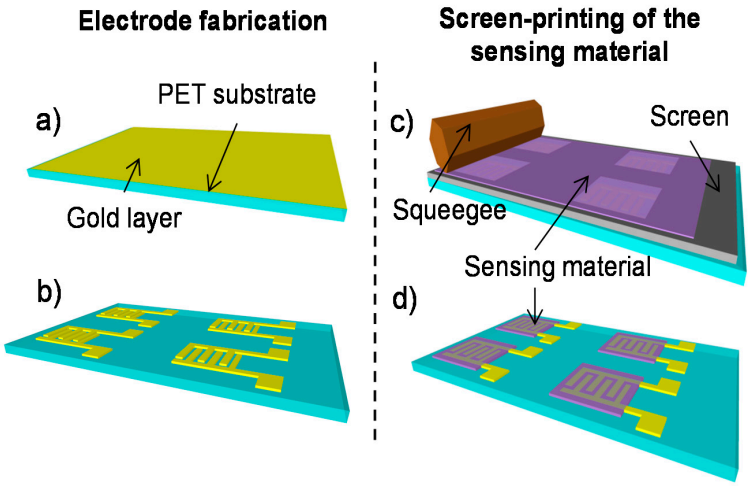

Figure 2. Process sequence of the humidity sensors: (**a**) Deposition of the gold layer on PET (Poly-Ethylene Terephthalate) substrate; (**b**) Laser ablation of the gold layer; (**c**) Screen-printing of the TiO_2 nanoparticles; (**d**) Sensors after screen-printing.

The following sections describe the process sequences in more detail.

2.1.1. Laser Ablation of the Interdigitated Electrodes

The deposited gold layer was patterned by laser ablation (Nd:YAG-1064 nm, Rofin, Plymouth, MI, USA) for the design of micro-scale interdigitated electrodes. This powerful technique used for the micromachining of microdevices consists of the creation of an effective heat zone by a focused laser beam, which induces a localized physical state transition allowing the ablation materials [34]. In order to obtain micro-scale and well-resolved electrodes, the laser ablation process was optimized as proposed in [35,36]. First, the pulse overlapping was adjusted by using the maximum available frequency of 65 kHz and a low raster speed of 80 mm/s in order to achieve a continuous ablation line without damaging the substrate by thermal accumulation. Next, to obtain the micro-scale features, the laser ablation process was optimized by modification of the current values. A current of 23 A was found to be an ideal value to succeed with the complete and selective ablation of the metal layer at the micro-scale. Using these parameters, the thin layer of gold was patterned without damaging the PET substrate.

2.1.2. Sensitive Layer: Preparation and Screen-Printing

A screen printing process, which is a cost-effective, time-saving, and mass-production fabrication process, was used for the deposition and patterning of the sensing material. This technique consists in using a squeegee for depositing a paste through a screen stencil, which allows for the direct patterning of functional pastes on a large variety of substrates [37,38].

In this work, a TiO_2 nanoparticles-based paste was used for the fabrication of the sensitive layer, and was developed specially for the screen-printing process. Water was chosen as the main solvent of the paste because it is readily available and environmentally friendly. First, a 2.5 wt % hydroxypropylmethyl cellulose (HPMC, Methocel® K15, Colorcon, Dartford, UK) was dissolved in water. Next, a 6.1/1 wt % propylene glycol/n-propanol mixture was prepared, where both the propylene glycol and n-propanol were of p.a. quality obtained from Kemika Zagreb, Croatia. Then, a 2.7 wt % solution of a dispersant (Solsperse 40000, Lubrizol, Wickliffe, OH, USA) in the propylene glycol/n-propanol mixture was prepared. The HPMC solution and the solspers solution were mixed at 1:1 wt ratio by means of an IKA RW20 overhead stirrer for 10 min at 1500 rpm. TiO_2 powder (anatase, Sigma Aldrich, St. Louis, MO, USA) was dispersed (IKA RW20, 1500 rpm for 20 min) in the mixture to obtain a 7.5 wt % dispersion of TiO_2. The screen-printing of the TiO_2 paste was performed using a semi-automatized screen-printer (EKRA 2H screen-printer, Dornstadt, Germany), which is a widespread industrially-applied piece of equipment. A screen was fabricated using a 30 µm thick photopolymer film (Koenen, Ottobrunn-Riemerling, Germany). The mesh used for the screen-printing of the TiO_2 paste onto the surface of the electrodes was characterized by a wire diameter of 30 µm. Finally, the samples were kept at room temperature for 2 days to attain complete dryness.

2.2. Measurements

The precision patterning of the devices and the morphology of the screen-printed TiO_2 film were examined by scanning electron microscope (HITACHI TM3030) and atomic force microscopy (AFM), whose images were taken with an NTEGRA prima microscope in semi-contact mode. The composition of the TiO_2 was investigated by Energy Dispersive X-Ray Analysis (Bruker XFlash), and the electrical characterization was performed using a Yokogawa–Hewlett-Packard semiconductor probe analyzer.

The humidity sensing properties of the fabricated sensors were investigated at room temperature (25 °C) by using an indigenously custom-designed humidity setup as described in [36]. The sensor to be analyzed was placed inside a sealed Teflon chamber, along with a reference sensor (Hanna instrument) that was used to monitor in real time the temperature and relative humidity (RH) inside the chamber. The water vapors were generated by driving gases (N_2 and O_2) inside a sealed bubbler containing water, and the resulting vapors were then carried to the experimental chamber where the sensors were tested. The humidity level inside the chamber was controlled by adjusting the

concentration of the driving gases with mass-flow controllers and flow meters (Brooks Instruments). The humidity sensing response was recorded through the change in resistance caused by varying the RH. A Keithley multimeter, driven by a custom-designed Labview-based interface, was used for monitoring in real time the resistance across the IDEs.

3. Results and Discussion

Using the process described above, the large-scale fabrication of humidity sensors has been successfully achieved. Figure 3a shows matrices of 3 × 3 sensors printed on PET substrate. Figure 3b depicts an SEM image of the ablated interdigitated electrodes on the PET substrate. This image indicates that the surfaces of the electrodes' structures subjected to pulse ablation are highly consistent and spatially well-resolved. An individual digit of an electrode is 700 µm long and 55 µm wide, and it is separated by a gap of 40 µm to the next digit. Here, small electrode geometry was obtained compared to the standard printed sensors, which are generally above 100 µm.

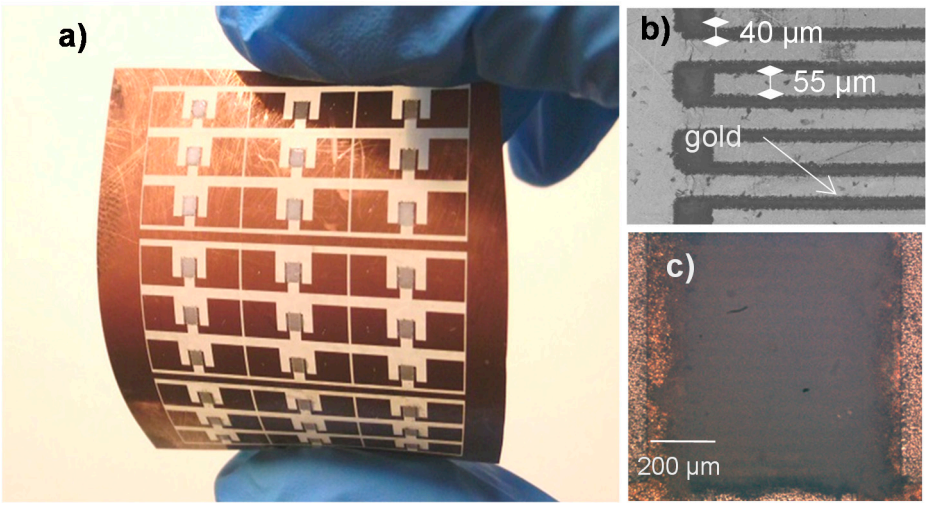

Figure 3. (**a**) Picture of 3 × 3 sensor matrices fabricated on PET substrate; (**b**) SEM image of the interdigitated electrodes; (**c**) Optical image of the humidity sensors.

Figure 3c shows an optical picture of the interdigitated electrodes covered by the screen-printed TiO_2 film. The resulting TiO_2 film is well aligned with the film, covering perfectly the surface of the electrodes. This perfect alignment of the screen-printed film is also confirmed at larger scale, as shown in Figure 3a. The screen-printed TiO_2 nanoparticle-based film, defining the active area of the humidity sensor, forms a rectangle of 1 mm width and 1.5 mm length (Figure 3b).

The thickness of the TiO_2 can be controlled by the number of printed layers. Indeed, Figure 4a,b represents a cross-section of the TiO_2 film after the printing of four layers and six layers, where the thicknesses were measured to be approximately 18 µm and 25 µm, respectively. The evolution of the thickness as function of the number of printed layers is summarized in Figure 4c.

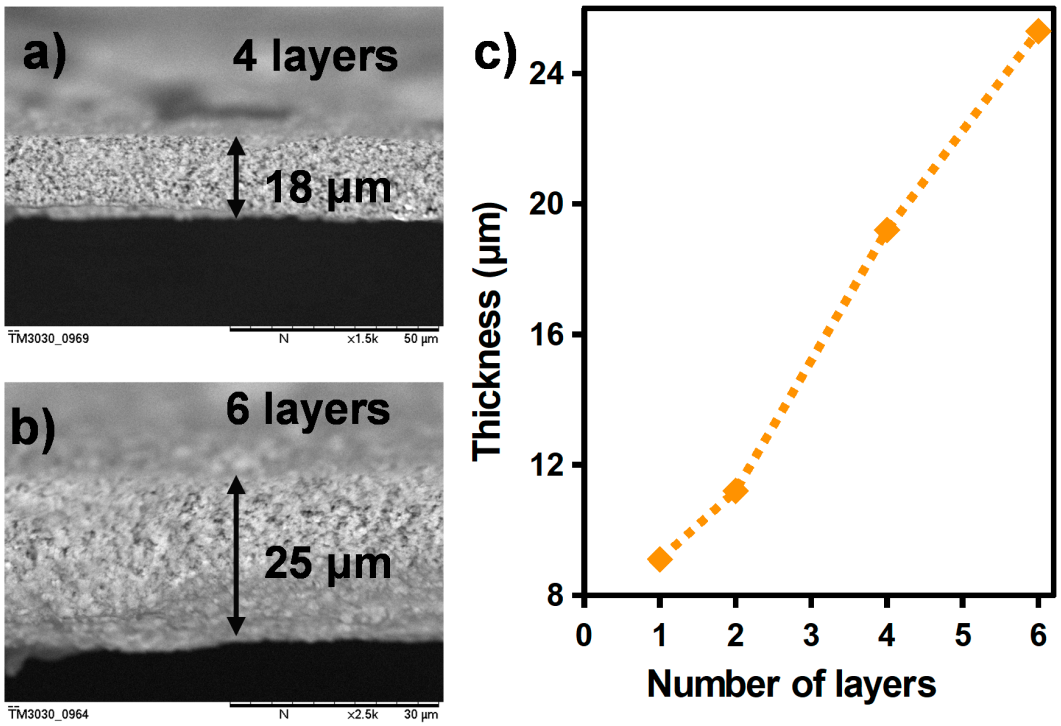

Figure 4. SEM image of a cross-section of the TiO_2 film (**a**) for four printed layers and (**b**) for six printed layers; (**c**) thickness of the final TiO_2 film as function of the number of printed layers.

The sensing properties are based on the change in the electrical conductance of the sensitive layer with the adsorbed water, which depends on the surface characteristics of the film. The surface morphology of the TiO_2 film was investigated using SEM and AFM techniques. Figure 5a shows the SEM image of a TiO_2 layer with high magnification, where the porous structure of the TiO_2 film can be observed, which is favorable for water vapor absorption due to the large surface area [39]. Figure 5b shows an AFM image of the TiO_2 film, where the spherical structure of the TiO_2 nanoparticles with a grain size of less than 100 nm, and the porosity of the film, can be clearly observed. Also, we can see in Figure 5d that the film formed by TiO_2 after screen-printing is quite uniform and homogeneous along the sensor. Next, an energy dispersive X-ray spectrometer (EDX) was employed to study the structural composition of the printed titanium dioxide film. Figure 5c shows the EDX spectrum of the selected area shown in Figure 5d, where the main peaks correspond to titanium and oxygen, indicating that the surface is well covered with TiO_2. The presence of carbon can be clearly observed, and it has been attributed to organic components of the functional paste. Note that, among them, an important component is the binder (hydroxypropylmethyl cellulose), since it assures a strong binding between TiO_2 nanoparticles and a good adhesion of the TiO_2 film with the substrate, improving the stability of the TiO_2 film.

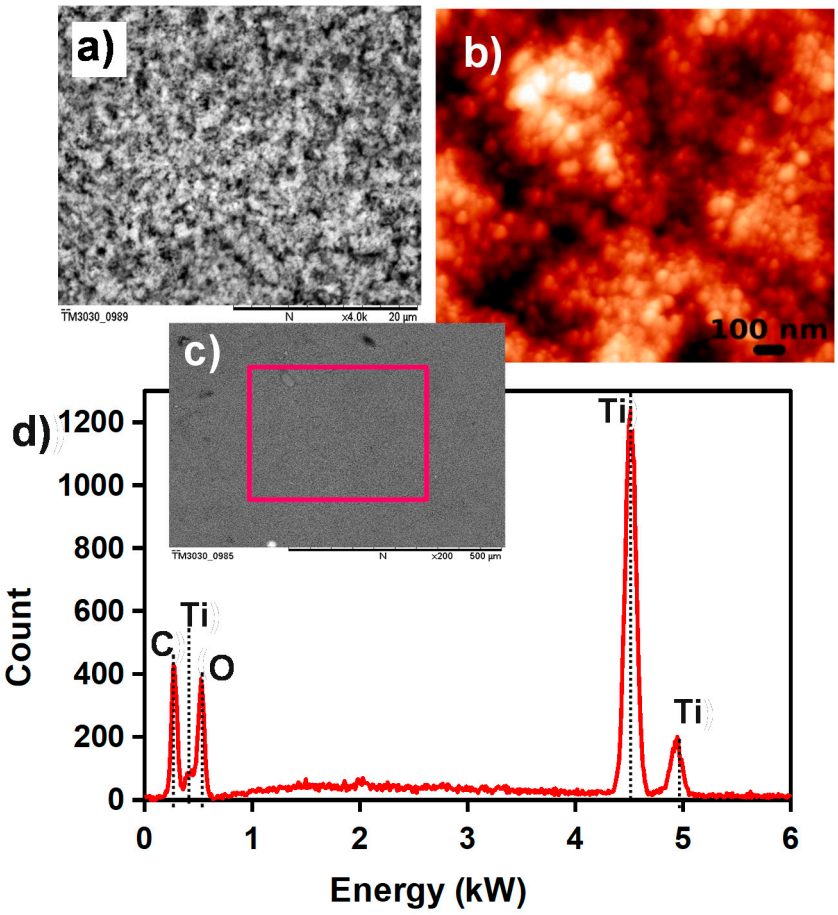

Figure 5. (**a**) SEM image of the screen-printed TiO_2 film; (**b**) AFM image of printed TiO_2 nanoparticles; (**c**) large area SEM image of the TiO_2 film; and (**d**) EDX spectrum of the selected area on TiO_2 film shown in (**c**).

TiO_2 film should possess good electrical performances to allow for precise and stable resistance measurements. Then, the electrical characteristics of the printed structures should be investigated as well. Current against voltage (I–V) measurements were obtained on sensors printed with one, two, four, and six layers by sweeping the applied voltage from −5 to 5 V. A typical current reading, as shown in Figure 6a, clearly demonstrates that the TiO_2 film provides a connecting Ohmic electrical contact between pairs of Au electrodes with constant resistance over the supply voltages. That means that a low voltage operation does not hinder the sensitivity, which is essential for low power operation. On the other hand, the conductance of the printed layer should be high enough to be measurable without a high-precision instrument. Figure 6a highlights the influence of the number of printed layers on the electrical performance of the film. For one printed layer, the variation in current is about 4 nA at 5 V bias, which reveals a poor conductance of the TiO_2 film. Generally, post-processing steps such as annealing are required to improve the conductivity of the material, leading to an increase in energy consumption and producing additional cost. In this work, in order to develop a low cost and low-temperature process adapted to flexible substrates, we have formulated a recipe for a functional paste that can be used for the printing of several TiO_2 layers, and that can preserve the original material physical and transport properties. Indeed, in Figure 6a, we can see that the sensor current increased as the number of successive printed layers is increased, due to the added TiO_2 nanopartices (NPs). This leads to a drop of resistance from about 1 GΩ to 266 MΩ (Figure 6b). With six printed layers, the resulting resistance (266 MΩ) is low enough to make the sensor compatible with a simple and low-powered electronic scheme, such as a Wheatstone bridge, for the signal read-out.

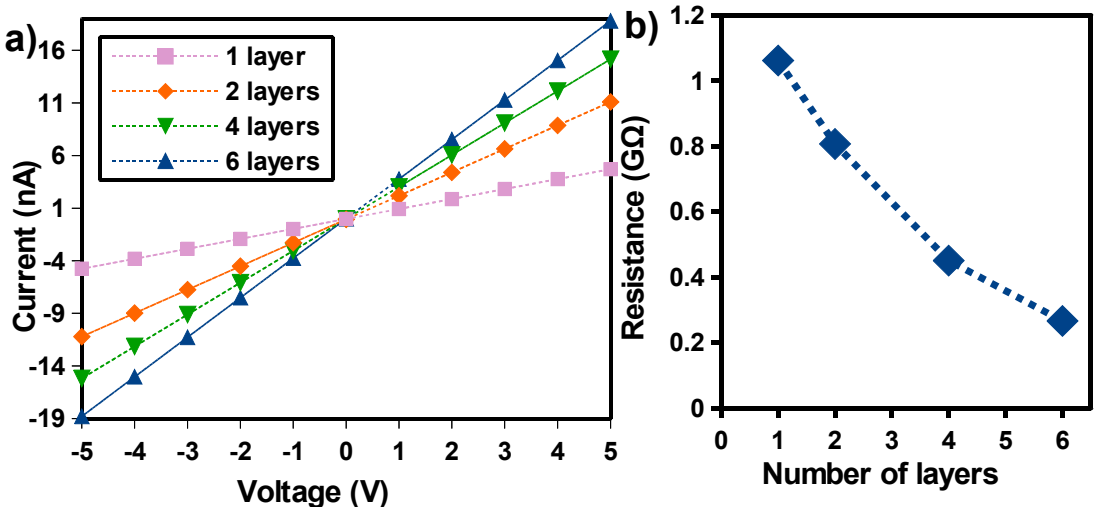

Figure 6. Current against voltage (I–V) characteristics of (**a**) the devices with different numbers of printed TiO_2 layers; (**b**) resistance of the TiO_2 as function of the number of printed layers.

Afterwards, humidity sensing performance was evaluated using the following equation to define the sensors' response:

$$S(\%) = \frac{R_{ini} - R_{mes}}{R_{ini}} \times 100$$

where R_{mes} are the resistances at a given humidity level, and R_{ini} is the resistance at zero humidity used as a baseline.

Reproducibility is one of the first requirements for a sensor's application. Typically, it is defined as a condition wherein the sensors exhibit multiple vapor adsorptions/desorption behaviors under cyclic operating conditions. In order to examine this, the humidity environments of the sensor were sequentially changed from 0 to 70% in periods of 30 min for several sorption and desorption processes. Figure 7 reveals that during the fourth response/recovery cycles, the sensor response shows a good sensing repeatability during cycling tests, which represents another advantage for its potential application. However, a drift of about 8% in the initial value of the response can be observed in Figure 7. This was attributed to residual moisture that had accumulated in the TiO_2 film after several sorption and desorption processes. Indeed, the highly porous structure of the TiO_2 film highlighted in Figure 5a,b can easily trap moisture, producing the observed drift in the measurements.

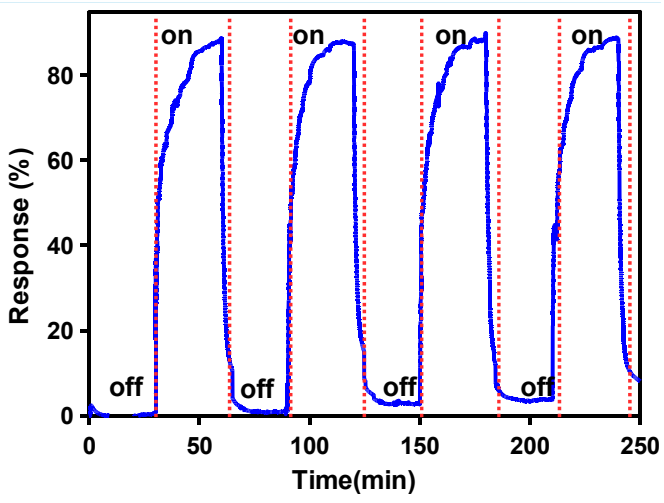

Figure 7. Sensor response under dynamic cycles between 0% and 72% relative humidity (RH), at 25 °C.

Next, in order to study further the characteristics of our humidity sensors, it is important to investigate the sensors' response at different humidity levels.

Figure 8a shows the sensors' response for several dynamic cycles of absorption/desorption at humidity levels varying from 0 to 70%. It is important to mention that low relative humidity levels were detected with designed miniaturized sensors, introducing a significant improvement in comparison to the other flexible humidity sensors found in the literature [40–43]. This can be attributed to the highly porous surface of the printed TiO_2 film, which results in a large surface area providing more surface active sites and paths for water molecule adsorption and diffusion [39].

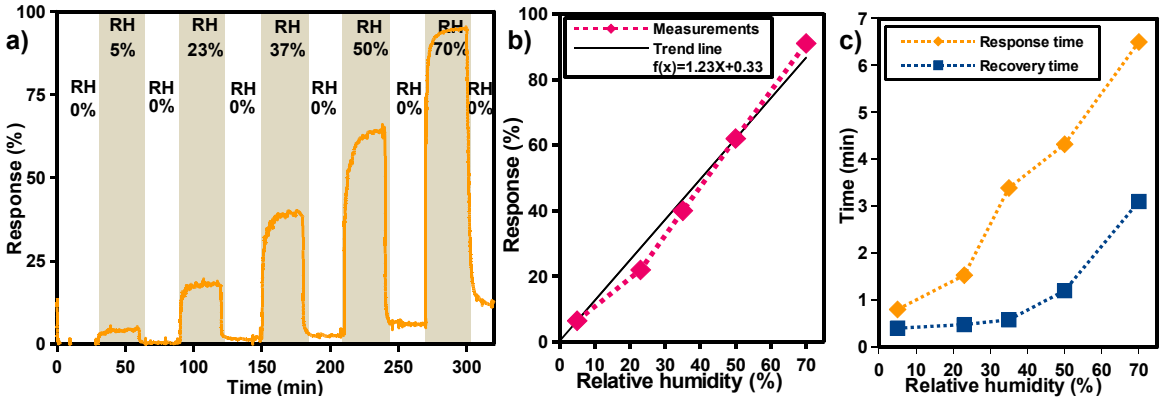

Figure 8. (**a**) response curve of the sensor to gradually increased humidity levels, ranging from 0 up to 72%; (**b**) sensor response as function of the relative humidity; (**c**) response and recovery time of the sensor as function of the relative humidity.

Figure 8b presents the sensors' response as a function of humidity level, where it can be observed that sensor response is linearly proportional to the relative humidity level, implying a more precise measurement at a low humidity level and simple calibration, which are important parameters for potential sensor application.

The response and recovery times are also very important factors to determine the performance of humidity sensors, and they also need to be evaluated. The response time is the time taken by a sensor to achieve 90% of the maximum response, and the recovery time is the time needed for the senor to drop to 10% of its initial response. Both parameters were calculated from a long cycle time (30 min), which was used to ensure that the device response reached its saturated limit without any noticeable drift.

Figure 8c shows the response and recovery time as function of the relative humidity level including the equilibration time of water vapor inside the test chamber. In this Figure, it can be seen that the response and the recovery times are fast in a range from 5 to 40 % RH, varying between 40 s and 3 min for the response times, and about 50 s concerning the recovery times. However, the response and recovery times become much slower at higher RH levels (>50% RH). This could be attributed to the humidity sensing mechanism. In fact, at low RH, the decrease of resistance is mainly due to the chemisorbtion of water molecules by the active sites available on the TiO_2 surface. In that case, the dominant charge transport mechanism is electronic transport, which is much faster than proton conduction. On the other hand, the subsequent layer of the water molecule is generally physisorbed by double hydrogen bonding with the hydroxyl groups formed on the previous water layer [30,39]. Afterwards, successive physisorbed water layers are accumulated on the surface of the TiO_2 film as the humidity level increases. In that case, the proton conduction mechanism becomes dominant, which could explain the slower response times for high humidity levels.

Mechanical stability is essential to flexible electronic devices, especially for applications where high stability over the mechanical deformation is required, such as wearable electronic and smart food packaging. Therefore, the influence of the mechanical strain on the electrical behavior of the devices

has to be explored. To do so, bending experiments were performed by attaching the flexible sensors to a cylinder (Figure 9a) and the curvature angle was calculated to be approximately 100°, as depicted in Figure 9b.

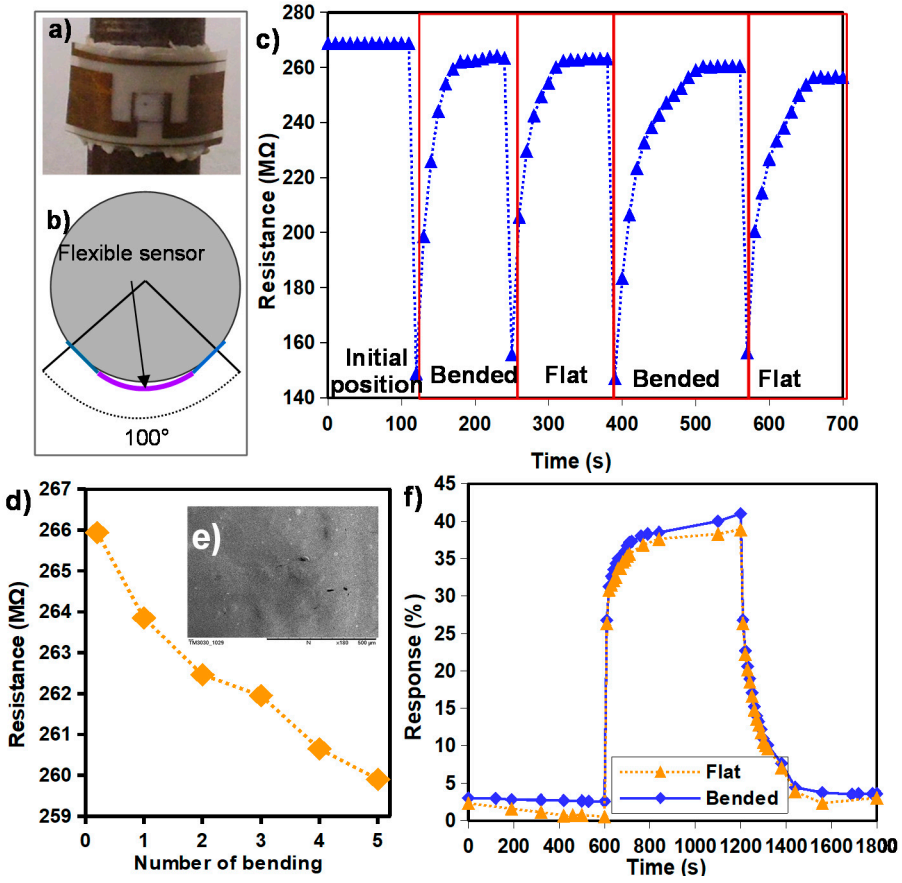

Figure 9. (**a**) picture of the sensor placed on cylinder; (**b**) schematic of the bended sensor; (**c**) resistance under dynamic bending cycles; (**d**) resistance value as function of the bending cycles; (**e**) SEM picture of the TiO_2 after bending cycles; (**f**) response curves of the sensor to 35% RH when tested in a flat and a bended position.

Figure 9c shows the resistance change during several bending and return to flat position cycles in periods of 5 min. It can be seen that the resistance decreased during the bending experiments, but it retrieved its initial value quickly after the mechanical excitation, i.e., after a relaxation time of about 1 min.

Figure 9c exhibits the resistance as a function of the number of bending cycles. The device showed only a slight decrease in resistance (2.3% of the initial value) after five cycles. Moreover, a scanning electron microscopy (SEM) analysis revealed no morphology change of the film caused by mechanical bending (Figure 9d).

To validate the stable sensing operation under mechanical deformation, humidity measurements were performed when the sensor was in a flat position and bended at 100°.

At each indicated position, the sensor was exposed to RH varying from 0 to 35% RH in periods of 10 min. Note that the measurements in a bended position were performed 2 min after bending the sensor in order to leave it enough time to recover its initial resistance value. Figure 9e shows that the response of the sensor when it was bended increased by less than 3% from that measured when it was in a flat position. It can be concluded that the sensors' response showed negligible effect over the mechanical strain.

The obtained results indicate that the TiO_2 paste formulation offers high mechanical stability for a TiO_2-sensitive layer when it is printed on a plastic substrate, which consequently allows the devices to be used for flexible sensor applications.

4. Conclusions

An original and innovative process for the large-scale production of flexible and miniaturized humidity sensors with TiO_2 nanoparticles as sensing material was proposed. This method results from the association of two different approaches: laser ablation and screen-printing. The first approach is coherent for the patterning of micro-scale interdigitated electrodes. The second one is particularly adapted for the industrial integration of metal-oxide-based sensitive film on flexible substrate. Both approaches are fast, cost-effective, and do not require annealing and chemical treatment, which makes them compatible with any kind of flexible substrates. The electrical measurements of the investigated sensors revealed Ohmic behavior, and the electrical properties of the devices were improved by printing successive layers. Mechanical testing showed very good stability of the electrical properties and humidity response of the investigated sensors. The humidity sensing properties were evaluated by the measurement of resistance change with variation in the humidity. The linear response of the fabricated sensitive layer, in range from 5 to 70% relative humidity, reveals great potential for environmental monitoring and humidity sensing applications. In addition, the sensors showed good repeatability and a relatively fast response time. Therefore, the possibility to fabricate miniaturized sensors in a large-scale manner, with preserved good sensing properties, paves the way to low-cost solutions for sensor technologies printed on flexible substrates.

Acknowledgments: This work was funded through FP7-REGPOT INNOSENSE GA No. 316191 (Reinforcement of BioSense Center—ICT for Sustainability and Eco-Innovation).

Author Contributions: G.D. conceived the idea and designed the experiments; A.S. and G.N. performed the experiments; J.K., M.R. and S.S. contributed in material preparation (TiO_2 paste); A.S., G.N., G.D. and M.R. analyzed the data; V.C.-B. and C.T. coordinated the research; G.D. wrote the paper.

References

1. Zhang, Y.; Yu, K.; Jiang, D.; Zhu, Z.; Geng, H.; Luo, L. Zinc Oxide Nanorod and Nanowire for Humidity Sensor. *Appl. Surf. Sci.* **2005**, *242*, 212–217. [CrossRef]
2. Arregui, F.J.; Liu, Y.; Matias, I.R.; Claus, R.O. Optical Fiber Humidity Sensor Using a Nano Fabry-Perot Cavity Formed by the Ionic Self-Assembly Method. *Sens. Actuator B Chem.* **1999**, *59*, 54–59. [CrossRef]
3. Southworth, D.R.; Bellan, L.M.; Linzon, Y.; Craighead, H.G.; Parpia, J.M. Stress-based vapor sensing using resonant microbridges. *Appl. Phys. Lett.* **2010**, *96*, 163503. [CrossRef]
4. Penza, M.; Anisimkin, V.I. Surface acoustic wave humidity sensor using polyvinyl-alcohol film. *Sens. Actuator A Phys.* **1999**, *76*, 162–166. [CrossRef]
5. Someya, T.; Sekitani, T.; Iba, S.; Kato, Y.; Kawaguchi, H.; Sakurai, T. A large-area, flexible pressure sensor matrix with organic field-effect transistors for artificial skin applications. *Proc. Natl. Acad. Sci. USA* **2004**, *101*, 9966–9970. [CrossRef] [PubMed]
6. Thuau, D.; Abbas, M.; Wantz, G.; Hirsch, L.; Dufour, I.; Ayelab, C. Piezoelectric polymer gated OFET: Cutting-edge electro-mechanical transducer for organic MEMS-based sensors. *Sci. Rep.* **2016**, *6*, 38672. [CrossRef] [PubMed]
7. Molina-Lopez, F.; Quintero, A.V.; Mattana, G.; Briand, D.; de Rooij, N. Large-area compatible fabrication and encapsulation of inkjet-printed humidity sensors on flexible foils with integrated thermal compensation. *J. Micromech. Microeng.* **2013**, *23*, 025012. [CrossRef]
8. Quddious, A.; Yang, S.; Khan, M.M.; Tahir, F.A.; Shamim, A.; Salama, K.N.; Cheema, H.M. Disposable, Paper-Based, Inkjet-Printed Humidity and H2S Gas Sensor for Passive Sensing Applications. *Sensors* **2016**, *16*, 2073. [CrossRef] [PubMed]
9. Oprea, A.; Courbat, J.; Bârsan, N.; Briand, D.; de Rooij, N.F.; Weimar, U. Temperature, humidity and gas sensors integrated on plastic foil for low power applications. *Sens. Actuators B Chem.* **2009**, *140*, 227–232. [CrossRef]

10. Deng, F.; He, Y.; Zhang, C.; Feng, W. A CMOS Humidity Sensor for Passive RFID Sensing Applications. *Sensors* **2014**, *14*, 8728–8739. [CrossRef] [PubMed]
11. Presmanes, L.; Thimont, Y.; Chapelle, A.; Blanc, F.; Talhi, C.; Bonningue, C.; Barnabé, A.; Menini, P.H.; Tailhades, P.H. Highly Sensitive Sputtered ZnO:Ga Thin Films Integrated by a Simple Stencil Mask Process on Microsensor Platforms for Sub-ppm Acetaldehyde Detection. *Sensors* **2017**, *17*, 1055. [CrossRef] [PubMed]
12. Moore, G.E. Cramming more components onto integrated circuits. *Proc. IEEE* **1998**, *86*, 82–85. [CrossRef]
13. Zhao, P.; Deng, N.; Li, X.W.; Ren, C.C.; Wang, Z.Y. Development of highly-sensitive and ultra-thin silicon stress sensorchips for wearable biomedical applications. *Sens. Actuators A Phys.* **2014**, *216*, 158–166. [CrossRef]
14. Kim, J.; Son, D.; Lee, M.; Song, C.; Song, J.K.; Koo, J.H.; Lee, D.J.; Shim, H.J.; Kim, J.H.; Lee, M.; et al. A wearable multiplexed silicon nonvolatile memory array using nanocrystal charge confinement. *Sci. Adv.* **2016**, *2*, e1501101. [CrossRef] [PubMed]
15. Wang, X.; Larsson, O.; Platt, D.; Nordlinder, S.; Engquist, I.; Berggren, M.; Crispin, X. An all-printed wireless humidity sensor label. *Sens. Actuators B Chem.* **2012**, *166–167*, 556–561. [CrossRef]
16. Salmerón, J.F.; Molina-Lopez, F.; Briand, D.; Ruan, J.J.; Rivadeneyra, A.; Carvajal, M.A.; Capitán-Vallvey, L.; de Rooij, N.F.; Palma, A.J. Properties and Printability of Inkjet and Screen-Printed Silver Patterns for RFID Antennas. *J. Electron. Mater.* **2014**, *43*, 604–617. [CrossRef]
17. Lee, C.Y.; Wu, G.W.; Hsieh, W.J. Fabrication of micro sensors on a flexible substrate. *Sens. Actuators A Phys.* **2008**, *147*, 173–176. [CrossRef]
18. Wang, L.; Luo, J.; Yin, J.; Zhang, H.; Wu, J.; Shi, X.; Crew, E.; Xu, Z.; Rendeng, Q.; Lu, S.; et al. Flexible chemiresistor sensors: Thin film assemblies of nanoparticles on a polyethylene terephthalate substrate. *J. Mater. Chem.* **2010**, *20*, 907–915. [CrossRef]
19. Zampetti, E.; Maiolo, L.; Pecora, A.; Maita, F.; Pantalei, S.; Minotti, A.; Valletta, A.; Cuscunà, M.; Macagnano, A.; Fortunato, G.; et al. Flexible sensorial system based on capacitive chemical sensors integrated with readout circuits fully fabricated on ultra-thin substrate. *Sens. Actuators B Chem.* **2011**, *155*, 768–774. [CrossRef]
20. Zampetti, E.; Pantalei, S.; Pecora, A.; Valletta, A.; Maiolo, L.; Minotti, A.; Macagnano, A.; Fortunato, G.; Bearzotti, A. Design and optimization of an ultra thin flexible capacitive humidity sensor. *Sens. Actuators B Chem.* **2009**, *143*, 302–307. [CrossRef]
21. Acuautla, M.; Bernardini, S.; Gallais, L.; Florido, T.; Patout, L.; Bendahan, M. Ozone flexible sensors fabricated by photolithography and laser ablation processes based on ZnO nanoparticles. *Sens. Actuators B Chem.* **2014**, *203*, 602–611. [CrossRef]
22. Fujishima, A.; Honda, K. Electrochemical Photolysis of Water at a Semiconductor Electrode. *Nature* **1972**, *238*, 37–38. [CrossRef] [PubMed]
23. Grätzel, M. Photoelectrochemical cells. *Nature* **2001**, *414*, 338–344. [CrossRef] [PubMed]
24. Konstantinou, I.K.; Albanis, T.A. TiO_2-assisted photocatalytic degradation of azo dyes in aqueous solution: Kinetic and mechanistic investigations: A review. *Appl. Catal. B Environ.* **2004**, *49*, 1–41. [CrossRef]
25. Ni, M.; Leung, M.K.H.; Leung, D.Y.C.; Sumathy, K. A review and recent developments in photocatalytic water-splitting using TiO_2 for hydrogen production. *Renew. Sustain. Energy Rev.* **2007**, *11*, 401–425. [CrossRef]
26. Millis, A.; Hunte, S.L. An overview of semiconductor photocatalysis. *J. Photochem. Photobiol. A Chem.* **1997**, *108*, 1–35. [CrossRef]
27. Dennis, J.O.; Ahmed, A.Y.; Khir, M.H. Fabrication and characterization of a CMOS-MEMS humidity sensor. *Sensor* **2015**, *15*, 16674–16687. [CrossRef] [PubMed]
28. Ghadiry, M.; Gholami, M.; Kong, L.C.; Yi, C.W.; Ahmad, H.; Alias, Y. Nano-Anatase TiO_2 for High Performance Optical Humidity Sensing on Chip. *Sensors* **2016**, *16*, 39. [CrossRef] [PubMed]
29. Montesperelli, G.; Pumo, A.; Traversa, E.; Bearzotti, A.; Montenero, A.; Gnappi, G. Sol-Gel Processed TiO_2-Based Thin Films as Innovative Humidity Sensors. *Sens. Actuators B Chem.* **1995**, *25*, 705–709. [CrossRef]
30. Wang, Z.; Shi, L.; Wu, F.; Yuan, S.; Zhao, Y.; Zhang, M. The sol-gel template synthesis of porous TiO_2 for a high performance humidity sensor. *Nanotechnology* **2011**, *22*, 275502. [CrossRef] [PubMed]
31. Hu, Y.C.; Dai, C.L.; Hsu, C.C. Titanium Dioxide Nanoparticle Humidity Microsensors Integrated with Circuitry on-a-Chip. *Sensors* **2014**, *14*, 4177–4188. [CrossRef] [PubMed]
32. Zhang, G.; Wu, Y.; Fu, P.; Wang, G.; Pan, S.; Chen, C. Nanocrystalline TiO_2 Electrodes Prepared by Water-Medium Screen Printing Technique. *Chem. Lett.* **2001**, *30*, 1042–1043.

33. Ito, S.; Chen, P.; Comte, P.; Nazeeruddin, M.K.; Liska, P.; Pechy, P.; Gratzel, M. Fabrication of Screen-Printing Pastes from TiO_2 Powders for Dye-Sensitised Solar Cells. *Prog. Photovolt.* **2007**, *15*, 603–612. [CrossRef]
34. Meijer, J.; Du, K.; Gillner, A.; Hoffmann, D.; Kovalenko, V.S.; Masuzawa, T.; Ostendorf, A.; Poprawe, R.; Schulz, W. Laser machining by short and ultrashort pulses, state of the art and new opportunities in the age of the photons. *CIRP Ann. Manuf. Technol.* **2002**, *51*, 531–550. [CrossRef]
35. Dubourg, G.; Zlebic, C.; Matovic, J.; Bengin, V.C. One-step patterning of a flexible piezoresistive MEMS sensor by 3D direct laser writing. In Proceedings of the 2015 IEEE 10th International Conference on Nano/Micro Engineered and Molecular Systems (NEMS), Xi'an, China, 7–11 April 2015; pp. 553–556.
36. Niarchos, G.; Dubourg, G.; Afroudakis, G.; Georgopoulos, M.; Tsouti, V.; Makarona, E.; Crnojevic-Bengin, V.; Tsamis, C. Humidity sensing properties of paper substrates and their passivation with ZnO nanoparticles for sensor applications. *Sensors* **2017**, *17*, 516. [CrossRef] [PubMed]
37. Cao, X.; Chen, H.; Gu, X.; Liu, B.; Wang, W.; Cao, Y.; Wu, F.; Zhou, C. Screen Printing as a Scalable and Low-Cost Approach for Rigid and Flexible Thin-Film Transistors Using Separated Carbon Nanotubes. *ACS Nano* **2014**, *8*, 12769–12776. [CrossRef] [PubMed]
38. Li, M.; Li, Y.-T.; Li, D.-W.; Long, Y.-T. Recent developments and applications of screen-printed electrodes in environmental assays—A review. *Anal. Chim. Acta* **2012**, *734*, 31–44. [CrossRef] [PubMed]
39. Bai, J.; Zhou, B. Titanium dioxide nanomaterials for sensor applications. *Chem. Rev.* **2014**, *114*, 10131–10176. [CrossRef] [PubMed]
40. Yang, T.; Yu, Y.Z.; Zhu, L.S.; Wu, X.; Wang, X.H.; Zhang, J. Fabrication of silver interdigitated electrodes on polyimide films via surface modification and ion-exchange technique and its flexible humidity sensor application. *Sens. Actuators B Chem.* **2015**, *208*, 327–333. [CrossRef]
41. Xuan, W.; He, X.; Chen, J.; Wang, W.; Wang, X.; Xu, Y.; Xu, Z.; Fu, Y.Q.; Luo, J. High sensitivity flexible lamb-wave humidity sensors with a graphene oxide sensing layer. *Nanoscale* **2015**, *7*, 7430–7436. [CrossRef] [PubMed]
42. Nakajima, T.; Nakamura, T.; Tsuchiya, T. Flexible humidity sensors composed of graphite-like carbon micro-pinecone arrays. *RSC Adv.* **2016**, *6*, 95342–95348. [CrossRef]
43. Li, W.; Xu, F.; Sun, L.; Liu, W.; Qiu, Y. A novel flexible humidity switch material based on multi-walled carbon nanotube/polyvinyl alcohol composite yarn. *Sens. Actuators B* **2016**, *230*, 528–535. [CrossRef]

IOP Conf. Series: Journal of Physics: Conf. Series **939** (2017) 012008 IOP Publishing doi:10.1088/1742-6596/939/1/012008

Flexible and highly sensitive humidity sensors using screen-printed TiO2 nanoparticles as sensitive layer

G Dubourg[1], J Katona[2], M Rodović[1], S Savić[1], G Kitic[1], G Niarchos[1] N Jancović and V Crnojević-Bengin

[1] Biosense Institute, University of Novi Sad, Novi Sad, Serbia
[2] Faculty of Technology, University of Novi Sad, Novi Sad, Serbia

Abstract. In this work, we present an original example of flexible and miniaturized humidity sensor using screen-printed TiO_2 nanoparticles as sensitive layer. The proposed sensors operate under room-temperature conditions and exhibit high sensitivity to changes in relative humidity. The humidity sensor consists of a TiO_2-based sensitive nanomaterial printed on the top of interdigitated electrodes (IDEs) patterned by laser ablation on flexible substrate. A TiO_2 screen-printing paste from commercially-available nanopowders was developed in order to allow large-scale fabrication of humidity sensors at low temperature. The I-V characteristic of the sensor shows good linearity and resistance measurements confirm the water vapour's absorption on the sensitive layer, showing high sensitivity in the range of 24 to 90% relative humidity, while exhibiting relatively fast response and recovery times, without the need of any refreshing method.

1. Introduction

Humidity sensors find applications from semiconductor manufacturing to soil moisture monitoring or in food industry and are generally fabricated on ceramic and silicon substrates. Nevertheless, recent advancements in the field of printed electronics show increased potential in substitution of rigid substrates by flexible substrates, due to their low cost and easy fabrication processing.

In parallel, semiconducting metal oxide nanostructures such as TiO_2 nanoparticles, SnO_2 nanowires, or ZnO nanorods have been reported to be good candidates for highly sensitive and stable humidity sensors due to their high surface-to-volume ratio [1][2][3]. Nevertheless, their integration in printed sensors fabricated on flexible substrates is still non trivial, since plastic substrates deform or melt at temperatures of only 100–200 °C [4], which makes them incompatible with the standard silicon and ceramic technologies. Lots of studies have focused on the fabrication of flexible electronic devices using metal oxide materials with good electrical and optical properties [5]. However, their integration as highly-sensitive materials into flexible chemical sensors is still lacking, since they are generally deposited by drop-casting or spin-coating methods [6] which cannot be consider for the mass-production of sensors. One of the main challenges is then the development of cost-effective and low temperature fabrication process allowing the large-scale production of flexible sensors with high performances.

In this work, we demonstrate the feasibility of screen-printed TiO_2 sensing material at low-temperature for the large-scale fabrication of humidity sensors on flexible substrate. The humidity sensors proposed and realized in this work show a high sensitivity in the range of 24 to 90% relative humidity and fast response and recovery times.

2. Materials and methods

A resistive transducer was chosen for the conception of the humidity sensor because it has a simple structure, a low fabrication cost, and it does not require complex read-out circuitry. Typically, it consists of a TiO_2-based sensitive nanomaterial deposited on top of gold interdigitated electrodes (IDEs) patterned on a flexible substrate.

As a principle, the absorption of water vapour by the sensitive film creates an increase of film electrical conductance due to the dissociation of water molecules to ionic functional hydroxyl groups resulting to a resistance change between interdigitated electrodes which can be easily measured.

2.1. Materials

TiO2 nanoparticles-based paste was used as sensitive layer and was developed for the screen-printing process. Water was chosen as the main solvent of the paste because it is cheap, environmental friendly and it can be evaporated at low temperature.

First, HPMC (hydroxypropylmethyl cellulose) was dissolved in water to increase its viscosity. Next, the resulting water/HPMC solution was mixed with a mixture of propylene glycol/propanol. In parallel, dispersant (Solspers 40000) was dissolved in a mixed solvent of water/propylene glycol/propanol, and TiO_2 powder (anatase, sigma Aldrich) was added to the solution. Afterwards, the dispersion was performed by ultrasonication for 20 min. The suspended TiO_2 nanoparticles suspension wereas added to the solution of HPMC in a ratio of 1:1 under vigorous stirring at RW20 in 2000 rpm during 20min, to give a final formulation.

2.2. Fabrication process

Keeping the intended final application closely in mind, we aimed to for the development of a simple and economic process for the fabrication of humidity sensors, in order to be able to preserve their attractiveness as low-cost, potentially mass-produced devices. The fabrication process of the sensors proposed in this work is fast, compatible with rolls-to-rolls technologies and does not require the high-cost semiconductor manufacturing equipment and high temperature steps normally used for silicon or ceramic microfabrication. It combines a laser ablation technique for the fabrication of the micro-scale electrodes and a screen-printing process for the patterning of the TiO_2 nanoparticles-based sensing material. The process sequence is illustrated in Figure 1.

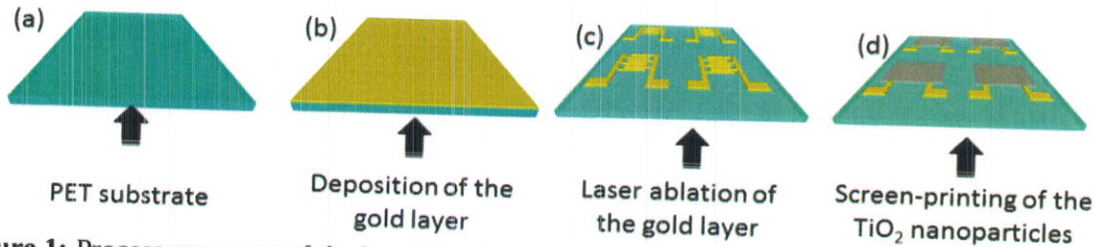

Figure 1: Process sequence of the humidity sensors: (a) Cleaning of the PET substrate. (b) Deposition of the gold layer by electron beam evaporation. (c) Laser ablation of the gold layer. (d) Screen-printing of the TiO_2 nanoparticles.

Initially, a commercial PET flexible substrate of 50 µm thick was cleaned with iso-propanol and dried at 80°C for 15 min. Next, a gold layer was deposited on the substrate by electron-beam evaporation. Afterwards, the resulting layer was directly patterned by laser ablation (Nd:YAG-1064 nm, Rofin) in order to create micro-scale interdigitated electrodes using a process inspired from [7]. The TiO_2 nanoparticles-based paste was then patterned on the surface of electrodes by screen-printing (EKRA 2H screen printer) which is a widespread industrially-applied method. A screen made of photosensitive film of 50 µm thick and a mesh of 40 µm thick were used to successfully achieve the deposition of the sensing material. Finally, the resulting devices were dried at 80°C for 30 min in an oven to accelerate the solvent evaporation. Note that the solvent evaporation can be also performed at room temperature during 1 day.

This process has the advantage to be fast and cost-effective; it allows also the mass-production of humidity sensors at low-temperature. In addition, due to their small size, the resulting devices can be easily integrated in a microchip for industrial use. The characterisation of the resulting humidity sensors is described in the following parts.

3. Results

3.1. Characterization of the device geometry

Using the process described above, the large scale fabrication of humidity sensors has been successfully achieved. Figure 2a shows a matrix of 3x3 sensors. The interdigitated electrodes are 600 µm long and 60 µm wide, and they are separated by a gap of 50 µm (Figure 2b). Here, small electrode geometry was obtained compared to the standard printed sensors generally above 100 µm which is very important for restive-type sensor performances [8].

The screen-printed TiO_2 nanoparticles layer forms a rectangle of 1 mm wide and 1.5 mm long covering perfectly the surface of electrodes (Figure 2c)

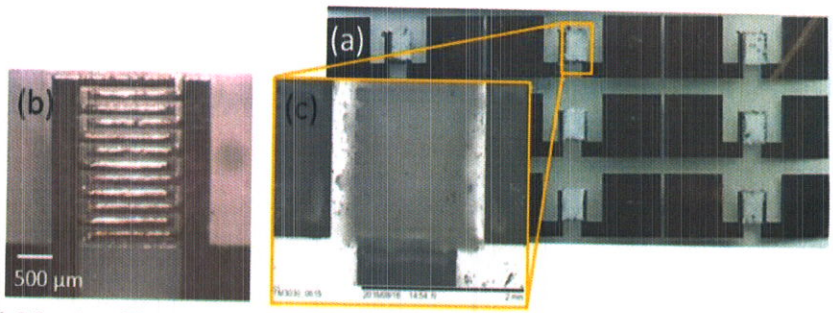

Figure 2 : (a) Matrix of humidity sensors fabricated on PET substrate. (b) Optical image of the intedigitated electrodes before the deposition of the TiO_2 nanoparticles. (c) SEM (scanning electronic microscope) picture of the TiO_2 layer screen-printed on the surface of electrodes.

3.2. Electrical characterization

Figure 2a shows the I–V characteristics of the humidity sensor and the patterned electrodes without coating of the sensitive layer measured at humidity levels of 12% and 40% using semiconductor parameter analyser. In Figure 3a, we can observe that the current did not flow on the unprocessed substrate implying that the PET substrate is an insulator. The I–V characteristics of the device with TiO_2 nanoparticles show Ohmic behaviour in both conditions, at 12% RH and 40% RH (Figure 3b). The resistance is constant over the supply voltages; the sensitivity is then identical regardless of the operation bias. In other words, a low voltage operation does not hinder the sensitivity which is essential for low power operation.

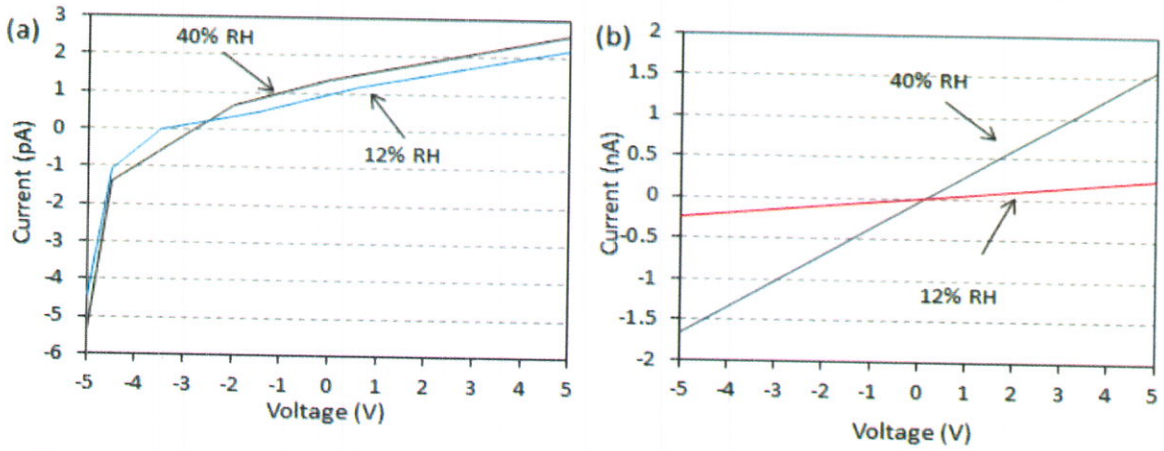

Figure 3: I–V characteristics measured under humidity levels of 12% and 40%, (a) for a device without TiO2 deposited on the electrodes, and (b) for a device with TiO_2 nanoparticles.

3.3. Humidity sensing properties

The humidity-sensing performances of the TiO_2-based sensors were investigated under various levels of relative humidity (RH) in a climatic test chamber with a control module (Hygrometer testo 608-H1) and at room temperature conditions (26°C). Figure 4a shows the sensor response when the relative humidity in the chamber was sequentially changing from 12% to 52% in periods of 10 min. The response curves are almost identical at a given humidity indicating repeatability of the results with a fast response time and almost immediate recovery. Figure 4b shows the resistance changes when the sensor was placed in different humidity conditions. In this figure, we can see that low concentration of humidity (24%) can be measured proving the ability of the sensors to be used for accurate humidity detection.

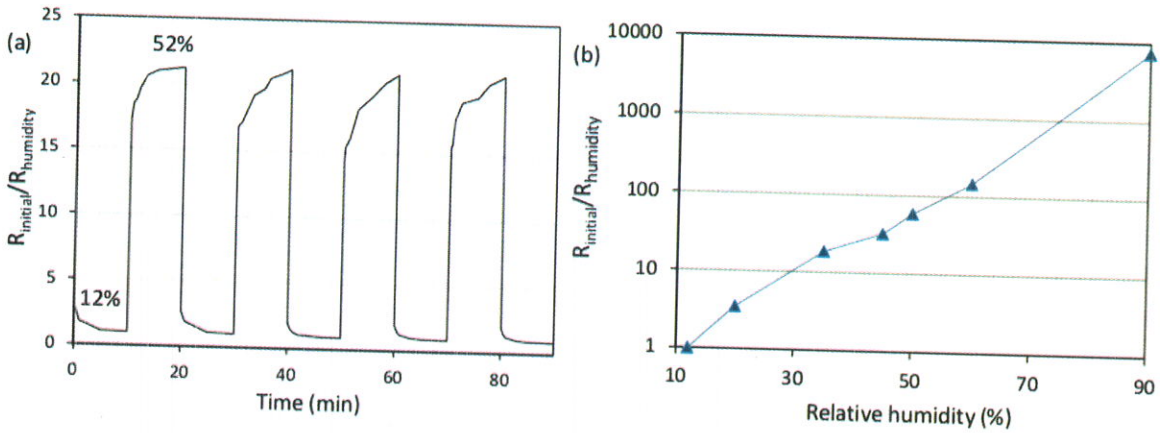

Figure 4: (a) Repeatability curves of the humidity sensor for humidity level variations from 12% to 52%. (b) Resistance changes of the sensor as function of the relative humidity.

4. Conclusion

The large-scale production of humidity sensors on flexible substrate was successfully achieved using a laser ablation method for the fabrication of micros-scale electrodes and a screen-printing technique for the patterning of the TiO2-based sensing material. Both methods are fast, cost-effective, and compatible with flexible substrate. This approach addresses the technological barriers that can hamper the development of chemical sensors on flexible substrates. In addition, the resulting humidity sensors exhibit high sensitivities in the range of 24 to 90% relative humidity and fast response and recovery times, which paves the way to large-scale fabrication of printed sensors on flexible substrate.

References

[1] Hu, Dai CL, Hsu CC 2014 *Sensors* **14** 4177-4188
[2] Zhang Y, Yu K, Jiang D, Zhu Z, Geng H, Luo L 2005 *Appl. Surf. Sci.* **242** 212–217
[3] Kuang Q , Lao C , Wang ZL, Xie Z , Zheng L 2007, *J. Am. Chem. Soc.* **129** 6070–6071
[4] McAlpine MC, Ahmad H, Wang D, Heath JR 2007 *Nat. Mater.* **6** 379-384
[5] Lai WH, Su YH, Teoh LG, Hon MH 2008 *J. Photochem. Photobiol. A* **195** 307–313
[6] Zheng ZQ, Yao JD, Wang B, Yang GW 2008 *Sci. Rep.* **5** 11070
[7] Dubourg G, Zlebic C, Matovic J, Bengin VC 2015 *Proc. Int. Conf on NEMS* 553-556
[8] Gerwen PV, Laureyn W, Laureys W, Huyberechts G, Op De Beeck M, Baert K, Suls J, Sansen W, Jacobs P, Hermans L, Mertens R 1998 *Sensor Actuat. B-Chem* **49** 1-2

Serbian Society for Innovative Materials in Extreme Conditions
Svetogorska 4, Vinča
11351 Belgrade
Republic of Serbia

Dr. Marko Radović
Group for Nano and Microelectronics
Biosense Institute
University of Novi Sad
Republic of Serbia

Date: 29.02.2020.

Dear Dr. Radović,

Your abstract entitled "Anatase nanoparticle films under extreme laser fluences" by Marko Radović, Georges Dubourg and Sanja Kojić has been accepted for presentation at 1st International Conference on Innovative Materials in Extreme Conditions (IMEC2020).

Your abstract, as well as all other accepted IMEC2020 contributions, will be included in The Book of Abstracts from 1st International Conference on Innovative Materials in Extreme Conditions - IMEC2020 (ISBN: 978-86-7306-158-8) published by Vinča Institute of Nuclear Sciences, University of Belgrade and Serbian Society for Innovative Materials in Extreme Conditions.

Thank you very much for your contribution.

SRPSKO DRUŠTVO ZA INOVATIVNE MATERIJALE U EKSTREMNIM USLOVIMA SIM-EXTREME BEOGRAD

President of the Serbian Society for Innovative Materials in Extreme Conditions
Dr Branko Matović

IMEC2020 1st International Conference on Innovative Materials in Extreme Conditions
19-20 March 2020, Belgrade, Serbia

Anatase nanoparticle films under extreme laser fluences

Marko Radovic[1], Georges Dubourg[1], Sanja Kojic[2]
[1]University of Novi Sad, Group for Nano and Microlectronics, Biosense Institute, Novi Sad, Serbia
[2]University of Novi Sad, Faculty of Technical Sciences, Novi Sad, Serbia

Conducted research introduces a rapid and cost-effective approach to technological processing of screen-printed films with anatase TiO_2 nanoparticles. The undertaken approach is based on the hierarchical combination of the screen-printing process and laser post-treatment. Investigation of surface morphology of screen-printed films revealed that higher laser fluences caused significant reduction in film thickness, trough evaporation of organic additives used in the paste matrix. EDX mapping of carbon content in untreated and laser sintered surface confirmed removal of organic additives. Laser sintering stimulated breaking of large agglomerates into much finer nano-sized particles and promoted formation of necking between individual grains. Crystal structure and vibrational properties of anatase TiO_2 nanoparticles was monitored with Raman spectroscopy before and after laser sintering. Obtained results point out that anatase polymorph was preserved during the sintering process, without appearance of other phases. From observation of the behavior of the most intense Eg Raman active mode, it was deduced that laser sintering provoked a formation of structural defects i.e. oxygen vacancies in TiO_2 nanoparticles, whose concentration increased in the samples treated with higher laser fluences. Mechanical properties of untreated and laser sintered samples were investigated with nanoindenter measurements using several load forces, in order to carefully probe the Young modulus and mechanical hardness. From the analysis of collected data, we established that overall improvement of the mechanical properties with laser sintering originates from formation of very dense ceramic layer with enhanced interconnectivity between individual TiO_2 nanoparticles. Measurements of current vs voltage characteristics clearly demonstrated that increase in laser fluence leads to drastic increase in current values and improvement of electric conductivity.

Developed processing technology was further exploited for fabrication of multifunctional devices printed on flexible substrates, with multisensing capability, which have attracted a lot of attention due to various applications, such as wearable electronics, soft robotics, interactive interfaces, and electronic skin design. The screen-printing is used for the patterning of silver interdigitated electrodes and the active layer based on TiO_2 nanoparticles, whereas the laser processing is utilized to fine-tune the UV and ethanol-sensing properties of the anatase active layer. Laser fluence was adjusted to enhance the electrical conductivity and optimize the UV photoresponse and ethanol-sensing characteristics at room temperature.

13th CONFERENCE for YOUNG SCIENTISTS in CERAMICS

PROGRAMME and BOOK OF ABSTRACTS

October 16-19, 2019
Novi Sad, Serbia

OC-85

ULTRA-SENSITIVE ELECTROCHEMICAL BIOSENSOR REALIZED USING LTCC TECHNOLOGY

Ivana Podunavac[1], Marko Radović[1], Jasmina Vidić[2], Goran Kitić[1], Vasa Radonić[1]

[1]*BioSense Institute, University of Novi Sad, 21000 Novi Sad, Serbia*

[2]*Micalis Institute, INRA, AgroParisTech, Université Paris-Saclay, France*

e-mail: ivana.podunavac@biosense.rs

Recently, biosensors found a number of applications in point-of-need diagnostics due to their high specificity and sensitivity, low-cost and fast response times. In this paper we propose a novel topology of electrochemical sensor realized using Low Temperature Cofired Ceramic (LTCC) technology.

We proposed electrochemical sensors based on three-electrodes (working, reference, and auxiliary). In the proposed design working electrode was realized in the shape of Sierpinski fractal gasket, while two other electrodes were realized to follow the curvature of the central electrode. In that manner the effective surface area between electrodes is increased resulting in increased sensitivity of the sensor.

The proposed sensor has been realized using a combination of a laser micromachining, screen printing, lamination, firing and spin coating processes. Design process startedwith the preparation of the substrate for the electrodes and with laser cutting of Ceram tape GC, glass ceramic based material. In the following step, gold conductive paste Heraeus TC7102 was deposited on the previously cut Ceram tape using screen printing process. After stacking of several supporting Ceram tape layers and layer with printed electrodes the whole structure was laminated in uniaxial press Carver 3895CEBunder the pressure of 1 t for 3 min at temperature of 75 °C. The sintering of the material has been performed using firing process in the oven at the maximal temperature of 865 °C, in total duration of ten hours. After firing the SU-8 resin was used to delimit the detection area enabling the use of very small sample volume (50 μL) for detection. The 3 μm resign was deposited using spin coating process trough protective mask and dried in oven at 95 °C for 2 min.

SEM TM3030 Hitachi was used for micrographs of fabricated electrodes, while the optical profilometer Huwitz HRM-300 was used for profiler analysis. The fabricated electrode was characterized using cyclic voltammetry (CV), and compared with commercial one. The applicability of the proposed sensor was demonstrated for detection of Campylobacter DNA sequence. The proposed electrochemical biosensor displayed good reproducibility and high stability, allows good immobilization of DNA and aptamers on the electrode surface and shows more 30 times better sensitivity in comparison with commercially available electrodes.

Book of Abstracts

14th International Conference
Advanced Carbon Nanostructures

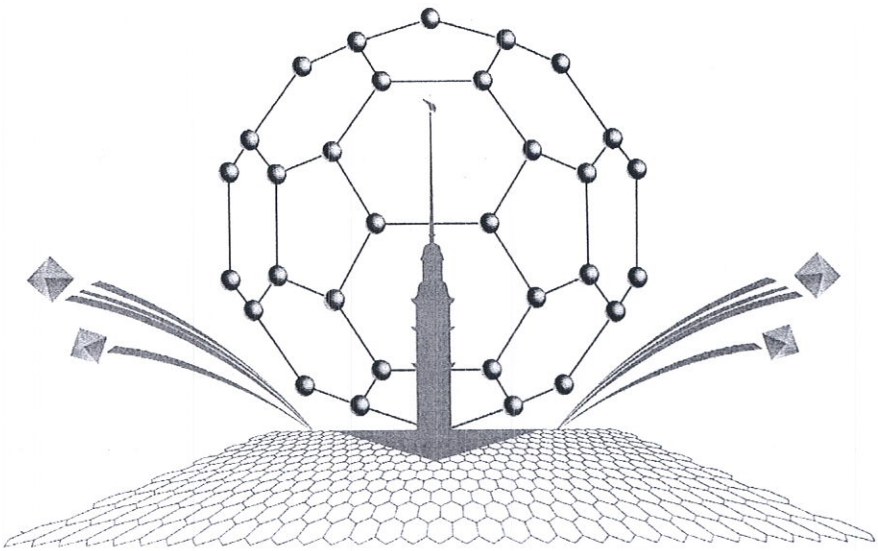

ACNS'2019

July 1 – 5, 2019
St Petersburg, Russia

Graphene & related materials

Cost efficient processing of GO for sensing applications

Marko Radovic [1] , *Ivan Bobrinetskiy* [1] , *Nikita Nekrasov* [2] , *Nikolay Struchkov* [2]

marrad@biosense.rs

[1] University of Novi Sad, Biosense Institute, Novi Sad, Serbia

[2] National Research University of Electronic Technology, Zelenograd, Russia

Constant scientific and technological advancements have imposed a staggering demand for scalable, robust and low cost solutions for design and fabrication of graphene based devices. Carried out research introduces a bottom-up approach (Figure 1), involving GO ink preparation, optimization of inkjet printing parameters, laser reduction and characterization of GO layer on micron-sized Au electrodes, for application in humidity and gas sensing.

The initial step in the research activities was to optimize the functional dispersion of GO flakes for inkjet printing. Optimization was performed by selection of additives, in order to reduce the surface potential and to obtain printed structures with desired thickness and morphology. Inkjet processing was performed on Fujifilm Dimatix DMP-3000 printer equipped with piezo controlled head, for drop-on-demand operation. Printed layer was incrementally treated by laser radiation for spatial reduction of GO and removal of additives. Main idea behind the laser treatment processing was to obtain gradient in conductivity of the laser reduced GO (LrGO) layer for application in sensing technologies. Raman spectroscopy was utilized as the most powerful probe for investigation of chemical bonding and presence of impurities in the graphene-based samples. From the obtained measurements of D band signature it was established that different levels of laser reduction can be achieved by precise control of the laser power and irradiation time. The resistance of LrGO was measured for each pair of electrodes with different LrGO modified by various duration of laser pulses. The initial resistance of GO channel was about 10 MOhms. Onset of decrease in resistance starts at 80 mW, going down to about 200 kOhms at 130 mW. Varying the time irradiation we demonstrated the decreasing of resistance down to 100 Ohms. For laser powers higher than 200 mW ablation process occurs, as detected by AFM. Investigated device demonstrates good sensitivity to humidity with fast response/recovery times.

From the analysis of obtained results it was established that undertaken approach offers cost-efficient solution to processing of GO nanomaterials for application in advanced technologies.

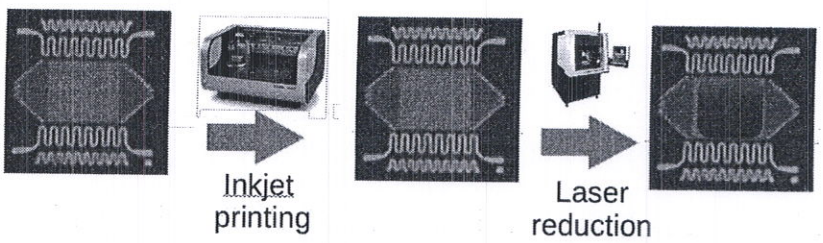

Figure 1. Schematic representation of cost efficient processing of GO on Si chip with interdigitated electrodes and heater elements.

16-20 JUNE 2019
LISBON
PORTUGAL

6th NANO TODAY CONFERENCE

nanotoday-conference.com

PROGRAM

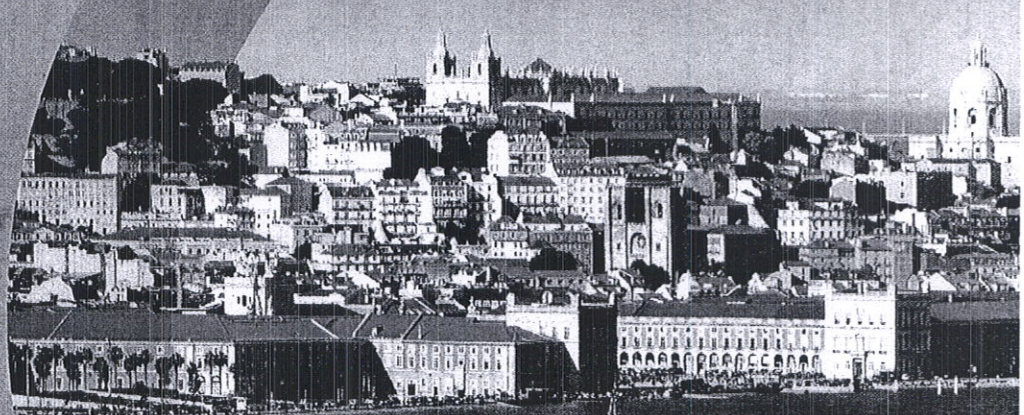

ELSEVIER

materialstoday
Connecting the materials community

[P1.9]

Enhanced structural and mechanical properties of laser modified titanium dioxide nanoparticles

M. Radovic*[1], G. Dubourg[1], S. Kojic[2], Z. Dohcevic-Mitrovic[3], B. Stojadinovic[3]

[1]University of Novi Sad, Biosense Institute, Serbia, [2]University of Novi Sad, Faculty of Technical Sciences, Serbia, [3]Institute of Physics Belgrade, Serbia

Surface morphology investigation of screen-printed films with TiO_2 nanoparticles, revealed that laser treatment has dual effect: 1) Evaporation of organic additives that were used in the printing paste matrix and 2) Laser-sintering of anatase TiO_2 nanoparticles. SEM/EDX mapping of organic species confirmed removal of organic additives at higher laser fluences, as a decrease of carbon content. Chemical composition and crystal structure was monitored with Raman spectroscopy before and after laser sintering. Obtained results point out that anatase polymorph was preserved during the sintering process, without appearance of other phases. From the behavior of the most intense E_g Raman active mode it was deduced that laser sintering provoked a formation of structural defects i.e. oxygen vacancies in TiO_2 nanoparticles. Mechanical properties were investigated with nanoindenter measurements using several load forces, in order to carefully probe the Young modulus and mechanical hardness. Overall improvement of the mechanical properties with laser sintering originates from formation of very dense ceramic layer with enhanced interconnectivity between individual TiO_2 nanoparticles. Increase in Young modulus and mechanical hardness with laser fluence is directly related to the sintering effect. Electrical conductivity of laser sintered samples were investigated by measuring the current vs voltage characteristics. Obtained results clearly demonstrated that increase in laser fluence leads to drastic increase in current values. Evaporation of organic components with laser treatment introduced better connectivity between particles, giving rise to superior electronic transport properties. Analysis of all the collected data clearly indicates that laser treatment leads to significant improvement of structural and mechanical properties of the screen-printed films, paving the road which leads from basic research to applications in advanced technologies.

Keywords: Laser sintering, TiO2, Mechanical properties

JOINT EVENT

November 2018 | Volume 9 | ISSN: 2157-7439 | Journal of Nanomedicine & Nanotechnology

PROCEEDINGS OF

28th International Conference and Expo on

Nanoscience and Nanotechnology

&

3rd World Congress and Expo on

Graphene & 2D Materials

NOVEMBER 26-28 | 2018

BARCELONA SPAIN

Marko Radović, J Nanomed Nanotechnol 2018, Volume 9
DOI: 10.4172/2157-7439-C1-NSN-GWW-018

Synthesis and screen-printing of SnO2 nanoparticles on flexible PET substrate for cost-efficient ethanol sensors

Marko Radovic

BioSense Institute, University of Novi Sad, Serbia

The presented research is a bottom-up approach involving synthesis, characterization and application of SnO2 nanomaterials in advanced technologies such as ethanol gas sensing. Tin oxide nanoparticles were synthesized with hydrothermal method, followed by calcination in ambient conditions at 550C. Characterization of structural properties with X-ray diffraction (XRD) technique revealed that synthesized sample has rutile crystal structure with crystallite size in nanometer range. SEM images of prepared sample unveiled that SnO2 nanopowders consist of spherical nanoparticles which are composed of agglomerated crystalls. Synthesized powder was screen-printed on flexible polyethylene terephthalate (PET) substrate with Ag interdigitated electrodes (IDE) for electrical measurements and integration in sensor platforms. Electrical characterization in DC regime revealed that SnO2 sample has very good conductivity for oxide material. The Cole-Cole plots, extracted from AC measurements, exhibited single semi-circle characteristic for grain boundary conduction. Gas sensing performance was evaluated at room temperature through detection of ethanol vapor. The obtained results indicated that synthesized and screen printed SnO2 nanoparticles have good and stable sensitivity with linear dependence on the concentration of target gas. The utilized multidisciplinary approach offers a very good alternative to fabrication of chemical gas sensors which are functionalized on rigid and expensive platforms like silicon or ceramics.

Biography

Marko Radovic has completed his PhD from Faculty of Physics at University of Belgrade, Serbia. He has published more than 20 papers in reputed journals.

marrad@biosense.rs

Notes:

3rd International Meeting

on

Materials Science for Energy Related Applications

held on September 25-26, 2018

at the University of Belgrade, Faculty of Physical Chemistry,

Belgrade, Serbia

is a satellite event of

PHYSICAL CHEMISTRY 2018

14th International Conference on Fundamental and Applied Aspects of Physical Chemistry

organized by

KTH
ROYAL INSTITUTE OF TECHNOLOGY
Stockholm, Sweden

UNIVERSITY OF BELGRADE
FACULTY OF PHYSICAL CHEMISTRY
Belgrade, Serbia

in co-operation with

THE SOCIETY OF PHYSICAL CHEMISTS OF SERBIA

Funded by

Swedish Research Council

INFLUENCE OF Co DOPING ON OPTICAL AND PHOTOCATALYTIC PERFORMANCES OF $SnO_{2-\delta}$ NANOCRYSTALS

S. Aškrabić[1], Z.D. Dohčević-Mitrović[1], V.D. Araújo[2], M. Radović[3], G.R. Costa[4], M.I.B. Bernardi[4], M.G. Nikolić[1]

[1]*Institute of Physics Belgrade, University of Belgrade, Belgrade, Serbia*
[2]*UACSA, UFRPE, BR 101 Sul, 5225, CEP 54510-000 Cabo de Santo Agostinho, PE, Brazil*
[3]*Nano and Microelectronics Group, BioSense Institute, Novi Sad, Serbia*
[4]*Instituto de Física de São Carlos, Universidade de São Paulo, USP, 13560-970, São Carlos – SP, Brasil*

Tin oxide (SnO_2) is a n-type semiconductor with large band gap (3.6 eV) at room temperature. Electronic, optical and electrochemical properties of SnO_2 promote itswide application in solar cells, catalysis, transparent conductive electrodes, solid state sensors, rechargeable Li batteries and optical electronic devices [1,2]. The mentioned properties are very much influenced by the presence of defects, particularly oxygen vacancies that introduce donor states inside the band gap, but also change optical and other properties that depend on the electronic structure [3]. These newly formed electronic states can also influence the photocatalytic activity of SnO_2. This work intends to explore how the doping with Co^{2+} ions influences the optical and photocatalytic properties of $SnO_{2-\delta}$nanopowders. It is expected that divalent Co ions would create more oxygen vacances changing the electronic structure of SnO_2 which can have a strong impact on potential applicability of these materials for organic pollutant remediation processes.

Undoped and Co-doped $SnO_{2-\delta}$ nanopowders (δ=0, 1, 3 and 5 mol%) were synthesized using microwave-assisted hydrothermal method. X-ray diffraction analysis confirmed the single phase tetragonal structure of the samples composed of very fine nanocrystals. Average crystallite size decreased with increased Co doping (from 2.5 nm in undoped sample to 2.2 nm in 5 % Co doped sample), implying that Co doping has an inhibiting effect on the crystal growth. In the Raman spectra of pure and Co-doped $SnO_{2-\delta}$, confinement effect strongly influenced the position and bandwidth of Raman modes. New modes, ascribed to defect modes, were present in undoped sample and were more intense than the Raman modes characteristic for tetragonal rutile SnO_2 [4]. The intensity of these modes decreased with Co doping.

Observed band gap broadening with Co doping, deduced from the results of spectroscopic ellipsometry, is partly ascribed to spatial confinement, but the Burnstein-Moss effect had significance influence on the band gap increase in these samples. From the band gap shift due to Burstein-Moss effect, the concentration of charge carriers was estimated. It was shown that doping of $SnO_{2-\delta}$ nanocrystals with Co^{2+} ions caused an increase in concentration of charge carriers and shift of the optical absorption edge toward UV region. PL spectroscopy is convenient method to investigate the defect structure of undoped and Co-doped $SnO_{2-\delta}$samples. In the PL spectrum of undoped $SnO_{2-\delta}$dominate two bands at 510 nm and 575 nm which can be ascribed to the in-plane oxygen vacancy defects and bridging oxygen vacancy defects. Co doping induced complete reduction of PL intensity. Even the smallest percent of Co doping almost completely quenched the luminescence. It is already known that Co^{2+} ions can act as luminescence quenchers for metal oxides like TiO_2 or ZnO, decreasing the intensity of PL emission by forming large number of nonradiative centers [5-7]. Therefore, it can be inferred that Co dopantacts as luminescence quencher for $SnO_{2-\delta}$nanocrystals too. The photocatalytic activity of pure and Co-doped $SnO_{2-\delta}$ nanopowders under UV light was investigated by the decomposition of methylene blue. The best photocatalytic performances exhibited undoped $SnO_{2-\delta}$, whereas increased Co doping reduced the photocatalytic activity. The reduction of the photocatalytic activity by Co-doping can be explained by introduction of band gap energy levels between the valence and conduction bands that would act as efficient recombination centers for photo-generated electron-hole pairs,decreasing their lifetime and giving the charge carriers less chance to generate free radicals on particle surfaces involved in the photocatalytic degradation of methylene blue.

References

[1] L. H. Jiang *et al.*, J. Phys. Chem. B, 2005, 109, 8774.
[2] J. Lee *et al.*, J. Nanosci. Nanotechno.2016, 16, 4973.
[3] M. Batzill and U. Diebold, Prog. Surf. Sci., 2005, 79, 47.
[4] A. Dieguez *et al.*, J. Appl. Phys., 2001, 90, 1550.
[5] V. Bonu *et al.*, Phys. Chem. Chem. Phys.,2015, 17, 9794.
[6] B. Choudhury and A. Choudhury, J. Lumin., 2012, 132, 178.
[7] S. Yamamoto, J. Appl. Phys., 2012, 111, 094310-1-6.

3rd International Meeting

on

Materials Science for Energy Related Applications

held on September 25-26, 2018

at the University of Belgrade, Faculty of Physical Chemistry,

Belgrade, Serbia

is a satellite event of

PHYSICAL CHEMISTRY 2018

14th International Conference on Fundamental and Applied Aspects of Physical Chemistry

organized by

KTH
ROYAL INSTITUTE OF TECHNOLOGY
Stockholm, Sweden

UNIVERSITY OF BELGRADE
FACULTY OF PHYSICAL CHEMISTRY
Belgrade, Serbia

in co-operation with

THE SOCIETY OF PHYSICAL CHEMISTS OF SERBIA

Funded by

Swedish Research Council

STABILITY OF F-CENTER DEFECTS DURING THE THERMAL TREATMENT OF NANOCRYSTALLINE CeO_{2-y}

B. Stojadinović[1], M. Radović[2], N. Tadić[3], S. Stojadinović[3], I. Belča[3], Z. Dohčević-Mitrović[1*]

[1]*Laboratory for nanocomposite structures and biovibrational spectroscopy, Institute of Physics, University of Belgrade, Belgrade, Serbia*
[2]*Nano and Microelectronics Group, BioSense Institute, Novi Sad, Serbia*
[3]*Faculty of Physics, University of Belgrade, 11000 Belgrade, Serbia*

The formation of different F center defect states inside the ceria gap have a strong impact on the
optical, catalytic, and magnetic properties of ceria nanocrystals [1-4]. These types of defects are
registered in various oxide nanomaterials, such as MgO [5] HfO_2 [6] and TiO_2 [7] and are usually formed at the nanoparticle surface during the process of synthesis. Non-stoichiometry at normal atmospheric conditions is more pronounced in nanocrystalline CeO_{2-y} composed of very small crystallites [8], due to the increase of surface-to-volume ratio of the nanocrystals, which reduces the formation energy of oxygen vacancies positioned close to a crystallite surface. Therefore, particle size has important influence on the formation of oxygen vacancy defects. The presence of oxygen nonstoichiometry in nanocrystalline CeO_{2-y} yields mix valence state of Ce ions. Namely, excess electrons that are left behind an oxygen release can be localized on 4f states of Ce ions changing the valence state of Ce^{4+} ions to Ce^{3+}, or can be localized on the oxygen vacancies forming F centers [9]. In this paper we focused our attention to the influence of annealing process on the microstructural changes of nanocrystalline CeO_{2-y} and stability of
oxygen vacancy defects *i.e.* F center defects. Nanocrystalline CeO_{2-y} powders were synthesized
by the self-propagating room temperature method (SPRT) and were annealed in air at different
temperatures in the range 200 – 800 °C. Structural and vibrational properties were investigated
by X-ray diffraction and Raman spectroscopy methods. Scanning tunneling microscopy/spectroscopy (STM/STS) have been employed to probe the electronic properties of
as-prepared and annealed CeO_{2-y} samples, because STM/STS can get more accurate relation between particle size and electronic properties compared with optical spectroscopy. X-ray diffraction analysis demonstrated that all

samples crystallized into fluorite type structure of CeO_2 and no amorphous or any other phase was detected. As-prepared CeO_{2-y} was composed of very small crystallites with the highest strain value due to the increased oxygen vacancy concentration and presence of Ce^{3+} ions. In annealed samples, crystallite size and microstrain significantly changed above 400 °C. The crystallite size was increased from 2.2 (as -prepared sample) to 44 nm (sample annealed at 800 °C). Microstrain values in the CeO_{2-y} samples annealed at higher temperatures decreased with increasing temperature of annealing, pointing at improved stoichiometry of these samples. Analysis of the Raman spectra has shown that the concentration of oxygen vacancies was the largest in as -prepared CeO_{2-y} sample and drastically decreased in samples annealed at 600 °C and 800 °C. STS spectra revealed that besides the filled and empty *4f* states ($4f^1$and $4f^0$states), different types of F center defects states were formed inside the band gap of as-prepared CeO_{2-y}. These additional states were ascribed to occupied and empty F^+ and F^0 center defect states [10]. With increasing of the annealing temperature up to 400 °C only the F^0 center defect states subsisted, whereas the localized F^+ states disappeared. In the sample annealed at 600 °C, F^0 states were barely visible whereas $4f^1$ and $4f^0$ states were shifted towards the valence and conduction band leading to the increase of the band gap. In the CeO_{2-y} sample annealed at 800 °C no evidence of *4 f* or defect states was present and the band gap approached the value of 4.3 eV. It can be concluded that readsorption of oxygen on the F^0 defects is much slower than that on the F^+ defects. At temperatures above 600 °C, the CeO_{2-y} oxygen vacancies were healed by oxygen intake, resulting in the improved stoichiometry of the temperature treated samples. These observations gave a new insight for understanding the reconstruction of defect sites at CeO_{2-y} surface at higher temperatures.

References

[1] L. Truffault *et al.*, J. Nanosci. Nanotechnol. 2011, 11, 4019.
[2] A. Corma *et al.*, Nature Mater. 2004, 3, 394.
[3] A. Trovarelli, Catalysis by Ceria and Related Materials, Imperial College Press, London, 2002.
[4] N. Paunović *et al.*, Nanoscale 2012, 4, 5469.
[5] T. König *et al.*, J. Am. Chem. Soc. 2009, 131, 17544.
[6] D. Muñoz Ramo *et al.*, Phys. Rev. B 2007, 75, 205336.
[7] N. Serpone, J. Phys. Chem. B 2006, 110, 24287.
[8] S Aškrabić *et al.*, J. Raman Spectrosc. 2012, 43 (1), 76.
[9] Xiaoping Han *et al.*, Phys. Rev. B 2009, 79, 100403(R).
[10] M. Radović *et al.*, J. Appl. Phys. 2014, 116, 234305.

12th CONFERENCE for YOUNG SCIENTISTS in CERAMICS

PROGRAMME and BOOK OF ABSTRACTS

October 18-21, 2017
Novi Sad, Serbia

OA-8

PREPARATION OF ZnO DISPERSIONS SUITABLE FOR SENSORS FABRICATION USING INKJET PRINTING

N. Omerović[1], S.M. Savić[2], M. Radović[2], J. Katona[1]
[1]*Faculty of Technology, University of Novi Sad, Novi Sad, Serbia*
[2]*Biosense Institute, University of Novi Sad, Novi Sad, Serbia*
e-mail: nejra.omerovic@hotmail.com

Inkjet printing enables a digitally controlled ejection of picoliter-sized droplets and their precise positioning onto a variety of substrates. Therefore, it shows great promise to be the right deposition technology used in applications such as electronic devices and displays, sensors or solar cells. For successful implementation of the technology the key element is precise chemical formulation of inkjet ink, which should be stable, printable and functional. Basically, functional inkjet inks are dispersions of materials with semiconducting, conducting, luminescent or magnetic functionalities. In this work, stable dispersions of ZnO nanoparticles were prepared using gum arabic (GA; natural polyanionic polysaccharide with carboxylic groups as anchors) and Solsperse® 40 000 (anionic phosphated alkoxylated polymer of Lubrizol) as dispersants. After adding an appropriate amount of ZnO in an aqueous solution of dispersant (GA or Solsperse), ball milling was performed in a Retch PM 100 planetary mill at a constant milling speed of 250 rpm using a YSZ (Yttrium Stabilized Zirconia) jar and balls. The effect of different milling times (15, 30, 60, 90, 120, 150 and 180 min) on average particle sizes and on particle size distribution was investigated. Inks were prepared by diluting ZnO dispersions with water and adding 1, 2-propylene glycol and n-propanol in appropriate ratios. An ageing test of 3 weeks for both dispersions and inks was performed. Prepared inks were printed as a sensitive sensor layer using a Fuji Dimatix DMP-3000 inkjet printer. After optimization of the basic printing parameters such as jetting voltage, frequency and waveform, stable droplets of prepared inks were obtained. Sensor fabrication was conducted in two steps. In the first step, interdigitated electrodes of commercial silver were printed on PET substrate, and in the second step 10 layers of functional ZnO inks were printed on top of the electrodes. Electrical characterization and humidity response measurements revealed that sensors with Solsperse dispersant possessed better electrical properties in comparison to GA and a very good response to high humidity levels with fast response times.

NINETEENTH ANNUAL CONFERENCE

YUCOMAT 2017

Hunguest Hotel Sun Resort Herceg Novi, Montenegro,
September 4-8, 2017
http://www.mrs-serbia.org.rs

Programme
and
The Book of Abstracts

Organised by:
Materials Research Society of Serbia

Endorsed by:
Materials Research Society,
European Materials Research Society
and
Federation of European Material Societies

O.S.IV.2.

Inkjet printing of TiO_2 nanoparticles on flexible substrates

Slavica M. Savić[1], Sanja Kojić[2], Jaroslav Katona[3], Jelena Vukmirović[3], Georges Dubourg[1], George Niarchos[1], Marko Radović[1]
[1]Biosense Institute, Research Institute for Information Technologies in Biosystems, Novi Sad, Serbia, [2]Faculty of Technical Sciences, University of Novi Sad, Novi Sad, Serbia, [3]Faculty of Technology, University of Novi Sad, Novi Sad, Serbia

The presented research focuses on development of functional dispersion of TiO_2 nanoparticles in the form of ink, which could be used for the inkjet printing of thin films on various substrates. Arabic gum from acacia tree was used to control the viscosity of the prepared ink and to serve as binder for nanoparticles on the surface of substrate. Particle size distribution measurements with Z-sizer revealed that TiO_2 nanoparticles have uniform distribution centered at around 120 nm. In order to determine the most suitable substrate for printing of the ink, water contact angle measurements were performed on Si, kapton and PET surfaces. The deposition of the ink was carried-out with Dimatix DMP-3000 piezo-controlled inkjet printer. Several layers of nanoparticles were printed on interdigitated electrodes in order to determine the optimal number of layers which will yield best electrical and humidity sensing performance. The characterization of electrical properties of the printed thin films was performed in the DC regime. Printed films were tested as humidity sensor components and obtained results point out to high sensitivity towards humidity with relatively fast response/recovery times.

O.S.IV.3.

Photocatalytic hollow TiO_2 and ZnO nanospheres prepared by atomic layer deposition

László Péter Bakos[1], Nóra Justh[1], Klára Hernádi[2], Gabriella Kiss[2], Balázs Réti[2], Zoltán Erdélyi[3], Bence Parditka[3] and Imre Miklós Szilágyi[1]
[1]Department of Inorganic and Analytical Chemistry, Budapest University of Technology and Economics, H-1111 Budapest, Hungary, [2]Department of Applied and Environmental Chemistry, University of Szeged, H-6720 Szeged, Hungary, [3]Department of Solid State Physics, University of Debrecen, H-4026 Debrecen, Hungary

In our research, carbon nanospheres were prepared by hydrothermal synthesis, and coated with TiO_2 and ZnO nanofilms using atomic layer deposition. Subsequently, through burning out the carbon core templates hollow metal oxide nanospheres were obtained. The substrates, the carbon-metal oxide composites and the hollow nanospheres were characterized with TG/DTA-MS, FTIR, Raman, XRD, SEM-EDX, TEM-SAED and their photocatalytic activity was also investigated. The results indicate that carbon nanospheres are not beneficial for photocatalysis, but the crystalline hollow metal oxide nanospheres have considerable photocatalytic activity.

ECerS2017

15th Conference & Exhibition of the European Ceramic Society

July 9–13, 2017, Budapest, Hungary

BOOK OF ABSTRACTS

AKCongress

sintered sample, combined symmetry of rhombohedral and orthorhombic with R3c (61.06%) and Pbam (34.94%) was deduced by the best fits. With increasing sintering time to 3 hour, orthorhombic phase (59.91%) leads over rhombohedral R3c phase (40.06%). Enormous enhancement was observed in the magnetization with increasing the sintering time. Such robust change in the magnetic properties may be attributed to the increase in canting angle of spins.

542

The influence of the dispersants on printing ink properties of metal oxides nanoparticles

Slavica M. Savić[1*], *Jaroslav Katona*[2], *Marko Radović*[1], *Jovana Stanojev*[1], *Georgios Niarchos*[1], *Georges Dubourg*[1], *Vesna Crnojević-Bengin*[1]

[1]Biosense Institute, University of Novi Sad, Zorana Đinđića 1, 21000 Novi Sad, Serbia;
[*]e-mail: slavicas@biosense.rs
[2]Faculty of Technology, University of Novi Sad, Bulevar Cara Lazara 1, 21000 Novi Sad, Serbia

Keywords: metal oxides, dispersants, milling, inkjet printing

Colloidal stability of inkjet printing inks is one of the key parameters for their good printing performance. The stability of particles dispersed in water–based inks is usually achieved by electrostatic, steric, or electrosteric stabilization. Adsorption of polyelectrolytes of increased molecular weight at the solid interface of dispersed particles is responsible for electrosteric stabilization. In this work, stable homogeneous suspensions of MOx (TiO_2 and ZnO) were prepared using gum arabic (GA) and solsperse 40000 as dispersants. GA is a natural polyanionic polysaccharide with carboxylic groups as anchors, while Solsperse 40000 is an anionic phosphated alkoxylated polymer of Lubrizol. Both dispersants provide electrosteric stabilization of pigments in water based inks. GA was employed as dispersant to study the effect on the surface properties of MOx nanoparticles. GA has been used as the stabilizing agent for ink pigments for a long time. It is well known that GA can make the MOx nanoparticles have a good dispersibility and stability in GA colloidal solution for its low viscosity. The investigations on the optimum concentration of dispersants and the mechanism determining the dispersion behavior of MOx in aqueous dispersants solution were performed. Suspensions of MOx and GA/Solsperse were prepared first by dissolving dispersants in water. MOx were added in appropriate amounts. The weight ratio between MOx and GA (solsperse) was varied from 1/1 to 3.5/1. The ball milling was performed in a Retch PM 100 planetary ball mill at constant milling speed of 250 rpm using YSZ jar and balls. The effects of different milling time (15, 30, 60, 90 and 180 min) on average particle sizes were investigated. Results show improved dispersion with reduction of average particle sizes with increasing of milling time. Different ink formulations composed of MOx/dispersants (with addition of 1, 2 propylene glycol and n-propanol) were prepared and their printability properties were tested using Inkjet printer Fuji Dimatix DMP-3000. The main goal of this work is to analyse the influences of different quantity of dispersants and milling conditions on the printing quality parameters of the ink using different substrates.

IBSC

The International Bioscience Conference and
the 6th International PSU–UNS Bioscience Conference - IBSC 2016
19-21 SEPTEMBER 2016, NOVI SAD, SERBIA

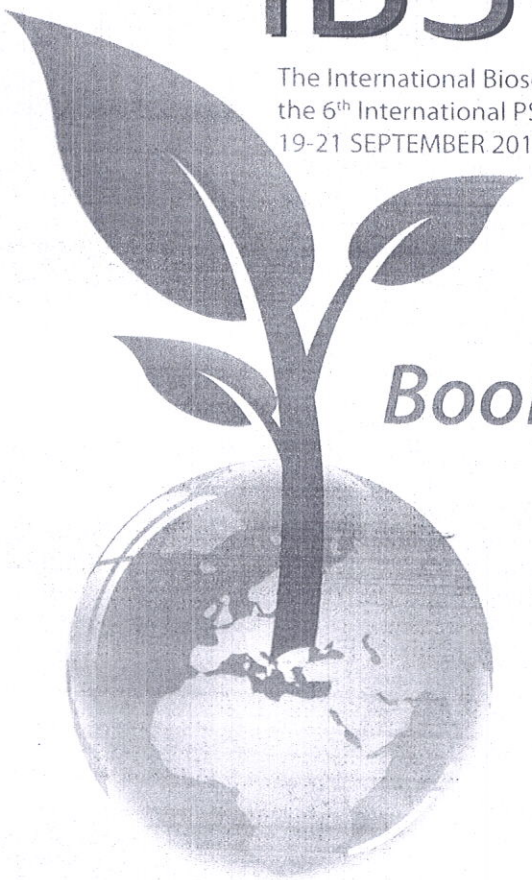

Book of Abstracts

IBSC2016 is organised jointly by:

University Prince of Songkla,
Thailand

University of Novi Sad,
Faculty of Sciences,
Serbia

ibsc2016.pmf.uns.ac.rs

T3-P-3

CHARACTERISATION OF SCREEN-PRINTED TIO2 NANOPARTICLES ON FLEXIBLE SUBSTRATE FOR HUMIDITY SENSING

Georges Dubourg[1], Marko Radović[1], Slavica M. Savić[1], George Niarchos[1], Goran Kitić[1], Tamara B. Ivetić[2], Massere Doumbia[1], Nikolina Janković[1] and Vesna Crnojević-Bengin[1]

[1] *Biosense Institute, University of Novi Sad, Serbia*
[2] *Department of Physics, Faculty of Sciences, University of Novi Sad, Serbia*

**Corresponding author: georgesdubourg@uns.ac.rs*

KEYWORDS: Nanomaterials; flexible substrate; humidity sensor; screen-printing.

INTRODUCTION: Printed electronics on flexible substrates using electrically functional inks is an emerging technology nowadays. Fabrication of printed electronic sensors has many advantages such as low-cost, lightweight, and being bendable, rollable, portable and foldable. In parallel, the increasing concern about environmental protection and food quality control has resulted in a continuous expansion in chemical sensor development and an important interest is now given to the production of cost effective, flexible, disposable and highly sensitive gas sensors. Although numerous types of printed chemical sensors have been established in agriculture, their introduction in the market has not yet been accomplished, and they are still remaining in the laboratories. A key parameter is the deposition of sensing materials that can be adapted to the printed electronics technological processes, such as printing methods since the active layer is usually deposited by spin-coating or micropipette drop casting, both of them methods which are not yet quite adapted for large-scale fabrication.

OBJECTIVES: The objectives of this work are the fabrication and characterization of chemical sensors using printed metal oxide nanoparticles as sensitive layers. Here, we present the production of humidity sensors using a screen-printing method for the deposition of TiO_2 nanoparticles.

METHOD / DESIGN: The humidity sensor consists of TiO2 nanoparticles screen-printed on top of interdigitated electrodes (IDEs) patterned on flexible substrate. The design of the sensors is simple and does not require the high-cost semiconductor manufacturing equipment and high temperature steps normally used for silicon microfabrication. Initially, a gold layer was deposited by electron-beam evaporation on commercial PET substrate. Afterwards, the resulting layer was directly patterned by laser ablation using a short pulse laser (Nd:YAG-1064 nm, Rofin), in order to create microscale interdigitated electrodes.TiO_2 anatase nanoparticles (Sigma-Aldrich, particle size 21nm) were used as the sensitive layer. A paste was prepared by homogenizing TiO_2 nanopowder and ethanol in a Retsch PM100 planetary ball mill. The homogenization was performed in a continual regime using YSZ (yttrium stabilized zirconia) balls (2 mm in diameter) with the constant disc rotation speed of 300 rpm for 3h.